APPLICATIONS OF POWDER INTERLAYERS FOR LARGE GAP JOINING

By
Wei-Dong Zhuang

S. B. Shanghai Jiao Tong University, 1988
S. M. Shanghai Jiao Tong University, 1991

Submitted to the Department of
Materials Science and Engineering
in Partial Fulfillment of the Requirements
for the Degree of

Doctor of Philosophy
in
Metallurgy

at the

Massachusetts Institute of Technology

February 1997

© 1997 Massachusetts Institute of Technology
All rights reserved

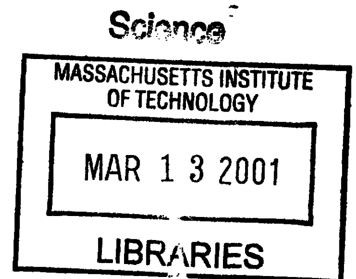

Signature of Author................
Department of materials Science and Engineering
January 10, 1997

Certified by..
Thomas W. Eagar
Department of Materials Science and Engineering
Thesis Supervisor

Accepted by..
Linn W. Hobbs
John F. Elliot Professor of Materials
Chair, Departmental Committee on Graduate Students

MASSACHUSETTS INSTITUTE
OF TECHNOLOGY
Science
LIBRARIES

Applications of Powder Interlayers for Large Gap Joining

by

Wei-Dong Zhuang

Submitted to the Department of Materials Science and Engineering
on January 10, 1997 in partial fulfillment of the requirements for the
Degree of Doctor of Philosophy in Metallurgy

Abstract

Large gap joints are frequently encountered in the manufacturing of massive components as well as in the repairing of damaged parts. Several methods using powder interlayers to produce large clearance transient liquid phase (TLP) joints have been developed and investigated in this work. One of the methods was using a mixture of powders of the melting point depressant (MPD) and the base material, from which a great amount of MPD (>30 vol.%) usually has to be used to eliminate residual porosity. To reduce the MPD in the joint, the liquid infiltrated powder interlayer bonding (LIPB) process was developed. For a material system that has a large mutual solubility between the liquid and the solid at the bonding temperature, a protective coating on the particles of the base material was applied to avoid excessive dissolution and inhibit early diffusional solidification, which can block the infiltration paths and prevent full infiltration. Direct coating of the MPD on the particles of the base material proved highly effective in producing tough and strong joints for certain material systems.

The classic liquid phase sintering (LPS) theory was adopted to explain the physical process as occuring in the powder interlayer during joining. Despite the general applicability of the theory, there are several other important factors have to be considered as well. For example, the reaction rate between the MPD and the base material can markedly affect the densification of a mixed powder interlayer. Fast growth of the intermetallic compounds as a result of reaction can significantly retard the liquid flow. For the infiltration process, kinetics of dissolution and diffusional solidification largely depend on the mutual solubility between the liquid (infiltrant) and the solid (powder interlayer). Dissolution is needed to open up closed pores in the powder interlayer. However, excessive dissolution is undesirable due to fast liquid saturation and subsequent diffusional solidification, which may prevent complete infiltration of the interlayer. A protective coating on the particles of the base material provides a way of reducing the dissolution rate, which facilitates full infiltration of the interlayer. The solubility factor is also crucial for direct coating of the MPD on the particles of the base material. Higher solubility of the base material in the MPD is preferred to maintain enough liquid for complete densification.

Experiments were performed on joining the materials including titanium alloy, Ti-6Al-4V, nickel base superalloy, Inconel 625, stainless steel, SS304, and commercially pure copper. Application of the particular joining process depends on careful choice of the MPD, the base powders as well as the geometry of the interlayers.

Thesis Supervisor: Prof. Thomas W. Eagar
Title: POSCO Professor of Materials Engineering
Head of the Department of Materials Science and Engineering

Table of Contents

Abstract.....2
List of Figures.....6
List of Tables.....16
List of Acronyms.....17
List of Symbols.....18
Acknowledgements.....23

1. Applications of Metal Powders for Joining Processes.....24
1.1 Introduction.....24
1.2 Characteristics of Metal Powders.....24
1.3 Applications to Welding Processes.....25
1.4 Applications to Brazing and Soldering.....27
1.5 Applications in Special Joining Processes.....28
1.6 Present Investigations.....29
1.7 Summary.....32
1.8 References.....32

2. Infiltration of Liquid Metal into Metal Powder Compacts.....41
2.1 Abstract.....41
2.2 Introduction.....42
2.3 Statement of the Problem.....44
2.4 Theory.....45
2.4.1 Infiltration without Dissolution.....45
2.4.2 Dissolution Kinetics.....47
2.4.3 Diffusional Solidification.....49
2.4.4 Discussion of Time Scales.....50
2.5 Experimental.....51
2.5.1 Materials.....51
2.5.2 Experimental Procedures.....52
2.6 Results and Discussion.....52
2.6.1 Infiltration of Straight Capillaries.....52
2.6.2 Powder Compact Infiltration.....54
2.6.3 Copper Butt Joints.....56
2.7 Summary and Conclusions.....57
2.8 Acknowledgment.....58
2.9 References.....58

Appendix A Dissolution of a Solid Cylinder Surrounded by a Layer of Unsaturated Liquid....83
Appendix B Diffusional Solidification in a Circular Capillary....85

3. Large Gap Joining of Ti-6Al-4V with Mixed Powder Interlayers....89
3.1 Abstract 89
3.2 Introduction....89
3.2.1 Silver-Base Brazing Alloys 90
3.2.2 Aluminum-Base Brazing Alloys....91
3.2.3 Other Brazing Alloys 92
3.2.4 Titanium Alloy Design....95
3.2.5 Equivalent Aluminum Content....96
3.2.6 Equivalent Molybdenum Content....96
3.3 Experimental Procedures....98
3.3.1 Materials....98
3.3.2 Preparation of β-titanium Brazes 98
3.3.3 Joining Procedures....98
3.4 Results and Discussion....99
3.4.1 Microstructures....99
3.4.2 Mechanical Properties 101
3.4.3 Fractography....103
3.5 Summary and Conclusions....104
3.6 Acknowledgments....105
3.7 References....105
Appendix Binary Titanium Phase Diagrams....127

4. High Temperature Brazing by Liquid Infiltration....134
4.1 Abstract 134
4.2 Introduction....134
4.3 General Considerations of the LIPB Process 135
4.4 Experimental Work....138
4.4.1 Materials 138
4.4.2 LIPB Procedure....138
4.5 Results and Discussion....139
4.5.1 Microstructures....139
4.5.2 Tensile Tests....140
4.6 Conclusions....141
4.7 Acknowledgments 142
4.8 References 142

5. Diffusional Breakdown of Nickel Protective Coatings on Copper in Silver-Copper Eutectic Melts....153

5.1 Abstract....153
5.2 Introduction....153
5.3 Experimental Procedure....155
5.4 Results....156
5.4.1 Samples Treated at 800°C....156
5.4.2 Samples Treated at 850°C....157
5.5 Discussion....158
5.5.1 Kinetics of Layer growth....158
5.5.2 Microstructures of the Diffusion Products....160
5.5.3 Barrier Layer Breakdown....161
5.6 Conclusions....162
5.7 Acknowledgments....163
5.8 References....163

6. Transient Liquid Phase (TLP) Bonding Using Coated Metal Powders....178
6.1 Abstract....178
6.2 Introduction....178
6.3 Experimental Procedure....180
6.4 Results and Discussion....181
6.4.1 Microstructures....181
6.4.2 Mechanical Properties....182
6.5 Conclusions....183
6.6 Acknowledgments....184
6.7 References....184

7. Thesis Summary and Future Work....196
7.1 Thesis Summary....196
7.2 Future Work....198
7.2.1 Ceramic/Metal Heterogeneous Joint....198
7.2.2 Near-Net-Shape Manufacturing....201
7.2.3 New Materials for Dental Amalgam....202
7.3 References....203

List of Figures

Figures for Chapter 1

Figure 1.1 Diagram of a forward-fed iron powder addition for butt joint weld 36
Figure 1.2 Diagram of a wire-fed iron powder addition......................................37
Figure 1.3 Schematic of typical powder spray morphology 38
Figure 1.4 The basic powder categories for thermal spray...................................38
Figure 1.5 Forms of powder filler metals used for brazing and soldering 39
Figure 1.6 Schematic drawing of powder-sheet layered composites 40

Figures for Chapter 2

Figure 2.1 Configurations of (a) mixed powderlayer bonding and (b) liquid infiltrated powder interlayer bonding (LIPB) process. The powder interlayer in (b) can have the same composition as the base material and the MPD can either be thin foils or coatings..63
Figure 2.2 Copper-silver binary phase diagram. Three alloys chosen as infiltrants are marked by 1, 2, and 3 respectively. The infiltration temperature is Tb = 850 °C...64
Figure 2.3 Schematic drawing of dissolution or isothermal solidification during unidirectional infiltration of liquid into straight capillaries. Note only diffusional solidification is depicted. In the case of dissolution, δ should be in the capillary wall instead of growing into the capillary itself 65
Figure 2.4 Melt saturation time as a function of capillary radius. Volume fraction of porosity, p, is calculated based on the straight capillaries.........................66
Figure 2.5 Time for diffusional solidification and infiltration of a circular capillary as a function of capillary radius. When the capillary radius is above 1.7 μm, full infiltration of the capillary can be achieved..66
Figure 2.6 Schematic drawing of preparing the samples for transverse infiltration tests: 250 μm diameter copper wires were wound on a copper mandrel and subsequently sintered. The cut sample has a dimension of about 8x8x8 mm^3.....67
Figure 2.7 Features of spherical copper powders (a), and irregular copper powders (b) used in preparing compacts for infiltration experiments..........................68

Figure 2.8 Schematic drawing of the apparatus for the experiments of straight capillary infiltration..69
Figure 2.9 Assembly for powder compact infiltration. The seam along the SS304 sleeve is for accommodating thermal expansion of the powder compact............70
Figure 2.10 Longitudinal infiltration of 177 micron nickel wires by Ag-Cu eutectic alloy. The infiltration temperature was 850°C, and infiltration was taken in 100 torr forming gas..70
Figure 2.11 Microstructure of the nickel capillaries infiltrated by Ag-Cu eutectic alloy. The infiltration was performed at 850°C for 11 seconds. The dark phase is Ag-Cu eutectic alloy, and relatively large nickel grains can be seen........71
Figure 2.12 Longitudinal infiltration of 100 micron copper wires by (a) Ag-Cu eutectic alloy and (b) 45Ag-55Cu alloy. The infiltration temperature was 850°C, and infiltration was taken in 100 torr forming gas...........................72
Figure 2.13 Microstructures of the infiltrated copper capillaries. (a) infiltrated by Ag-Cu eutectic at 850°C for 5.36 seconds. The area is close to the bottom of the capillaries (liquid entrance). (b) same capillaries, but at the upper part......73
Figure 2.14 Microstructure of the infiltrated copper capillaries. The infiltrant was 45Ag-55Cu, and infiltration was performed at 850°C for 11.86 seconds. The area is close to the bottom of the capillaries (liquid entrance)...................74
Figure 2.15 Microstructure of transversely infiltrated copper wires by Ag-Cu eutectic alloy at 850°C for 13 seconds. The area is close to the bottom of the capillaries (liquid entrance). Arrow indicates infiltration direction 75
Figure 2.16 Microstructure of transversely infiltrated copper wires by 45Cu-55Ag alloy at 850°C for 2 minutes. The partially dissolved copper wires are of the first layer of the capillary. Arrow indicates infiltration direction.................75
Figure 2.17 Initial volume fraction of porosity in the compacts in relation to Ni or Cr powder addition. Compressive pressure was 310 MPa, and each compact was 3.5 g 76
Figure 2.18 Infiltration efficiency as related to the shape of the powders and the amount of Cr and Ni powders added into the compacts...........................76
Figure 2.19 Volume fraction of residual porosity in the infiltrated area in relation to the powder shape and the amount of Cr and Ni powders added into the compacts 77

Figure 2.20 Microstructures of Ag-Cu eutectic infiltrated compacts of spherical Cu powders with various amount of Ni powder addition. (a) no addition; (b) 2 wt% Ni, the white areas are nickel powders; (c) 25 wt% Ni and (d) 50 wt% Ni. Infiltrations were performed at 850°C for 5 minutes in 100 torr forming gas 78
Figure 2.21 Microstructures of Ag-Cu eutectic infiltrated compacts of spherical Cu powders with various amount of irregular Cr powder addition. (a) 2 wt% Cr; (b) 5 wt% Cr and (c) 10 wt% Cr. The white areas are chromium powders. The infiltrations were performed at 850 °C for 5 minutes in 100 torr forming gas 79
Figure 2.22 Microstructures of Ag-Cu eutectic infiltrated compacts of irregular Cu powders with various amount of spherical Ni powder addition. (a) no addition; (b) 5 wt% Ni, the white areas are nickel powders; (c) 25 wt% Ni and (d) 50 wt% Ni. The infiltrations were taken at 850 °C for 5 minutes in 100 torr forming gas..80
Figure 2.23 Microstructure of a copper joint made by LIPB method. Joining was performed at 850 °C for 60 minutes in vacuum. The powder interlayer was consisted of spherical copper powders. Copper-Silver eutectic was the infiltrant and silver concentration in the joint was 8 wt%.............................81
Figure 2.24 A copper joint with joint gap about 22 mm made by LIPB process. Two copper powder interlayers with 2 wt% chromium powder addition were used. Copper-silver eutectic was the infiltrant. Joining was performed at 850°C for 30 minutes in vacuum. The markers are in inches................................81
Figure 2.25 Copper butt joint made by the LIPB process. The powder interlayer is consisted of Ni-coated copper powders. (a) assembly before bonding, and (b) the as-received joint after bonding. Joining was performed at 850°C for 30 minutes in vacuum..82

Figures for Chapter 3

Figure 3.1 Categories of the binary titanium alloys 109
Figure 3.2 Features of (a) CPTi powders and (b) Ti-6Al-4V powders used in the investigation. Note the irregular shape of the CPTi powders.........111

Figure 3.3 Microstructure of a joint bonded at 950°C for one hour. The interlayer is 250 micron thick Type I brazing alloy (Ti-12Zr-14Cr-12Cu-12Ni). White intermetallic compounds can be seen to precipitate in the center of the joint.......113
Figure 3.4 Microhardness across the joints using Type I brazing alloy (Ti-12Zr-14Cr-12Cu-12Ni) as the interlayer...113
Figure 3.5 Energy dispersive spectra (EDS) of the white phases shown in Figure 3.3..114
Figure 3.6 Microstructure of a joint bonded at 950°C for 30 minutes. The base metal is Ti-6Al-4V and the interlayer is Type I brazing alloy, with a thickness of 150 microns..115
Figure 3.7 Microstructure of a joint bonded at 950°C for 8 hours. (a) the interface between the base metal, Ti-6Al-4V and the interlayer. (b) the interlayer. The interlayer contains 50 wt% Type I brazing alloy, and the rest is equal mixtures of CPTi and Ti-6Al-4V powders. The white spots are intermetallic compounds, and the black holes are residual pores in the interlayer..............................116
Figure 3.8 (a) Microstructure of a joint bonded at 1140°C for 15 minutes. The interlayer contains 45 wt% Type II brazing alloy, and the rest are equal mixtures of CPTi and Ti-6Al-4V powders. Precipitation of α-phase can be observed in a β-matrix. The black holes are residual pores in the interlayer. (b) Microhardness across the joint shown in Figure 3.8(a)..........................117
Figure 3.9 Microstructure of a joint bonded at 1140°C for 15 minutes. (a) the interface between the base metal, Ti-6Al-4V and the interlayer. (b) the interlayer. The interlayer contains 50 wt% Type II brazing alloy, and the rest are equal mixtures of CPTi and Ti-6Al-4V powders 118
Figure 3.10 Microstructure of a joint bonded at 1140°C for 15 minutes, showing second phase precipitation in a β-titanium matrix. The interlayer contains 60 wt% Type II brazing alloy, and the rest are mixtures of CPTi and Ti-6Al-4V powders...119
Figure 3.11 Back scattering image of the joint illustrated in Figure 3.10 under SEM....119
Figure 3.12 View of an as-bonded sample for mechanical testing. Joining was performed at 1140°C for 15 minutes. The interlayer contains 60 wt%

Type II brazing alloy, and the rest are equal mixtures of CPTi and Ti-6Al-4V powders. The original thickness of the interlayer was 5 mm......................120
Figure 3.13 Sample dimensions for tensile testing 120
Figure 3.14 Tensile strength of the joints using 5 mm thick powder interlayers. The as-received strength of the Ti-6Al-4V base metal is also plotted..............121
Figure 3.15 Tensile strain of the joints as tested in Figure 3.14............................121
Figure 3.16 Tensile strength of the joints containing 45 wt% Type II brazing alloy. The joints were homogenized at 920°C for 8 hours after bonding at 1140°C for 15 minutes. The strength of similarly treated Ti-6Al-4V is also given in the chart..122
Figure 3.17 Fracture surface of Ti-6Al-4V base metal soaked at 1140°C for 15 minutes and subsequently diffusion treated at 920°C for 8 hours. (A) appearance at low magnification, and (b) appearance at higher magnification 123
Figure 3.18 Fracture surface of a joint bonded at 1140°C for 15 minutes and subsequently diffusion treated at 920°C for 8 hours. The interlayer contains 45 wt% Type II brazing alloy, the rest are equal mixture of CPTi and Ti-6Al-4V powders. (a) appearance at low magnification, and (b) appearance at higher magnification 124
Figure 3.19 Fracture surface of a joint bonded at 1140°C for 15 minutes and subsequently diffusion treated at 920°C for 8 hours. The interlayer contains 50 wt% Type II brazing alloy, the rest are equal mixture of CPTi and Ti-6Al-4V powders. (a) appearance at low magnification, and (b) appearance at higher magnification 125
Figure 3.20 Fracture surface of a joint bonded at 1140°C for 15 minutes and subsequently diffusion treated at 920°C for 8 hours. The interlayer contains 60 wt% Type II brazing alloy, the rest are equal mixture of CPTi and Ti-6Al-4V powders. (a) appearance at low magnification, and (b) appearance at higher magnification 126

Figures for Chapter 4

Figure 4.1 Schematic showing the stages of the LIPB process. Widening stage is absent since the dissolution mainly occurs between the powders and the MPD foils. The stages may overlap depending on the rates of infiltration and diffusion 144
Figure 4.2 Schematic drawing of a phase diagram shows a simple eutectic reaction between the MPD and the powder particles. C denotes the base metal concentration in the diagram. Four stages of the LIPB process is also illustrated 145
Figure 4.3 Microstructures of infiltrated joints. (2a). 0.6 mm nickel powder interlayer infiltrated by Ni-P eutectic at 950°C for 60 minutes. The base metal is nickel and the phosphorus content in the joint is 2.4 wt%. (2b). Same as (2a), only the interlayer is increased to 1.5 mm. (2c). 0.65 mm nickel powder interlayer infiltrated by MBF-1005 at 1000°C for 30 minutes. The base metal is Inconel 625 and the designed silicon content is 2 wt%..............................146
Figure 4.4 Microstructures of infiltrated joints with 3.54 mm thick Ni-20Cr powder interlayers. (3a). Interface between Inconel 625 and the powder interlayer infiltrated by Ni-P eutectic at 980°C for 60 minutes. (3b). Same as (3a), microstructure of the interlayer. (3c). Ni-B eutectic as the infiltrant, 1125°C, 60 minutes infiltrated and (3d). Microstructure of the interlayer 147
Figure 4.5 Specimen used for tensile tests..148
Figure 4.6 Results from tensile tests on the joints infiltrated by Ni-P eutectic at 980°C for 60 minutes. The powder interlayer was Ni-20Cr and the overall phosphorus content in each joint was 1.8 wt% 149
Figure 4.7 Fracture appearance of Ni-P eutectic infiltrated Ni-20Cr powder interlayer joints. (6a). Speicmens showing fracture in the powder interlayers. (6b). Fracture surface of the sample tested at room temperature. (6c). Same as (6b), showing some oxides in the interlayer 150
Figure 4.8 Results from tensile tests on the joints infiltrated by Ni-B eutectic at 1125°C for 60 minutes. The powder interlayer was Ni-20Cr and the designed boron content in each joint was 0.33 wt%..................................151
Figure 4.9 Fracture surface of the Ni-B eutectic infiltrated joint. The powder interlayer was Ni-20Cr and the designed boron content in each joint was 0.33 wt%. Residual porosities can be seen from the photographs 152

Figures for Chapter 5

Figure 5.1 Microstructural evaluation at the solid/liquid interface at 800°C for (a) 1 minute, (b) 8 minutes, (c) 15 minutes, and (d) 40 minutes. The growing phase is (Cu, Ni, Ag) ternary solid solution..............................165

Figure 5.2 Fast interdiffusion between Ni and Cu at grain boundaries of the Cu substrate caused local breakdown of the Ni diffusion barrier. Ag diffused across the (Cu, Ni, Ag) ternary solid solution and penetrated along Cu grain boundaries, forming Ag-Cu liquid. The arrows show the fast diffusion paths. The sample was plated with 12 μm Ni and treated at 800°C for 15 minutes..166

Figure 5.3 Electron microprobe analysis on the sample tested at 800°C for one minute. (a) back scattering image, the solid line indicates the analysis path. (B) concentration profile 167

Figure 5.4 Electron microprobe analysis on the sample tested at 800°C for fifteen minutes. (a) back scattering image, the solid line indicates the analysis path. (B) concentration profile 168

Figure 5.5 Electron microprobe analysis on the sample tested at 800°C for forty minutes. (a) back scattering image, the solid line indicates the analysis path. (B) concentration profile 169

Figure 5.6 Microstructures of the samples with 12 μm Ni plating and soaked in Ag-Cu eutectic liquid at 850°C for (a) 1 minute, (b) 5 minutes, and (c) 15 minutes..170

Figure 5.7 Microstructures of the samples with 1μm Cr undercoating prior to 12 μm Ni deposition. They were soaked in Ag-Cu eutectic liquid at 850°C for (a) 15 minutes and (b) 40 minutes, respectively 171

Figure 5.8 Electron microprobe analysis on the sample with 1 μm Cr undercoating on the Cu substrate. The sample was soaked at 850°C for fifteen minutes. (a) back scattering image, the solid line indicates the analysis path. (B) concentration profile...172

Figure 5.9 Electron microprobe analysis on the sample with 1 μm Cr undercoating on the Cu substrate. The sample was soaked at 850°C for forty minutes.

(a) back scattering image, the solid line indicates the analysis path. (B) concentration profile.....173
Figure 5.10 Copper-silver binary phase diagram. Co indicates the original eutectic composition of the liquid. At 800 °C, growth of (Cu, Ni, Ag) solid solution depletes Cu in the liquid. Thus the liquid composition ahead of the growing phase moves toward two phase region as illustrated by the arrow in the diagram, which causes interface instability of the growing front. C1 is the composition detected by EPMA.....174
Figure 5.11 The thickness of the growing (Cu, Ni, Ag) solid solution as a function of square root of time. The tests were performed at 800°C. The dotted line is according to equation (2), with an interdiffusion coefficient of $3.5x10^{-11}$ cm^2/sec.....175
Figure 5.12 The relation between the growth rate V of the ternary (Cu, Ni, Ag) solution and R, the average cell radius at 800°C. The calculation is based on equation (3) with an interdiffusion coefficient $3.5x10^{-11}$ cm^2/sec.....176
Figure 5.13 Schematic drawing of the four stage sequential breakdown of the Ni diffusion barrier between the Cu substrate and the Ag-Cu eutectic liquid.....177

Figures for Chapter 6

Figure 6.1 Features of the as-received metal powders. (a) Ni-20Cr alloy powders, and (b) 304L stainless steel powders.....187
Figure 6.2 Ni-10 wt%P electrolessly coated base metal powders. (a) Ni-20Cr alloy powders with 16 wt% coating. (b) 304L stainless steel powders with 16.3 wt% coating.....188
Figure 6.3 Microstructure of the Ni-20Cr powder interlayer after bonding at 1000°C for 1 hour in vacuum. The overall phosphorus content in the joint is about 1.6 wt%. Phosphides are uniformly distributed in the interlayer.....189
Figure 6.4 Microstructure of the 304L stainless steel powder interlayer after bonding at 1000°C for 1 hour in vacuum. The overall phosphorus content in the joint is about 1.63 wt%. Many residual pores indicates little shrinkage of the interlayer.....189
Figure 6.5 Liquidus projection of the Fe-Ni-P ternary phase diagram.....190
Figure 6.6 Vertical section of the Fe-Ni-P ternary phase diagram with varying phosphorus concentration.....190

Figure 6.7 A typical tensile test sample as-bonded with a Ni-20Cr powder interlayer Joining was performed at 1000 °C for 1 hour, showing the squeezing and bulging of the interlayer. The markings are in inches.............................191
Figure 6.8 The same sample shown in Figure 6.7 after the tensile test. Failure is in the interlayer with apparent plastic deformation of the base metal. Strong bonding between the interlayer and the base metal can be seen from the sample. The markers are in inches...191
Figure 6.9 Fracture surface of the Ni-20Cr powder interlayer 192
Figure 6.10 Fracture surface as shown in Figure 6.9. Under higher magnification, considerable ductility of the joint is evident 192
Figure 6.11 Mechanical properties of the joints with Ni-20Cr powder interlayers bonded at 1000°C for 1 hour, showing tensile strength and strain in relating to interlayer thickness 193
Figure 6.12 Tensile strength of joints with 304L stainless steel powder interlayers bonded at 1000°C for 1 hour, showing tensile strength in relating to interlayer thickness 194
Figure 6.13 Tensile strength of joints with 304L stainless steel powder interlayers bonded at 1000°C for 1 hour, showing tensile strength in relation to overall P contents...194
Figure 6.14 Mechanical properties of joints with 1.2 mm 304L stainless steel powder interlayers. Higher bonding temperature increases the joint strength and ductility..195

Figures for Chapter 7

Figure 7.1 Comparison of methods for brazing alumina to Kovar........................207
Figure 7.2 Coefficient of thermal expansion (CTE) of some metals and ceramics 208
Figure 7.3 Residual stress as a function of bonded area and geometry...................209
Figure 7.4 Methods of reducing thermal stresses...210
Figure 7.5 Si_3N_4/Steel joints directly brazed by three powder interlayers. The first layer adjacent to the steel for both samples contains 15 vol.% Nb powders, and the thickness is about 0.2 mm. The middle layer in samples A and B contains 70 vol.% WC particles with a thickness of 1 mm. The third layer which joins Si_3N_4 contains 15 vol.% short P-55 graphite fibers and 35 vol.%

Nb powders for samples A and B, respectively. The layer thickness is about 0.6 mm. The bonding agent is Ag-Cu eutectic plus 4.5 wt% Ti for all the layers. Joining was performed at 880°C in a vacuum furnace 211
Figure 7.6 Microstructure of the middle powder interlayer (70 vol.%WC) after bonding, showing full densification of the interlayer. The particles are WC..212
Figure 7.7 Back scattering image under SEM showing the interface between the third interlayer and Si_3N_4. The gray particles are Nb powders.....................212
Figure 7.8 Schematic drawing of large area ceramic/metal bonding by applying a patterned powder interlayer..213
Figure 7.9 The sequence of three dimensional printing (3DP) process.....................214
Figure 7.10 Microstructure of an experimental gallium-based dental amalgam after 72 hours of trituration. The particles are Ag-Cu eutectic alloy................214

List of Tables

Tables for Chapter 1

Table 1.1 Characteristics of a Powder Particle 35
Table 1.2 Characteristics of a Mass of a Powder..35
Table 1.3 Characterictics of Porosity in a Mass of Loose Powders..........................36
Table 1.4 Typical Formula of an E7018 Electrode Coating (Flux)...........................37

Tables for Chapter 3

Table 3.1 Analysis of Titanium Brazing Alloy Design Needs 110
Table 3.2 Chemical compositions (wt%) and mechanical properties
of the as-received Ti-6Al-4V Bar..112
Table 3.3 Chemical compositions of the titanium brazing alloys 112
Table 3.4 Results of EDS Analysis 114

Tables for Chapter 4

Table 4.1 Chemical compositions of the infiltrants used 148
Table 4.2 Chemical compositions of the base metals used......................................148

List of Acronyms

ADB	Activated Diffusion Bonding
AFML	Air Force Materials Laboratory
CTE	Coefficient of Thermal Expansion
DB	Diffusion Bonding
EDX	Energy Dispersive X-ray
EPMA	Electron Probe Microscopic Analysis
FGM	Functional Gradient Material
GTAW	Gas Metal Arc Welding
LID	Liquid Interface Diffusion
LIPB	Liquid Infiltrated Powder interlayer Bonding
LPS	Liquid Phase Sintering
LTTLP	Low Temperature Transient Liquid Phase
MPD	Melting Point Depressant
NSF	National Science Foundation
P/M	Powder Metallurgy
RP	Rapid Prototyping
SAW	Submerged Arc Welding
SEM	Scanning Electron Microscopy
SHS	Self-propagate High temperature Synthesis
SLS	Selective Laser Sintering
3DP	Three Dimensional Printing
TLP	Transient Liquid Phase

List of Symbols

Symbols for Chapter 2

A = area of the solid/liquid interface

α = R_o/R, dimensionless thickness

β = dimensionless constant according to a binary phase diagram

η = viscosity, mNs/m^2

γ = surface tension, N/m

C = base metal concentration in the liquid, weight fraction

$C^{\alpha o}$ = initial MPD concentration in liquid

$C^{\alpha L}$ = MPD concentration in liquid which is in equilibrium with α

$C^{\beta L}$ = MPD concentration in liquid which is in equilibrium with β

C_B^o = initial base metal concentration in the liquid

$C_B^{\beta o}$ = initial base metal concentration in the solid

$C_B^{\beta L}$ = base metal concentration at saturation in the liquid

$C_B^{\beta s}$ = base metal concentration in the solid which is in equilibrium with a saturated liquid

C^s = concentration of the MPD in the base metal due to diffusion

C_e = shape factor of a capillary

D_L = MPD or base metal diffusivity in liquid, cm^2/s

D_s = MPD diffusivity in the base metal, cm^2/s

ε = δ/R, dimensionless thickness

δ_c = thickness of dissolution or diffusional solidification, μm

δ_s = maximum dissolution thickness, μm

ξ = thickness of the growing solid solution

F_x = attraction force between two particles with a liquid in the neck, N

F_o = attraction force when the neck diameter is 1/4 of the particle diameter, N

G_α = dimensionless constant, for calculating solid/liquid interface movement

G_β = dimensionless constant, for calculating solid/liquid interface movement

h = height of liquid rise, mm

K = dissolution rate, mm/s

λ = constant for diffusion equation, λ=1 and 2 are for cylindrical and spherical diffusion, respectively

θ = contact angle

R_c = capillary radius, μm

R_o = wall thickness of a straight capillary, μm

R = $R_c + R_o$

p = volume fraction of porosity in a powder bed

P_x = equivalent external pressure, atm

t = time, seconds

t_{sat} = saturation time of the liquid due to dissolution, seconds

τ = $D_s t/R^2$, dimensionless time

T_b = infiltration temperature

T_c = tortuosity of capillaries

V = volume of liquid, mm^3

V_d = dissolution rate, μm/s

X = (R-r)/R, dimensionless thickness

ψ = dimensionless concentration

Symbols for Chapter 3

α = α-titanium phase

β = β-titanium phase

L = liquid metal

γ = binary titanium intermetallic compound

Symbols for Chapter 4

A = faying surface area, mm^2

α = MPD rich phase

β = base metal rich phase

C_B^i = initial base metal concentration in the infiltrant

C_B^o = initial base metal concentration in the liquid

$C_B^{\beta o}$ = initial base metal concentration in the solid

$C_B^{\beta L}$ = base metal concentration at saturation in the liquid

$C_B^{\beta s}$ = base metal concentration in the solid which is in equilibrium with a saturated liquid

k = shrinkage factor

ρ_l = liquid density, g/mm^3

ρ_s = solid density, g/mm^3

P = volume fraction of residual porosity

Δ_o = initial relative density of a powder interlayer

t_o = initial thickness of a powder interlayer, mm

V^L = total volume of liquid after dissolution

V^s = volume of solid remain in the joint after dissolution

W_{MPD} = total weight of MPD in the joint, grams

W_{base} = weight of the base metal powder in the joint, grams

Symbols for Chapter 5

D_s = solid state interdiffusion coefficient

D_L = diffusivity of solute in the liquid metal

G = temperature gradient

G_c = gradient due to constitutional undercooling

k = partition coefficient

m = liquidus slope, K/wt%

ϕ = degree of constitutional undercooling

γ = surface tension, N/m

λ_i = the minimum wavelength of the instability of the tip

MW_{Ni} = molecular weight of nickel

MW_{Cu} = molecular weight of copper

MW_{Ag} = molecular weight of silver

ρ_s = (Cu, Ni, Ag) solid density, g/mm^3

ρ_o = density of bulk Ni, g/mm^3

ρ_i = density of Ni at the solid/liquid interface, g/mm^3

R = radius of a growing cell, mm

t = time, seconds

Γ = Gibbs-Thomson coefficient, mK

V = growth rate of the (Cu, Ni, Ag) solid solution, mm/s

x = mole fraction of Cu in (Cu, Ni, Ag) solid solution

y = mole fraction of Ni in (Cu, Ni, Ag) solid solution

z = mole fraction of Ag in (Cu, Ni, Ag) solid solution

Symbols for Chapter 6

β = dimensionless constant according to a binary phase diagram

C_i = initial MPD concentration in the filler metal

C_L = the saturation concentration of the MPD in the liquid

D_s = the MPD diffusivity in the base metal

t_{is} = isothermal solidification time, seconds

Wo = initial thickness of the filler metal

Symbols for Chapter 7

α_c = coefficient of thermal expansion of ceramic, x10^{-6} °C^{-1}

α_m = coefficient of thermal expansion of metal, $x10^{-6}\,^{\circ}C^{-1}$

α_{11} = coefficient of thermal expansion of soft metal interlayer, $x10^{-6}\,^{\circ}C^{-1}$

α_{12} = coefficient of thermal expansion of hard metal interlayer, $x10^{-6}\,^{\circ}C^{-1}$

σ_s = yield strength, MPa

E = Young's modulus

ACKNOWLEDGMENTS

I am deeply grateful to Professor Thomas W. Eagar for his guidance and support both on this thesis and other projects. He gave me the opportunity to pursue my own ideas and allowed me the freedom to be creative, while maintaining my research on a productive path. His view toward science and engineering has added much to my materials experience and will have a lasting effect in my life.

I would also like to thank my thesis committee members, Professors Yet-Ming Chiang and Uday B. Pal, for their valuable comments which helped me to produce a much better thesis.

I gratefully acknowledge the National Science Foundation (NSF) for the grant, DMR-930144, which supported this research and my stay at MIT.

I also appreciate the friendship and support from the Welding and Joining Lab graduate students and staff. In particular I thank Bill MacDonald for teaching me lab staffs, as well as Vivek Dave, Bryan Blackwell, Ren-Kae Shiue, Jeff Nystrom, Cheryl Klepser and John Matz for the enlightening discussions. I thank Hillary Sheldon and Denise Wilsey for their help with my work.

My particular appreciation goes to Liao Ling and Sean Peterson for their assistance in my experiments.

Thanks to Ying-Ling Xie for assisting my mechanical testing and Neil for SEM work. I also would like to thank many friends around MIT who made my life more fun and interesting.

Finally, I would like to thank my parents for their continued support. I want to thank my wife, Yuan, for her understanding and support over the last three years. Without her love and encouragement I would not be able to be where I am today.

APPLICATIONS OF METAL POWDERS FOR JOINING PROCESSES

1.1 Introduction

A metal powder particle represents a rather unique piece of metal. It is characterized by a very small mass and a relatively large surface area. Metal powders offer a low cost, highly efficient route of producing near net shape parts with complex geometry in the powder metallurgy (P/M) industry. With continuous improvement of their physical and chemical properties, and the availability of a variety of metal powders, a lot of applications have been explored which would benefit from this material.

Application of metal powders in joining processes is under active study. A review of the state-of-art of metal powders in the joining industry, including welding, brazing and soldering, and special joining processes, is presented here. Applications rather than manufacturing of the metal powders are addressed.

With the general view of the applications of metal powders in mind, the thesis work is then outlined.

1.2 Characteristics of Metal Powders

Due to the unique metallurgical form of metal powders, their physical and chemical properties are characterized both by those of an individual powder particle as well as by the powder mass. Table 1.1 shows 16 characteristics of a powder particle. These can be divided into two groups of variables: material variables and variables which are influenced by the process of powder manufacture. Table 1.2 lists 9 characteristics of a mass of powder, of which the first one is the individual particle characteristic[1]. In joining applications, some of the variables noted in these tables must be considered, such as particle size and the amount of surface oxide. Further, some of the variables are of utmost importance in particular joining processes. For instance, impurity level should be minimized and accurately controlled to provide metal powder with a consistent flow point during brazing and soldering. Also, in some applications like plasma spray hardfacing,

where metal powders may be melted or not melted, the above mentioned variables are not sufficient to characterize the powder mass. The second component of the powder mass, its porosity, needs careful consideration. Table 1.3 gives the main characteristics of porosity in a loose powder. In many cases, the pore may undergo more changes than the powder particle itself. Mechanical properties of the joints depend to a large extent on the changes of the pores during processing.

1.3 Applications in Welding Processes

In 1993, more than 15,000 tons of iron powders were shipped for welding applications[2]. Most of these were used for manufacturing of welding electrodes. Shielded metal arc welding electrodes are manufactured by extruding a flux onto the surface of a mild steel core wire of predetermined diameter and length. The flux coating has a great effect on the nature of the weld produced. The type of coating may influence considerably the depth of penetration, the amount of weld deposit, the fluidity of the puddle, and the formation of slag. In addition, the type of coating dictates the welding speed, the type of current used, and the polarity. Iron powders are added in the flux coating to boost the deposition rate. They usually account more than 30 weight percent in the coating. A typical formula for an E7018 electrode coating is shown in Table 1.4[3]. Metal powders other than iron powders are used in flux coatings, too. Small amount of ferro-chromium and/or ferro-manganese powders are used to alloy the weld, whereas E7018 electrodes with addition of aluminum powders to the covering were found to be capable of handling high humidity conditions and to be tolerant of abuse[4].

Iron powder addition also finds applications in the submerged arc welding (SAW) process, where heat input is restricted in order to maintain high fracture toughness of the weld. In their paper, Rodgers and Lochead[5] discussed two methods of introducing iron powders into the weld pool. The first is called forward-fed iron powder additions, as illustrated in Figure 1.1. The system utilizes an essentially standard SAW setup, with the exception that a metered delivery of iron powder is laid on the workpiece just ahead of the main flux and wire delivery systems. The metal powder is consumed as the weld pool progresses along the joint line. This process is also known as "bulkwelding". This technique using tandem wire plus iron powder additions achieved deposition rates of approximately 22 kg/h (48 lb/h) with heat inputs of less than 3.5 kJ/mm. Analysis showed almost 100% utilization of the iron powder.

The second method is called wire-fed iron powder additions. In contrast to the previous technique, this system feeds the iron powder directly onto the welding wire, which, in this case, is used in a single wire setup. The process is illustrated in Figure 1.2. The magnetic field generated around the wire attracts and holds the powder addition, carrying it through the flux burden directly into the weld pool. With iron powder feed rates of 12-18 kg/h (26-40 lb/h), deposition rates of 19-25 kg/h (42-55 lb/h) can be accomplished in a single pass weld. The technique has been demonstrated to be suitable to tubular fabrication in thickness up to 40 mm (1.6 in.), with some 50-100% increases in deposition rates. The process also lends itself to application on fillet welds, which enhances productivity remarkably.

Another way of introduce iron powders into the weld pool is reported in [6]. In producing its industrial size washing machines, Washex machinery Corporation used Alloy Rods Coreweld 70, which is a metal powder, composite electrode that combines the high deposition rate of a flux cored wire with the high efficiency of a solid wire. The fluxing ingredients have been virtually eliminated from the core of this wire and replaced with metal powders. The only slag formed by this wire consists of small islands of silicates. Multiple passes can be made without deslagging.

In recent years, metal powders find increasing applications in hardfacing processes to enhance the wear and/or corrosion resistance of a surface[7,8]. Metal powders are used in oxyacetylene spray torches, plasma, and detonation gun equipment and in a variety of other welding equipment, such as plasma arc surfacing. The powders used in the former processes are not usually fused with the substrate. Powders used with transferred arc plasma and gas tungsten arc welding (GTAW) are fused to the substrate. Powders are usually made in the size range of 5 to 100 μm. They are introduced in the thermal spray torch in a variety of ways, but a requirement of the process is that they melt and can be propelled at the substrate to be coated. The ease of melting depends on the torch design, the nature of the powder used (round, irregular, spongelike, etc.), and the flame temperature. Powder coatings are formed by overlapping splat-cooled droplets of the melted powder, as shown in Figure 1.3. Apart from some contaminants from the reaction from the molten droplets with the medium that the droplets passed through on their way to the workpiece, there are usually some voids in the deposit from incomplete conformance of the splat-cooled droplets with each other.

The hundred or so specific powders available from major manufacturers can be roughly categorized into six groups based on the material system. Figure 1.4 shows the basic powder categories and lists some specific powder systems in each of these categories.

A cermet is a material composed of a ceramic and a metal, where metal powders act as binders of ceramic particles.

1.4 Applications in Brazing and Soldering

There are several advantages to use metal powders in brazing and soldering processes. Filler metals in the form of powder do not require sufficient ductility to be formed into wires. In fact, even highly brittle alloys may be produced and used as powders. The range of possible compositions, therefore, is unlimited. The final choice of filler metal, then, may be made solely on joining characteristics and on the resulting properties of the bonded connection. A second attribute in favor of metal powders is associated with the fact that the filler metal exists in discrete and very uniform particles. This allows the metering of precise quantities of brazing alloy to the area to be joined. In this connection, too, is the further capability of combining the filler metal with a flux and delivering the mixture to the bonding area. This type of operation is easily automated and well suited for high-speed, high-volume production. Finally, metal powders provide a form which may readily be adapted to complex joining areas. The use of standard preforms may be impossible due to both specific geometric configurations and the resulting economics. Hence, metal powders offer a very versatile approach to joining.

The type of product in which metal powders are employed depends upon the particular type of brazing and soldering applications. Today, there are four types of primary forms being used extensively through the industry, which are illustrated in Figure 1.5[9]. In some cases, a simple application of the brazing or soldering powder is sufficient to meet the joining requirement, like in the joining of jewelry and other small components. Bonding is usually done by manual assembly and gas torch heating. A further modification of the use of a filler metal is that of brazing or soldering paste, which consists of a finely divided metal powder and a binder. Flux can also be added into such powder pastes. Paste preparation is accomplished by a variety of mixing techniques. A homogeneous blending of all constituents is very important. The viscosity of the paste is determined by the amount and the type of the binder used. The method of paste application is dictated by the final viscosity.

One of the main advantages of powder paste is the ability to meter precise quantities to the joining area. The application of a predetermined volume is most common. This is done usually by a dispensing gun which is fed with paste from a pressurized supply tank. Such a system lends itself to highly automated production.

Paste also can be applied manually either as a single dab or continuous beads. Where more complex configurations are to be joined, powder paste "patterns" can be made using screen printing techniques. Such pre-printed solder cream has been adapted in the semiconductor industry for precise soldering of surface mounted devices[10].

A brazing tape consists of a mixture of filler metal powder and organic binder. Using powder rolling techniques, the mixture is rolled into thin strip with thicknesses from 25 to 125 μm (0.001 to 0.05 in). The strip is then baked at low temperature to drive off most of the binder and therefore "set" the filler metal powder. The resulting strip is flexible and can be easily cut or stamped to produce brazing preforms. Consequently, the amount of filler available for brazing can be accurately controlled on the joining area.

In some applications, glass powders are combined with filler metal powders to produce powder preforms. The glass serves two primary functions: first it surrounds the metal particles and protects them from oxidation while heating to the brazing temperature. Second, it acts as a fluxing agent by removing oxidation from the parts to be brazed. The brazing preforms are pressed from a mixture of glass and metal powders, together with a binder. The green preforms are then heated to a temperature sufficient to drive off the binder and sinter the glass and metal powders into one coherent structure. After this treatment, the preforms can be handled without breaking. Such preforms allow joining by induction, torch or gas burner heating in the air rather than in a reduced atmosphere.

Many filler metal compositions are commercially available in their powder form. Some of the more common types include copper-base, silver-base, nickel-base, and aluminum-base alloys. Advances in the handling of metal powders will provide further brazing and soldering products. For example, extensive research in lead-free solders is underway to accommodate the increased world-wide emphasis on reducing risks of lead to health.

1.5 Applications in Special Joining Processes

Transient liquid phase (TLP) bonding is a joining technique using a melting point depressant (MPD) layer between the two parts to be jointed. When heated up to and held at the bonding temperature, the interlayer goes through dissolution, widening, isothermal solidification and homogenization stages to form a solid bond[11, 12]. Since solid state diffusion is the rate controlling process in the latter two stages, the whole process usually takes a long time, or else requires very thin joints, which is inefficient for commercial applications.

In order to reduce the time for isothermal solidification and solid state homogenization, a powder interlayer transient liquid phase bonding technique was first studied by Nakao et al [13,14]. However, successful use of the process can be dated back to 1978. The service center of GE Aircraft Engines applied powder mixtures of superalloys and MPDs to repair hot-corroded engine components[15]. The primary advantage of using powder interlayers lies in that the isothermal solidification and the solid phase homogenization time can be greatly reduced, especially when the joining clearance is wide. According to Nakao, the isothermal solidification time for the powder interlayer is only 1/80 of that for thin foil interlayers. Such fast isothermal solidification kinetics is achieved by three dimensional diffusion around the metal powder particles and much shorter diffusion paths of the MPDs. In other words, inserted metal powders act as sponges which absorb the MPDs quickly. Nonetheless, the study of powder interlayer bonding is still very limited. Many aspects, such as the diffusion kinetics into the powder, the selection of powder insert layers, remain unclear.

Self-propagating, high temperature synthesis (SHS) can be used to bond both similar and dissimilar metals. A unique feature of this technique is the ability to stack either metal powders or metal powders and foils, to make a composite[16-18]. The advantages of using powders are many, among them the ability to make complicated shapes, to use low cost starting components, and to design the properties of the layered composite through careful selection of layer composition, thickness and location. A number of TiAl matrix composites with strengthening dispersions have been produced at the Bureau of Mines using the powder-sheet method. Figure 1.6 shows a schematic representation of the composite design.

1.6 Present Investigations

As has been stated above, metal powders are widely used in a variety of joining processes. They offer a low cost, highly efficient way of successful production of many items from cruise ships to glass frames. One of the interesting joining processes, the TLP bonding process (also termed diffusion brazing (DB) by the American Welding Society), has been extensively studied in the MIT joining laboratory[11]. A fundamental understanding of TLP bonding has been achieved with respect to binary alloy systems with a planar joint geometry that solidify by the diffusion of the MPD from the liquid into the solid base metal. An analytical model was developed using a moving boundary analysis to predict the bonding time for these binary systems as a function of the diffusivities and phase

relationships between the MPD and the joint metal. By carefully conserving the mass of the liquid interlayer, experimental results for copper TLP bonded with silver were found to be in complete agreement with the analytical model. Extrusion of the liquid from the joint area or formation of intermetallics was found to reduce the bonding time by up to three orders of magnitude. An analytical solution for determining the diffusion occurring during heatup was derived. Experimental measurements of the dissolution rate were found to be in agreement with a published model. Low temperature transient liquid phase (LTTLP) bonding was investigated[19,20], and it was found that a large number of interlayers from indium and bismuth systems showed high remelt temperatures. LTTLP joining of Cu using In-Sn alloys has been used successfully in electronic packaging[21].

One major disadvantage of TLP bonding is that only joints with very small clearance (usually less than 50 microns) can be made efficiently. Increasing joint clearance inevitably results in impractically long holding time and/or formation of intermetallic compounds in the joint. This work initially followed Nakao's approach by introducing a powder interlayer consisting of a mixture of the MPD and the base material into the joint. Such a configuration relaxes the stringent requirements on the joint clearance, and allows much shorter bonding time as compared to standard TLP bonding. The kinetics of this process is discussed in chapter 2 of this thesis based on liquid phase sintering (LPS) theory. The mixed powder method has been successfully applied to the joining of titanium alloys, which is presented in chapter 3. Titanium alloy Ti-6Al-4V is joined with judiciously designed titanium base MPDs.

For the powder mixture method, a fairly large amount of MPDs, from 30 volume percent to even more than 60 volume percent, depending on the nature of the powders used and the mutual solubility and/or reactivity between the MPD and the base material powders, are needed to completely eliminate residual pores in the joint. In the case of joining Ti-6Al-4V, a simple titanium-based braze alloy was found to be able to produce an intermetallic-free joint only with joint clearance less than 150 microns. Much thicker joints can be made using powder mixtures of the base metal and the MPD. However, at least 50 vol.% of MPDs had to be introduced to eliminate the residual porosity in the joint. Such amounts of MPDs often lead to degraded mechanical properties. Efforts to reduce the use of MPDs resulted in the development of the Liquid Infiltrated Powder interlayer Bonding (LIPB) process. Kinetic models of this process are also presented in chapter 2. The powder interlayer has the same composition as the base material and the MPDs are thin foils or coatings that are placed between the powder interlayer and the faying surface. At the bonding temperature, a layer of wetting liquid forms either by melting of the MPDs or reacting of the MPDs with the powder particles. The liquid subsequently infiltrates into the

powder interlayer by capillary attraction. Here two factors may contribute to the less use of MPDs for joining: firstly, the MPD powders are removed from the powder interlayer, hence a higher packing density of the of the base material powders can be applied as long as the interlayer can be totally infiltrated. Secondly, planar infiltration causes uniform shrinkage of the powder interlayer, which allows full densification of the powder interlayer with much less MPDs remaining in the joint. Infiltration joining of a nickel-base superalloy, Inconel 625, is described in chapter 4.

On designing the LIPB process, the infiltration distance is very important to obtain a sound joint. The mutual solubility between the liquid and the solid has to be taken into consideration, which usually is large in metal-metal systems. When mutual-solubility is low, the infiltration distance largely depends on the sintering rate of the solid particles. On the other hand, high liquid solubility in the solid can cause significant particle growth, whereas high solid solubility in the liquid can greatly raise the solidus temperature and cause the liquid to solidify. In both cases, infiltration stops when the capillary paths are blocked. It is not surprising that infiltration processing is such a complex engineering problem that few material systems can meet the requirements for ideal infiltration. To simplify the process, a new approach has been investigated in this work. A protective coating is applied on the base material powders. For a material system which has large mutual solubility between the infiltrant and the base metal, such a thin layer coating is essential to retard dissolution kinetics and hence be able to lend time for complete infiltration. Nonetheless, such a coating which is compatible with the infiltrating liquid and allows full infiltration before the coating disappears due to diffusion or chemical reaction may be difficult to find. The kinetic study of this process based on Ag-Cu eutectic liquid/Ni coating/Cu base metal is presented in chapter 5. The mechanism of the diffusion barrier breakdown was studied.

In chapter 6, base metal powders coated with MPDs are used directly to join 304 stainless steels. This represents the simplest way of large gap TLP bonding developed in this work. The amount of MPD can be quantitatively controlled by deposition process. Meanwhile, the liquid amount is greatly reduced as compared with conventional LPS. However, based on the microstructural observations and mechanical properties of the resultant joints, careful selection of the MPDs and the base metal powders is very important to ensure a quality joint, as is pointed out in the chapter.

The last chapter addresses future work. Functional gradient materials (FGM) are extensively studied nowadays, which is believed to be a method to solve the problem of joining ceramics to metals. However, there are few methods available to produce FGMs of usable size, and frequently the cost of the process is too high. Primary work using

multiple powder interlayers, combined with infiltration and screen printing techniques, indicates the feasibility of making large size, ceramic to metal joints. Other applications of metal powders include infiltration of rapidly formed parts by rapid prototyping (RP) techniques as injection modeling dies, and mercury-free dental amalgams.

1.7 Summary

The metal powder approach to joining is unique and, as such, is rather specialized. It affords the capability of using new filler metals which heretofore have not been available and, in some instances, accomplish joining more efficiently or easier. The method, however, is not intended to be an overall substitute for conventional welding, brazing and soldering techniques.

There are applications where metal powders have a distinct advantage. Generally, these involve those where the simultaneous placement of brazing or soldering alloy and flux facilitates high volume production. Other applications include bonding of joints with complex geometry such that conventional techniques are not economically attractive.

This thesis has been divided into five papers with emphasis on the further development of the TLP bonding process. As such, there is some repetition, but each paper essentially describes different aspects of materials and processes.

1.8 References

1. H.Hausner, New Types of Metal Powders, Gordon and Breach Science Publishers; pp. 1-8, 1964.

2. Donald G.White, "*State of the North American P/M Industry: 50 Years of Progress*", Powder Manufacturing and Industry Trends; Advance in Powder Metallurgy & Particulate Materials-1994, vol. 1, pp. 1-10.

3. D.L.Olson, et al., "*Nature and behavior of Fluxes Used for Welding*", Welding, Brazing and Soldering, ASM Handbook, 1993, vol. 6, pp. 55-63.

4. L.Andersen, "*Aluminum Powders Helps Covered Electrode Stay Dry*", Welding Journal, vol. 69, no. 11, pp. 60, 1990.

5. K.J.Rodgers and J.C.Lochhead, "*Submerged Arc Welding Metal Powder Additions, Productivity and Properties*", Welding Journal, vol. 66, pp. 21-27, 1987.

6. "*Metal Powder Continuous Electrode Saves Washing Machine Production Time*", Welding Journal, vol. 63, no. 1, pp. 53-54, 1984.

7. Kenneth G. Budinski, Surface Engineering for Wear Resistance, Prentice-Hall; pp. 242-287, 1988.

8. Robert C.Tucker, Jr., "*Thermal Spray Coatings*", Surface Engineering, ASM Handbook, 1994, vol. 5, pp. 497-509.

9. Robert J.MacDonald, "*Metal Powders-Their Role in Brazing*", Welding Journal, vol. 50, no. 5, pp. 327-331, 1971.

10. D.C.Beeferman, "*Soldering Creams for Electronic Surface Mounted Devices*", Welding Journal, vol. 65, no. 1, pp. 37-42, 1986.

11. W.D. MacDonald, "*Kinetics of Transient Liquid Bonding*", Ph.D. Thesis, 1993, MIT.

12. W.D. MacDonald and T.W. Eagar, "*Transient Liquid Bonding Processes*", The Metal Science of Joining, The Minerals, Metals & Materials Society, 1992, pp. 93-100.

13. Y. Nakao, et al., "*Transient Liquid Insert Metal Diffusion Bonding of Nickel-base Superalloys*", Advanced Joining Technologies, Proceedings of the International Institute of Welding Congress on Joining Research, July, 1990, pp. 129-144.

14. Y. Nakao, et al., "*Advanced Transient Liquid Insert Metal Diffusion Bonding Using Alloying Powder*", The 5th International Symposium of the Japan Welding Society, April, 1990, pp. 139-144.

15. Wayne A. Demo and Stephen J. Ferrigno, "*Brazing Method Helps Repair Aircraft Gas-turbine Nozzles*", Advanced Materials & Processes, no. 3, 1992, pp. 43-45.

16. J.A. Hawk. Et al., "*Self-Propagating, High Temperature Synthesis as a Technique to Join Metals*", Proceedings of the 1993 MRS Symposium on Joining and Adhesion of Advanced Inorganic Materials, vol. 314, pp. 183-194.

17. R.W.Messler, Jr. And T.T.Orling, "*Fundamentals of the SHS Joining Process*", Proceedings of the 1993 MRS Symposium on Joining and Adhesion of Advanced Inorganic Materials, vol. 314, pp. 177-183.

18. R.W.Messler, Jr. And T.T.Orling, "*Joining by SHS*", Advanced Processing Techniques, Advances in Powder Metallurgy & Particulate Materials, 1994, vol. 6, pp. 273-285.

19. J. W. Roman, "*An Investigation of Low Temperature Transient Liquid Phase Bonding of Silver, Gold and Copper*," SM Thesis, Department of Material Science and Engineering, MIT, 1991.

20. J. W. Roman and T. W. Eagar, "*Low Stress Die Attach by Low Temperature Transient Liquid Phase Bonding*," Symposium Proceedings of the International Society for Hybrid Microelectronics (ISHM), 1992.

21. M. M. Hou and T. W. Eagar, "*Low Temperature Transient Liquid Phase (LTTLP) Bonding for Au/Cu and Cu/Cu Interconnections*," Journal of Electronic Packaging, 114, pp. 443-447, 1992.

Table 1.1: Characteristics of a Powder Particle

Material Characterristics	Characteristics due to the Process of Fabrication
(1) Structure (bcc, fcc, amorphous, etc.) (2) Theoretical density (3) Melting point (4) Plasticity (5) Elasticity (6) Purity (impurities)	(1) Particle size (particle diameter) (2) Particle shape (3) Density (porosity) (4) Surface conditions (oxidation) (5) Microstructure (crystal grain structure) (6) Type and amount of lattice defects (7) Gas content within a particle (8) Adsorbed gas layer (9) Amount of surface oxide (10) Reactivity

Table 1.2: Characteristics of a Powder Mass

(1) Particle characteristics (Table 1.1)
(2) Average particle size
(3) Particle size distribution
(4) Specific surface
(5) Apparent density
(6) Tap density
(7) Flow of the powder
(8) Friction conditions between the particles
(9) Compressibility

Table 1.3: Characterictics of Porosity in a Mass of Loose Powders

(1) Total pore volume, P
(2) Pore volume between powder particles, P_1
(3) Pore volume within powder particles, P_2=P-P_1
(4) Number of pores between powder particles, n
(5) Average pore size
(6) Pore size distribution
(7) Pore shape

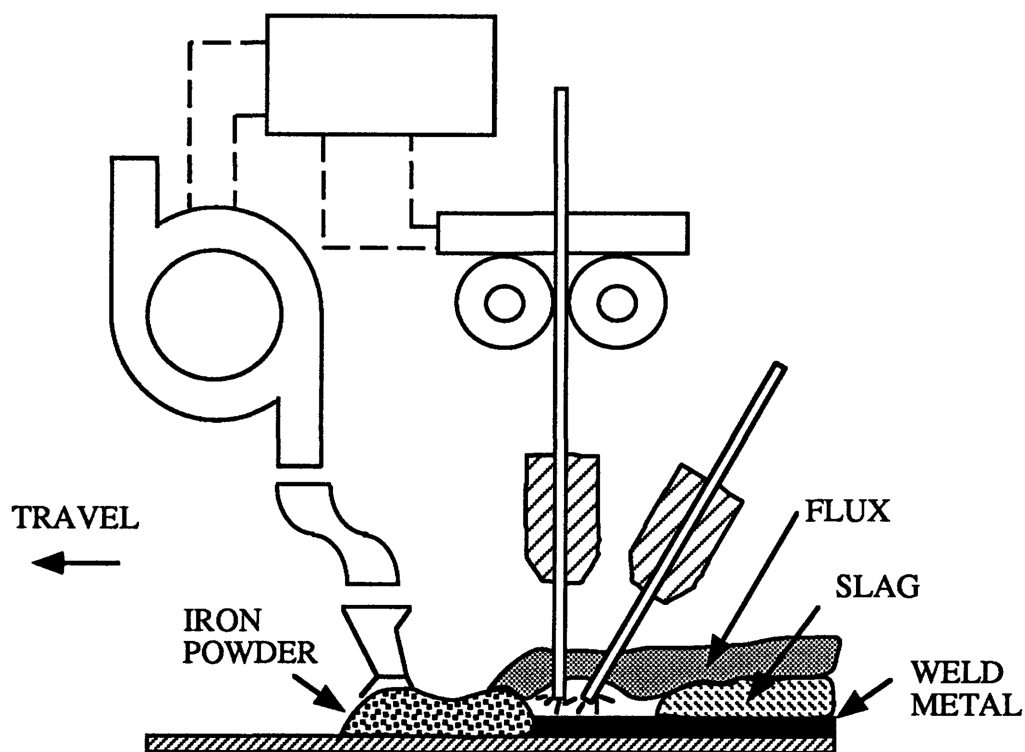

Figure 1.1. Diagram of a forward-fed iron powder addition for butt joint weld.

Table 1.4: Typical Formula of an E7018 Electrode Coating (Flux)

Ingredient	Percent
Iron powder	35
Ferro manganese	2
Mica	2
Ferrosilicon	2
Ferrotitanium	2
Rutile	5
Potassium feldspar	3
Limestone	20
Solomite	8
Fluorspar	18
Aluminum-magnesium	3
Potassium silicate	Binder

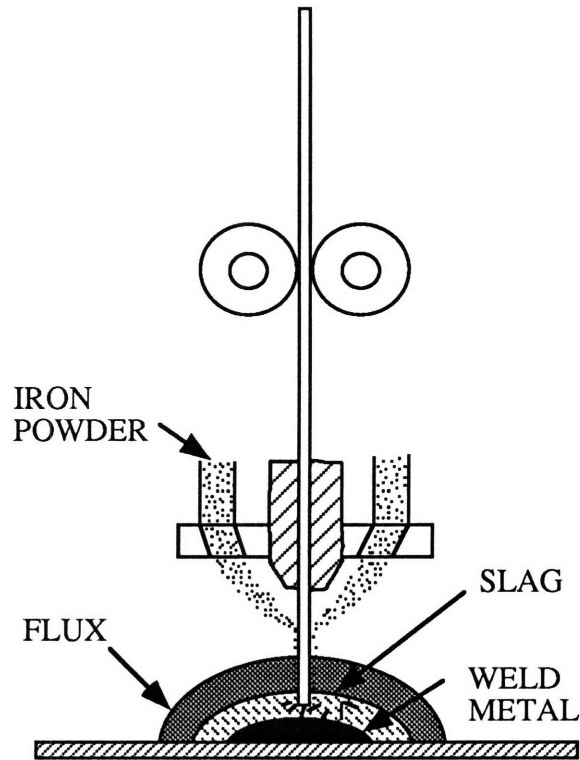

Figure 1.2. Diagram of a wire-fed iron powder addition.

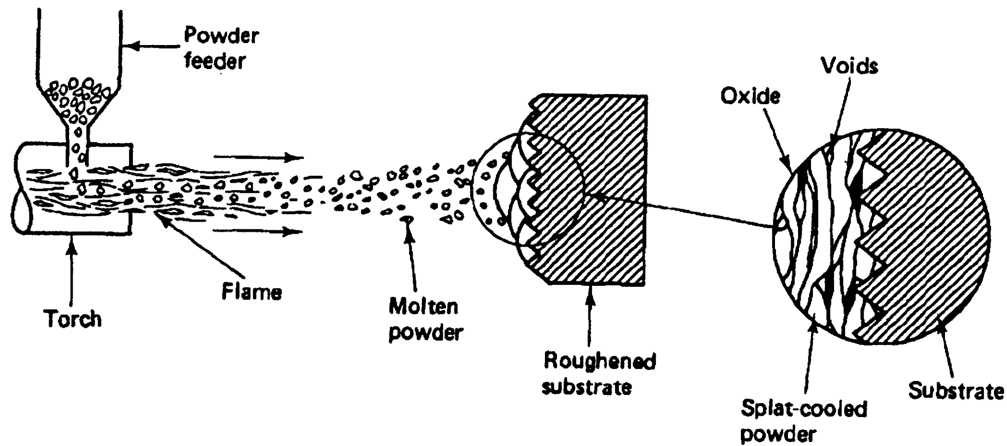

Figure 1.3. Schematic of typical powder spray morphology.

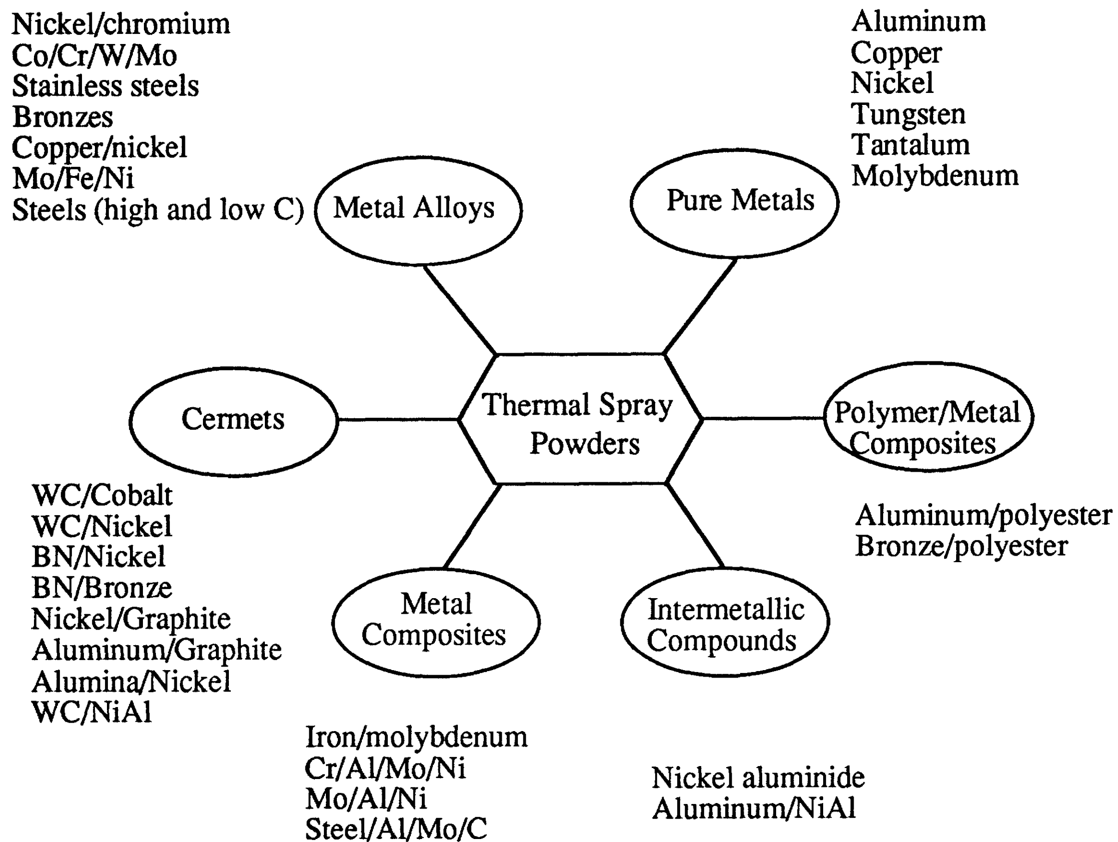

Figure 1.4. The basic powder categories for thermal spray.

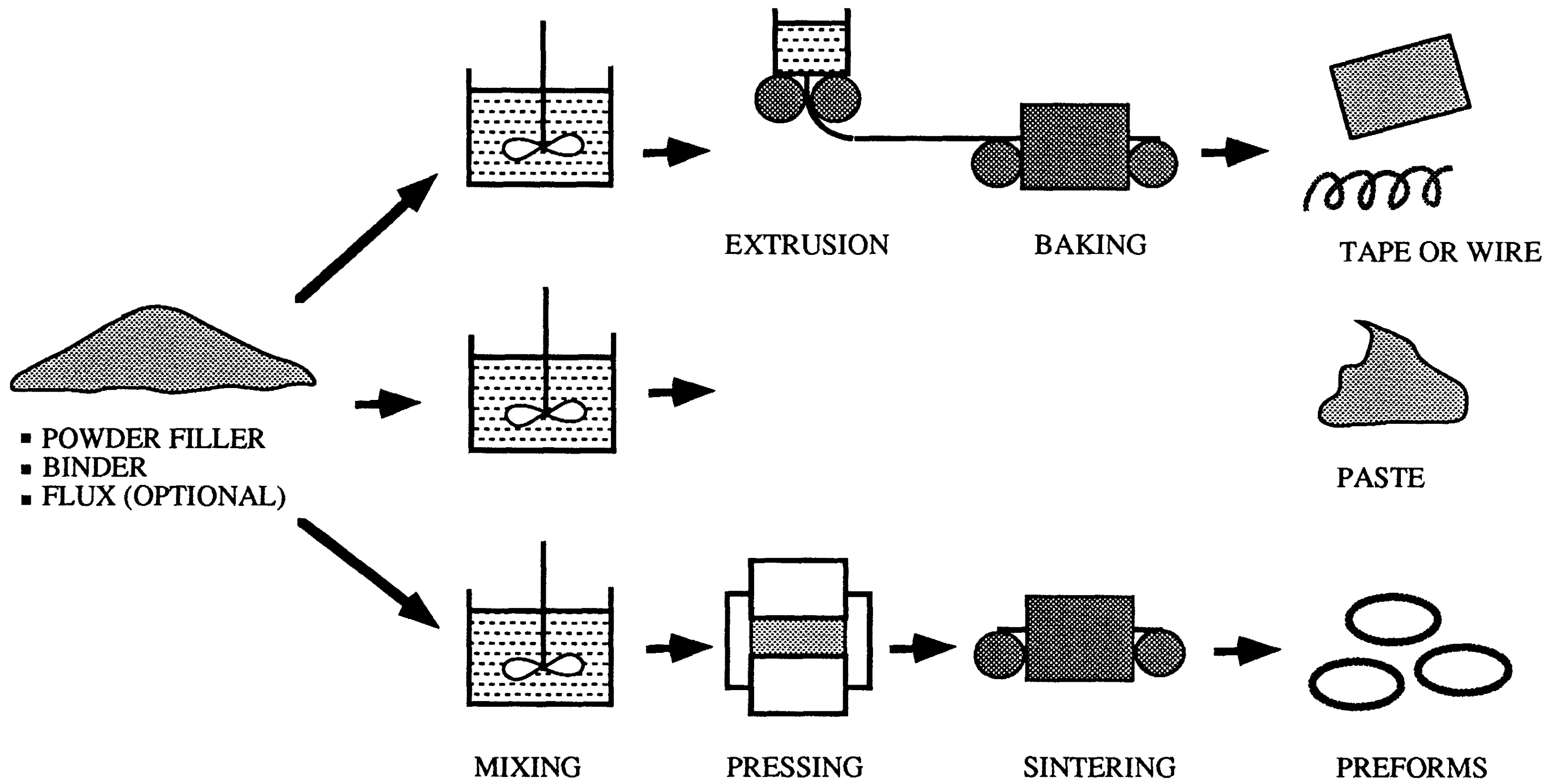

Figure 1.5. Forms of powder filler metals used for brazing and soldering.

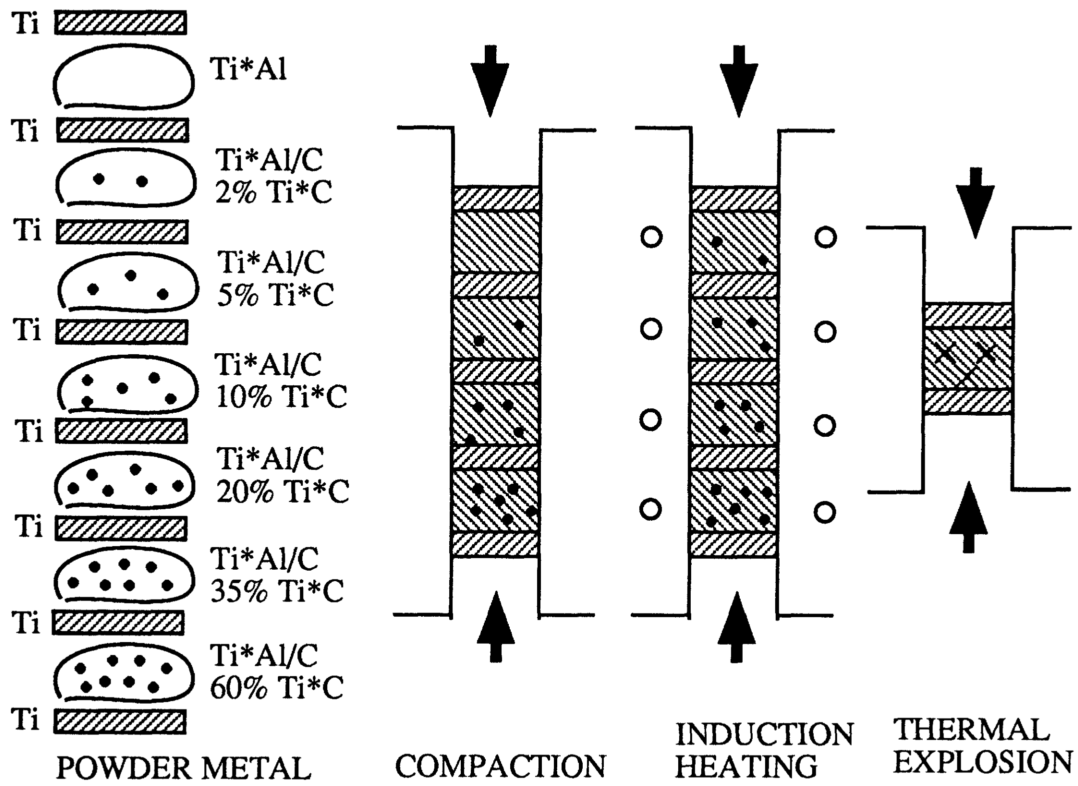

Figure 1.6. Schematic drawing of powder-sheet layered composites.

Presented at 26th International Conference on Brazing and Soldering
Cleveland, OH April, 1995

INFILTRATION OF LIQUID METAL INTO METAL POWDER COMPACTS

2.1 Abstract

The liquid infiltrated powder interlayer bonding (LIPB) process is proposed to make large gap, transient liquid phase (TLP) joints. Some basic aspects of the LIPB process are discussed. In the LIPB process, a joint with high mechanical properties requires a low volume fraction of porosity in the powder interlayer and low concentrations of MPDs in the joint. To achieve the fully infiltrated large gap joint, it is essential to maintain an open pore structure at the initial stage of infiltration, while allowing complete elimination of pores behind the infiltration front. Approximate analytical solutions are applied to describe dissolution of the capillaries and isothermal diffusional solidification during infiltration. Longitudinal infiltration tests with relatively large Cu capillaries showed much faster kinetics of infiltration than diffusional solidification, therefore, the analysis of the two processes can be decoupled. The Washburn equation is applicable to straight capillary infiltration, provided the infiltrants and the base material have little interaction at the infiltration temperature. When the interaction is strong, the infiltration kinetics is perturbed because of the non-equilibrium nature of the system as observed in infiltrating copper capillaries by Cu-Ag alloys. Transverse infiltration was much slower and infiltration distance depended on the dissolution kinetics. The results of powder compact infiltration experiments revealed greatly decreased infiltration rate as compared with those of straight capillary tests. This is caused by the tortuosity and very small effective radius of the capillaries due to liquid induced attraction. Diffusional solidification and infiltration kinetics can no longer be decoupled under these circumstances. Full infiltration of the powder compacts needs tight control of the rearrangement rate of the particles such that a relatively large capillary radius can be maintained to prevent diffusional solidification before full infiltration. Meanwhile, the extent of the rearrangement should be able to finally close the pores behind the infiltration front. Small amounts of chromium or nickel powder addition into spherical Cu powders were found to affect the

rearrangement significantly, whereas little effect was observed for irregular Cu powders. Copper/copper butt joints with clearance up to 22 mm have been successfully made.

2.2 Introduction

The transient liquid phase (TLP) bonding process involves introducing a liquid phase with its melting temperature lower than that of the base material to be joined, similar to the case in liquid phase sintering (LPS). However, the liquid eventually solidifies through solid state diffusion of the melting point depressant (MPD) into the base material, when a TLP joint is isothermally held at the bonding temperature for a long time. Consequently, the process is only applicable to small gap joints[14-16] with clearances up to several tens of microns. Such tight control on joint clearance makes it difficult to use TLP for large component manufacturing. Over time, some efforts have been made to produce large gap joints in brazing practices. Nakao et al.[17] studied TLP bonding of nickel-base superalloys by applying a superalloy powder interlayer. J.W. Chasteen and G.E. Metzger[18] studied wide clearance brazing of Hastelloy X using a pre-sintered powder insert and external liquid feeding. Lugscheider[19, 20] used virtually the same method to join stainless and carbon steels with nickel base filler metals. Kinetic studies on using mixed powder interlayers[21] showed that large amounts of liquid (above 30 volume percent) are needed to eliminate pores in the joint. Unfortunately, a high percentage of the liquid often ends up with a joint with severely impaired mechanical properties.

The liquid infiltrated powder-interlayer bonding (LIPB) process is designed to take advantage of the high mechanical properties resulting from isothermal solidification in TLP bonding, while allowing a much thicker joint to be made. The basic joint configuration includes a powder interlayer and two layers of MPD (Figure 2.1). The powder interlayer can have the same composition as the base material and the MPDs are thin foils or coatings that are placed between the powder interlayer and the faying surface. At the bonding temperature, a layer of wetting liquid forms either by melting of the MPDs or reacting of the MPDs with the powder particles. The liquid subsequently infiltrates into the powder interlayer by capillary attraction. Rearrangement of powder particles in the presence of the liquid eliminates pores behind the liquid front. Rapid solidification and homogenization are possible due to the limited amount of MPDs used and the fast kinetics of short-path, three-dimensional diffusion.

Fundamental principles involved in LPS provide a basis for understanding liquid metal infiltration into metal powder compacts, as well as a guide for its application to joining processes. LPS is defined as a thermal treatment (sintering) involving both liquid and solid phases such that the sintered compact has improved interparticle bonding and increased strength. It has been extensively studied both theoretically and experimentally in recent years[1-10]. One of the ways to obtain the liquid phase during sintering is by using mixed powders with differing chemistries. The liquid can result from melting of one component or formation of a eutectic. Further, the liquid during sintering could be transient or persistent depending on the solubility relationship. Some material characteristics such as mutual solubility between the solid and the liquid, and the interfacial energies between them (wetting versus non-wetting), play important roles during LPS. They greatly affect the rate of sintering and the microstructure evolution. These variants coupled to process factors like particle size, green density, sintering temperature, time and atmosphere can further affect the material formed by LPS.

The classic theory of LPS defines three overlapping stages by assuming good wetting of the liquid towards the solid and solubility of the liquid for the solid[11-13]. Initially, the powder mixture is heated to a temperature where a liquid forms. Prior to liquid formation, a solid solution may form by diffusion, and this may introduce a major amount of densification or swelling. With liquid formation densification starts due to the capillary force exerted by the wetting liquid on the solid particles. The elimination of porosity occurs as the system minimizes surface energy. At this stage, particles rearrange themselves in response to the capillary action. The amount of densification attained by rearrangement depends on the amount of liquid, contact angle, dihedral angle, particle size and solubility of the solid in the liquid. Full density is only possible when enough liquid is formed. Usually about 35 volume percent liquid is needed to obtain full density.

The second stage of classic LPS is termed solution-reprecipitation, which causes microstructural coarsening (or Oswald ripening) of the material. The coarsening is due to a distribution in grain sizes. Material is transported from small grains which have a higher solubility in their surrounding liquid to the large grains by diffusion in the liquid. The net result is progressive growth of the larger grains. Since diffusion changes grain shape, the grains can pack tighter, and such grain shape accommodation leads to pore elimination. Thus solution-reprecipitation not only contributes to grain coarsening, but also to densification.

The last stage of LPS is referred to as solid state sintering. A solid skeleton now exists and densification is low. Solid state diffusion contributes to grain and pore coalescence. This stage is generally avoided in practice during LPS, in order that the material properties are not severely degraded.

The difference between LPS and LIPB lies in the different volume fraction of liquid in the two processes. LPS usually has to be performed with the liquid volume fraction above 30%. When in systems with liquid phase contents less than 10 vol.%, primary re-arrangement leads essentially to a local densification of a limited number of particles[22]. In contrast, LIPB allows the overall volume fraction of liquid to be less than 20%, while still obtaining full densification. Lesser amounts of liquid are required for a mechanically sound joint. This is achieved by first extracting MPDs from the mixed powder interlayer. Meanwhile, the green density of the interlayer can be increased as long as it can be fully infiltrated.

2.3 Statement of the Problem

Infiltration phenomena can be seen frequently in every day life. The simplest example is water infiltration of a dry sponge. Infiltration kinetics has been studied extensively because of its importance in many industries, including wood, petroleum and agriculture. The results generated in these fields also have been adopted to the P/M industry. Unfortunately, the success of such transformation is limited because in most systems previously studied, there is little interaction between the infiltrating liquid and the solid particles. However, in metal-metal systems, the interaction may be severe, especially at high temperatures. Such interaction leads to dissolution of powder particles during infiltration, and causes erosion or even slumping of the compact.

The rate of dissolution of a solid material in the presence of a liquid phase has been investigated by a number of researchers[23-26]. The rate has been found to be very high. Since in most cases dissolution of the solid material increases both the capillary radius and the liquid viscosity, it tends to slow down liquid infiltration. Furthermore, fast dissolution saturates the liquid quickly, and diffusional solidification may set in before the compact is fully infiltrated, depending on the capillary radius and the kinetics of diffusion. The competition between infiltration and dissolution therefore will markedly affect the microstructure of the infiltrated compacts.

On the other hand, dissolution may be necessary for successful infiltration of those powder compacts with high green densities, since the pores in such compacts are usually not inter-connected. In other words, there are many closed-end capillaries which are extremely difficult to infiltrate by a non-reacting liquid. Dissolution can help to open the closed pores and inter-connect the capillaries. It is therefore evident that successful infiltration of a powder compact needs to

control the infiltration as well as the dissolution rates, which, at the same time, are both related to the geometry of the powder compact.

2.4 Theory

2.4.1. *Infiltration without Dissolution*

The transport of a liquid through a porous solid or powder compact is central to filtration and melt infiltration. Surface tension and viscosity of the melt provide the driving force for and resistance to infiltration, respectively. In addition, the geometry of the porous solid also has a major effect on the dynamics of the process. The simplest model, by Washburn[27], assumes that the pores can be represented by an array of parallel, identical cylindrical capillaries. The Washburn equation predicts the distance, to which a liquid spontaneously infiltrates into a porous powder compact as a function of the time, the viscosity of the liquid, the surface tension, the wetting angle and the capillary radius:

$$h = \left(\frac{R_c \gamma \cos\theta}{2\eta}\right)^{1/2} t^{1/2} \tag{1}$$

where h is the height of rise of the column of liquid at time t, R_c is the capillary radius and η is the viscosity of the liquid. γ is the liquid-gas surface tension, and θ is the liquid-solid contact angle. Followinf the Washburn equation, a number of similar equations were derived[28-32]. Since a simple array of uniform capillaries is an overly simplified approximation to the actual pores, equation (1) tends to underestimate the infiltration times. The pores can more realistically be considered as cylinders having cusped triangular cross sections that vary in area along the length of the pores and open periodically to form various-shaped chambers. Such a geometry can be modeled by parallel, circular cylinders, but having alternating regions of large and small diameter. In a close packed powder compact, the large segment is connected by four small-diameter channels. The periodic change of the diameter of a capillary has been used by Bartell and Osterhoff[28] to modify the Washburn equation:

$$h = \left(\frac{R_c \gamma \cos\theta}{2\eta\, T_c^2}\right)^{1/2} t^{1/2} \qquad (2)$$

where T_c is called tortuosity of capillaries. For close packed, spherical powders, T_c goes to $\pi/2$. The equation now can be expressed as:

$$h = \frac{2}{\pi}\left(\frac{R_c \gamma \cos\theta}{2\eta}\right)^{1/2} t^{1/2} \qquad (3)$$

Equation (3) has been widely used in the P/M industry over the years[31, 32].

In recent years, a more rigorous treatment on liquid infiltration of porous powder compacts was reported by Yokoda et al.[33-35]. In addition to consider the tortuosity (T_c) and shape factor (C_e) of capillaries, the capillary pressure was modified by considering the dynamic pressure exerted at the neck between two particles:

$$P = \frac{3\sqrt{2}}{4\pi} R_c^2 (F_x - F_o) \qquad (4)$$

where F_x is the attraction force between two particles with a liquid in the neck and F_o is the force when the neck diameter is one fourth of the particle diameter. The rate of infiltration was derived as:

$$V_i = \frac{dh}{dt} = \frac{C_e\, p\, R_c^2}{\eta\, T_c^2\, h} - \left\{\frac{2\gamma \cos(\theta)}{R_c} - \rho g h - \frac{3\sqrt{2}}{4\pi R_c^2}(F_x - F_o)\right\} \qquad (5)$$

where C_e is the shape factor ($=T_e/32$) of the capillaries, and p is the volume fraction of porosity in the powder bed. Equation (5) had been used successfully by Yokoda to describe water infiltration of glass powder sintered compacts with various particle sizes and pores.

In summary, a great deal of work has been done on modeling liquid infiltration of porous media. When there is no interaction between the infiltrant and the porous solid, or when the interaction can be neglected, close predictions can be made of the infiltration kinetics provided the geometry of the porous media has been carefully considered.

2.4.2. *Dissolution Kinetics*

Dissolution of a solid material in contact with a liquid phase with a flat interface has been studied by a number of authors. It is generally agreed that dissolution of the base metal during TLP bonding is controlled by transport of solute in the liquid phase rather than by interface reaction. Tuah-Poku[36] applied Fick's law to calculate the dissolution kinetics as he performed TLP bonding of Ag/Cu/Ag sandwich joints. A direct solution was given, showing that movement of the solid/liquid interface is proportional to the square root of time. Nakao et al.[37] presented a different approach to the kinetics of the dissolution process. The Nernst-Brunner theory was applied to predict the dissolution rate of a solid into a liquid:

$$C = C_{sat} [1 - \exp (- K ({}^{A}\!/\!{}_{V}) t] \qquad (6)$$

where C = solute concentration in the liquid;

C_{sat} = solute concentration at saturation;

K = the dissolution rate;

V = volume of liquid;

A = area of the solid/liquid interface; and

t = time.

Although their experimental data fit well as predicted by equation (6), there is an inherent problem using the Nernst-Brunner theory applied to TLP bonding. The theory was derived based on the key assumption that the liquid zone can be considered as a constant volume bulk layer with a thin, constant boundary film at the solid/liquid interface. In the TLP bonding process, however, the thickness of the liquid boundary is on the order of $2(D_L\ t)^{1/2}$, where D_L is the diffusivity of the solute in the liquid. Assuming a diffusivity of about 10^{-6} cm^2/s, a holding time of 100 seconds means a boundary thickness of 200 μm, which is in the same range of the total liquid width of a TLP joint. It follows that the assumption of a thin liquid boundary layer and a bulk liquid apparently is not applicable. Nakagawa et al.[38] first pointed out this discrepancy and they

applied a finite difference solution to model the dissolution kinetics during TLP bonding. Solid state diffusion of solute was also included in their study.

Liu et al.[39] derived an analytical solution which governs the planar dissolution process in a binary system. The model assumes concentration independent diffusion coefficients and that dissolution is controlled only by the MPD diffusion into a quiescent liquid. The rate of base metal dissolution is then given by:

$$V_d = \frac{C^{\alpha L} - C^{\beta L}}{C^{\alpha o} - C^{\alpha L}} \frac{\exp(-G_\alpha^2)}{\operatorname{erf}(G_\beta) + \operatorname{erf}(G_\alpha)} \sqrt{\frac{D_L}{\pi t}} \tag{7}$$

where $C^{\alpha o}$, $C^{\alpha L}$, and $C^{\beta L}$ are the solute concentrations given by the phase diagram, as shown in Figure 2. G_α and G_β are dimensionless constants. Equation (7) is not applicable to the initial transition period, where it predicts an infinite dissolution rate of the base metal. It is believed that equation (7) indicates a decreasing dissolution rate with time, since the liquid bocomes more and more saturated with time.

To account for the dissolution of solid particles during melt infiltration of a powder compact, an estimation of the dissolution kinetics is needed to understand the process. This can be approximated by modeling the dissolution of a circular, cylindrical capillary being infiltrated with a liquid. Since it is a moving boundary problem with a non-planar interface and finite boundaries, numerical analysis is usually required to obtain a solution. However, an analytical approximation sometimes provides useful estimations even if it is not as accurate as the numerical result. By assuming steady state diffusion in the liquid phase, the dissolution rate of a capillary, which is depicted in Figure 3, can be expressed as (appendix A):

$$V_d = \frac{D_L (C_B^{\beta L} - C_B^{o})}{(R_o - \delta)(C_B^{\beta L} - C_B^{\beta o})} \ln^{-1}\left(\frac{R_o - \delta}{R_o + R_c}\right) \tag{8}$$

where C_B^{o} is the initial solute concentration in the liquid, $C_B^{\beta o}$ is the initial solute concentration in the base metal, and $C_B^{\beta L}$ is the saturation concentration. R_c is the capillary radius and R_o is the thickness of the base metal before dissolution. Equation (8) is only applicable for a short period of time since the melt concentration in the center of the capillary is fixed when performing the

calculation. The dissolution rate decreases as the melt is gradually saturated. The saturation time of the melt is derived as:

$$t_{sat} = \frac{R_c}{V_d} \left[\left(\frac{C_B^{\beta o} - C_B^{o}}{C_B^{\beta o} - C_B^{\beta L}} \right)^{1/2} - 1 \right] \tag{9}$$

From equation (9), it is evident that the larger the capillary radius, the longer the time needed for melt saturation. Equation (9) is implicit, since the dissolution rate, V_d, is also a function of time. However, when initial dissolution rate is employed as given by equation (8), a minimum saturation time can be estimated.

2.4.3 *Diffusional Solidification*

Solubility between the infiltrant and the base material can play an important role in affecting the infiltration kinetics. When the base metal is soluble in the infiltrant, dissolution of the base material may increase the capillary radius effectively and facilitate infiltration. On the other hand, if the infiltrant is soluble in the base metal, diffusion away of MPDs can cause isothermal solidification of the melt and infiltration stops as soon as the capillary is blocked by the growing solid phase at the infiltration temperature. For a mutually soluble system, kinetics of infiltration and solidification will determine the maximum infiltration distance into a compact. An analysis based on straight capillaries and a binary single eutectic system (see the phase diagram in Figure 2.2 and nomenclature in Figure 2.3) is performed with the following assumptions:

(1) The infiltrant is saturated with the base material so that no dissolution of the base metal will occur as infiltration proceeds (i.e. the liquid has the composition of $C^{\beta L}$ indicated in Figure 2.2).

(2) Diffusion in the liquid is fast so that the MPD concentration across the liquid phase is uniform and is given by the phase diagram.

(3) There is no temperature gradient across the solid/liquid interface and

(4) Perturbation at the solid/liquid interface is small or the maximum growth is at the root of each capillary.

An integral method similar to that used by Poots[40] to solve the heat transfer problems is applied to predict the solidification time (appendix B). The implicit expression of the solidification time of a capillary is then:

$$t_s = \frac{R^2}{2D_s\,\alpha(1-\alpha)}\left[\frac{3\beta+2}{9}(1-\alpha^3) + \frac{2\beta+1}{8}(\alpha^4-1) + \frac{3\alpha^4-4\alpha^3}{6}\ln\left(\frac{1}{\alpha}\right)\right] \quad (10)$$

where $\alpha = R_o/R$, and $R = R_o + R_c$. R_o and R_c are the capillary wall thickness and capillary radius, respectively. D_s is the diffusivity of MPD in the base metal. Since β is related to the equilibrium partition coefficient, a lower β or a higher MPD solubility in the base material will lead to a shorter solidification time.

2.4.4 *Discussion of Time Scales*

If a powder compact is simulated as an array of circular, straight capillaries, the Washburn equation (equation (3)) often predicts a short time for full infiltration. For instance, in the case when copper capillaries with their length = 100 mm and R_c= 10 μm are infiltrated by a Ag-Cu eutectic melt at 850 °C, it will take about 14 seconds to finish infiltration as calculated the Washburn equation. The thermodynamic data used for this calculation was extracted from the literature[41, 42]. The actual infiltration time may be even shorter due to an increase of the capillary radius as a result of dissolution. However, such time decrease may be alleviated by simultaneous increase of the viscosity of the melt. An estimation on the melt saturation using equation (9) and the initial dissolution rate of the base metal gives a time of 0.32 seconds (R_o= 10 μm and corresponding porosity, p=25%, D_L= 10^{-6} cm^2/sec), which is more than an forty times shorter than the time needed for infiltration. Figure 2.4 shows the melt saturation time as a function of capillary radius calculated based on the initial dissolution rate. The actual saturation time may be longer due to the decreasing dissolution rate. Nonetheless, it is highly possible that the melt is saturated shortly after the initiation of infiltration. Calculation according to equation (10) shows that the isothermal solidification time is about 76 minutes for 20 μm diameter capillaries. Such a long time indicates that diffusional solidification is insignificant when relatively large capillaries are infiltrated. However, as the capillary radius decreases, the time for infiltrating the same distance goes up rapidly, which is illustrated in Figure 2.5. With small capillaries, the diffusional solidification time is about the same as is needed for complete infiltration. Further decreasing of the capillary radius will produce incomplete infiltration.

When infiltrating real powder compacts, the situation is more complex. First of all, the radius of the capillary is no longer uniform. There are a lot of sites where the capillary radii are in the sub-micron range, and these attract the liquid in different directions. Secondly, there may be a number of closed-end capillaries where the liquid is difficult to infiltrate, and finally, diffusional solidification may need to be considered because of reduced infiltration rate. This can be illustrated with the Ag-Cu binary system. Assuming an effective capillary diameter of 2 μm with 25 vol.% porosity, and taking T_e= 1.3[43], then from equation (5), a 10 mm thick powder compact will take more than 18 seconds for full infiltration. But calculation based on equation (10) shows that isothermal solidification may be complete in just 20 seconds. Because of the much faster kinetics of dissolution, the melt is effectively immediately saturated once infiltration starts. Therefore, any further increase of the thickness of the powder compact or decrease of the capillary radii will result in diffusional solidification and incomplete infiltration.

2.5 Experimental

2.5.1 *Materials*

Copper shots (99.9%) and silver granules (99.9%) were used to make Cu-Ag alloys by arc melting. Three alloys 45Cu-55Ag, 28Cu-72Ag and 16Cu-84Ag (by weight percent) were prepared as infiltrants. The three compositions are shown in the Cu-Ag binary phase diagram in Figure 2.2. The 16Cu-84Ag alloy was later abandoned due to its high reactivity with copper.

Twenty copper wires (>99.9%) of diameter 100 μm, 150 mm in length were used to provide straight capillaries for each infiltration test. These wires were first sintered in a close packed array in vacuum at 1000°C for 20 hours, with the resultant capillary radius of about 10 μm. Nickel wires of diameter 177 μm were also used in the experiments without sintering. Transverse infiltration samples were made of 250 μm diameter copper wires which were wounded on a rectangular cylinder and sintered in vacuum at 1000 °C for 20 hours. After sintering, the wires were cut from the cylinder and both ends perpendicular to the longitudinal direction of the wires (edge surfaces) were coated with BN powders to prevent wetting from this direction during infiltration. The transverse samples for infiltration tests are illustrated in Figure 2.6.

Spherical and irregular copper powders (> 99.9% pure) with variable Ni and Cr powder additives were used in powder compact infiltration experiments. The sizes of all the powders were less than 44 microns (-325 mesh). Figures 2.7(a) and (b) show the typical features of the Cu powders. Each compact had the same amount of powder (3.5 grams) and was pressed in a 9.55 mm diameter tool steel die without binder. Copper powder compacts containing a small amount of irregular nickel or chromium powders (both with sizes less than 44 μm) were also tested for infiltration. Mixing of the powders was done in a self-made ball milling chamber. Each batch was mixed for 30 minutes.

2.5.2 *Experimental Procedures*

All the experiments were performed in a bell jar furnace. Figure 2.8 depicts the schematic drawing of the apparatus. The furnace had a constant temperature zone of about 150 mm. The temperature gradient was monitored with three thermocouples during infiltration and the temperature difference was adjusted to be no more than 2°C between the top and the bottom of the hot zone. Before heating, the bell jar was first evacuated to 2.5×10^{-5} torr and refilled with forming gas (95% N_2 and 5% H_2) to about 100 torr. At 850 °C ± 2 °C, infiltration was started by lowering the sample at a speed about 100 μm/s. A timer was triggered as soon as the capillary front touched the liquid. After infiltration, the sample was pulled up and quenched with forming gas.

In the infiltration of powder compacts, the volume ratio of infiltrant and the porosity was taken as 1.05. The Cu-Ag infiltrant was placed directly on the top of the compact and each run was held at 850°C for 5 minutes, followed by immediate gas quench. Figure 2.9 shows the assembly of the sample. The infiltration efficiency was taken as the ratio of the areas infiltrated to the entire area of the cross section of the compact. Metallurgical examinations were performed to reveal the microstructure of the infiltrated compacts. A point counting method (ASTM Specification E562) was employed in determining the volume fraction of residual porosity. Large gap copper to copper butt joints were made by applying infiltrated Cu powder compacts as the interlayers.

2.6 Results and Discussion

2.6.1 *Infiltration of Straight Capillaries*

According to the Washbun equation for straight capillaries (equation (1)), a parabolic relationship should apply between the infiltration height and the time when there is little interaction between the infiltrant and the solid. However, most confirmations of equation (1) come from experiments using aqueous solutions as the infiltrants. In metal-metal systems, little data is available. The modified version (equation (3)) is widely accepted in the P/M industry, even though there are extensive interactions between the melt and the base metal. In this chapter, a system consisting of Cu-Ag eutectic infiltrant/Ni straight capillaries was selected to test the Washburn equation, since the mutual solubility between Ag and Ni at the infiltration temperature (850°C) is very small, and the interdiffusion between Cu and Ni is negligible as compared to the infiltration kinetics. Figure 2.10 shows the experiment results. Good agreement between the prediction and the experiment data is observed. Figure 2.11 shows the microstructure of the infiltrated Ni capillaries. In the case when 100 micron copper wires were infiltrated at 850 °C, a larger scattering of the experimental data was observed as illustrated in Figure 2.12(a). The predition of the infiltration distance by the Washburn equation is represented by the parabolic curve in Figure 2.12(a). Microstructural examination of the infiltrated capillaries close to the initial infiltration front revealed severe dissolution of the copper wires, which produced a number of Ag-saturated Cu islands in the capillaries (Figure 2.13(a)). Dissolution experiments on planar Cu/Ag interfaces performed by MacDonald[44] showed that copper was attacked within less than a second as the Ag-Cu eutectic melt and Cu base metal were put in contact at 820°C. Non-uniform dissolution was observed in both MacDonald's experiments and the current experiments. Grain boundaries of copper were preferentially dissolved, which may assist the detachment of the copper drops formed by dissolution into the melt. Such dissolution mechanism may lead to shorter melt saturation times than predicted by equation (9). Figure 2.13(b) shows the microstructure of the same infiltrated capillaries shown in Figure 2.13(a), but at the middle of the capillaries. No islands of copper rich phase can be found in the capillaries, indicating a saturated melt. Base metal dissolution may accelerate infiltration kinetics by increasing the capillary radius, Thus reducing the rate of rise of the liquid. The Washburn equation may no longer be valid when this situation occurs.

When the infiltrant was changed from Ag-Cu eutectic to 45Cu-55Ag, the saturated melt at 850°C, the data scattering were reduced, as shown in Figure 2.12(b). Since the infiltration temperature is very close to the liquidus of the infiltrant, its viscosity may be higher than that of the

eutectic alloy, therefore a lower infiltration rate can be expected. Assuming twice the melt viscosity, a good agreement between the prediction and the experimental results can be found, as illustrated in Figure 2.11(b). Figure 2.14 is the microstructure of the infiltrated capillaries, showing some grooving adjacent to copper grain boundaries. Such grooving may caused by fast diffusion of silver along copper grain boundaries and lead to a rough solid/liquid interface.

Transverse infiltration experiments were performed using sintered 250 μm copper wires. The features were much different as compared with the longitudinal infiltration. In Figure 2.15, dissolution can be clearly seen when Cu-Ag eutectic was used as the infiltrant. Infiltration requires dissolution of the necks between the sintered copper wires and proceeds as soon as the neck between the two wires is dissolved away. Due to extremely fast dissolution kinetics, the liquid approaches its saturation composition at the infiltration temperature quickly, reducing the opening of further necks, and causing the dissolution rate to go to a minimum and inhibiting further infiltration. Infiltration distance in this case can not be described by the Washburn equation. In most cases, less than 4 mm infiltration distance could be achieved in 15 seconds. Further holding often led to complete dissolution of the necks and separation of the wires. When 45Cu-55Ag was used as the infiltrant, little infiltration was observed as illustrated in Figure 2.16. It is quite evident that dissolution is essential to the infiltration of closed-end capillaries.

2.6.2 *Powder Compact Infiltration*

Due to mechanical inter-locking among the irregular copper powder particles, these were found easier to be pressed into compacts. Spherical copper powders were more difficult to press and a much higher pressure (close to 300 MPa) was required to make the compacts with the 9.55 mm die. To simplify the process, a fixed pressure of 310 MPa was chosen to make all the compacts. Adding powder particles of higher modulus than copper such as nickel and chromium powders (-325 mesh) can effectively change the pore structure of the compacts. This is depicted in Figure 2.17. The volume fraction of porosity in the as-pressed compacts, which was calculated by the density method, increases with the addition of Ni or Cr powders. Figure 2.16 also reveals that compacts of irregular copper powders have higher initial volume fraction of porosity than those of spherical particles. In addition, it can be speculated that infiltration kinetics can be affected by Ni or Cr additions because Ni is readily wetted by Cu-Ag infiltrant, but Cr is non-wettable at the infiltration temperature.

Figures 2.18 and 2.19 show the infiltration efficiency and volume fraction of residual porosity in the infiltrated area as a function of Ni or Cr contents in the compacts, respectively. Small amounts of Ni additions was found to be beneficial in increasing the infiltration efficiency

and decreasing the residual porosity for compacts of spherical powders. As the Ni content exceeded about 5 wt%, the infiltration efficiency started to decrease and the compact with the highest Ni content exhibited lowest infiltration efficiency. However, the volume fraction of porosity in the infiltrated area began to increase beyond 5 wt% Ni and reached a maximum (6%) at about 50 wt% Ni. Further increases of the Ni content resulted in decreasing the volume fraction of porosity again, and compacts with 95 wt% Ni showed no residual pores in the infiltrated area. The microstructures are illustrated in Figure 2.20. As compared with the copper-rich compacts, the nickel-rich compacts exhibited lower infiltration efficiency. This may be caused by the different geometries and infiltration kinetics in these powder compacts. It can be expected that little dissolution of the Ni particles occurs during the infiltration of the Ni-rich compacts, thus the closed-end capillaries are more difficult to infiltrate. Adding irregular Cr powders to the compacts of spherical Cu powders led to similar effects as the Ni additions, only that Cr addition was more effective. Compacts with 5 wt% Cr addition revealed about 95% infiltration efficiency and virtually no residual pores. The microstructures of the infiltrated compacts are presented in Figure 2.21. In contrast to spherical Cu powders, no beneficial effect on infiltration was observed for nickel powder additions to the compacts of irregular Cu powders. The copper-rich compacts exhibited decreasing infiltration efficiency and increasing residual pores with the increased Ni additions. Microstructures of the infiltrated compacts are shown in Figure 2.22.

From the experimental results described above, it is evident that infiltration kinetics of powder compacts is much slower than that predicted by the Washburn equation, which assumes infiltration of straight capillaries. One important phenomena during infiltration of powder compacts is the movement of the particles in the presence of the liquid. Because of strong attraction between the adjacent powder particles exerted by the wetting liquid, the particles are pulled together and re-packed to eliminate pores behind the infiltration front. This force can be expressed as an equivalent external compression pressure P_x[45]:

$$Px = 2\sqrt{2}\pi\,(\gamma / r)\cos(\theta) \tag{11}$$

where r is the radius of the particle. This compacting pressure can exceed 10 atms. between two 15 micron spheres with a thin layer of wetting liquid in between. The disadvantage of particle rearrangement is the reduced capillary path for infiltration. As has been discussed in 2.4.4, dissolution of the Cu particles has complex effects. Firstly, dissolution helps to dissolve particle contacts and form liquid "cushions" between the particles, which may facilitate rearrangement.

Secondly, dissolution results in increasing the capillary radius and opening the closed-end capillaries, which may facilitate infiltration. However, since dissolution kinetics is fastest in these sub-micron capillaries, the infiltrant is saturated almost instantly and diffusional solidification may set in and become the controlling step during infiltration. Consequently, maintaining a large enough effective capillary radius is essential to make fully infiltrated thick powder compacts. To meet this requirement, particle rearrangement has to be controlled to such an extent that it will allow infiltration to proceed without pulling particles too close to each other, while still being able to eliminate residual pores in the infiltrated area. It is highly possible that addition of Ni or Cr powders can help to manipulate the rearrangement process. The solubility of Ni or Cr in Ag-Cu eutectic melts at 850°C is so small that the contacts of Cu particles around a Ni or Cr particle are more difficult to melt away than Cu/Cu particle contacts. In other words, Cu particles around a Ni or Cr particle are more difficult to rearrangement themselves. Thus, particle rearrangement slows down around Ni or Cr particles which provides time for infiltration. Cr additions are more effective because Cr is non-wettable by the Ag-Cu eutectic melt. Then the melt is repelled from reaching the Cu/Cr contacts. In the case of irregular copper powders, severe mechanical interlocking significantly increases the resistance to particle rearrangement and addition of Ni powders has little effect. In fact, powder compacts without Ni addition showed the highest infiltration efficiency and lowest residual porosity.

2.6.3 *Copper Butt Joints*

When designing LIPB joints, it is generally required that the infiltrant contains less MPD such that the mechanical properties of the joints can be maintained. Nonetheless, it is difficult for such a base-metal-saturated infiltrant to dissolve the particle contacts and break through the closed-end capillaries. As has been observed in the transverse infiltration tests, infiltration is strongly influenced by the dissolution of these closed-end capillaries. Therefore Cu-Ag eutectic is a better infiltrant than 45Cu-55Ag, although the latter one has less MPD in the alloy. Thus Cu-Ag eutectic was selected as the infiltrant in making Cu/Cu butt joints. Compacts of spherical copper powders were chosen as the interlayers. Figure 2.23 shows the microstructure of a LIPB joint with an interlayer thickness of about 0.3 mm. Rough interfaces between the base metal and the interlayer indicate a little dissolution of the base metal and subsequent interdiffusion across the interface. The interlayer has completely homogenized. Since the designed overall content of Ag (MPD) in the interlayer was about 8 wt%, which is the solidus composition according to the binary phase diagram at the joining temperature (850°C), no residual liquid should exist at the end of isothermal

holding. Precipitation of α (Ag-rich) phase in β (Cu-rich) matrix can be expected upon cooling and this is discernible in Figure 2.23. Large size copper butt joints with 22 mm gaps were also successfully made. The overall MPD (Ag) concentration in the joint was designed to be 8 wt%, and the joint is shown in Figure 2.24. Since infiltration was performed horizontally, two powder interlayers (11 mm thick each) with 2 wt% Cr addition were used and Cu-Ag eutectic foils were evenly placed between the faying surface/interlayer as well as between the two interlayers. Such a configuration can reduce the total liquid amount at each interface and avoid loss of liquid due to gravity at the infiltration temperature.

An alternative approach of controlling dissolution at the initial stage of infiltration is by direct applying a protective coating on individual powder particles. For copper powders, nickel coating can be selected. Figure 2.25(a) shows a copper joint assembly with a Ni-coated Cu powder interlayer, and Figure 2.25(b) reveals the same joint after bonding. Complete infiltration can be observed from this as-bonded joint.

2.7 Summary and Conclusions

In this chapter, some fundamental aspects of the LIPB process have been studied. Approximate analytical solutions are proposed to describe the kinetics of dissolution as well as isothermal diffusional solidification. Experiments were performed on longitudinal, straight capillaries, transverse, closed-end capillaries, powder compacts, and Cu/Cu large gap butt joints. The conclusions can be summarized below:

(1) To make mechanically sound, thick TLP joints, the volume fraction of liquid in the joint has to be decreased. The liquid phase is transitional according to the phase diagram, which is in contrast to persistent liquid phase sintering (LPS) processes.

(2) Planar front liquid infiltration of a powder compact was found to reduce the residual pores while still allowing a small amount of liquid to be used.

(3) The Washburn equation is applicable to straight capillary infiltration, provided the infiltrants and the base material have little interaction at the infiltration temperature. When the interaction is strong, the infiltration kinetics is perturbed because of the non-equilibrium nature of the system as observed in infiltrating copper capillaries by Cu-Ag alloys.

(4) Transverse infiltration was much slower and infiltration distance depended on the dissolution kinetics. A saturated melt of 45Cu-55Ag could not infiltrate the transverse capillaries, which are similar to the closed-end capillaries in powder compacts.
(5) The results of powder compact infiltration experiments revealed greatly decreased infiltration rate as compared with the outcome of straight capillary tests. This is caused by the tortuosity and very small effective radius of the capillaries due to liquid induced attraction. Because of fast dissolution kinetics and small capillaries, infiltration may be stopped by diffusional solidification.
(6) Dissolution of powder particles has to be adequately controlled such that on the one hand, the closed-end capillaries can be opened up, and the capillary radius is maintained large enough for finishing infiltration before diffusional solidification; and on the other hand, the particles can rearrange themselves to eliminate pores behind the infiltration front.
(7) Small amounts of Ni or Cr powder additions were found to be able to affect the rearrangement of spherical Cu powders. Infiltration efficiency was improved, and residual pores were reduced. However, such an effect was negligible when using irregular Cu powders.
(8) Copper/copper butt joints with clearances up to 22 mm have been successfully made. Metallurgical examination showed strong bonds at the interface of the base metal and the powder interlayer. Uniform precipitation of an α (Ag-rich) phase was observed in fine grains of β (Cu-rich) matrix in the interlayer.

2.8 Acknowledgment

The authors would like to thank National Science Foundation (NSF) for supporting this research under the contract number DMR-9301444.

2.9 References

1. G. S. Hoppin, et al., "*Activated Diffusion Bonding*", Welding Journal 49(11), 1970, pp. 505-s to 509-s.

2. D. S. Duvall, et al., "*Methods for Diffusion Welding the Superalloy Udimet 700*", Welding Journal 51(2), 1972, pp. 41-s to 49-s.

3. D. S. Duval, et al., "*TLP Bonding: a New Method for Joining Heat Resistant Alloys*", Welding Journal 53(4), 1974, pp. 203 to 214.

4. Y. Nakao, et al., "*Transient Liquid Insert Metal Diffusion Bonding of Nickel-base Superalloys*", Advanced Joining Technologies, Proceedings of the International Institute of Welding Congress on Joining Research, July, 1990, pp. 129-144.

5. J. W. Chasteen, and G. E. Metzger, "*Brazing of Hastelloy X with Wide Clearence Butt Joints*", Welding Journal, 58(4), 1979, pp.111-s to 117-s.

6. E. Lugscheider, Th. Schittny, and E. Halmoy, "*Metallurgical Aspects of Additive-Aided Wide-Clearance Brazing with Nickel-Based Filler Metals*", Welding Journal, 68 (1), 1989, pp. 9-s to 13-s.

7. E. Lugschider, V. Dietrich, and J. Mittendorff, "*Wide Joint Clearance Brazing with Nickel-Base Filler Metals*", Welding Journal, 67(2), 1988, pp. 47-s to 51-s.

8. W. D. MacDonald, W.D. Zhuang, X.Y. Liu, and T.W. Eagar, "*Kinetics of TLP Bonding Using Powder Interlayers*", submitted to Welding Journal.

9. T. J. Whalen and M. Humenik, "*Sintering in the Presence of a Liquid Phase*", Sintering and Related Phenomena, G.C. Kuczynski, N. Hooton, and C. Gibbon (eds.), Gordon and Breach, 1967, New York, NY, pp. 715-774.

10. W. J. Huppmann and H. Riegger, "*Modeling of Rearrangement Processes in Liquid Phase Sintering*", Acta Metall., vol. 23, 1975, pp. 965-971.

11. T. H. Courtney, "*Densification and Structural Development in Liquid Phase Sintering*", Metall. Trans., vol. 15A, June, 1984, pp.1065-1074.

12. Hyo-hoon Park, et al., "*Pore Filling Process in Liquid Phase Sintering*", Metall. Trans., vol. 15A, June, 1984, pp. 1075-1080.

13. G. Petzow and W.A. Kaysser, "*Basic Mechanisms of Liquid Phase Sintering*", Sintered Metal-Ceramic Composites, edited by G.S. Upadhyaya, Elsevier Science Publishers B.V., Amsterdam, 1984.

14. R. M. German, Liquid Phase Sintering, Plenum Press, New York, NY, 1985.

15. R. M. German, "*The Use of Phase Diagrams in Predicting Sintering Behavior*", Annual Powder Metallurgy Conference Proceedings, Boston, May, 1986, pp. 235-247.

16. W. A. Kaysser, "*Liquid Phase Sintering*", Powder Metallurgy-An Overview, edited by I. Jenkins and J.V. Wood, The Institute of Metals, 1991, pp. 183-197.

17. Dong-Duk Lee, et al., "*A Direct Observation of the Grain Shape Accommodation during Liquid Phase Sintering of Mo-Ni Alloy*", Scripta Metall., 1990, vol. 24, pp. 927-930.

18. A. P. Savitskii, "*Relation between Shrinkage and Phase Diagram*", Science of Sintering, 1991, vol. 23, no. 1, pp. 3-17.

19. F. V. Lenel, "*Sintering in the Presence of a Liquid Phase*", Trans. AIME, 1948, vol. 175, pp. 878-896.

20. H. S. Cannon and F.V. Lenel, "*Some Observations on the Mechanism of Liquid Phase Sintering*", Plansee Proceeding, edited by F. Benesovsky , Metallwerk Plansee, Reutte, Austria, 1953, pp. 106-121.

21. W. D. Kingery, "*Densification During Sintering in the Presence of a Liquid Phase I*", J. Appl. Phys., 1959, vol. 30, pp. 301-309.

22. V. Smolej, S. Pejovnik, and W.A. Kaysser, "*Rearrangement During Liquid Phase Sintering of Large Particles*", Powder Met. Int., 1981, vol. 14, pp. 126-128.

23. W. Nernst, "*Theorie der Reaktionsgeschwindigkeit in heterogenen Systemen*", Z. Phisikal Chem., 1904, vol.47, pp. 52-55.

24. J. M. Lowell and B. Chalmers, "*The Isothermal Transfer from Solid to Liquid in Metal Systems*", Trans. TMS-AIME, 1959, vol. 215, pp. 499-506.

25. A. Hibino, "*Estimation of Kinetic Parameters for Combustion Synthesis of Ni3Al Intermetallic Compound by Dipping Ni Wire into Al Melt*", Journal of the Japan Institute of Metals, 1993, vol. 57, no. 7, pp. 767-773.

26 E. W. Washburn, "*The Dynamics of Capillary Flow*", Phys. Rev., 1921, vol. XVII, no. 3, pp. 273-283.

27. G. Picket, "*Rate of Rise of Water in Capillary Tubes*", J. Appl. Phys., 1944, vol. 15, pp. 623.

28. W. E. Brittin, "*Liquid Rise in a Capillary Tube*", J. Appl. Phys., 1946, vol. 17, pp. 37-44.

29. J. R. Ligenza, and R. B. Bernstein, "*The Rate of Rise of Liquids in Fine Vertical Capillaries*", Journal of American Chemical Society, 1951, vol. 73, pp. 4636-4638.

30. T. E. Bartell and H. J. Osterhof, "*The Pore Size of Compressed Carbon and Silica Membranes*", J. Phys. Chem., 1928, vol. 32, pp. 1553-1571.

31. S. Banerjee, R. Oberacker, and C. G. Goetzel, "*Mechanism of Capillary-Force Induced Infiltration of Iron Skeletons with Cast Iron*", The International Journal of Powder Metallurgy & Powder Technology, 1984, vol. 20, no. 10, pp. 325-340.

32. J. Lezanski, "*Kinetics of Liquid Infiltration in Porous Materials from Powders*", Archives of Metall., 1989, vol. 34, Iss. 1, pp. 93-108.

33. M. Yokota, et al., "*Influence of Necks between Powder Particles on the Penetration of Liquids into Sintered Glass Powder Porous Bodies*", Journal of the Japan Institute of Metals (in Japanese), 1981, vol. 45, no. 8, pp. 776-780.

34. M. Yokota, et al., "*On the Mechanism of Penetration of Liquids into Sintered Glass Powder Porous Bodies*", Journal of the Japan Institute of Metals (in Japanese), 1979, vol. 44, no. 2, pp. 191-196.

35. M. Yokota, "*Basis and Application of Infiltration Techniques for Powder Metallurgy*", Powders and Powder Metallurgy (in Japanese), 1991, vol. 38, no. 4, pp. 464-471.

36. I. Tuah-Poku, M. Dollar, and T. B. Massalski, "*A Study of the Transient Liquid Phase Bonding Process Applied to a Ag/Cu/Ag Sandwich Joint*", Metall. Trans., 1988, 19A (3), pp. 675-686.

37. Y. Nakao, et al., "*Dissolution Phenomenon of Base Metal into Liquid Insert Metal*", Quarterly Journal of Japan Welding Society", 1988, pp. 67.

38. H. Nakagawa, et al., "*Modeling of Base Metal Dissolution Behavior during Transient Liquid Phase Brazing*", Metall. Trans., 1991, 22A, pp. 543-555.

39. S. Liu, et al., "*Modeling of Brazing Process that Use Coatings and Interlayers*". Welding Journal, 1991, 70(8), pp. 207-s to 215-s.

40. G. Poots, "*On the Application of Integral-Methods to the Solution of Problems Involving the Solidification of Liquids Initially at Fusion Temperature*", Int. J. Heat Mass Transfer, 1962, vol. 5, pp. 525-531.

41. P. Sebo, B. Gallois and C.H.P. Lupis, "*The Surface Tension of Liquid Silver-Copper Alloys*", Metall. Trans., 1977, 8B, pp. 691-692.

42. P.R. Sharps, et al., "*Wetting and Spreading in the Cu-Ag System*", Acta Metall., 1981, vol. 29, pp. 855-865.

43. T. Iida, "*Physical Properties of Liquid Metals III*", Journal of the Japan Welding Society, 1994, vol. 63, no. 2, pp. 70-75.

44. W. D. MacDonald, "*Kinetics of Transient Liquid Phase Bonding*", Ph.D. Thesis, 1993, MIT.

45. Ronald B. Heady and John W. Cahn, "*An Analysis of the Capillary Forces in Liquid Phase Sintering of Spherical Particles*", Metall. Trans., 1970, vol. 1, no. 1, pp. 185-189.

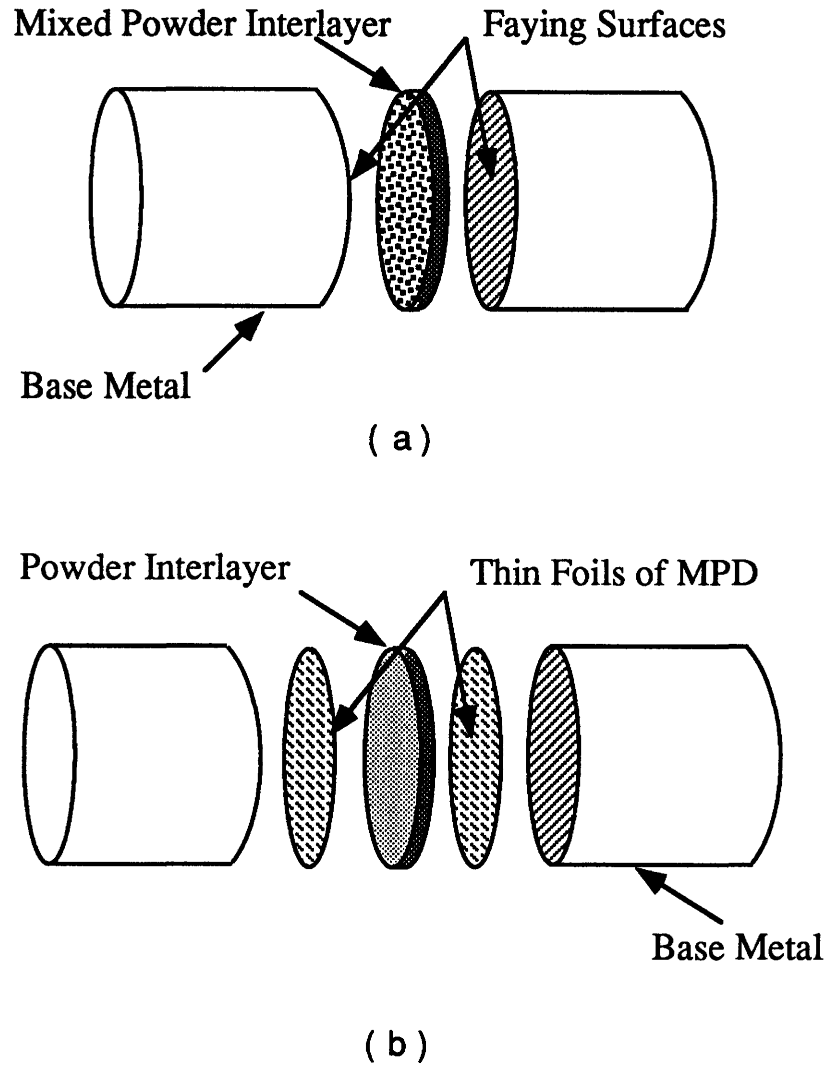

Figure 2.1. Configrations of (a) mixed powderlayer bonding and (b) liquid infiltrated powder interlayer bonding (LIPB) process. The powder interlayer in (b) can have the same composition as the base material and the MPD can either be thin foils or coatings.

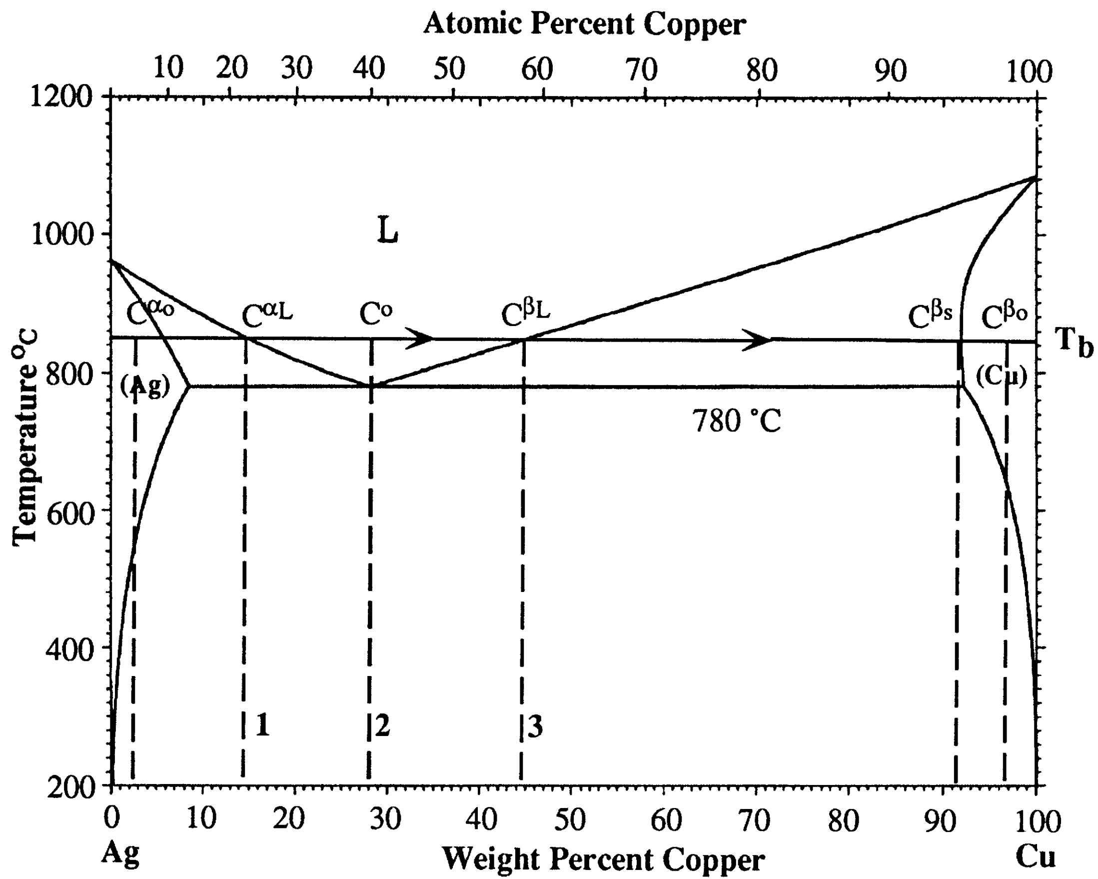

Figure 2.2. Copper-silver binary phase diagram. Three alloys chosen as infiltrants are marked by 1, 2, and 3, respectively. The infiltration temperature is T_b = 850 °C.

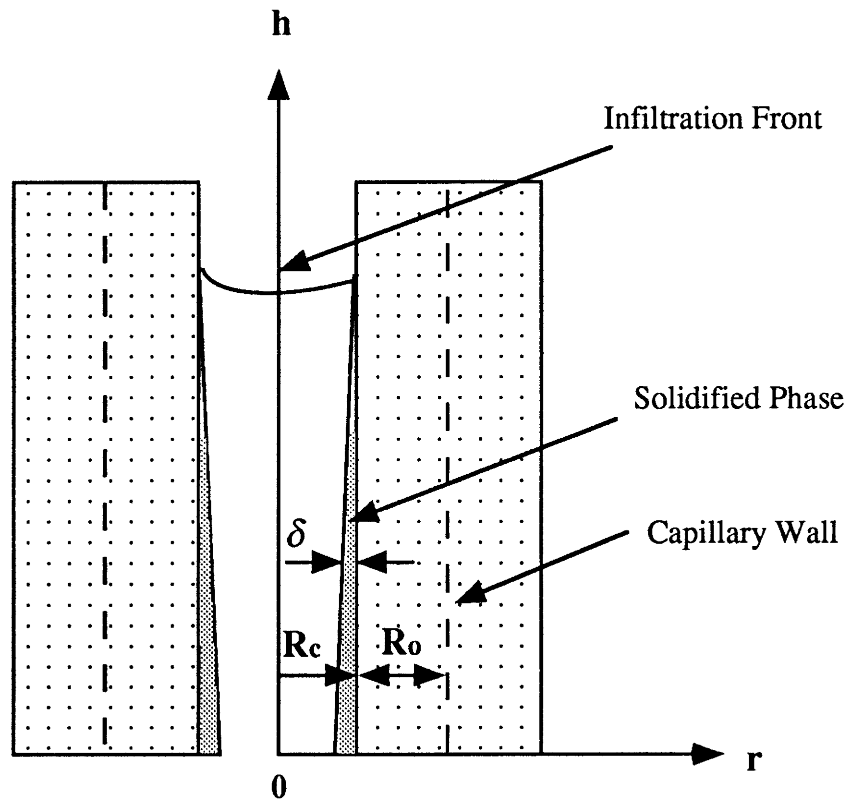

Figure 2.3. Schematic drawing of dissolution or isothermal diffusional solidification during unidirectional infiltration of liquid into straight capillaries. Note only diffusional solidification is depicted. In the case of dissolution, δ should be in the capillary wall instead of growing into the capillary itself.

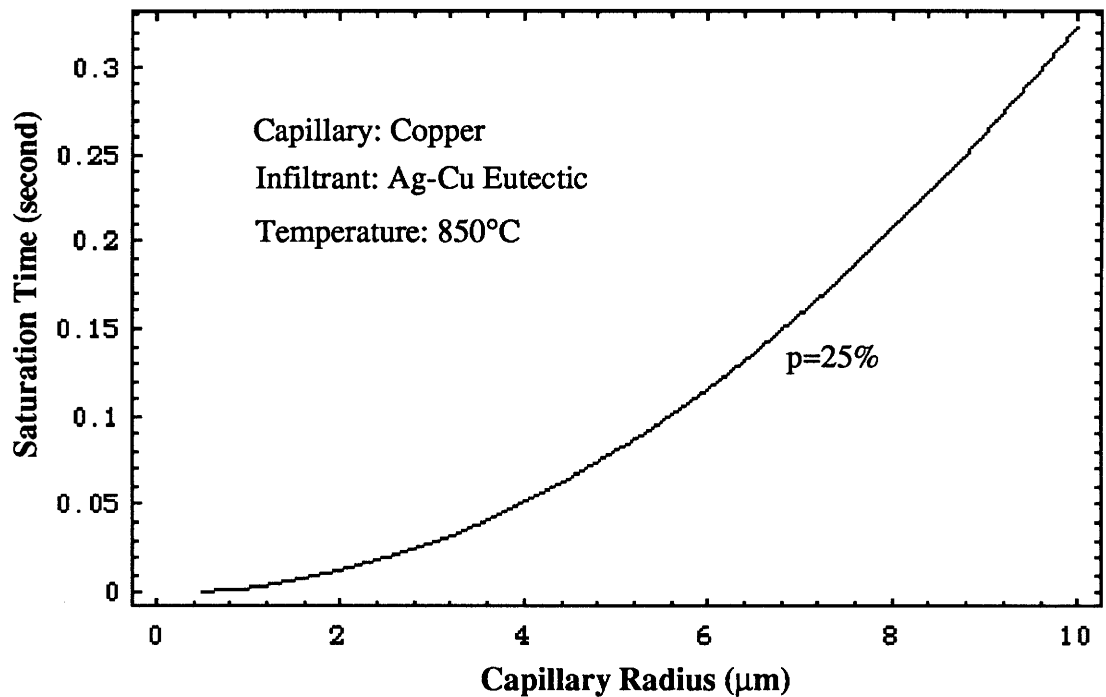

Figure 2.4. Melt saturation time as a function of capillary radius. Volume fraction of porosity, p, is calculated based on the straight capillaries.

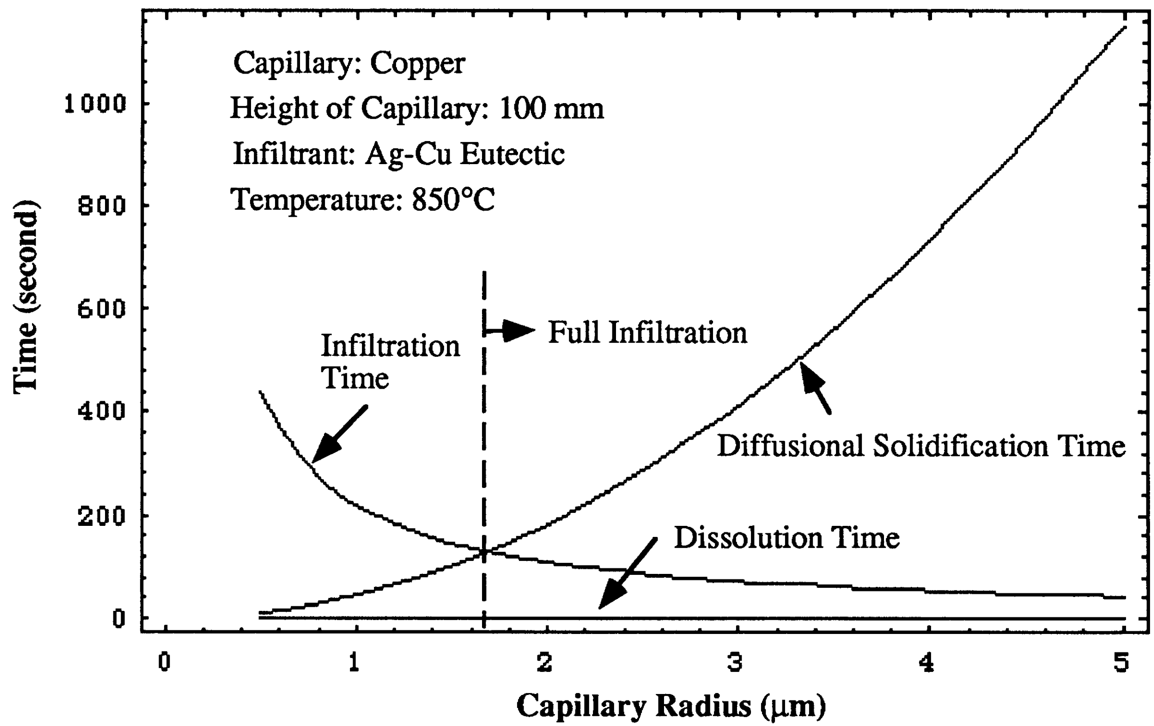

Figure 2.5. Time for diffusional solidification and infiltration of a circular capillary as a function of capillary radius. When the capillary radius is above 1.7 μm, full infiltration of the capillary can be achieved.

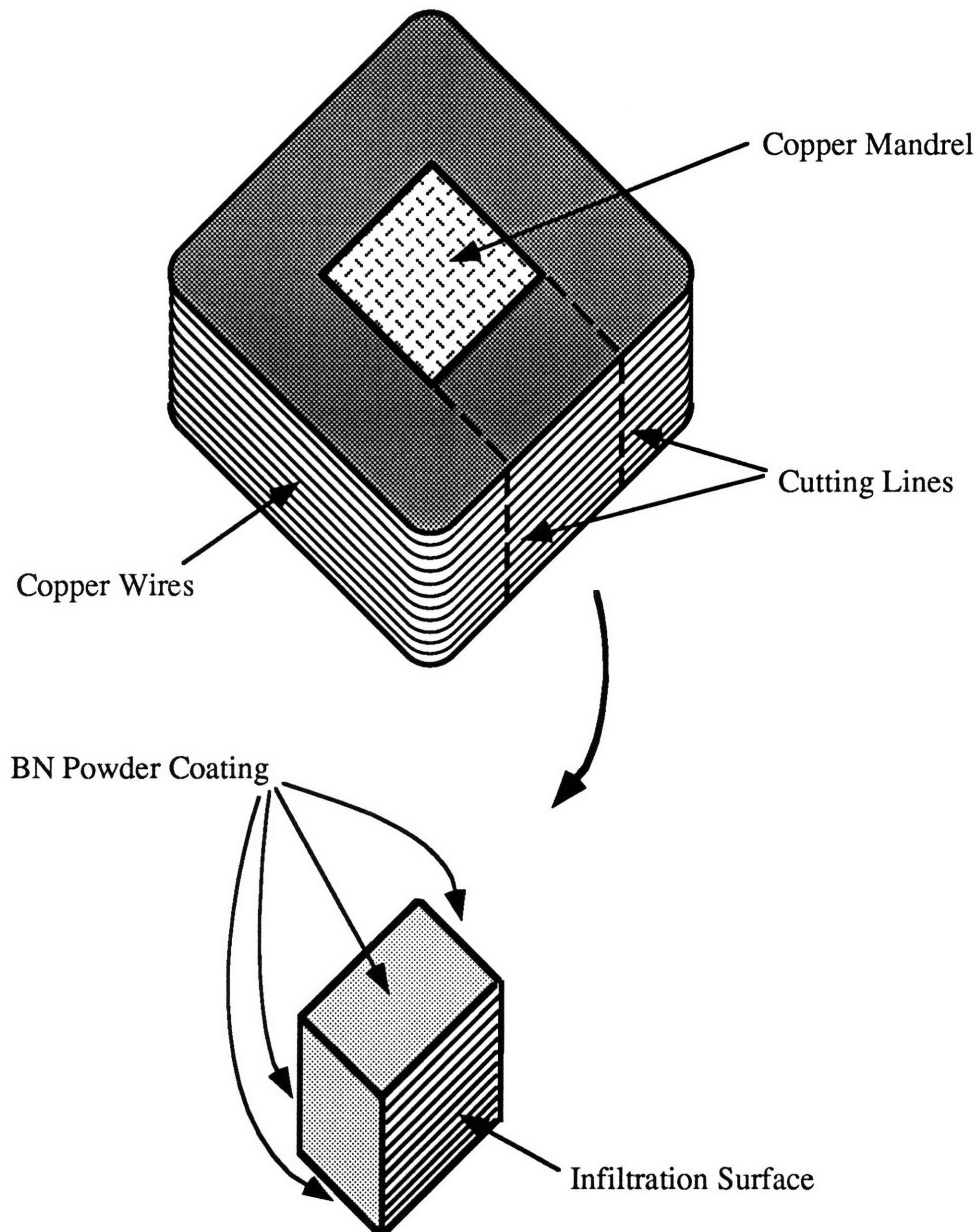

Figure 2.6. Schematic drawing of preparing the samples for transverse infiltration tests: 250 μm diameter copper wires were wound on a copper mandrel and subsequently sintered. The cut sample has a dimension of about 8x8x8 mm^3.

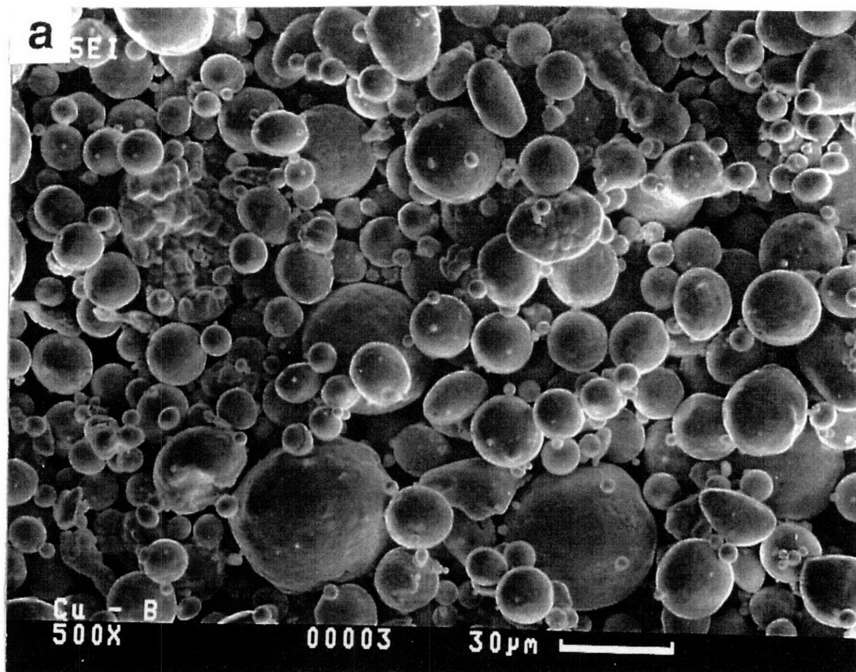

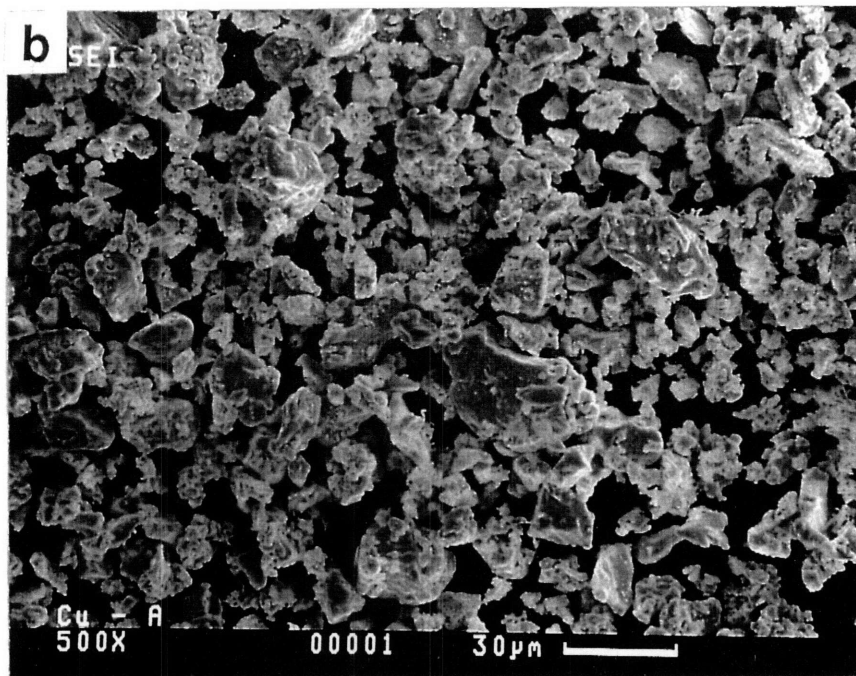

Figure 2.7. Features of spherical copper powders (a), and irregular copper powders (b) used in preparing compacts for infiltration experiments.

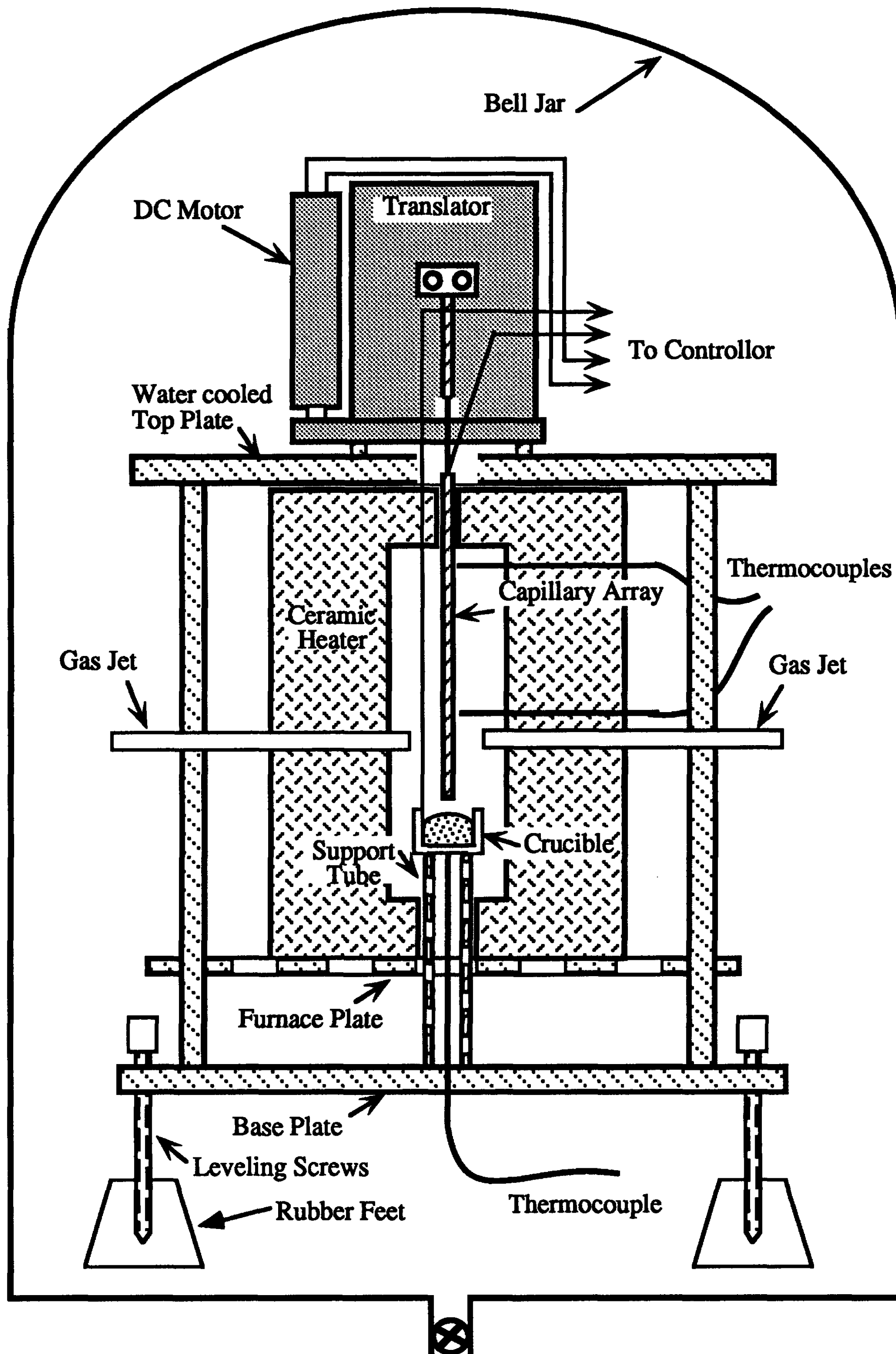

Figure 2.8. Schematic drawing of the apparatus for the experiments with straight capillary infiltration.

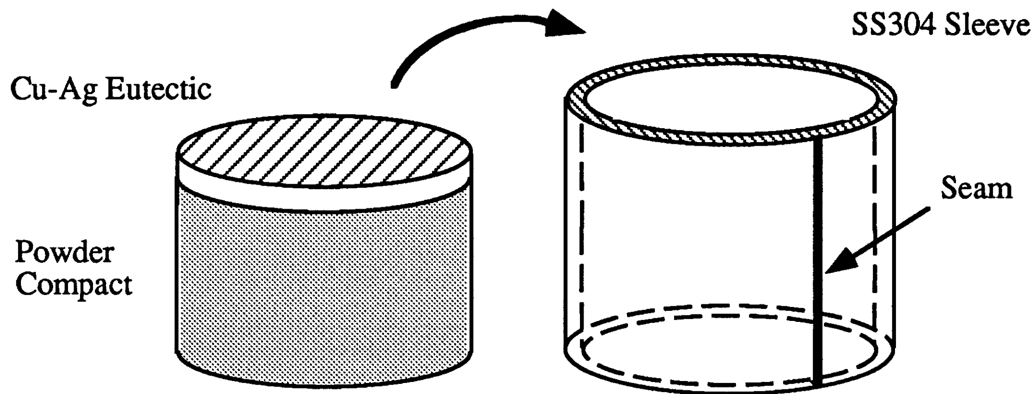

Figure. 2.9. Assembly for powder compact infiltration. The seam along the SS304 sleeve is for accommodating thermal expansion of the powder compact.

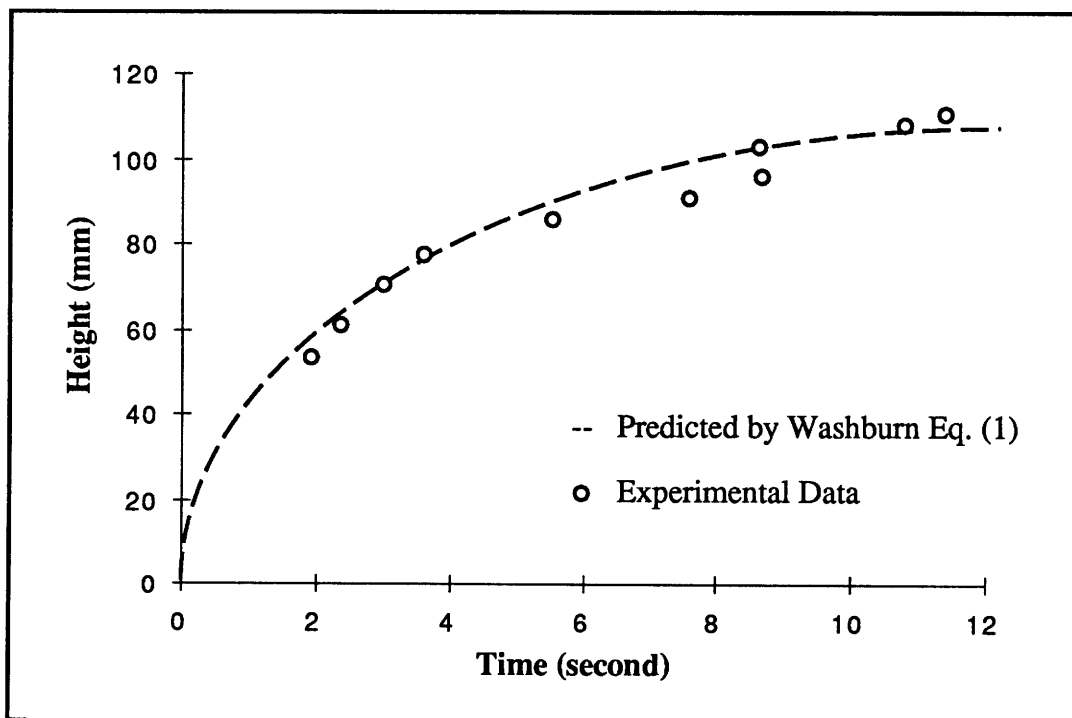

Figure. 2.10. Longitudinal infiltration of capillaries formed by 177 micron nickel wires with Ag-Cu eutectic alloy at 850 °C. Infiltration was undertaken in 100 torr forming gas.

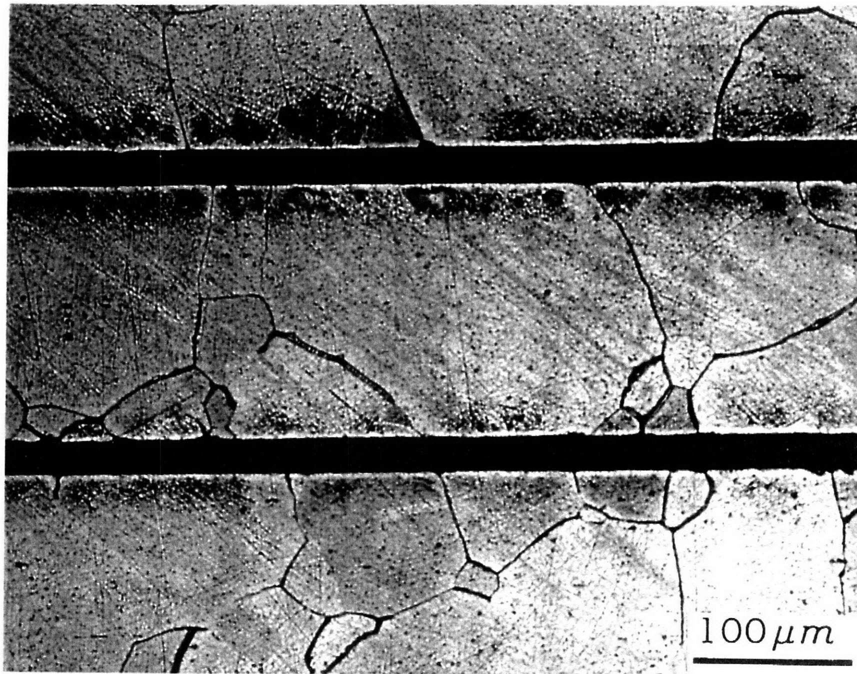

Figure 2.11. Microstructure of the nickel capillaries infiltrated by Ag-Cu eutectic alloy. The infiltration was performed at 850°C for 11 seconds. The dark phase is Ag-Cu eutectic alloy, and relatively large nickel grains can be seen.

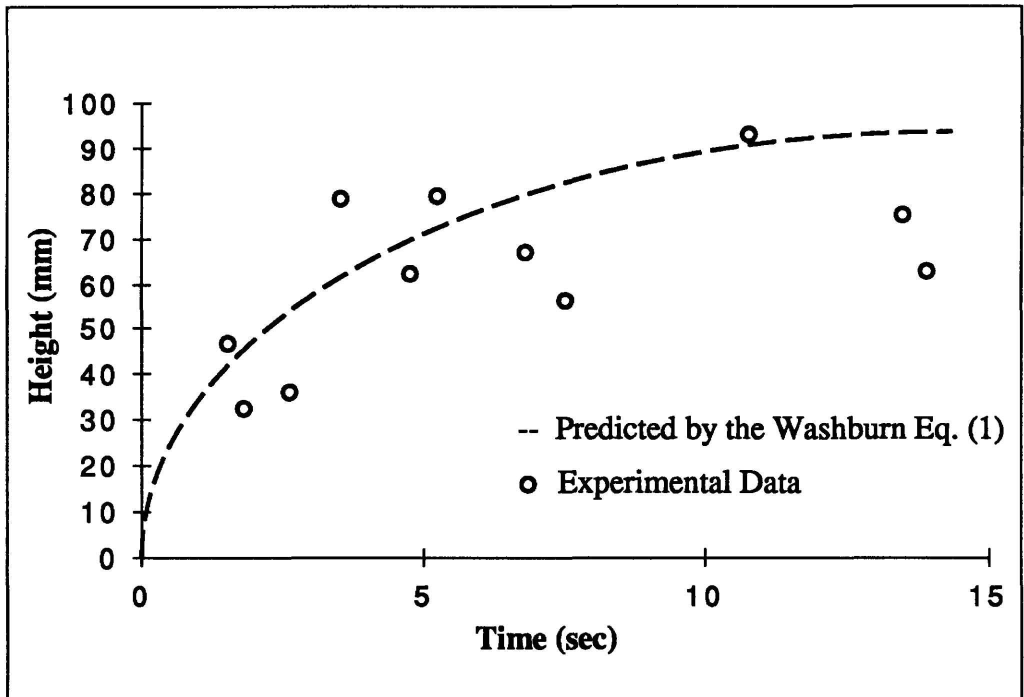

(a)

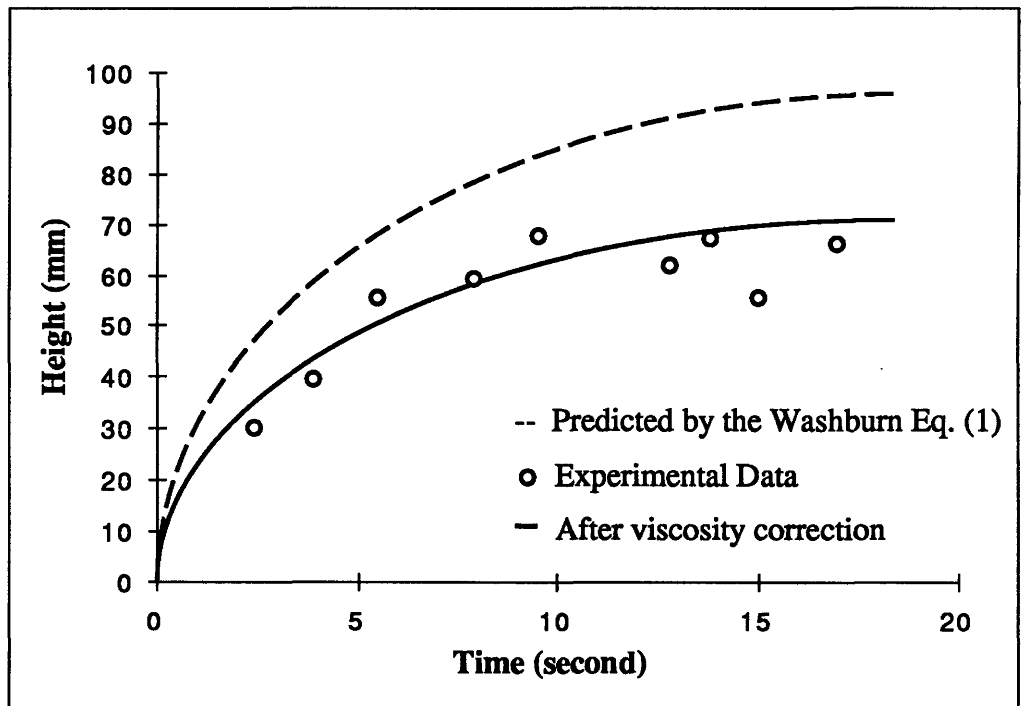

(b)

Figure. 2.12. Longitudinal infiltration of capillaries formed by 100 micron copper wires with (a) Ag-Cu eutectic alloy, and (b) 45Ag-55Cu alloy at 850 °C. Infiltration was performed in 100 torr forming gas.

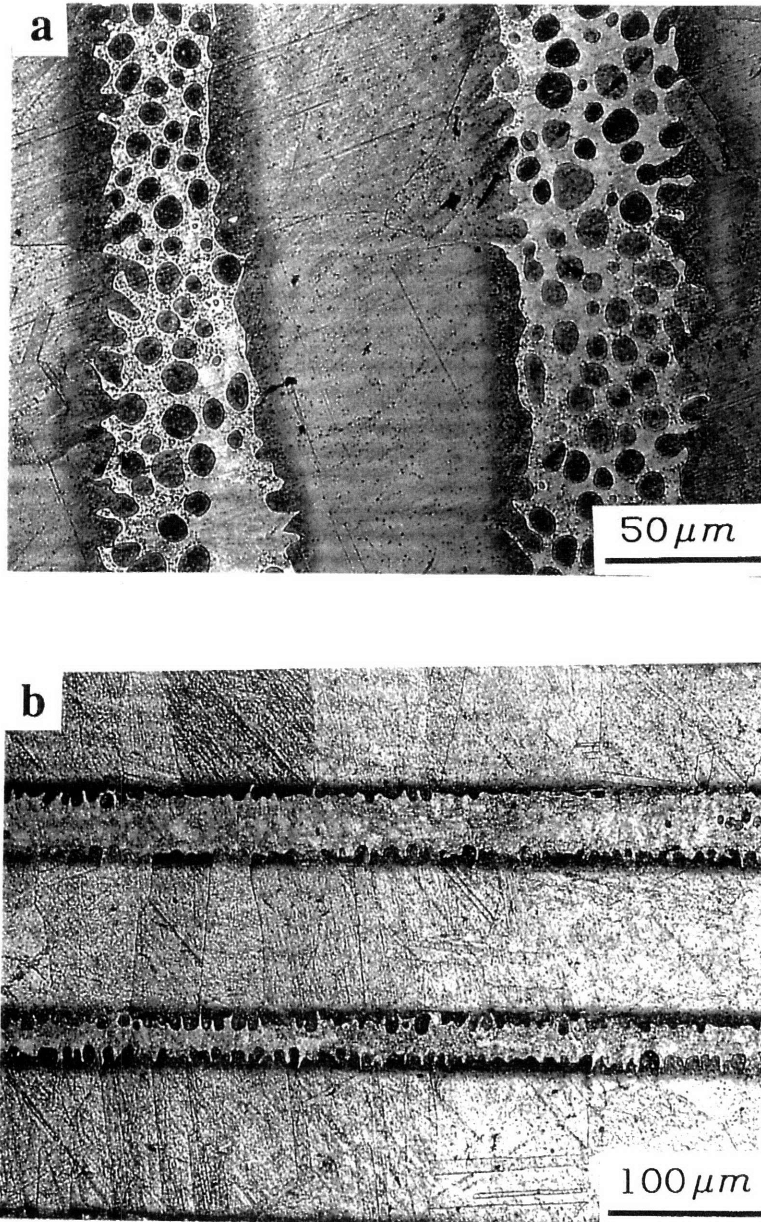

Figure 2.13. Microstructures of the infiltrated copper capillaries. (a) infiltrated by Ag-Cu eutectic at 850°C for 5.36 seconds. The area is close to the bottom of the capillaries (liquid enteance). (b) same capillaries, but at the upper part.

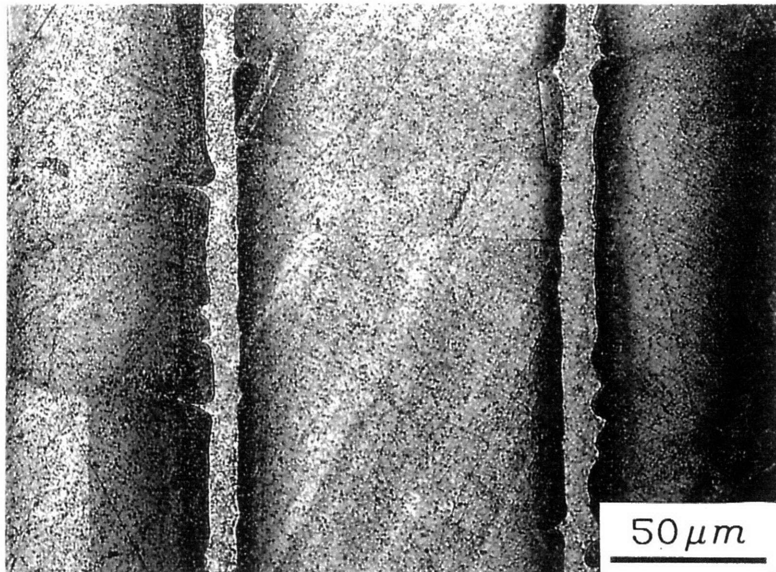

Figure 2.14. Microstructure of the infiltrated copper capillaries. The infiltrant was 45Ag-55Cu, and infiltration was performed at 850°C for 11.86 seconds. The area is close to the bottom of the capillaries (liquid entrance).

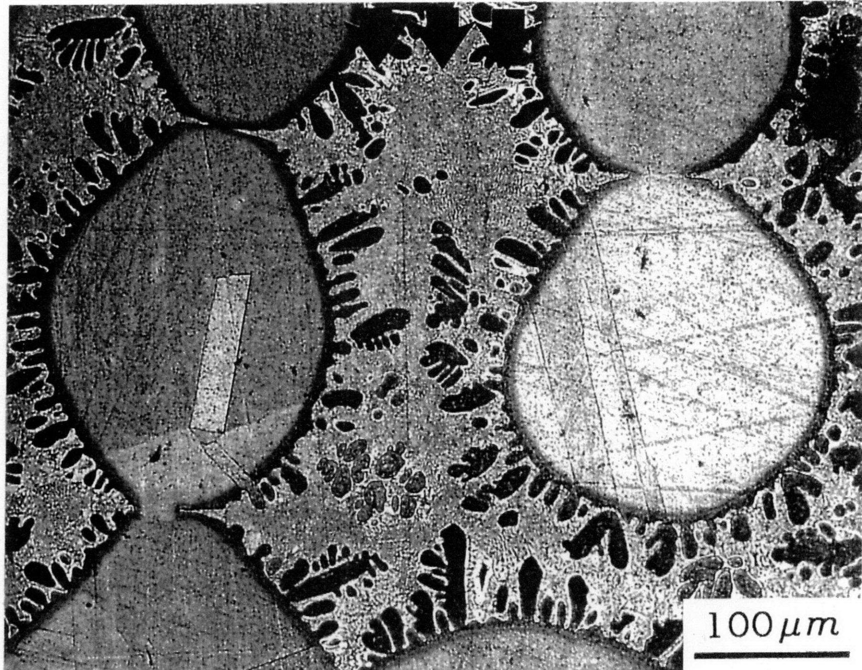

Figure 2.15. Microstructure of transversly infiltrated copper wires by Ag-Cu eutectic alloy at 850 °C for 13 seconds. The area is close to the bottom of the capillaries (liquid entrance). Arrow indicates infiltration direction.

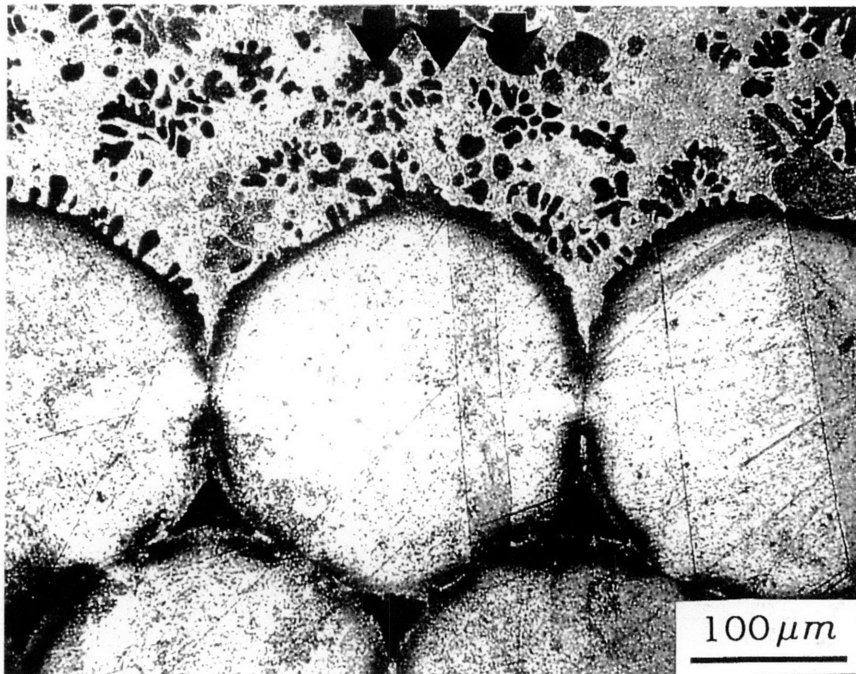

Figure 2.16. Microstructure of transversly infiltrated copper wires by 45Cu-55Ag alloy at 850 °C for 2 minutes. The partially dissolved copper wires are of the first layer of the capillary. Arrow indicates infiltration direction.

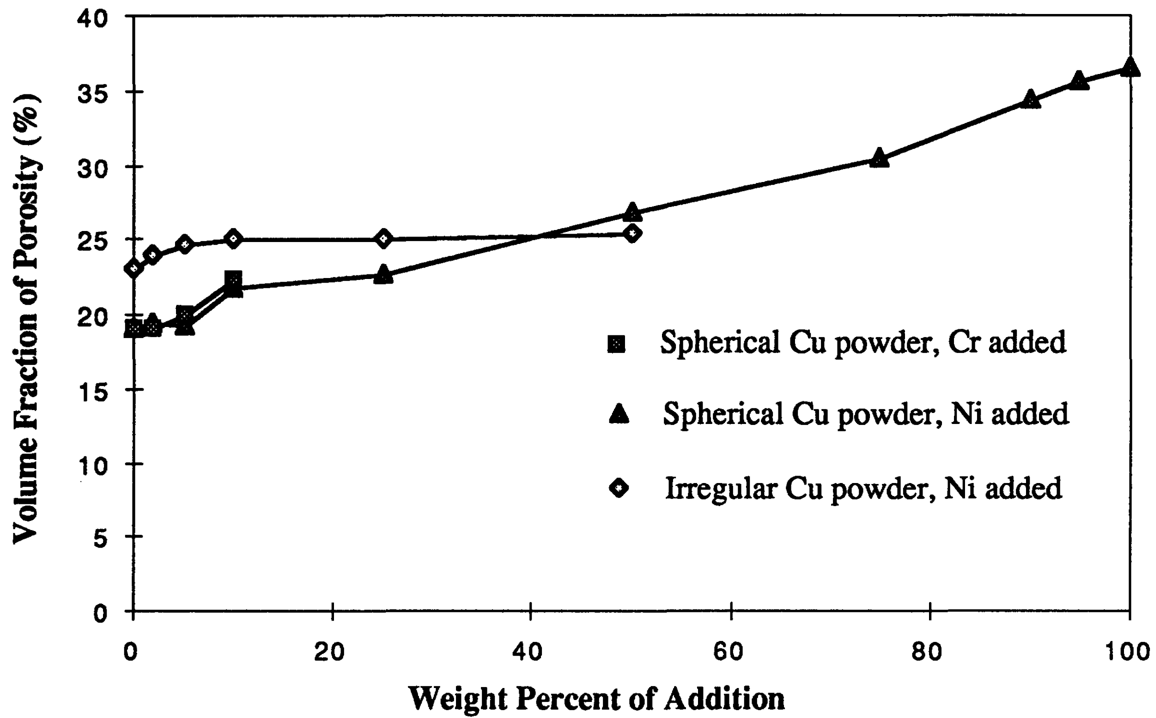

Figure 2.17. Initial volume fraction of porosity in the compacts in relation to Ni or Cr powder addition. Compressive pressure was 310 MPa, and each compact was 3.5 g.

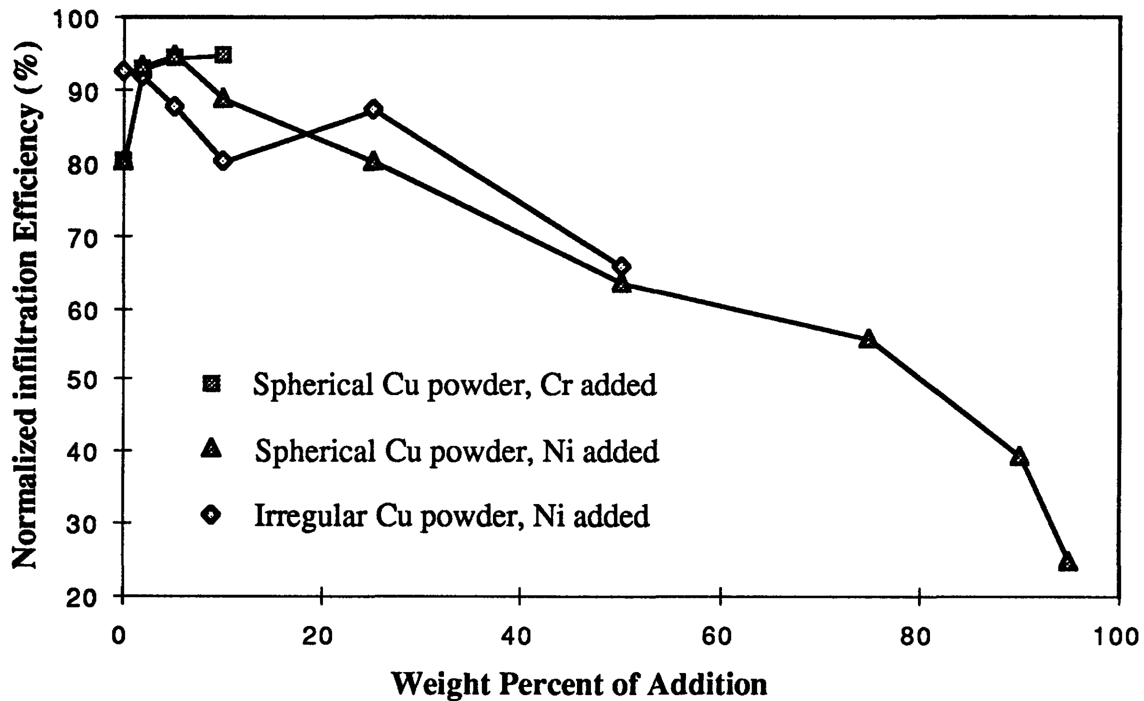

Figure 2.18. Infiltration efficiency as related to the shape of the powders and the amount of Cr and Ni powders added into the compacts.

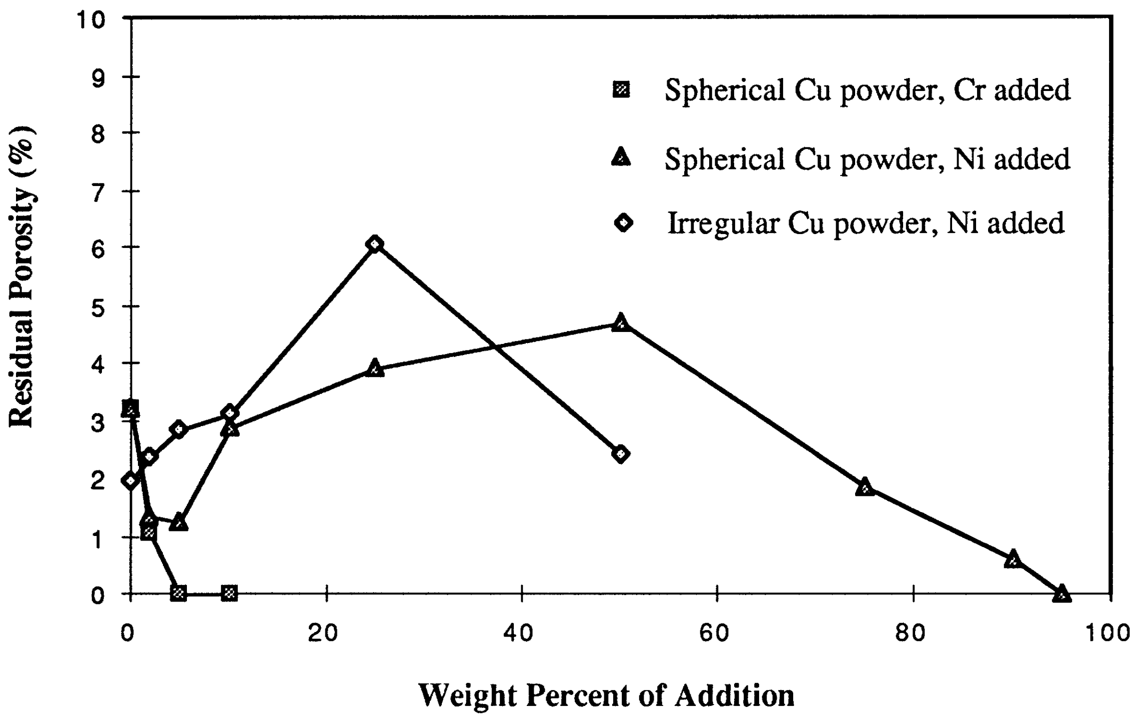

Figure 2.19. Volume fraction of residual porosity in the infiltrated area in relation to the powder shape and the amount of Cr and Ni powders added into the compacts.

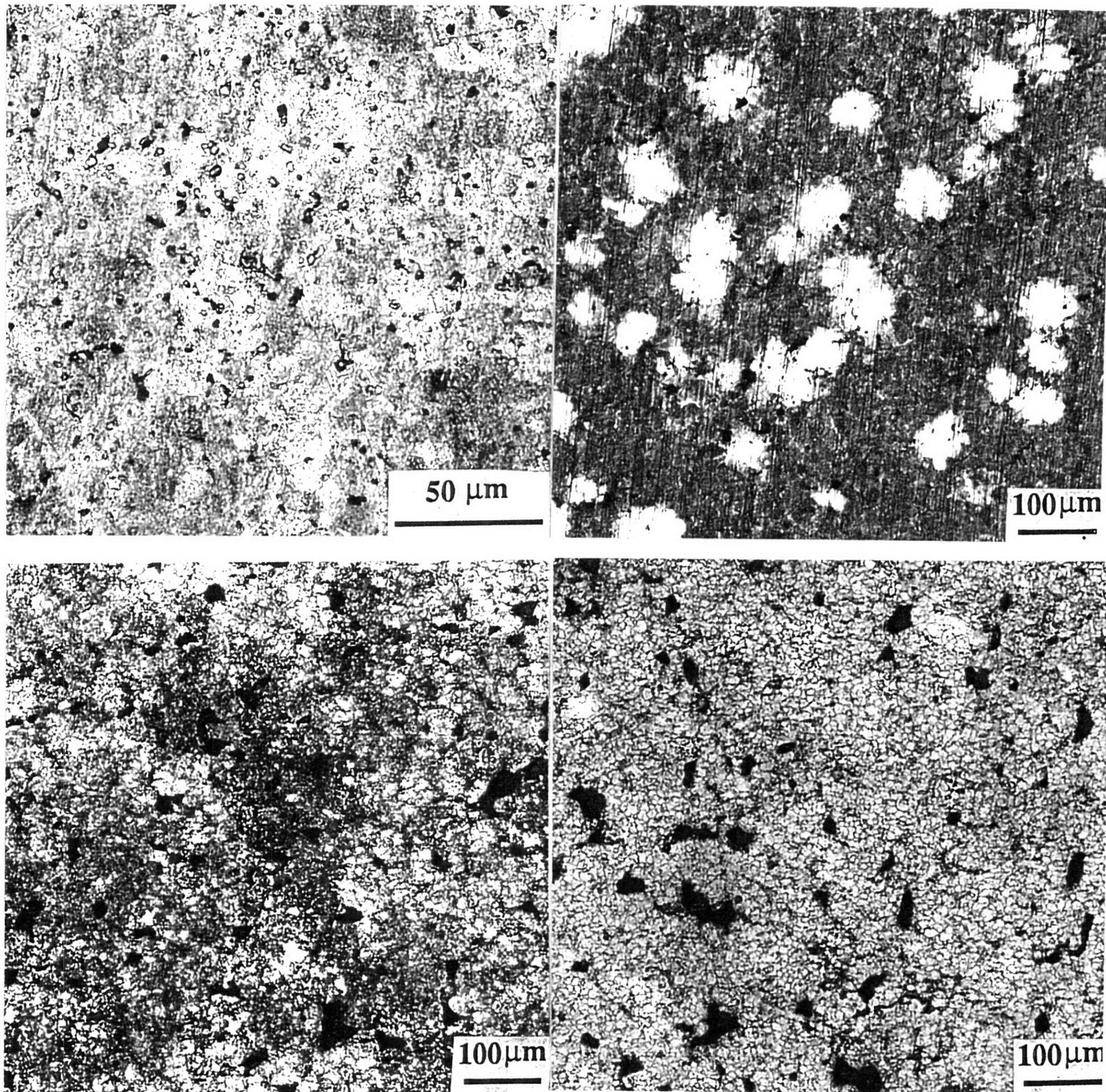

Figure 2.20. Microstructures of Ag-Cu eutectic infiltrated compacts of spherical Cu powders with various amount of Ni powder addition. (a) no addition; (b) 2 wt% Ni, the white areas are nickel powders; (c) 25 wt% Ni and (d) 50 wt% Ni. Infiltrations were performed at 850°C for 5 minutes in 100 torr forming gas.

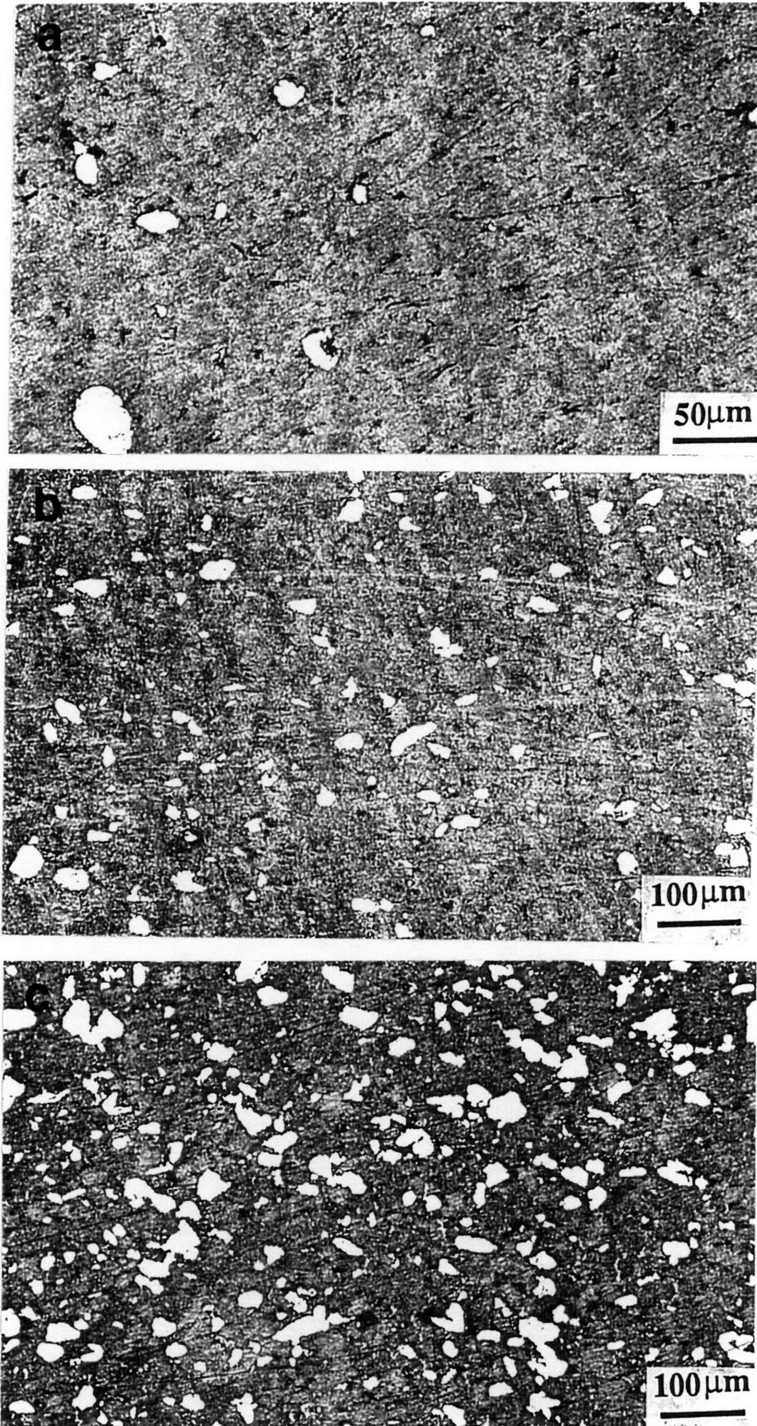

Figure 2.21. Microstructures of Ag-Cu eutectic infiltrated compacts of spherical Cu powders with various amount of irregular Cr powder addition. (a) 2 wt% Cr; (b) 5 wt% Cr and (c) 10 wt% Cr. The white areas are chromium powders. The infiltrations were performed at 850 °C for 5 minutes in 100 torr forming gas.

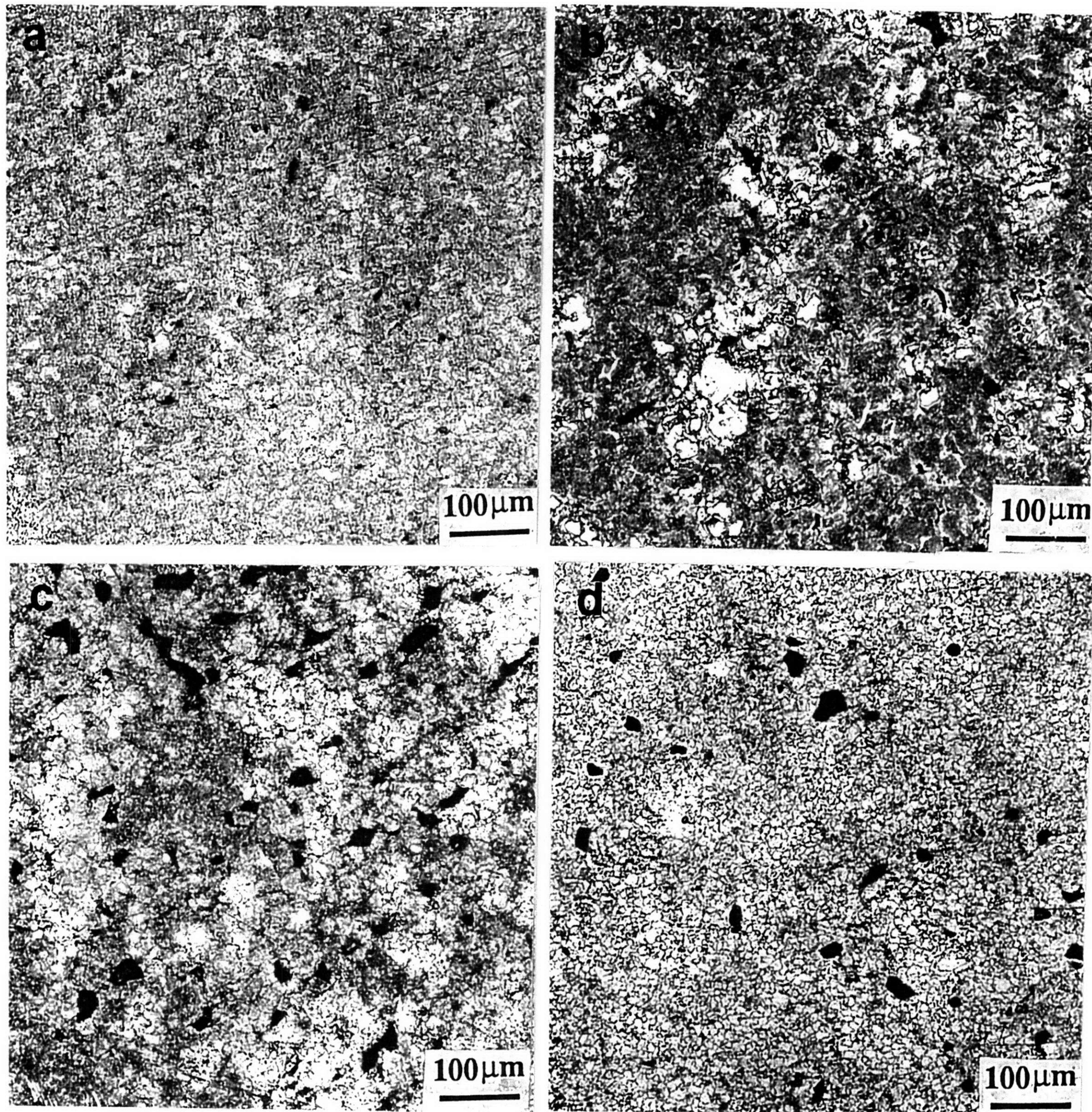

Figure 2.22. Microstructures of Ag-Cu eutectic infiltrated compacts of irregular Cu powders with various amount of spherical Ni powder addition. (a) no addition; (b) 5 wt% Ni, the white areas are nickel powders; (c) 25 wt% Ni and (d) 50 wt% Ni. The infiltrations were taken at 850 °C for 5 minutes in 100 torr forming gas.

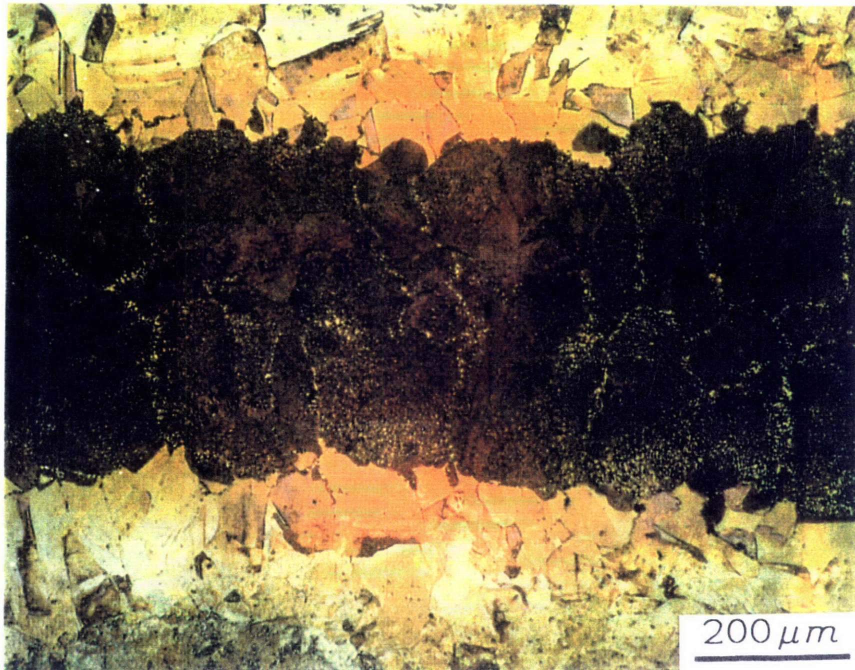

Figure 2.23. Microstructure of a copper joint made by the LIPB method. Joining was performed at 850 °C for 60 minutes in vacuum. The powder interlayer was consisted of spherical copper powders. Copper-Silver eutectic was the infiltrant and silver concentration in the joint was 8 wt%.

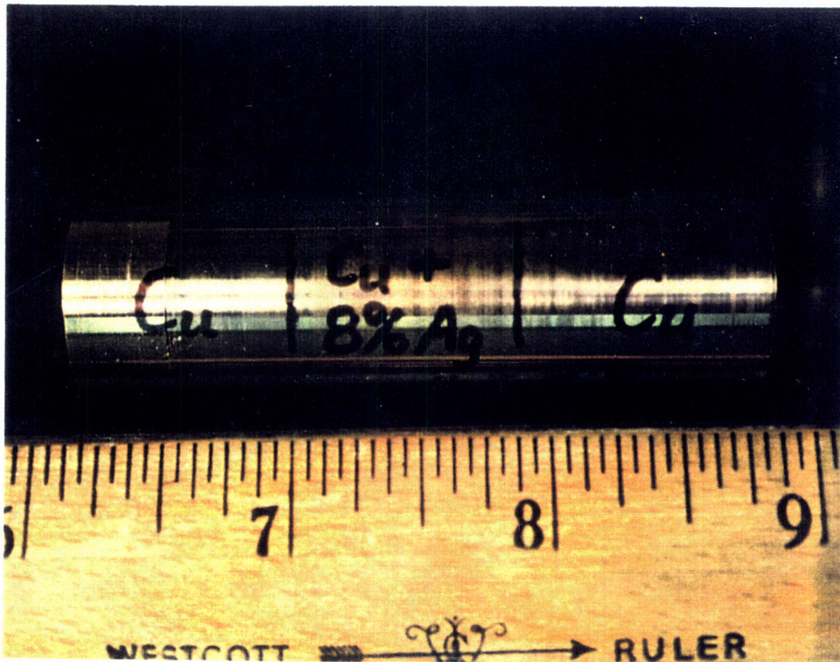

Figure 2.24. A copper joint with joint gap about 22 mm made by the LIPB process. Two copper powder interlayers with 2 wt% chromium powder addition were used. Copper-silver eutectic was the infiltrant. Joining was performed at 850°C for 30 minutes in vacuum. The markers are in inches.

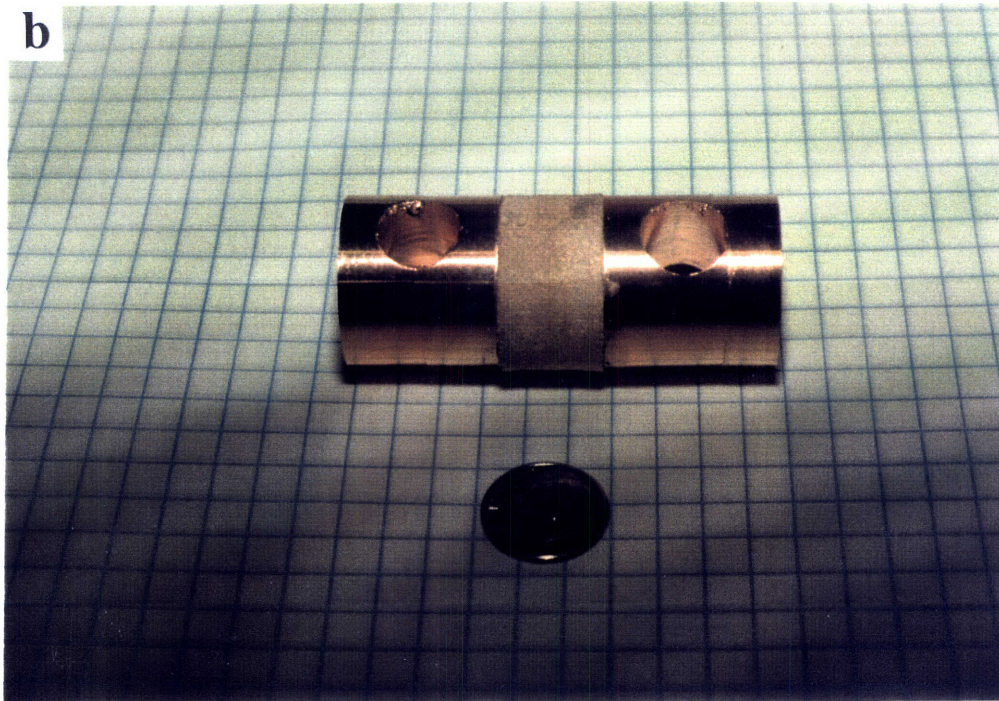

Figure 2.25. Copper butt joint made by the LIPB process. The powder interlayer consisted of Ni-coated copper powders. (a): assembly before bonding, and (b): the as-received joint after bonding. Joining was performed at 850°C for 30 minutes in vacuum.

Appendix A Dissolution of a Solid Cylinder Surrounded by a Layer of Unsaturated Liquid

An analytical solution for the dissolution of a circular, cylindrical capillary when infiltrated by an unsaturated liquid is extremely difficult. In most cases, numerical methods have to be used to obtain a solution. However, such solutions usually contain less physical sense, and therefore is difficult to compare with the parallel process, in this case, the infiltration kinetics. Thus, an approximate analytical solution will provide some useful information for comparing the different kinetics.

Instead of modeling the dissolution of a hollow cylinder with a liquid in it, the dissolution of a solid cylinder with diameter R_o, surrended by a layer of liquid with thickness of R_c is treated. The derivation is based on the assumptions of uniform dissolution and controlling mechanism of solute diffusing in the liquid. Also for short time, it is assumed that the liquid concentration at R_o+R_c is not disturbed. A steady state diffusion profile:

$$C_B^L = A + B \ln r \tag{A1}$$

is employed to simulate the concentration from the solid/liquid interface into the liquid, with the boundary conditions:

$$C_B^L\,(\,r = R_o - \delta\,,\,t > 0\,) = C_B^{\beta L} \tag{A2}$$

$$C_B^L\,(\,r = R_o + R_c\,,\,t > 0\,) = C_B^o \tag{A3}$$

where C_B^L denotes the solute concentration in the liquid. C_B^o is the initial solute concentration in the liquid, and $C_B^{\beta L}$ is the solute concentration at the solid/liquid interface. δ is the dissolution thickness of the solid. The mass balabce is given by:

$$(C_B^{\beta o} - C_B^{\beta L})\, d\delta = -D_L \left(\frac{\partial C_B^L}{\partial r}\right)_{r = R_o - \delta} \tag{A4}$$

where D_L is the solute diffusivity in the liquid, and $C_B^{\beta o}$ is the solute content in the solid. Solving equations from (A1) to (A4), the dissolution rate can be obtained:

$$V_d = \frac{D_L (C_B^{\beta L} - C_B^o)}{(R_o - \delta)(C_B^{\beta L} - C_B^{\beta o})} \ln^{-1}\left(\frac{R_o - \delta}{R_o + R_c}\right) \quad \text{(A5)}$$

and the initial dissolution rate results by setting $\delta = 0$:

$$V_d = \frac{D_L (C_B^{\beta L} - C_B^o)}{R_o (C_B^{\beta L} - C_B^{\beta o})} \ln^{-1}\left(\frac{R_o}{R_o + R_c}\right) \quad \text{(A6)}$$

During infiltration of the circular, cylindrical capillary, time for saturation of the liquid due to dissolution is very important, since subsequent diffusional solidification may block the capillary and prevent full infiltration of the capillary. The liquid becomes saturated when its solute concentration goes up to $C_B^{\beta L}$, and the solid is dissolved by δ_s:

$$C_B^{\beta L} = \frac{C_B^o \rho_L R_c^2 + C_B^{\beta o} \rho_S \delta_s (\delta_S + 2R_c)}{\rho_L R_c^2 + \rho_S \delta_s (\delta_s + 2R_c)} \quad \text{(A7)}$$

where ρ_L andρ_s are the densities of liquid and solid, respectively. The dissolution thickness can be expressed as:

$$\delta_s = V_d t_{sat} \quad \text{(A8)}$$

where t_{sat} is the saturation time of the liquid. Solving equations (A7) and (A8) simontaneously by letting $\rho_L = \rho_s$, the saturation time is obtained:

$$t_{sat} = \frac{R_c}{V_d}\left[\left(\frac{C_B^{\beta o} - C_B^o}{C_B^{\beta o} - C_B^{\beta L}}\right)^{1/2} - 1\right] \quad \text{(A9)}$$

Appendix B Diffusional Solidification in a Circular Capillary

Diffusional solidification starts once the liquid is saturated and is soluble in the solid. The solidifying phase grows toward the circular capillary and may block the liquid flow as soon as the capillary is entirely solidified. During infiltration, the growth rate of the solid phase is more important than the exact concentration profile. Hence an approximate solution using the integral method is adopted to estimate the solidification time. The process is assumed to be controlled by solid state diffusion. Figure 3 shows a schematic drawing for this derivation. The initial condition is given by:

$$\delta = 0\,,\ C^s(r, t=0) = C^{\beta o}\,,\ (R_c \leq r \leq R_o + R_c) \qquad \text{(B1)}$$

where δ is the thickness of the solidified phase, and C^s indicates the concentration of MPD. $C^{\beta o}$ is the initial MPD content in the solid. The boundary conditions are:

$$\frac{\partial C^s}{\partial r} = 0\,,\ r = R_o + R_c,\ (t > 0) \qquad \text{(B2)}$$

$$C^s = C^{\beta s},\quad r = R_c - \delta\ (t > 0) \qquad \text{(B3)}$$

$$C^s = C^{\beta L}\,,\ 0 \leq r \leq R_c - \delta\ (t > 0) \qquad \text{(B4)}$$

where R_c is the radius of the capillary and R_o is the thickness of the circular cylinder. $C^{\beta L}$ is the MPD concentration in the saturated liquid, and $C^{\beta s}$ is the solubility limit of the solid at the given infiltration temperature, as shown in Figure 2. The mass balance at the solid/liquid interface is given by:

$$(C^{\beta L} - C^{\beta s})\frac{d\delta}{dt} = -D_S\left(\frac{\partial C^s}{\partial r}\right)_{r = R_c - \delta} \qquad \text{(B5)}$$

where D_s is the solute diffusivity in the solid. The above equations can be represented by the following dimensionless variables:

$$\varepsilon = \frac{\delta}{R} \tag{B6}$$

$$X = \frac{R - r}{R} \tag{B7}$$

$$\tau = \frac{D_s t}{R^2}, \qquad R = R_c + R_o \tag{B8}$$

$$\psi(X, \tau) = \frac{C^s - C^{\beta o}}{C^{\beta s} - C^{\beta o}} \tag{B9}$$

Then the initial condition changes to

$$\varepsilon(t = 0) = 0 \tag{B10}$$

The corresponding boundary conditions now become

$$\frac{\partial \psi}{\partial X} = 0, \; X = 0, \; (t > 0) \tag{B11}$$

$$\psi = 1, \; X = \alpha + \varepsilon, \; (t > 0), \tag{B12}$$

where $\alpha = R_o/R$. Interfacial mass balance now becomes:

$$\beta \frac{d\varepsilon}{d\tau} = \left(\frac{\partial \psi}{\partial X}\right)_{X = \alpha + \varepsilon} \tag{B13}$$

where β equals to $(C^{\beta L} - C^{\beta s}) / (C^{\beta s} - C^{\beta o})$ and the diffusion equation can be expressed as:

$$\frac{\partial}{\partial X}\left\{(1 - X)^{\lambda} \frac{\partial \psi}{\partial X}\right\} = (1 - X)^{\lambda} \frac{\partial \psi}{\partial \tau} \tag{B14}$$

where $\lambda = 0$ is for planar diffusion, $\lambda = 1$ and 2 are for cylindrical and spherical diffusion, respectively. Thus for the circular cylinder, the diffusion equation is:

$$\frac{\partial}{\partial X}\left\{(1-X)\frac{\partial \psi}{\partial X}\right\} = (1-X)\frac{\partial \psi}{\partial \tau} \tag{B15}$$

Integrating equation (B15) from $X = \alpha$ to $X = \alpha+\varepsilon$, which is the solidified region, and using equation (B13) gives:

$$\beta\left[1-(\alpha+\varepsilon)\right]\frac{d\varepsilon}{d\tau} - (1-\alpha)\left(\frac{\partial \psi}{\partial X}\right)_{X=\alpha} = \int_{\alpha}^{\alpha+\varepsilon}(1-X)\frac{\partial \psi}{\partial \tau}\,dX \tag{B16}$$

Solution of equation (B16) is approximated by the concentration profile:

$$\psi = \frac{X^2}{(\varepsilon+\alpha)^2} \tag{B17}$$

which satisfies equations (B11) and (B12). Substituting equation (B17) into equation (B16), and using $\varepsilon(\tau = 0) = 0$, one obtains:

$$\tau = \frac{1}{2\alpha(1-\alpha)}\{\frac{3\beta+2}{9}[(\alpha+\varepsilon)^3-\alpha^3] + \frac{2\beta+1}{8}[\alpha^4-(\alpha+\varepsilon)^4] + \frac{3\alpha^4-4\alpha^3}{6}\ln\left(\frac{\alpha+\varepsilon}{\alpha}\right)\} \tag{B18}$$

Complete solidification is attained when $\alpha+\varepsilon = 1$. Then the solidification time can be expressed as:

$$t_s = \frac{R^2}{2D_s\,\alpha(1-\alpha)}\left[\frac{3\beta+2}{9}(1-\alpha^3) + \frac{2\beta+1}{8}(\alpha^4-1) + \frac{3\alpha^4-4\alpha^3}{6}\ln\left(\frac{1}{\alpha}\right)\right] \tag{B19}$$

For a given materials system and the geometry of the capillaries, the latter part of the equation (B19) is a constant. Thus the isothermal solidification time can be represented as:

$$t_s = \frac{K\ R^2}{2\ D_s} \tag{B20}$$

where K is the constant.

LARGE GAP JOINING OF Ti-6Al-4V WITH MIXED POWDER INTERLAYERS

3.1 Abstract

Titanium based brazing alloys containing Cr, Fe, Cu, and Ni as β-stabilizers have been studied for joining titanium alloy, Ti-6Al-4V. Two of these alloys were selected for use in producing large gap joints. Ti-12Zr-14Cr-12Cu-12Ni (Type I) brazing alloy can be used to braze Ti-6Al-4V below its β-transus temperature. Joints of thickness up to 150 microns can be made in a normal brazing cycle without prolonged holding. The interlayer consists of a β-titanium alloy with no precipitation of intermetallic compounds. The second brazing alloy, Ti-12Zr-14Cr-6Fe-5Cu-5Ni (Type II), has to be brazed above the β-transus temperature of Ti-6Al-4V. Its powders were mixed with pure titanium and Ti-6Al-4V powders, and the mixture was used as the joining interlayer. Five millimeter thick interlayers were used to produce joints for microstructural examination and mechanical testing. It was found that residual pores in the interlayers were related to the amount of the brazing alloy in the interlayer. A fully densified interlayer can be obtained with 60 wt% brazing alloy in the interlayer. The as bonded joints revealed tensile strength equal to 50% that of the base metal. Diffusional treatment of the joints improves the joint efficiency to about 70%.

3.2 Introduction

Titanium and its alloys have been used in applications that take advantage of its specific properties, such as high strength-to-weight ratio, high temperature strength, and corrosion resistance. Aerospace applications include airframe and engine components. Due to its excellent corrosion resistance, titanium also find applications in

chemical/petrochemical processing, marine exposure, and medical uses. There are also emerging applications in the automotive, medical, and consumer products industries.

Titanium alloys are available in commercially pure and in alloy compositions. They are generally categorized into four groups, depending on the principal phases present in the microstructure:

1. Commercial pure (CPTi) alloys (hexagonal close packed, or hcp)
2. Alpha alloys (hcp)
3. Alpha-beta alloys
4. Beta alloys (body centered cubic, or bcc)

Pure titanium transforms from alpha to beta as the temperature exceeds 880°C (beta-transus). By alloying, the transformation temperature can be raised, which stabilizes the alpha phase, or depressed to room temperature, which results in all beta phase. Alloying produces a variety of microstructures, which has a marked effect on mechanical properties as well as the response to joining processes.

Many titanium joining methods, including welding, brazing, diffusion boding, and adhesive bonding have been developed over the last four decades. Among them brazing has been studied extensively and an historical overview of the process development is summarized below.

3.2.1 *Silver-Base Brazing Alloys*

Initial research on brazing titanium using silver-base brazing alloys was performed in the 1950s. One of the first studies was carried out by DeCeoo and Parks in 1953 [1]. Silver, aluminum and copper brazing alloys were studied. Silver was found to braze titanium well and the joints had good ductility due to the ductile nature of the TiAg intermetallic compound. Tiner [2] studied microstructures of the silver brazed titanium joints. Pure silver, and Ag-Cu eutectic, Ag-Cu-Sn, Ag-Cu-Zn-Cd, Ag-Mn commercial brazing alloys were used. High temperatures (1100°C) and long holding times (10-15 min.) were found to produce joints with the highest shear strength (150 MPa) in the case of pure silver filler. Tiner attribute this to the formation of a solid solution of silver in titanium. Work on silver based brazing alloys were continued by Key et al. [3], Kaarlela et al. [4], Suezawa [5], Heberard et al. [6] and Takehiko et al. [7]. Key used a Ag-5Al-0.5Mn brazing alloy, and reported "satisfactory" brazing in his paper. However, little testing were done on the joints. Kaarlela gave a comprehensive review on the historical background, alloy melting and rolling, physical metallurgy, and engineering testing results based on the Ag-Al-Mn brazing alloy system. The alloy was developed under Air Force

sponsorship for titanium honeycomb sandwich brazing. Among the alloys tested, Ag-5Al-0.5Mn was found to give good resistance to corrosion and high temperature (425°C) oxidation. Kaarlela also summarized mechanical properties of brazed titanium panels, including shear strength, bending fatigue strength, and stress corrosion resistance. Supplemental work was done by Suezawa on a Ag-4Al-0.5Mn alloy. He conducted tests by means of metallographic and Scanning Electron Microscopy/Energy Dispersive X-ray (SEM/EDX) analysis. High temperature strength and impact strength of the joints were also evaluated. Heberard developed a new brazing alloy, 50Ag-25Cu-25In, which could be brazed at 680°C. He concluded that although the alloy was suitable for use at room temperature and clean atmospheres, it should not be used when exposed to a salt environment. Brazing of titanium in the air with Ag-30Zn filler metal, aided by a AgCl-10LiF flux was studied by Takehiko. Small Cu additions to the filler metal were found to increase the strength of the joint; whereas Ni additions had the reverse effect.

One of the benefits of using silver based brazing alloys is that they can be readily brazed below the β-transus temperature, thus the brazing heating cycle will have little affect on the mechanical properties of the titanium base material. However, there are several drawbacks of these silver brazing alloys, one being their susceptibility to chlorine ion induced corrosion, and the other being their low strength at high temperature. These are difficult to overcome, resulting in limited by industry.

3.2.2 *Aluminum-Base Brazing Alloys*

Compared to silver-base brazing alloys, aluminum based brazing alloys add much less weight to the brazed structure due to their lower density. Hence they were exploited for brazing aircraft components. Wells [8] reported the results of the program supported by the Air Force Materials Laboratory (AFML). Large area titanium alloy laminates were brazed with a series of aluminum alloys. Laminates made with the brazing filler metal 22 (a Al-7.5Si alloy clad to a core of aluminum alloy 6951), exhibited the highest shear strength, S-N fatigue strength, and strain-to-failure tension. They also exhibited good damage tolerance behavior.

Considerable work on brazing titanium has been carried out at the Boeing Company using aluminum brazes. The program was aimed at fabricating acoustically treated tailpipes and cowl assemblies for jet engine noise reduction. The design typically consisted of a perforated inner skin, honeycomb core and a solid outer skin. A review of Boeing's effort was presented by Kimball [9] in 1980. The brazing was performed in a vacuum furnace using 3003 aluminum as the filler. The assembly was heated to the braze melting point,

660°C, and held at this temperature until thermal uniformity had been reached. The temperature was then raised 20°C as rapidly as possible and held for three minutes. The short brazing time was necessary in order to minimize the formation of the brittle intermetallic, TiAl. Long term service evaluation of aluminum brazed (AB Ti) jet engine acoustic tailpipes was reported by Elrod [10]. He noted that corrosion of the braze fillets occurred in tailpipes that had had been operated in a moist environment. Elrod concluded that AB Ti was not acceptable for jet engine acoustic tailpipes unless the engine was operated in a dry environment.

3.2.3 *Other Brazing Alloys*

One of the most popular brazing alloys for titanium is Ti-15Cu-15Ni, which has a melting range between 900 and 960°C. The alloy was described at the First international AWS-WRC Brazing Conference in 1970 by Howden and Monroe [11]. They concluded that Ti-15Cu-15Ni could produce strong joints with excellent corrosion resistance. The authors also studied a beryllium containing brazing alloy Ti-48Zr-2Be. It was found to have good flow characteristics and to produce minimal base-metal erosion. A silver-palladium-gallium filler metal (Ag-9Pd-9Ga), which flows at 900 to 915°C, is another excellent brazing filler metal which can fill large gaps[12]. On many occasions, copper and nickel laminated foils have been used for the brazing of titanium structures, because of the difficulty in making Ti-15Cu-15Ni into thin foils[13].

While the conventional brazing filler metals are being studied and developed, a somewhat different joining process is also being extensively investigated, especially in the aerospace industries. The process is now usually called transient liquid phase (TLP) bonding. But at the time, a handful of names like activated diffusion bonding (ADB), liquid interface diffusion (LID) bonding, were given by different authors or companies. All the methods are based on the same mechanism. An interlayer, or the melting point depressant (MPD) reacts with the base metal to form an eutectic liquid at the joining temperature. The liquid fills asperities in the joint. Isothermal holding results in diffusion of the MPD into the base metal, which causes solidification to occur. Subsequent annealing leads to a ductile, precipitate-free joint which has somewhat similar chemical and mechanical properties as the base metal along with a much higher remelt temperature. TLP bonding differs from conventional brazing in that only a small amount of MPD is used, and the process depends on isothermal solidification. With conventional brazing, the braze alloy is still fixed at, or close to, the eutectic composition after cool down.

The very first paper on TLP bonding of titanium was published in 1959 by Lynch et al.[14], who successfully bonded titanium using a thin shim of nickel at 955°C (1751°F). About a decade later after this paper, Northrop Corporation started to publish TLP bonding of titanium using copper interlayers[15-17]. The most successful method of TLP bonding of titanium was developed and commercialized at Rohr Industries in the early seventies. This method is described in the open literature by Woodward[18], Schwartz[19, 20], and Norris[21-23]. A thin copper-nickel interlayer was used to make RohrBond™ components. RohrBond™ components are sandwich structures that comprise of Ti-6Al-4V face sheets TLP bonded to a titanium honeycomb core. These structures allow the honeycomb to have minimum weight, but excellent high temperature strength and corrosion resistance.

The most recent brazing alloy development for titanium joining is reported by Onzawa, et al.[24]. Titanium based Ti-Zr-Cu-Ni quaternary amorphous thin foils with a thickness from 20 to 60 microns were produced by a rapid solidification technique. The alloys have a melting range from 800 to 900°C, which is at least 100 °C lower than the most widely used Ti-Cu-Ni alloy. Onzawa conducted tensile tests, fatigue tests, and corrosion tests on the brazed joints of commercially pure titanium (CPTi) and Ti-6Al-4V. It was found that base metal tensile strength could be obtained when the brazing temperature was above 900 °C, but below the β-transus temperature. Tensile strength decreased sharply to less than 50% of the base metal when brazing was performed below the α-β transformation temperature. TLP bonds were obtained by longer holding time at the brazing temperature. Joints brazed at 900 °C for 10 minutes showed a fatigue strength of about 600 MPa, which is more than 80% of the base metal Ti-6Al-4V. All the brazed joints exhibited excellent corrosion resistance.

In another paper, the same authors studied microstructures of the TLP bonded CPTi and Ti-6Al-4V joints using Ti-20Zr-20Cu-20Ni amorphous foils[25]. According to the observation and analysis with STEM/EDX, lamellar structures of α-Ti and Ti_2Cu eutectoid were found in the joint. Onzawa employed a thin film diffusion approach to calculate the diffusion of Zr, Ni and Cu in titanium. The results are generally in agreement with his experiment data. Applications of Ti-Zr-Cu-Ni amorphous brazing foils were further investigated by Onzawa et al.[26], Lugscheider and Broich[27] on joining different titanium alloys. Since the brazing alloy is brittle at room temperature, it can not be prepared

through the conventional casting and rolling route. Flexible ribbons can be produced by rapid solidification. However, such ribbons for brazing are expensive. Moreover, since the ribbon is very thin and narrow (3 to 5 mm), the applications may be limited.

Palladium containing brazing alloys were studied by Izui and Suezwa[28, 29] for high temperature use. Three types of Pd-Cu system braze alloys, 30Pd-40Au-30Cu, 30Pd-60Cu-10Co, and 30Pd-60Cu-10Ni were developed. Brazing has to be performed above the β-transus temperature of Ti-6Al-4V for these brazes. Nearly 80% joint efficiency was obtained when the joint gap was 0.1 mm and 30Pd-60Cu-10Ni was used. Joints brazed with 30Pd-60Cu-10Co retained their highest strength at up to 800 °C.

Titanium joining is difficult mainly because of its distinctive metallurgical properties. Many factors have to be considered when designing a brazing alloy for titanium. So far, the TLP bonding process shows great success on joining titanium and its alloys. However, this process is only applicable to joints with very small clearances. Due to easy formation of brittle intermetallic compounds of titanium with most of the transition metals, large joint gaps with the braze alloy often lead to catastrophic failure of the joint. Relaxation of the restriction on joint gap for titanium brazing will facilitate the fabrication of titanium components. On the other hand, since titanium structures and parts are more and more widely used, repair of the worn or damaged items is becoming increasingly important due to its relative high material and process expense. An attempt has been made by MacDonald et al.[30] to address these needs. A mixed powder interlayer, consisting of Ti and Ti-15Cu-15Ni powders, was used for large gap joining of Ti-6Al-4V. Principally, this method can be explained according to the theory of transient liquid phase sintering. Ti-15Cu-15Ni powders melt at the joining temperature, flow around the Ti powders in the interlayer, and cause rearrangement of the Ti particles. Such rearrangement densifies the powder interlayer. Meanwhile, interdiffusion between the Ti-Cu-Ni liquid and the Ti powders raises the liquidus temperature and results in isothermal solidification of the interlayer. In the end, a TLP bond is produced, without significant limitations on the joint gap. For the process to work, however, there are several problems that have to be considered. First is the reaction rate of Ti with the alloying elements Cu and Ni. Ideally, such a reaction should be inhibited until the end of the fluid flow. Unfortunately, Ti reacts rapidly with both Cu and Ni, forming intermetallic compounds even during heat up. This leads to the second problem, namely the residual pores in the interlayer. Intermetallic formation increases the resistance to fluid flow, and therefore reduces shrinkage of the powder interlayer. To control residual pores in the joint, the third problem, namely the amount of liquid former (Ti-15Cu-15Ni) in the powder interlayer has to be carefully

chosen. There is a trade-off between the amount of liquid and the mechanical properties of the joint. More liquid reduces the residual pores and is good for the mechanical properties, but more liquid means more intermetallic compounds will form which can cause brittleness of the joint. Thus less liquid can result in more ductile joints, but residual pores increase which also impairs the mechanical properties. Experiments showed that Ti-15Cu-15Ni is not suitable for the purpose of large gap joining with mixed powder interlayers. The present work attempts to design the possible compositions of powder interlayers for titanium joining.

3.2.4 *Titanium Alloy Design*

The basic tools now available for titanium alloy design are physical and mechanical properties of binary titanium alloys, although it is generally agreed that these properties are dominated by their electronic states. Several commercially successful titanium alloys, including a forging alloy, Ti-10V-2Fe-3Al, a high strength ductile sheet alloy, Ti-15V-3Cr-3Sn-3Al, and Ti-2Ni, a high strength corrosion resistant alloy , were designed using these basic tools[31]. Binary titanium alloys can generally be assigned to one of the two major categories —α-stabilized or β-stabilized systems. Molchanova[32] recommended subdividing the former into two more groups according to the degree of α stabilization: (1) those of limited α stability, in which decomposition of α takes place by peritectoid reaction into β plus a compound (e.g., Ti-Al); and (2): those of complete α stability, in which the α phase can co-exist with the liquid (e.g., Ti-O and Ti-N). Molchanova also recommended subdividing β-stabilized alloys into two categories: (1) β-isomorphous systems, such as Ti-Mo and Ti-Zr, which show extensive β-solubility ranges; (2) β-eutectoid systems, in which the β phase has a limited solubility range and is able to decompose into α and a compound (e.g., Ti-Cr and Ti-Cu). This class can be further subdivided into two more subgroups depending on whether the β decomposition is rapid (e.g., Ti-Cu and Ti-Ni) or sluggish (e.g., Ti-Cr, Ti-Mn and Ti-Fe). The groups of binary alloys are depicted in Figure 3.1.

Commercial multicomponent alloys are generally composed of mixtures of α and β stabilizers, depending on the ratio of the relative abundance of the α- and β-stabilizing

components. This ratio can be most conveniently expressed in terms of α-stabilizing and β-stabilizing "equivalencies".

3.2.5 *Equivalent Aluminum Content*

Aluminum and oxygen elevate the (α+β)/α transus when alloyed into titanium. These are regarded as strong stabilizers of the α-phase. Tin is also an α-stabilizer, although not a strong one. Since zirconium has the effect of slightly lowering the temperature of the (α+β)/α transus, it may be regarded as a neutral addition. On the other hand, zirconium has similar chemical properties to titanium, and may substitute for titanium in a multicomponent alloy and thereby add weight to its α-stabilizing component. For this reason it may be regarded as an α-stabilizer.

According to Rosegery[33], the equivalent aluminum content of an alloy containing aluminum, zirconium, tin and oxygen is:

$$[Al]_{eq} = [Al] + [Zr]/6 + [Sn]/3 + 10[O] \qquad (1)$$

where [x] indicates the weight percent of element x.

3.2.6 *Equivalent Molybdenum Content*

The β-stabilizing strength of transition-element additions into titanium is indicated by the rates at which they lower the martensite transus and hence the degree to which they permit the retention of the β phase at room temperature. Thus Mo-equivalence of an alloy is used for intercomparison of the transition elements:

$$[Mo]_{eq} = [Mo] + [Ta]/5 + [Nb]/3.6 + [W]/2.5 + [V]/1.5 + 1.25[Cr] + 1.25[Ni] + 1.7[Mn] + 1.7[Co] + 2.5[Fe] \qquad (2)$$

Transformation of a number of multicomponent titanium-base alloys into their Al- and Mo-equivalent formats provides a useful guide for alloy classification described above as well as new alloy design.

The basic tools for titanium alloy design can be equally useful for designing titanium based brazing alloys. The principal driving force for titanium brazing alloy

development is the capability of producing high strength, ductile joints. Secondary considerations include melting temperature, corrosion resistance, and cost of the braze. Table 3.1 outlines how these factors might be translated into alloy characteristics which then formulate brazing alloy evaluation criteria. A critical scan of this table will reveal that almost no commercial braze can meet all the important features for which the alloy development is aimed. Silver-based alloys show unacceptable corrosion resistance. The popular Ti-15Cu-15Ni braze has excessive amounts of rapid β-eutectoid formers (Cu and Ni), which results in brazed joints of low ductility. Even Ti-37.5Zr-15Cu-10Ni or Ti-20Zr-20Cu-20Ni amorphous brazing foils are difficult for brazing titanium parts with clearances greater than 50 microns, because of their large contents of Cu, Ni as well as Zr. Mechanically sound joints must rely on TLP bonding process. Thus it is clear that a new approach is imperative for large gap titanium brazing. A review of the compositions of the four categories of titanium alloys shows that only β-titanium alloys can be heavily alloyed while still maintaining their high strength and ductility. The β-stabilizers are the transition metals frequently added into titanium alloys. At this point, it is realized that theoretically the microstructure of a brazing alloy can be manipulated in such a manner as to closely resemble that of a β-titanium alloy. Meanwhile, the melting range of such an alloy has to be low enough to allow conventional brazing practice. It turns out that a powder mixture of a β-titanium brazing alloy and CPTi is a possible solution to fulfill such requirements. The microstructure of Beta C (Ti-3Al-8V-6Cr-4Mo-4Zr) is targeted as the final microstructure of the mixed powder interlayer[34]. When selecting alloying elements, Zr is selected as the principal α-stabilizer due to its capability of depressing the melting point of Ti. β-isomorphous elements show little help in depressing the melting temperature of the braze. Trial studies on V and Nb additions indicate they are not good candidates for this alloy. This leaves β-eutectoid elements as the only additions to the brazing alloy. Among them, Cu and Ni are most effective on lowering the melting temperature. However, they should be added as little as possible because of the fast eutectoid reaction rates. Palladium additions are finally abandoned due to high cost. Sluggish eutectoid formers, Cr and Fe are then selected as the principal β-stabilizing additions. Thus is born an alloy development plan consisting of a composition matrix involving Ti, Cr, Fe, Cu, Ni plus a certain amount of Zr.

3.3 Experimental Procedures

3.3.1 *Materials*

The base metal used in this investigation is Ti-6Al-4V alloy. The extruded half inch diameter (12.5mm) solid bar has small, equiaxed grains. Table 3.2 gives chemical compositions and mechanical properties of the as received bar. 99.4% pure CPTi powders were purchased as -325 mesh. They are irregular in shape, as illustrated in Figure 3.2(a). Ti-6Al-4V alloy powders were supplied by Nuclear Metals, Inc. The powders were produced by the rotating electrode process. They are spherical and Figure 3.2(b) shows the typical shape. The as received powders were sieved and those with sizes from 44 to 74 microns (-200+325 mesh) were used in this study. Alloying elements at least 99.9% pure were bought in the form of granules, which were combined with 99.9% pure Ti sponge for the preparation of β-titanium brazes.

3.3.2 *Preparation of the β-titanium Brazes*

Seven kinds of β-titanium brazes, with combinations of Zr, Cr, Fe, Pd, Cu, and Ni alloying elements, were prepared. The alloys were produced by arc melting of a button (5g) in a water-cooled copper crucible. The chamber was first flushed with high purity argon for one minute before arc striking. Each charge was melted six times, turning it over after each melt. The alloy beads then were crushed in a closed die into small grains, followed by one hour ball milling using Yttrium stabilized ZrO_2 as the milling balls. The resulting alloy powders were sieved and those with sizes less than 44 microns (-325 mesh) were collected for brazing use. Table 3.3 shows the compositions of the β-titanium brazing alloys and their nominal melting temperatures. Two types of brazing alloys, Ti-12Zr-14Cr-12Cu-12Ni (Type I) and Ti-12Zr-14Cr-6Fe-5Cu-5Ni (Type II) were selected in the joining experiments.

3.3.3 *Joining Procedures*

The prepared alloy powders were mixed with CPTi powders for one hour. The volume fraction of the alloy powders was varied from 30% to 60%. From the theory of liquid phase sintering, a fully dense compact is only obtainable with liquid volume fraction above 30% in the case that the liquid is insoluable in the solid and there is no reaction (forming intermetallic compound) between the liquid and the solid particles. For the

powder mixture in this study, however, extensive diffusion or reaction between the liquid and titanium powders at the bonding temperature has to be compensated by increasing the amount of liquid. The optimal liquid quantity has to be determined by experiments. In some cases, Ti-6Al-4V spherical powders were added to replace some of the CPTi powders (50 vol% of total CPTi), since spherical powders are easy to densify and requires less liquid. After mixing, the powder mixture was pressed into 9.5mm diameter, 3 mm to 6 mm thick compacts.

Butt joints were made in a fused quartz tube vacuum furnace. Small samples were prepared for microstructural examination. Tensile test specimens were made in the same furnace with a tantalum holder. A minor pressure of about 0.5 MPa was applied during joining. The joining temperature was 950 °C for the Type I interlayers, and 1140 °C for the Type II interlayers, respectively. The heating rate above 900 °C was close to 15 °C/min. Samples with 950 °C joining temperature were air cooled after one hour holding. At 1140 °C, samples were held for 15 minutes, then furnace cooled to 920 °C, diffusion treated for 8 hours at this temperature, and then air cooled. Ti-6Al-4V bars were treated by the same procedure for comparison of the mechanical properties. During each joining cycle, the vacuum level was always maintained better than 2.5×10^{-5} torr.

3.4 Results and Discussion

3.4.1 *Microstructures*

Figure 3.3 shows the microstructure of a joint brazed at 950°C for one hour using the Type I brazing alloy. The joint gap was 250 microns. Precipitation of white intermetallic phases can be seen in the central region of the joint. Results of microhardness testing across the joint is depicted in Figure 3.4, which shows the much higher hardness (580 Hv) of these white phases. EDX results indicates that such white phases are complex intermetallic compounds, containing all the elements in the Type I brazing alloy. The composition is close to $Ti_{15}Zr_{1.5}Cr_{1.0}Cu_{2.0}Ni_{5.5}$, which is illustrated in Figure 3.5 and Table 3.4. The composition of the surrounding phase is also given in Table 3.4. Calculations on Al- and Mo-equivalencies based on Equations (1) and (2) indicate that the surrounding phase is a β-titanium alloy. Reducing the joint clearance to 150 microns, and keeping the

rest of the parameters unchanged, resulted in a joint free of precipitation of the intermetallic compounds. This is shown in Figure 3.6. It can be seen that the microstructure changes from equiaxial $\alpha+\beta$ phases in the base metal to acicular $\alpha+\beta$ phases adjacent to the interface of the base metal and brazing alloy, and finally to β phases in the middle of the joint. The microhardness across the joint is also shown in Figure 3.4. It is evident that the hardness of the β-titanium phase is somewhat higher than that of the base metal.

From observations of the microstructures of the joints, it is clear that the joint clearance should not exceed 150 microns when applying Type I brazing alloy and a normal brazing cycle without long time isothermal holding. Otherwise, precipitation of intermetallic compounds may markedly impair the mechanical properties of the joint. Compared to the amorphous TiZrCuNi brazing alloys, Type I brazing alloy allows a three fold increase in the joint clearance. Further increase in the joint gap only can be accomplished by finding a way to control the concentration of the alloying elements in the joint and thus eliminate the unwanted intermetallic compounds. An interlayer consisting of a mixture of Type I and CPTi/Ti-6Al-4V powders was tested for such a purpose. Figures 3.7(a) and (b) show the microstructure of the joint bonded at 950°C for 8 hours. The joint gap was 5 mm, with 50 wt% Type I added. Despite the lengthy holding time and overall low concentrations of the alloying elements in the joint, precipitation of the intermetallic compounds was still observed (white phases in Figure 3.7(b)). Meanwhile, a considerable volume fraction of residual pores also remained in the joint after bonding. Diffusion of Cu in the titanium matrix is fast at the brazing temperature (950°C). Even if Ti-Cu intermetallic compounds (Ti_2Cu and TiCu) form in the interlayer, they can be diffused away during isothermal holding since the brazing temperature is very close to the melting point of these compounds. On the other hand, Ti-Ni intermetallic compounds (TiNi and $TiNi_3$) melt above 1300°C. These compounds are much more difficult to homogenize due to sluggish diffusion. This explains the reason for Ni enrichment in the multicomponent intermetallic compound (Table 3.4). Elements like Cu and Ni readily react with titanium to form intermetallic compounds at the brazing temperature (950°C). Such fast reactions consume liquid quickly, and may not leave enough liquid for rearranging the solid titanium particles. At the same time, the reaction products may block the flow of liquid and slow down densification of the interlayer. All these factors may contribute to residual pores in the interlayer.

The above analysis suggests that to fulfill the requirements of large gap titanium joining, not only the concentration of intermetallic-forming elements (Ni and Cu) need to be reduced, but the bonding temperature also has to be raised to suppress the formation of intermetallic compounds and to better homogenize the joint. This suggests the development of Type II brazing alloy with much less Cu and Ni. Figure 3.8 shows the microstructure of a 5 mm thick joint bonded at 1140°C for 15 minutes. The interlayer contained 45 wt% Type II brazing alloy. As compared with the microstructures in Figures 3.7(a) and (b), considerably less intermetallic compound forms, and fewer, smaller pores exist. Increasing the amount of Type II brazing alloy and diffusion treating of the joint further reduce residual pores in the interlayer, as illustrated in Figures 3.9(a) and (b). The microstructure is similar to Beta C titanium alloy, with fine α-phase precipitates in the β-phase grains. In contrast, large acicular α phases precipitate in the base metal (Figure 3.9(a)) due to brazing above the β-transus temperature. Good bonding between the base metal and the interlayer can be seen in Figure 3.6(a). In fact, no fracture was found at the interface during mechanical testing of the joints. As the amount of Type II brazing alloy was increased to 60 wt%, the whole interlayer fully densified after diffusion treatment. However, a considerable amount of second phase precipitation was found in the joint. Figure 3.10 shows the optical microstructure, and Figure 3.11 is the back scattering image of these precipitates in the SEM. The EDX on these second phases indicated that they consisted of titanium and about 4.5 wt% zirconium. Such precipitates are also found in Beta C titanium alloys[35]. It was experimentally determined that these precipitates are beneficial to this material by improving the ductility and retarding grain growth at high temperatures, due to their stability.[35]

3.4.2 *Mechanical Properties*

Tensile test samples were made using 5 mm thick powder interlayers which contained Type II brazing alloy. Figure 3.12 gives a typical view of a tensile test sample prior to machining. This sample contains 60 wt% Type II brazing alloy, and significant bulging of the interlayer is observed due to the large amount of liquid present at the bonding temperature. When the amount of Type II addition was decreased, the extent of bulging was also reduced. Figure 3.13 shows the size of the sample subject to tensile testing.

The test results are depicted in Figures 3.14 and 3.15. The strength of the base metal decreased slightly after high temperature soaking. Since the $\alpha + \beta \rightarrow \beta$ phase

transformation occurs at about 1005°C for the Ti-6Al-4V alloy, brazing at 1140°C resulted in coarsening of the β phase and subsequent large α phase precipitation after cooling below the β-transus temperature. The as brazed joints exhibited lower tensile strength as compared to that of the base metal. All of the as-brazed samples broke in the interlayers. The samples with least amount of Type II addition showed the highest tensile strength, although the volume fraction of porosity in their interlayers were also the highest.

As has been observed from the microstructures, when the amount of Type II in the interlayer exceeds 50 wt%, few residual pores remain in the joint. Nonetheless, this does not lead to a high strength joint. In fact, the joint strength is affected more by the total amount of alloying elements in the joint. Because of the thick interlayers used, it is almost impossible to rely on solid state diffusion of these alloying elements into the base metal to enhance joint strength as in the case of the thin film TLP bonding process. Thus, the amount of alloying elements remaining in the joint depends solely on the ratio of Type II brazing alloy and CPTi/Ti-6Al-4V in the interlayer. Less Type II addition would be beneficial to the strength of the joint, but this also means liquid in the interlayer, a more difficult joint to make, and more residual pores. Homogenizing was performed on some tensile testing samples to facilitate a more even distribution of the alloying elements in the interlayer. Despite no obvious microstructural change after treating, the tensile strength was improved markedly, as illustrated in Figure 3.16. The strength of the as received Ti-6Al-4V is also given in the figure. The maximum tensile strength reaches the lower level of the annealed β-titanium alloys (700 MPa).

Although the elongation of these samples reached the level of hardened β-titanium alloys, it is still fairly low as compared to the level achievable for an annealed β-titanium alloy. Such low elongation indicates that the interlayers are fairly brittle even though the amount of β-stabilizers was carefully controlled. β-isomorphous elements such as Mo and V are the primary β-stabilizers used in commercial β-titanium alloys. However, these elements are extremely difficult to add into the Type II braze because they tend to raise the melting point of the braze. Instead, β-eutectoid elements such as Cr and Fe are the major β-stabilizers in the Type II braze. These elements may cause intrinsic brittleness of the resultant β-titanium alloy. On the other hand, it is well recognized that β-titanium alloys are susceptible to inclusions of interstitial elements such as oxygen and nitrogen[35].

These interstitial elements can embrittle β-titanium alloys. Unfortunately, the powder interlayers may contain a high level of oxygen and/or nitrogen after bonding, and this can lead to premature failure of the joints. Oxygen and/or nitrogen pick up may come from different stages of joining. Firstly, the oxygen level in CPTi and Ti-6Al-4V powders varies from 1000 ppm to 2000 ppm, depending on the various production routes. Nitrogen content in these powders is usually low. Secondly, oxygen and/or nitrogen may be introduced during preparation of the brazing alloys by arc melting and subsequent ball milling. Finally, long time soaking at high temperatures of the interlayers may further increase the content of these interstitial elements.

3.4.3 *Fractography*

Figures 3.17(a) and (b) show the fracture surfaces of the high temperature soaked Ti-6Al-4V base metal under SEM. Dimples and shear lips indicate ductile failure of the material. In Figures 3.18(a) and (b), the fracture appearance of the as bonded joint with 40 wt% Type II addition in the interlayer is depicted. The large spherical particles are Ti-6Al-4V powders. Higher magnification in Figure 3.18(b) shows a mixed failure of the material. The fracture of Ti-6Al-4V particles are mostly brittle as can be seen from their cleavage-like facets. However, the surrounding areas which were occupied by CPTi powders exhibit a certain amount of plastic deformation before failure. Since the residual pores are small and evenly distributed in the interlayer, it is likely that after bonding, there is no liquid remaining in the joint. However, the joint is not fully densified and homogenized.

As the amount of Type II brazing alloy increased in the interlayer, the fracture became more brittle in nature. This is illustrated in Figures 3.19(a) and (b) as well as in Figures 3.20(a) and (b). The white spots found in these photographs are (Ti, Zr) second phases. In powder metallurgy of titanium alloys, it is frequently observed that such cleavage fracture is associated with inclusions like tungsten[36, 37]. After careful searching and viewing the fracture surfaces with SEM, it is concluded that the fracture is related more to the intrinsic properties of the interlayer material in this case.

3.5 Summary and Conclusions

In this study, a series of titanium-based brazing alloys were investigated for large gap TLP bonding of Ti-6Al-4V. The alloys were formulated using basic design rules of titanium alloys and the requirements of a brazing alloy. Among them, Type I and Type II brazing alloys were used for further investigation of the microstructures as well as the mechanical properties of the joints. The following conclusions were drawn from this study:

1. The Type I brazing alloy, which has chromium in partial substitution for zirconium and decreased total amount of copper and nickel, can be used to join Ti-6Al-4V below its β-transus temperature. The brazing gap can be as large as 150 microns with the normal brazing cycle (no prolonged holding), and the joint is free of brittle intermetallic compounds.
2. The amount of alloying elements in Type II brazing alloys are reduced as compared with the Type I braze, so that brazing is performed above the β-transus temperature of Ti-6Al-4V. Interlayers with powder mixtures of Type II brazing alloy and CPTi/Ti-6Al-4V were successfully used in large gap TLP bonding of Ti-6Al-4V.
3. Microstructural examinations of the joints show β-titanium phases in the interlayer. The number and size of residual pores decreases with increasing Type II brazing alloy in the interlayer. A fully densified interlayer can be obtained with 60 wt% Type II in the mixture.
4. Tensile testing of the as bonded butt joints revealed about 50% strength of the base metal. The strength decreases as the amount of Type II increases. Diffusional treatment of the joints improves their strength to about 70% of the base metal.
5. The relatively low strength of the interlayer may be due to intrinsic behavior of the material, since only eutectoid-forming elements are added as β-stabilizers. However, interstitial elements such as oxygen and nitrogen, which can embrittle β-titanium can also contribute to loss of strength.

3.6 Acknowledgments

I would like to thank National Science Foundation (NSF) for supporting this research under contract number DMR-9301444. Thanks also to Shean Peterson and Liao Lin for their assistance with this work.

3.7 References

1. DeCecco, N. A. and Parks, J. N. 1953. The brazing of titanium. *Welding Journal*, 32 (11), pp. 1071-1081.

2. Tiner, N. A. 1955. Metallurgical aspects of silver brazing titanium. *Welding Journal*, 34 (9), pp. 846-850.

3. Key, R. E. et al. 1972. Titanium structural brazing. Proceedings of the Fifth AWS-WRC International Brazing Conference, May 7-9, Houston, Texas.

4. Kaarlela, W. T., and Margolis, W. S. 1974. Development of the Ag-Al-Mn brazing filler metal for titanium. *Welding Journal*, 53 (10), pp. 629-636.

5. Suezawa, R. 1980. An investigation of silver alloy brazing of titanium alloy. Proceedings of the Fourth International Conference on Titanium, Kyoto, Japan, May 19-22.

6. Heberard, X., et al. 1980. Low-temperature brazing (680°) to Ti-6Al-4V titanium alloy. *Titanium* 80 (4), pp. 2415-2422.

7. Takehiko Wantanabe, Yutaka Higo, Takayuki Miki, and Atushi Yanagisawa, 1994. Brazing of titanium with Ag-based filler metals in air, *Quarterly Journal of the Japan Welding Society*, vol. 12, no. 4, pp. 502-508.

8. Wells, R. R. 1975. Low-temperature large-area brazing of damage tollerant titanium structures. *Welding Journal*, 54 (10), pp. 348-s to 356-s.

9. Kimball, C. E., 1980. Acoustic structures, Proceedings of the 11th International AWS-WRC Brazing Conference, Los Angeles, April 15-17.

10. Elrod, S. D., Service evaluation of aluminum-brazed (AB Ti) jet engine tailpipe extensions, NASA Contractor Report 3617.

11. Howden, D. G. and Monroe, R. W. 1972. Suitable alloys for brazing titanium heat exchangers. *Welding Journal*, 51 (1), pp. 31-36.

12. Schwartz, M. M., 1963. Brazed honeycomb structures, *WRC Bulletin 92*, November, pp.

13. Lan, S. W. 1982. Laminated brazing metals for titanium assemblies. *Welding Journal*, 61 (10), pp. 23-28.

14. Lynch, J. F., et al., 1959. Brazing by the diffusion-controlled formation of a liquid intermediate phase, *Journal of the American Welding Society*, February, pp. 85-s to 89-s.

15. Wells, R. R., et al., 1968. Thin film diffusion brazing of titanium members utilizing copper intermediates, U.S. Patent No. 3,417,461.

16. Freedman, A. H. 1971. Basic properties of thin film diffusion brazed joints in Ti-6Al-4V. *Welding Journal*, 50 (8), pp. 343s to 356s.

17. . Wells, R. R. 1976. Microstructural control of thin film diddusion brazed titanium. *Welding Journal*, 55 (1), pp. 20s to 27s.

18. Woodward, J. R. 1973. Titanium honeycomb sandwich fabrication process. Proceedings of the Fifth Int. Tech. Meeting, Kiamesha Lake, NY.

19. Schwartz, M. M. 1978. Diffusion brazing titanium sandwich structures. *Welding Journal*, 57 (9), pp. 35-38.

20. Schwartz, M. M. 1973. Rohrbond. Proceedings of the Fifth Int. Tech. Meeting, Kiamesha Lake, NY.

21. Norris, B. 1986. Liquid interface diffusion (LID) bonding of titanium structures. Proceedings of the Designing with Titanium Conference, Bristol University, July, U.K. pp. 83-86.

22. Norris, B. and Gojny, F. 1987. Joining processes used in the fabrication of titanium and Inconel honeycomb sandwich structures. 1st. International SAMPE Metals and Metals Processing Conference, Cherry Hill, NJ. pp. 183-190.

23. Norris, B. 1988. The development of titanium brazing technologies. *Titanium* 88 (3): pp. 120-125.

24 Onzawa, T., Suzumura, A., and Ko, M. 1987. Structure and mechanical properties of CP Ti and Ti-6Al-4V alloy brazed joints with Ti-base amorphous filler metals, *Quarterly Journal of the Japan Welding Society*, vol. 5, no. 2, pp. 205-211.

25. Onzawa, T., Suzumura, A., and Ko, M., 1989. Microstructure of titanium joint made with Ti-Zr brazing fillers, *Quarterly Journal of the Japan Welding Society*, vol. 7, no. 4, pp. 455-460.

26. Onzawa, T., Suzumura, A., and Ko, M., 1989. Diffusion brazing of Ti-21V-4Al β-type titanium alloy using Ti-base filler, *Quarterly Journal of the Japan Welding Society*, vol. 7, no. 4, pp. 460-467.

27. Lugscheider, E. and Broich, U. 1995. Mechanical properties of high-temperature brazed titanium materials, *Welding Journal*, 74 (5), pp. 169-s to 176-s.

28. Suezawa, Y. and Izui, H. 1987. *Journal of the Society of High Temperature ofJapan*, vol. 13, no. 6, pp. 265.

29. Suezawa, Y. and Izui, H, 1993. Ti-6Al-4V joints brazed with Pd-Cu alloys, *J. Soc. Mat. Sci., Japan*, vol. 42, no. 478, pp. 881-887.

30. MacDonald, W. D., Zhuang, W. D., Liu, X. Y. and Eagar, T. W. 1993. Kinetics of powder interlayer diffusion brazing. submitted to *Welding Journal.*

31. Hall, J. A. Progress with the new titanium alloys, The Metallurgy of Light Alloys, pp. 116-131.

32. Molchanova, E. K., 1965. Phase diagrams of titanium alloys [translation of Atlas diagram sostoyaniya titanovyk splavov], Israel Program for Scientific Translations, Jerusalem.

33. Rosenberg, H. W., 1970. Titanium alloying in theory and practice, The Science, Technology and Application of Titanium, Pergamon Press, pp. 851-859.

34. Materials properties handbook: Titanium Alloys, 1993, edited by R.Roger, E. W. Collings, and G. Welsch. ASM Publication.

35. Wood, R. A., 1972. Beta titanium alloys, MCIC Report, September.

36. Scarich, G. V., et al., 1980. Relationship between mechanical properties, contaminants, and fracture topography of HIP Ti-6Al-4V powder metallurgy products, Powder Metallurgy of Titanium Alloys, published by the Metallurgical Society of AIME, pp. 103-114.

37. Dawson, D. B., and litchny, M. G., 1980. Characterization of the tensile properties of hot isostatically pressed Ti-6Al-6V-2Sn, Powder Metallurgy of Titanium Alloys, published by the Metallurgical Society of AIME, pp. 115-125.

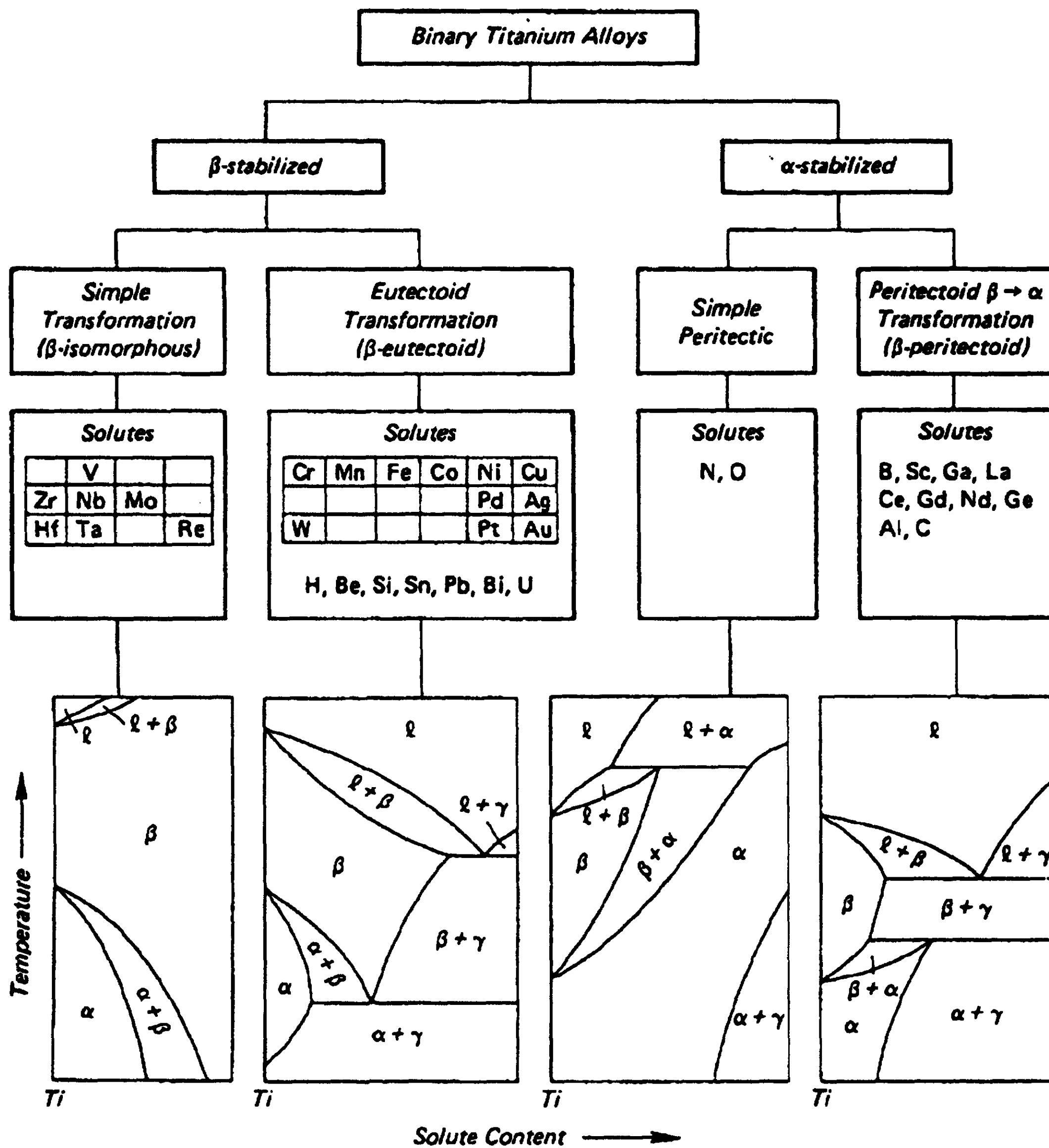

Figure 3.1. Categories of the binary titanium alloys.

Table 3.1. Analysis of Titanium Brazing Alloy Design Needs

Application Consideration	Brazing Alloy Characteristic
A. High Mechanical Properties	1. Maximum Ti 2. Minimum fast eutectoid formers such as Ni and Cu 3. Beta isomorphous alloying additions, Mo, V. Sluggish eutectoids Fe, Cr, Co Mn at minimum levels. 4. Low level of interstial elements, O and N. 5. No embrittling phases (Omega)
B. Ease of Brazing Practice	1. Adding α-stablizers Zr, Ag to depress the melting temperature of titanium 2. Adding β-stablizers Cu, Ni, Co, Pd, Cr, Fe Mn to lower the melting point of titanium. 3. Minimum use of Mo, Ta, Nb, Sn
C. Corrosion Resistance	1. Avoid Ag-based brazing alloys. 2. Avoid Al-based brazing alloys 3. Titanium base brazing alloy with additions of Au, Pd, Mo, Ni. 4. Low Al equivalent.
D. Minimum Cost	1. Minimum precious elements, Au, Pd, Ag. 2. Conventional alloy form (powders) rather than the ribbons from rapid solidification. 3. Minimum process cost.

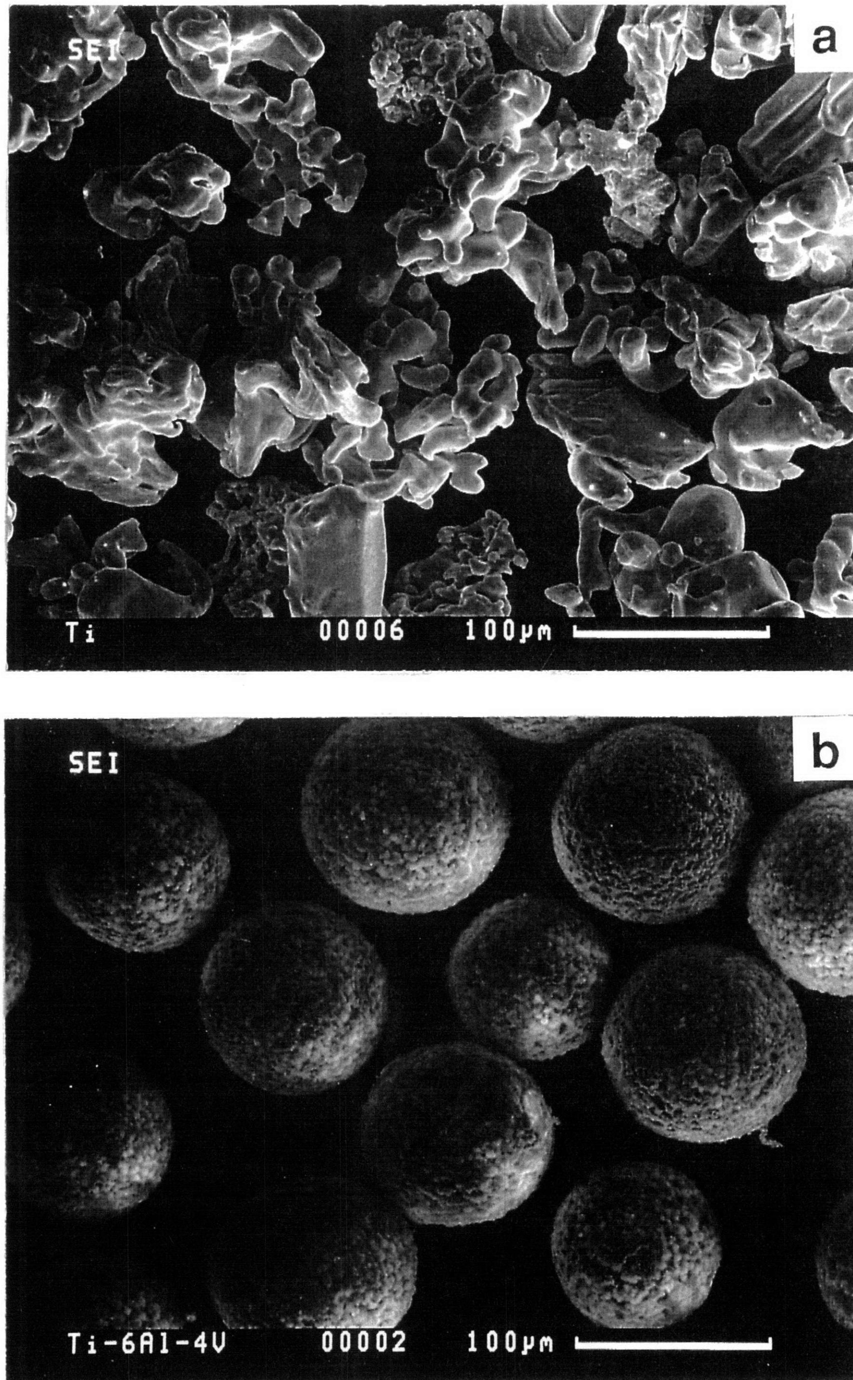

Figure 3.2. Features of (a) CPTi powders and (b) Ti-6Al-4V powders used in the investigation. Note the irregular shape of the CPTi powders.

Table 3.2. Chemical compositions (wt%) and mechanical properties of the as-received Ti-6Al-4V Bar

Elements	O	N	C	Al	Fe	V	Y	H	Ti
Ti-6Al-4V	0.19	0.009	0.014	6.30	0.17	4.07	0.001	0.0039	Bal.
Yield Strength (MPa)		1050							
Tensile Strength (MPa)		1110							
Elongation (%)		16.8							

Table 3.3. Chemical compositions of the titanium brazing alloys (wt%)

Element	Zr	Cr	Fe	V	Cu	Ni	Ti	Tm (°C)
Braze 1 (Type I)	12	14	-	-	12	12	Bal.	930
Braze 2	10	8	-	-	9	9	Bal.	970
Braze 3	12	12	-	-	6	10	Bal.	960
Braze 4	11	15	-	-	8	10	Bal.	1070
Braze 5	12	12	10Co	-	5	8	Bal.	980
Braze 6 (Type II)	12	14	6	-	5	5	Bal.	1100
Braze 7	10	12	-	12	10	10	Bal.	1100

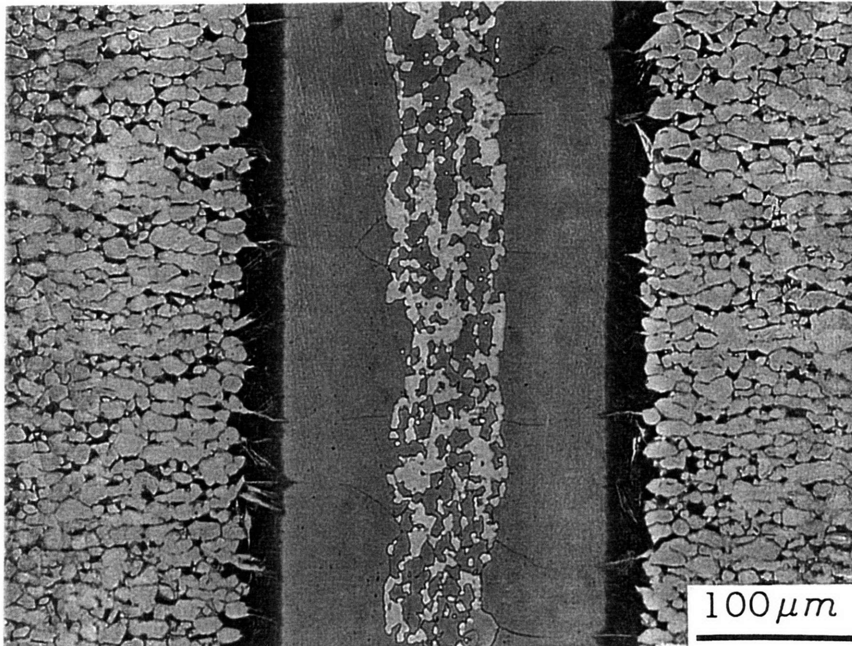

Figure 3.3. Microstructure of a joint bonded at 950°C for one hour. The interlayer is 250 micron thick Type I brazing alloy (Ti-12Zr-14Cr-12Cu-12Ni). White intermetallic compounds can be seen to precipitate in the center of the joint.

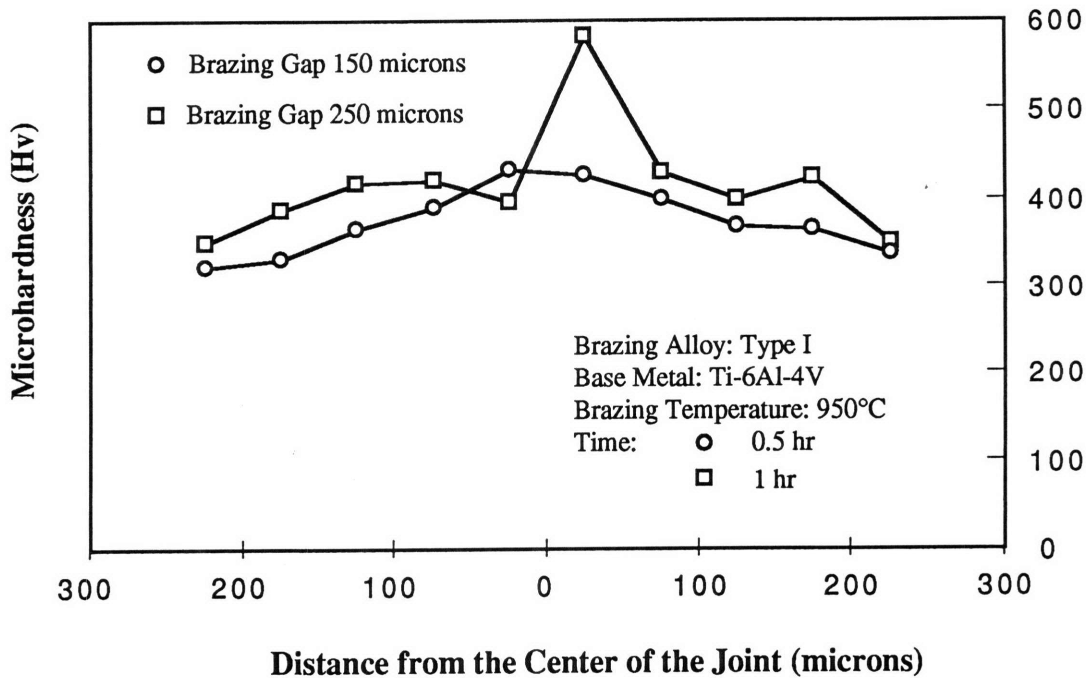

Figure 3.4. Microhardness across the joints using Type I brazing alloy (Ti-12Zr-14Cr -12Cu-12Ni) as the interlayer.

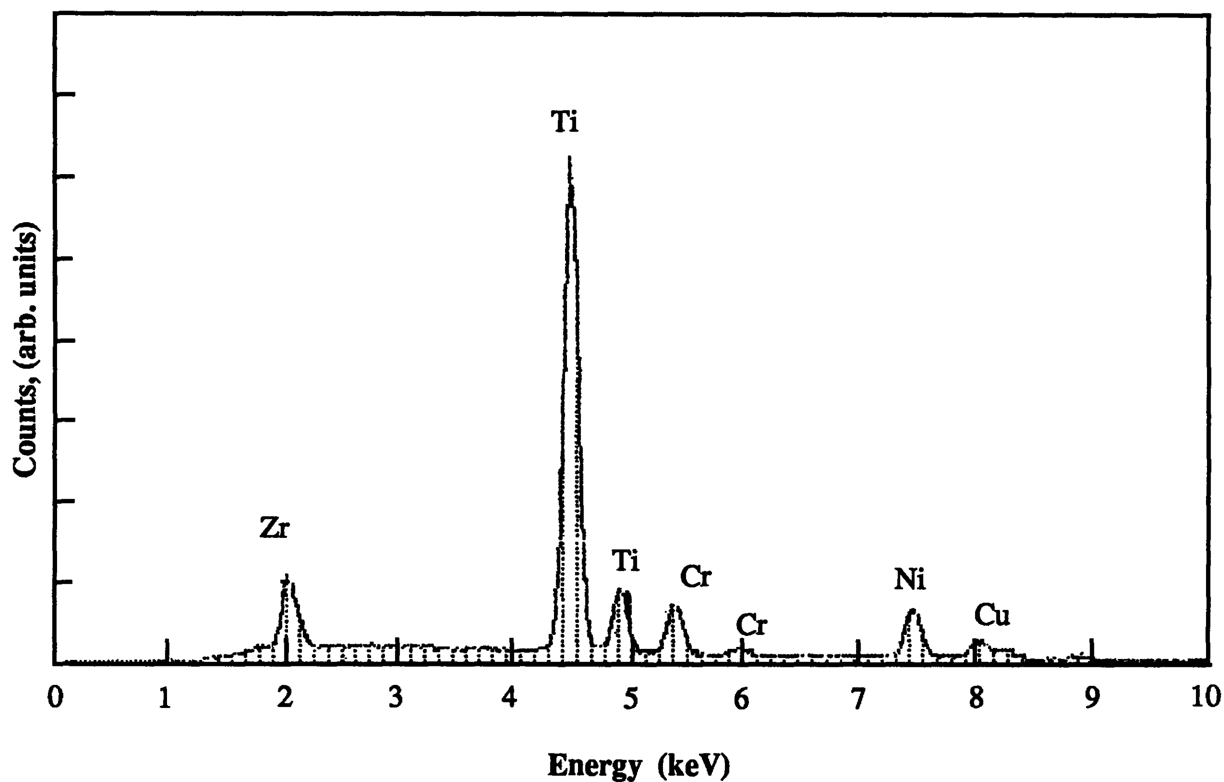

Figure 3.5. Energy dispersive spectra (EDS) of the white phases shown in Figure 3.3.

Table 3.4. Results of EDS Analysis

	White Phase		Matrix	
Elements	at.%	wt.%	at.%	wt.%
Ti	60.74	53.86	80.62	75.67
Cr	4.14	3.97	6.17	6.28
Zr	5.26	8.85	3.66	6.51
Ni	21.65	23.60	4.18	4.83
Cu	8.22	9.71	5.37	6.71

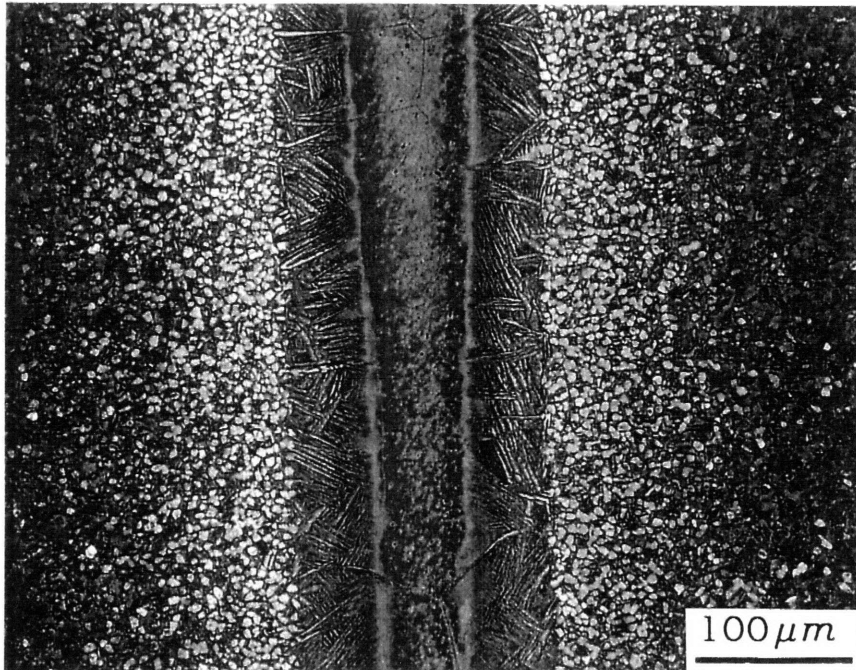

Figure 3.6. Microstructure of a joint bonded at 950°C for 30 minutes. The base metal is Ti-6Al-4V and the interlayer is Type I brazing alloy, with a thickness of 150 microns.

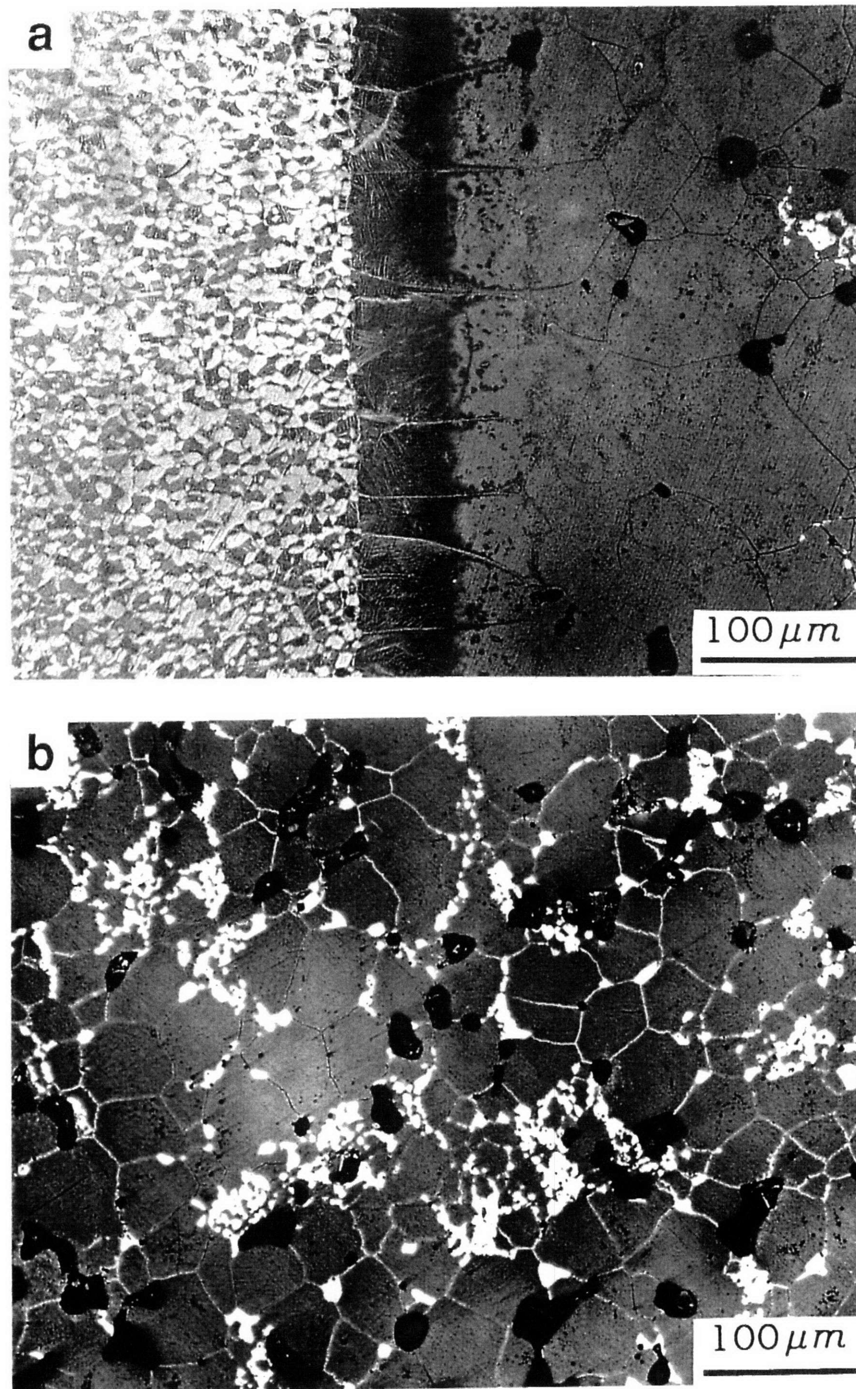

Figure 3.7. Microstructure of a joint bonded at 950°C for 8 hours. (a) the interface between the base metal, Ti-6Al-4V and the interlayer. (b) the interlayer. The interlayer contains 50 wt% Type I brazing alloy, and the rest is equal mixtures of CPTi and Ti-6Al-4V powders. The white spots are intermetallic compounds, and the black holes are residual pores in the interlayer.

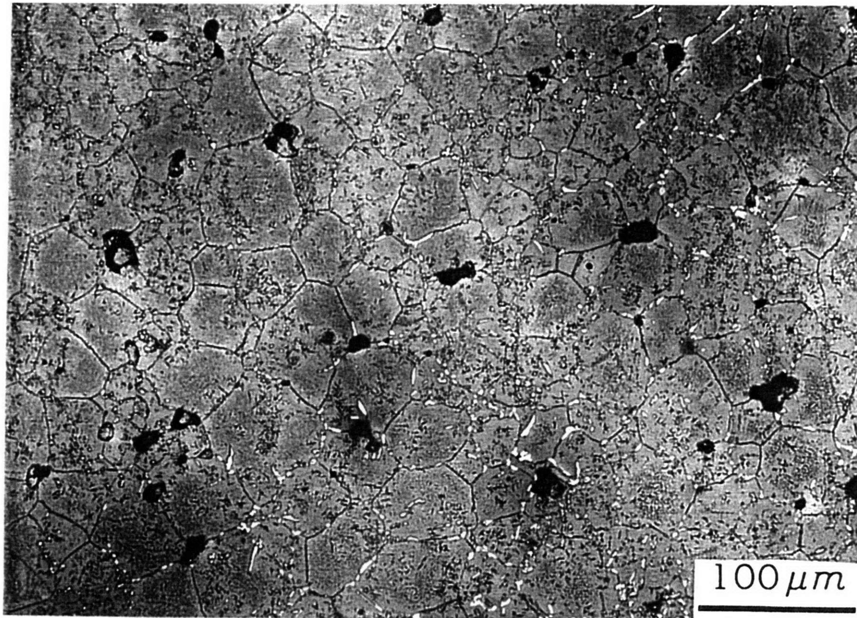

Figure 3.8(a). Microstructure of a joint bonded at 1140°C for 15 minutes. The interlayer contains 45 wt% Type II brazing alloy, and the rest are equal mixtures of CPTi and Ti-6Al-4V powders. Precipitation of α-phase can be observed in a β-matrix. The black holes are residual pores in the interlayer.

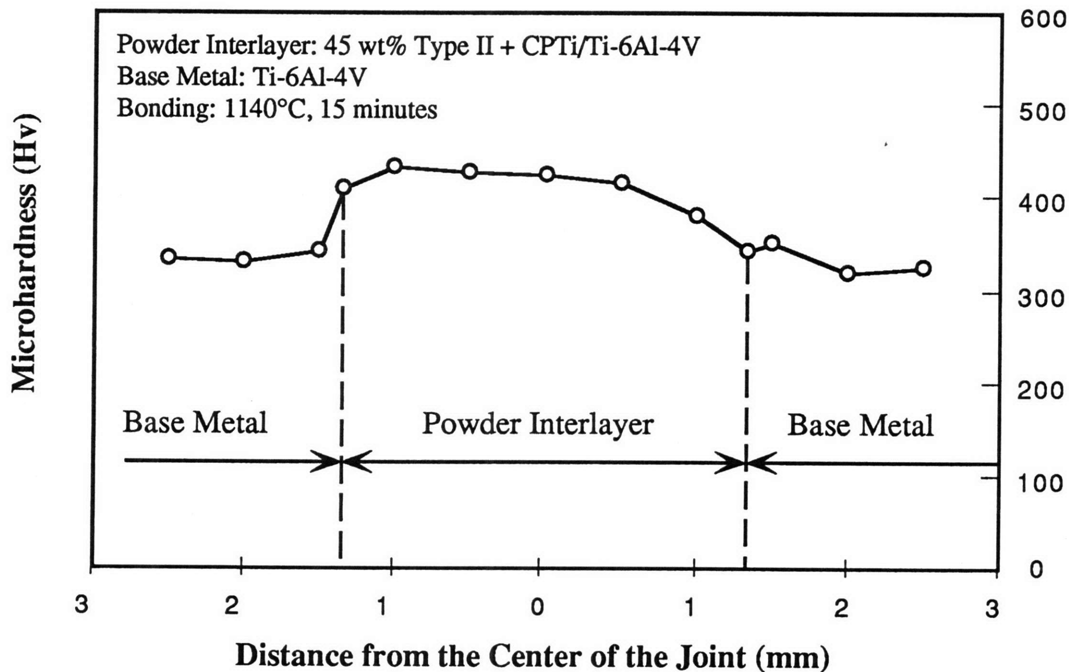

Figure 3.8(b). Microhardness across the joint shown in Figure 3.8(a).

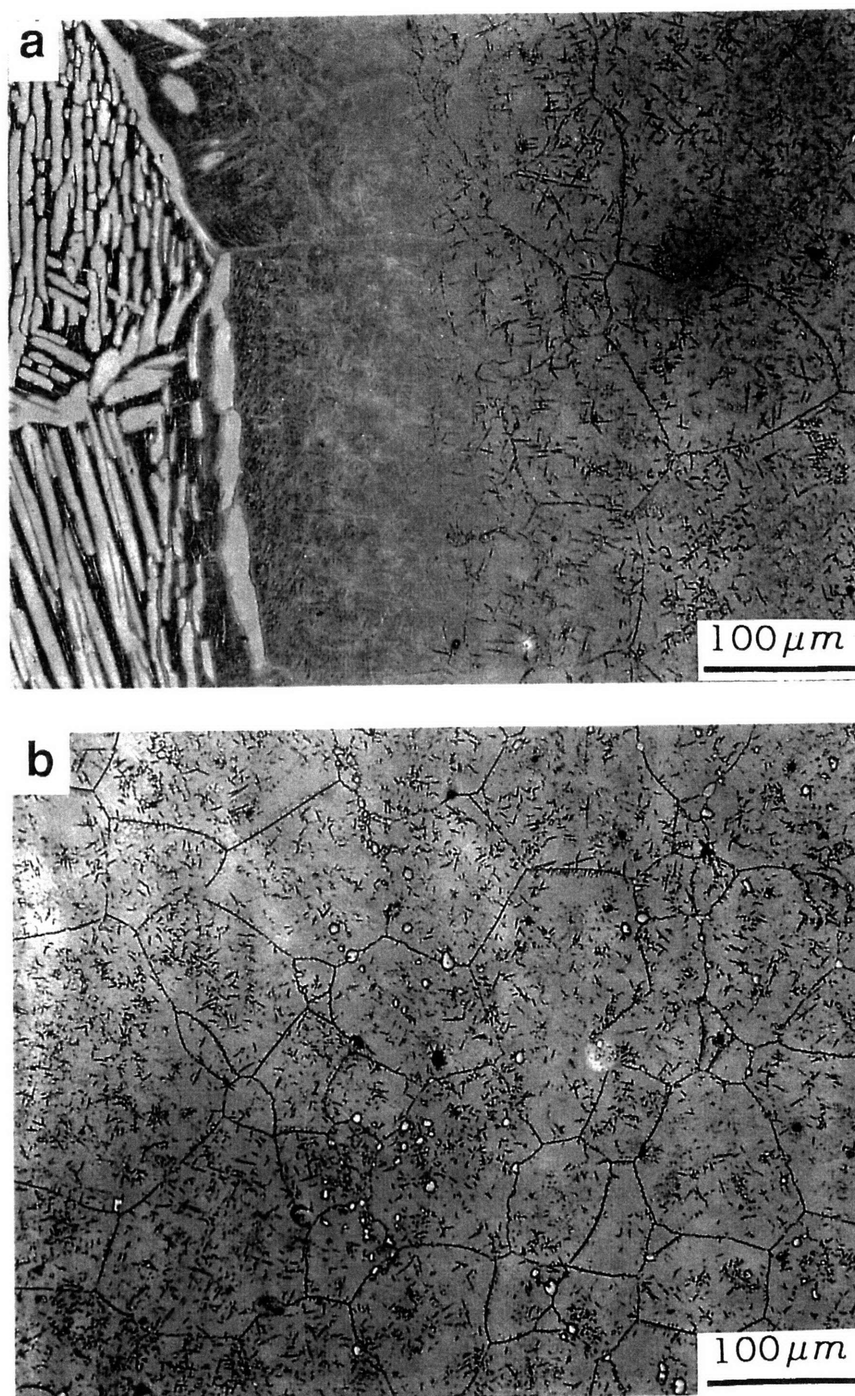

Figure 3.9. Microstructure of a joint bonded at 1140°C for 15 minutes. (a) the interface between the base metal, Ti-6Al-4V and the interlayer. (b) the interlayer. The interlayer contains 50 wt% Type II brazing alloy, and the rest are equal mixtures of CPTi and Ti-6Al-4V powders.

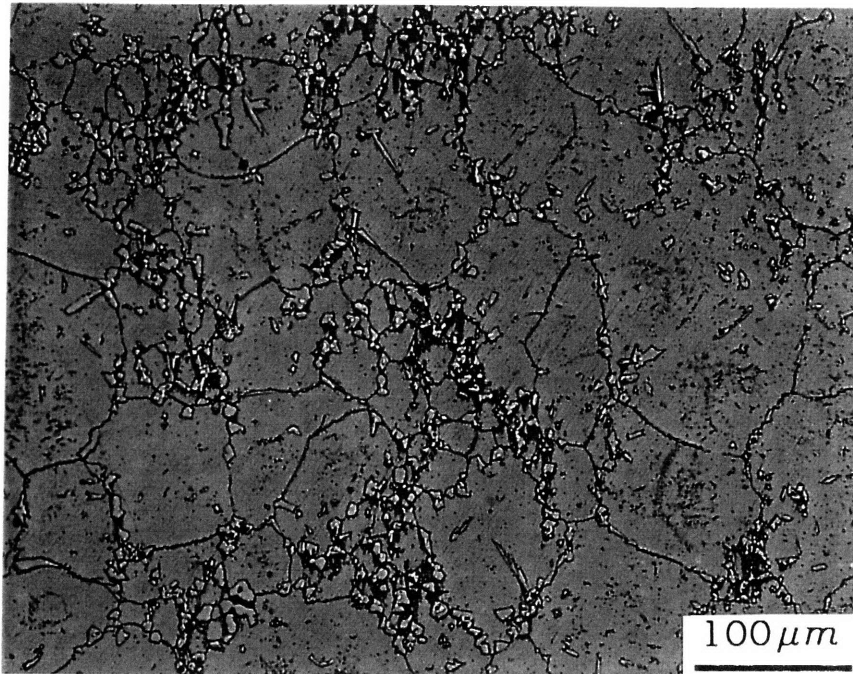

Figure 3.10. Microstructure of a joint bonded at 1140°C for 15 minutes, showing second phase precipitation in a β-titanium matrix. The interlayer contains 60 wt% Type II brazing alloy, and the rest are mixtures of CpTi and Ti-6Al-4V powders.

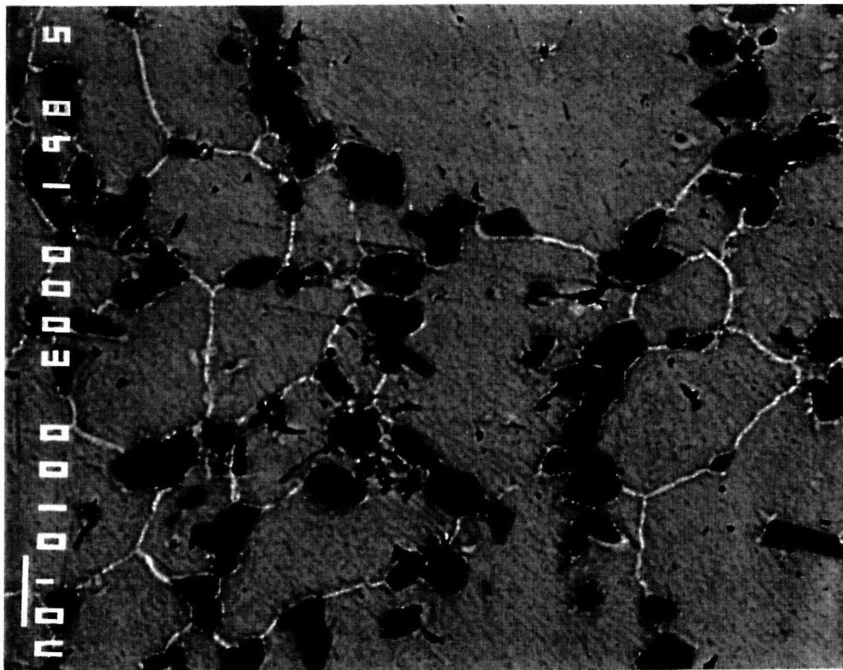

Figure 3.11. Back scattering image of the joint illustrated in Figure 10 under SEM.

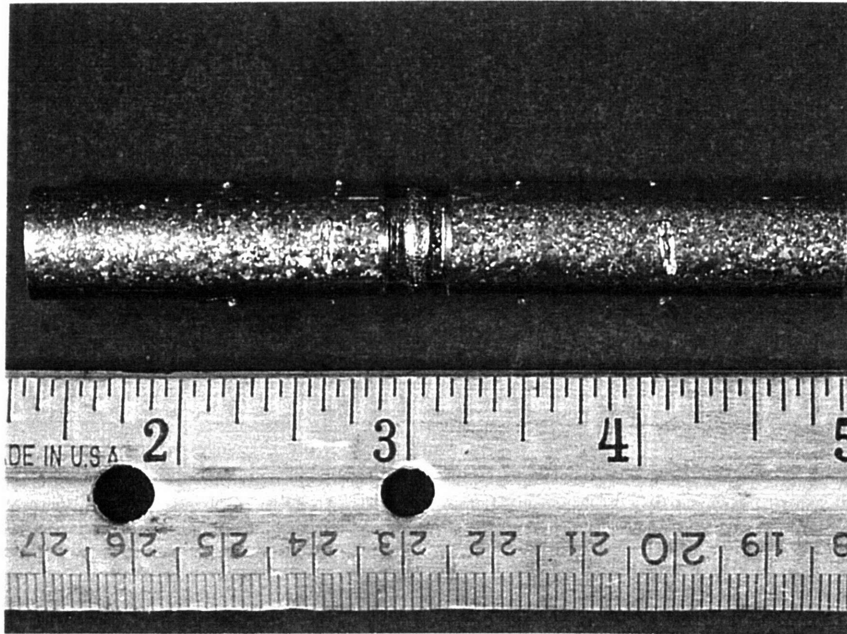

Figure 3.12. View of an as-bonded sample for mechanical testing. Joining was performed at 1140°C for 15 minutes. The interlayer contains 60 wt% Type II brazing alloy, and the rest are equal mixtures of CPTi and Ti-6Al-4V powders. The original thickness of the interlayer was 5 mm.

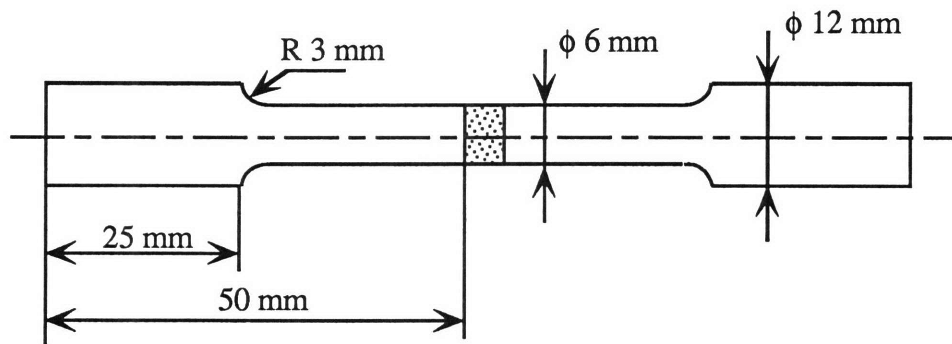

Figure 3.13. Sample dimensions for tensile testing.

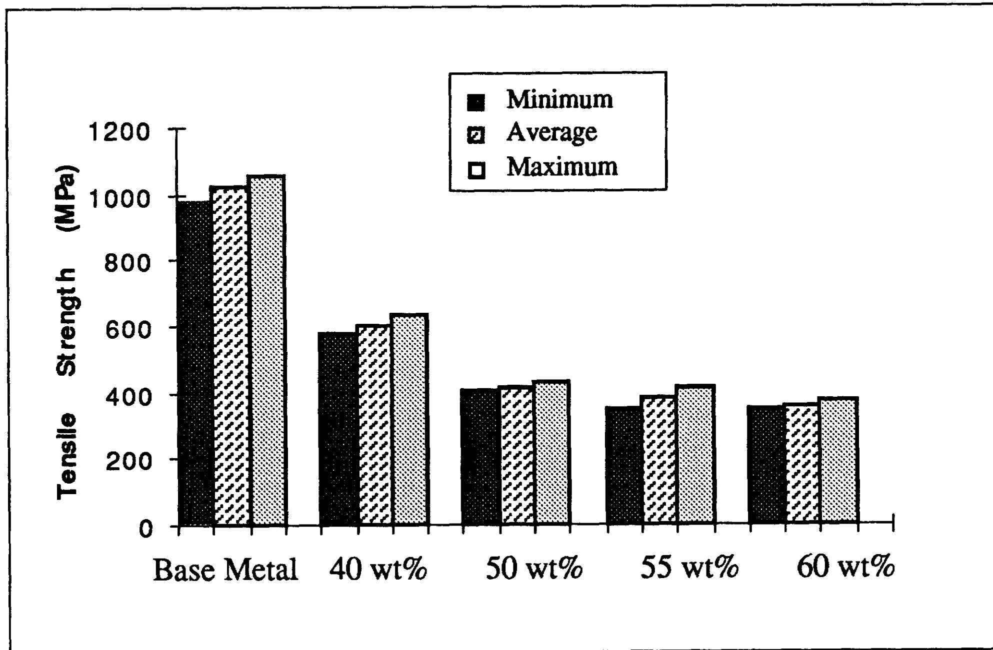

Figure 3.14. Tensile strength of the joints using 5 mm thick powder interlayers. The as-received strength of the Ti-6Al-4V base metal is also plotted.

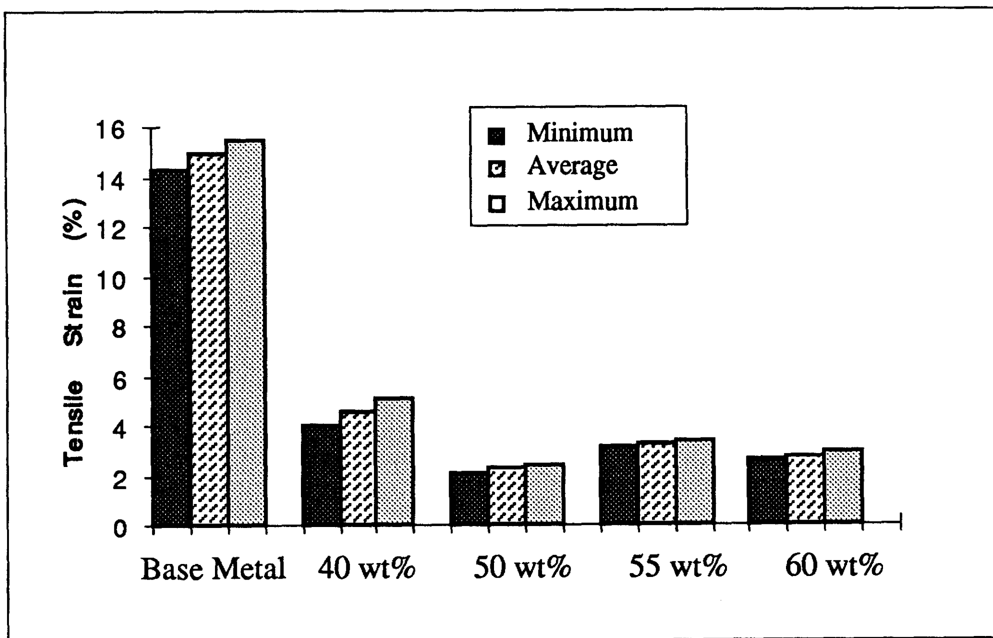

Figure 3.15. Tensile strain of the joints as tested in Figure 3.14.

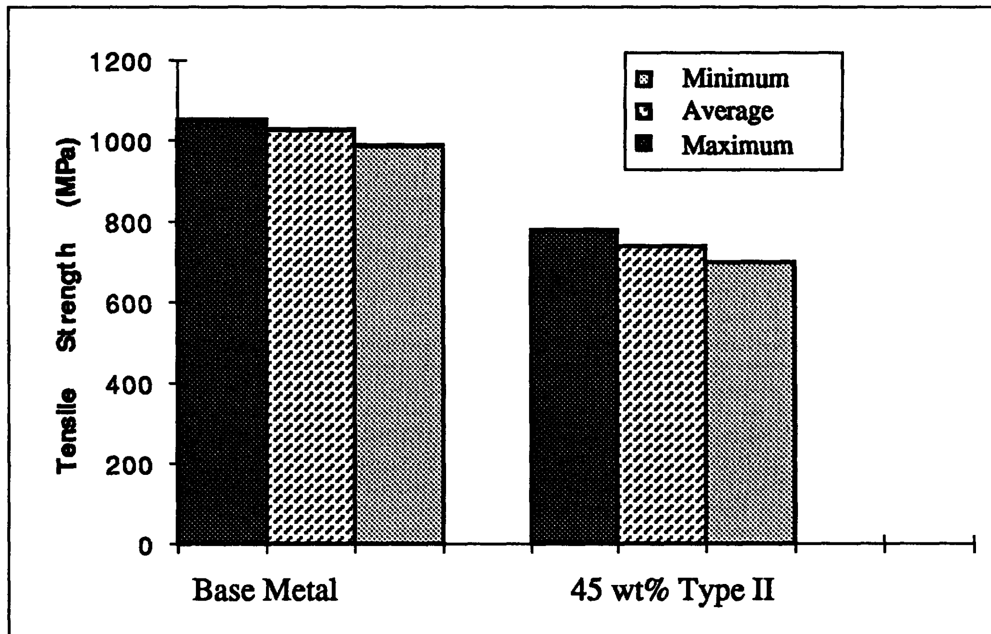

Figure 3.16. Tensile strength of the joints containing 45 wt% Type II brazing alloy. The joints were homogenized at 920°C for 8 hours after bonding at 1140°C for 15 minutes. The strength of similarly treated Ti-6Al-4V is also given in the chart.

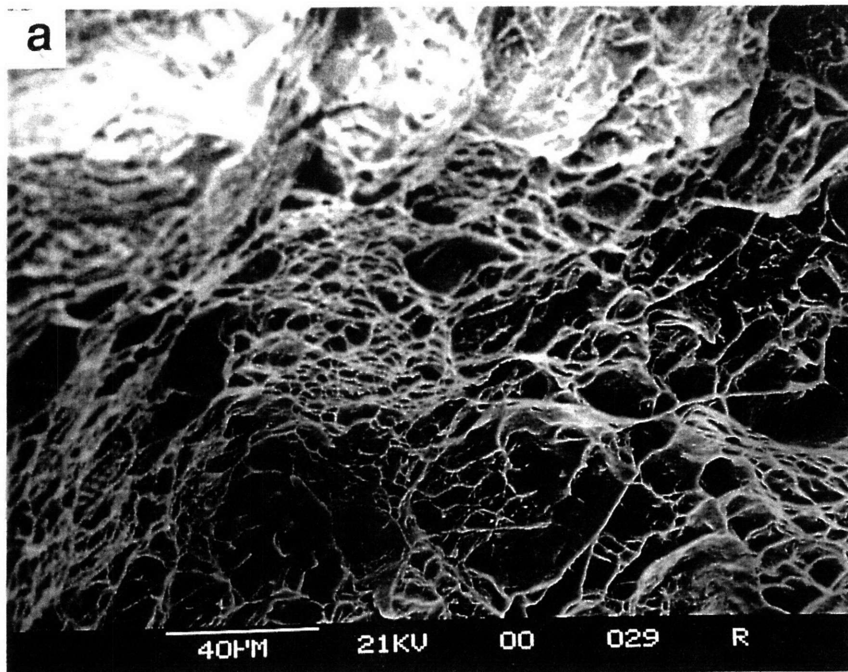

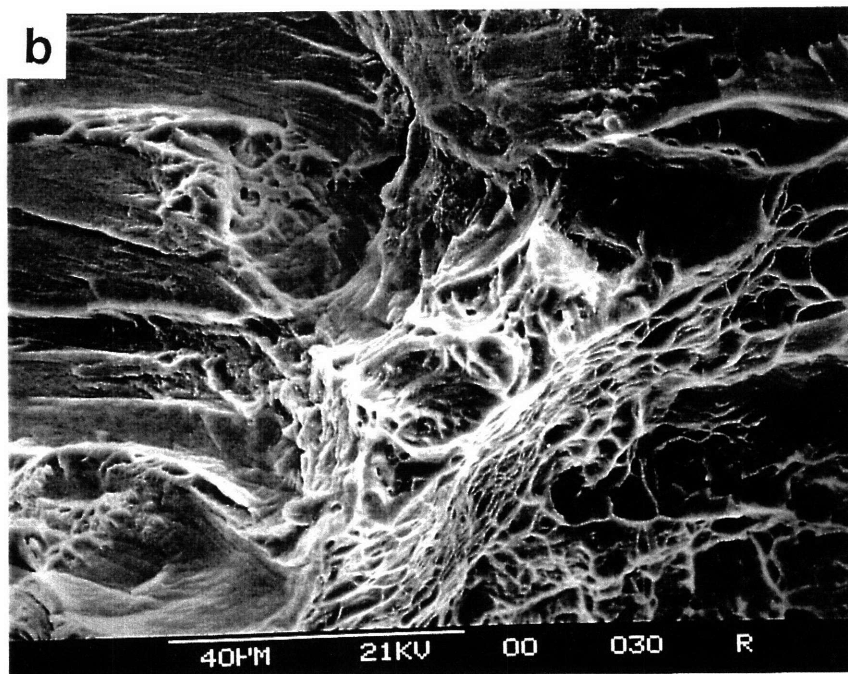

Figure 3.17. Fracture surface of Ti-6Al-4V base metal soaked at 1140°C for 15 minutes and subsequently treated at 920°C for 8 hours. (a) appearence at low magnification, and (b) appearence at higher magnification.

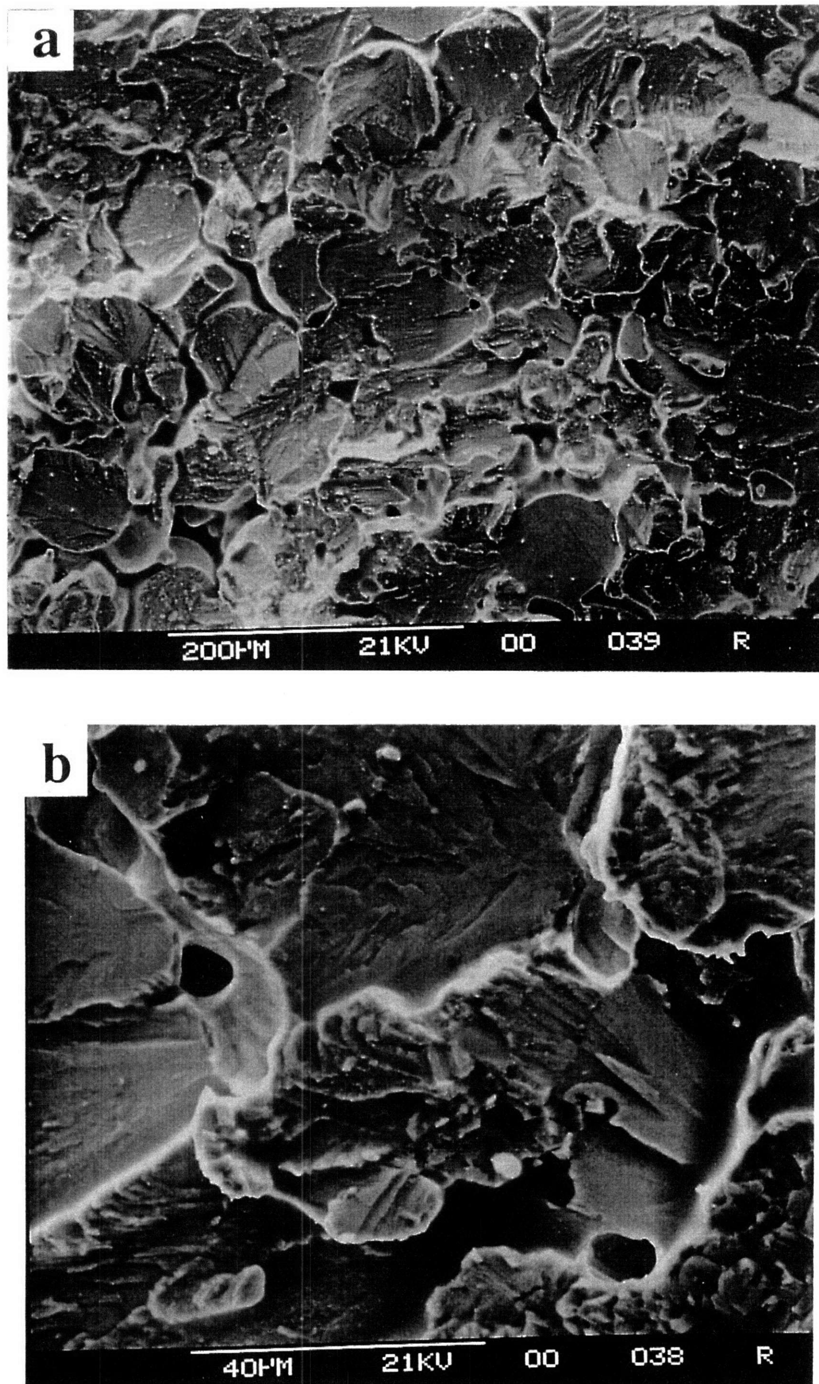

Figure 3.18. Fracture surface of a joint bonded at 1140°C for 15 minutes and subsequently diffusional treated at 920°C for 8 hours. The interlayer contains 45 wt% Type II brazing alloy, the rest are equal mixture of CPTi and Ti-6Al-4V powders. (a) appearence at low magnification, and (b) appearence at higher magnification.

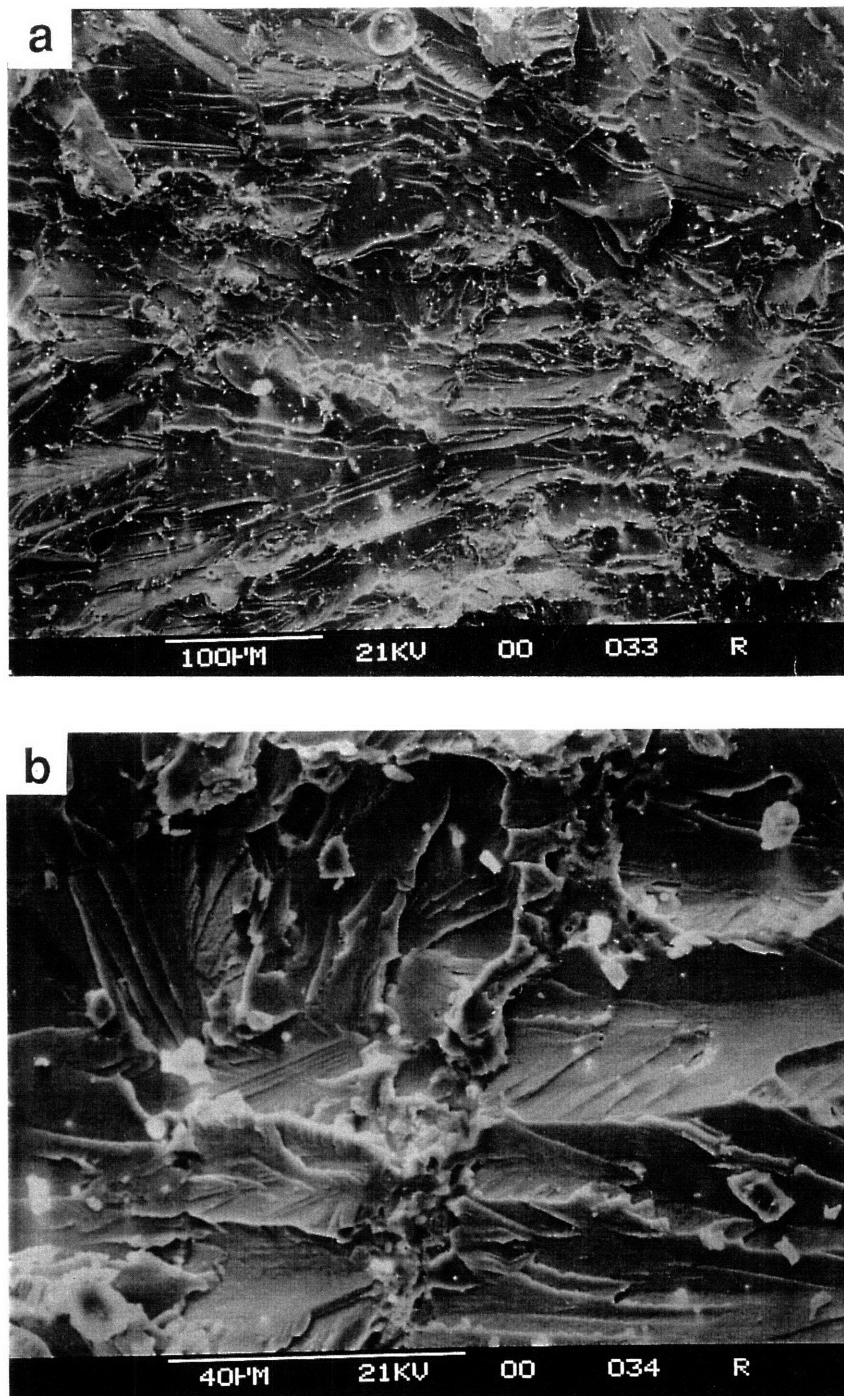

Figure 3.19. Fracture surface of a joint bonded at 1140°C for 15 minutes and subsequently diffusion treated at 920°C for 8 hours. The interlayer contains 50 wt% Type II brazing alloy, the rest are equal mixtures of CPTi and Ti-6Al-4V powders. (a) appearence at low magnification, and (b) appearence at higher magnification.

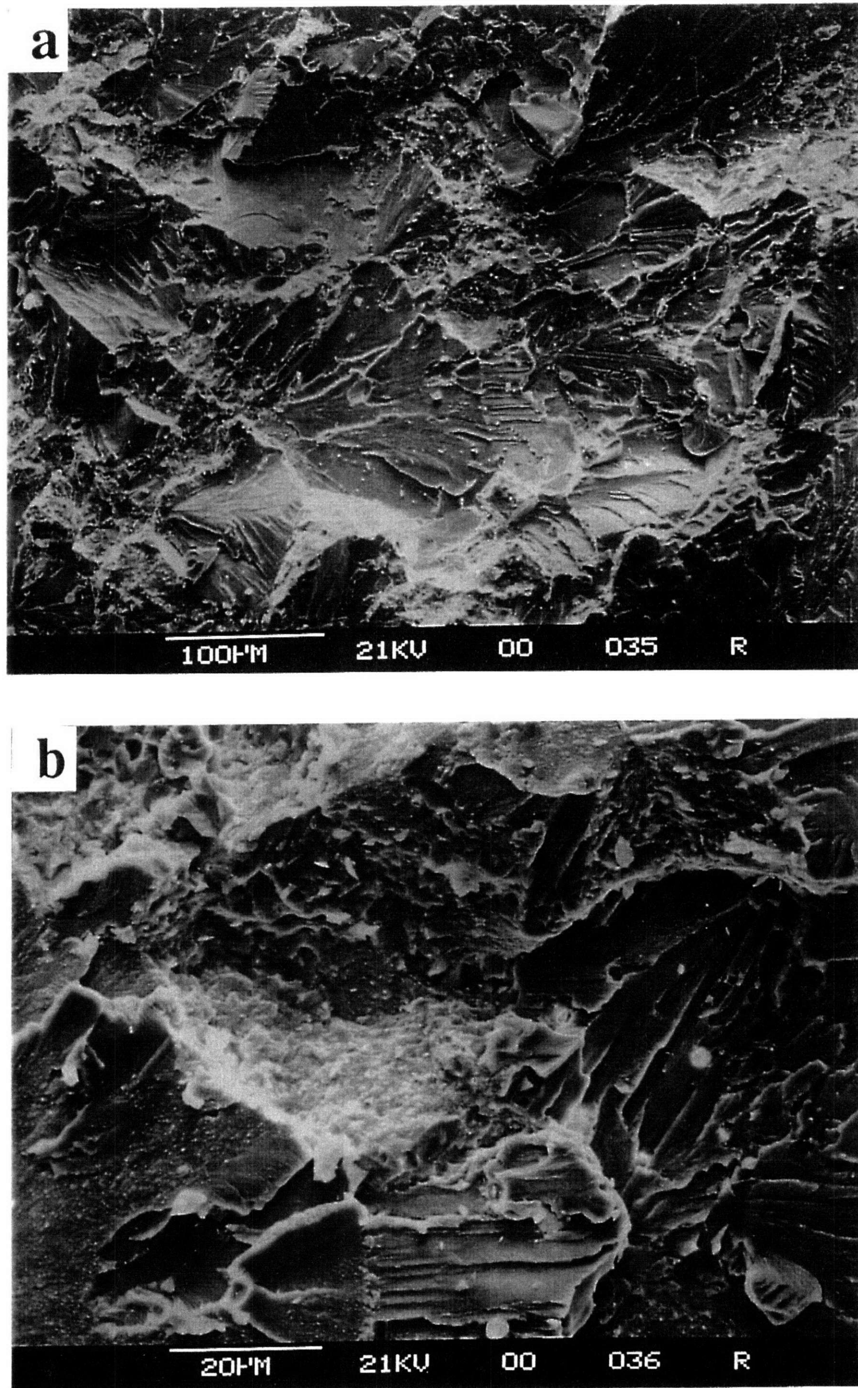

Figure 3.20. Fracture surface of a joint bonded at 1140°C for 15 minutes and subsequently diffusion treated at 920°C for 8 hours. The interlayer contains 60 wt% Type II brazing alloy, the rest are equal mixtures of CPTi and Ti-6Al-4V powders. (a) appearence at low magnification, and (b) appearence at higher magnification.

Appendix: Binary Titanium Phase Diagrams

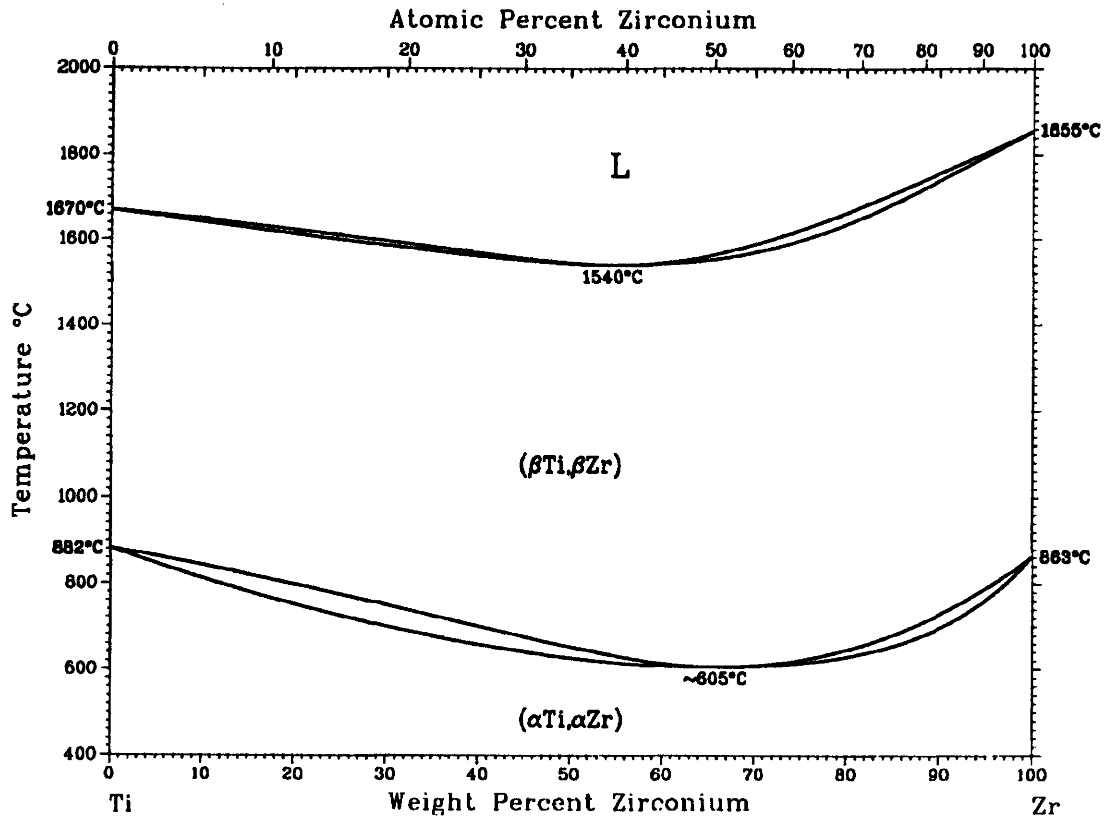

After Massalski, Titanium-Zirconium Phase Diagram.

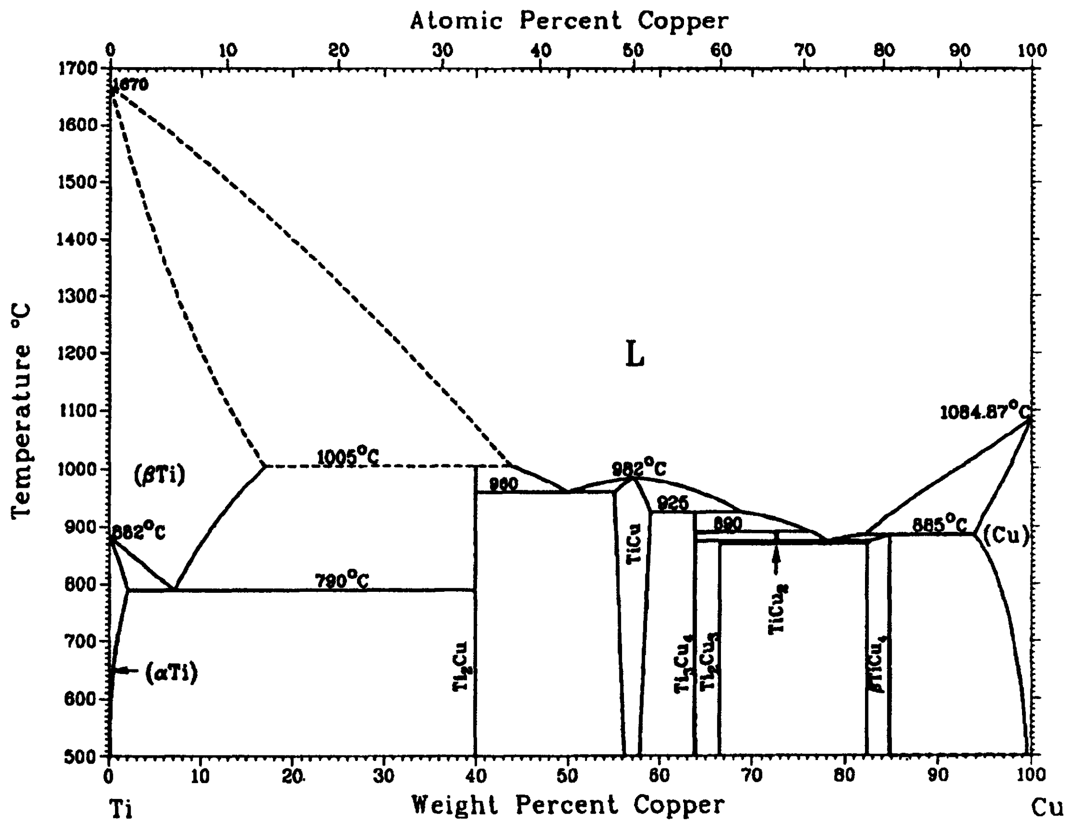

After Massalski, Titanium-Copper Phase Diagram.

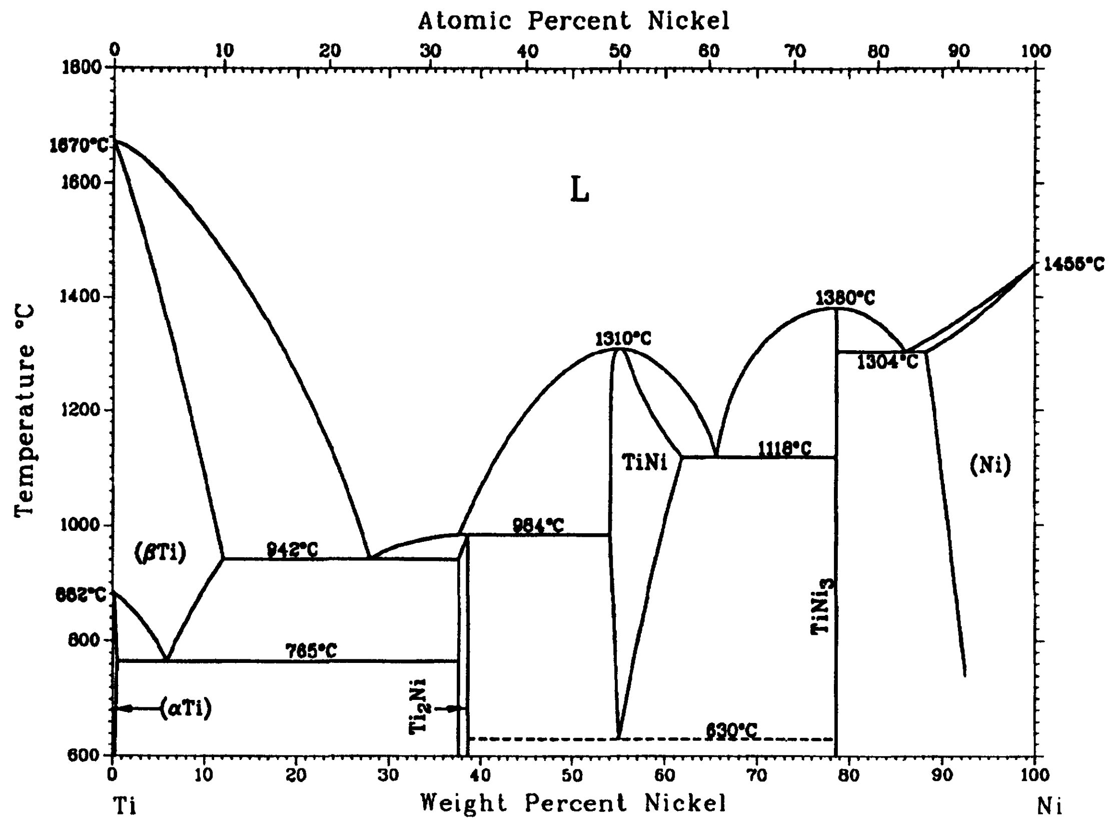

After Massalski, Titanium-Nickel Phase Diagram.

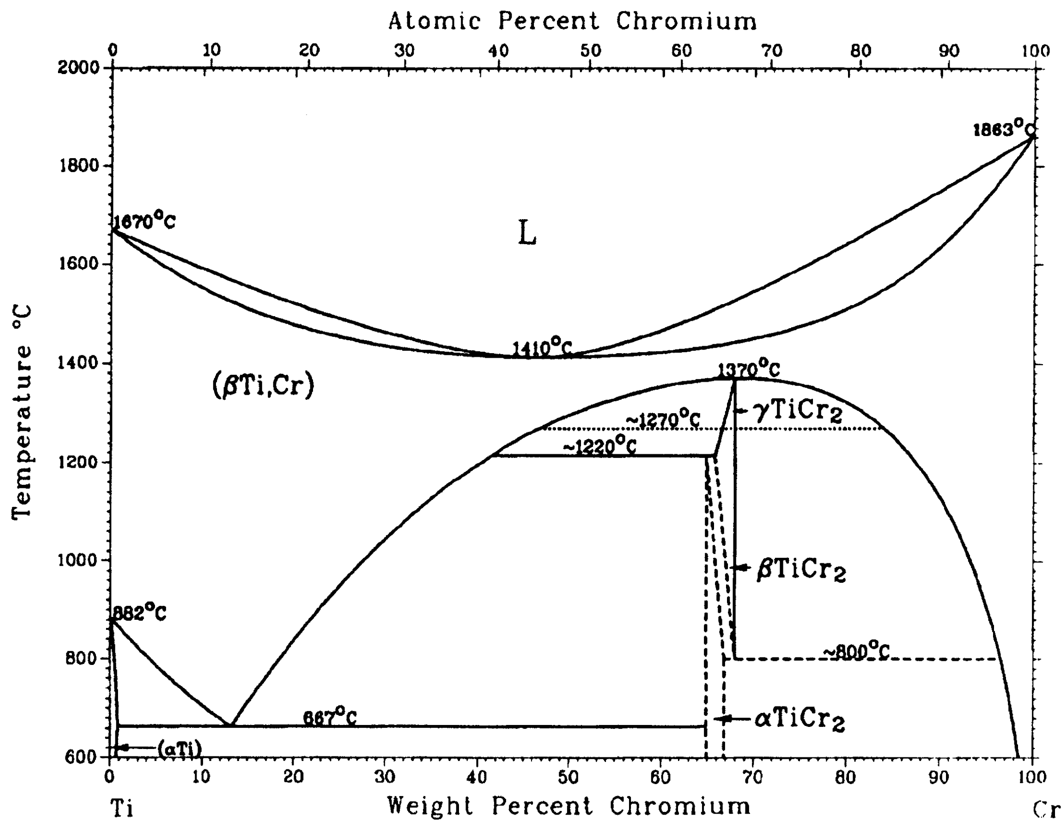

After Massalski, Titanium-Chromium Phase Diagram.

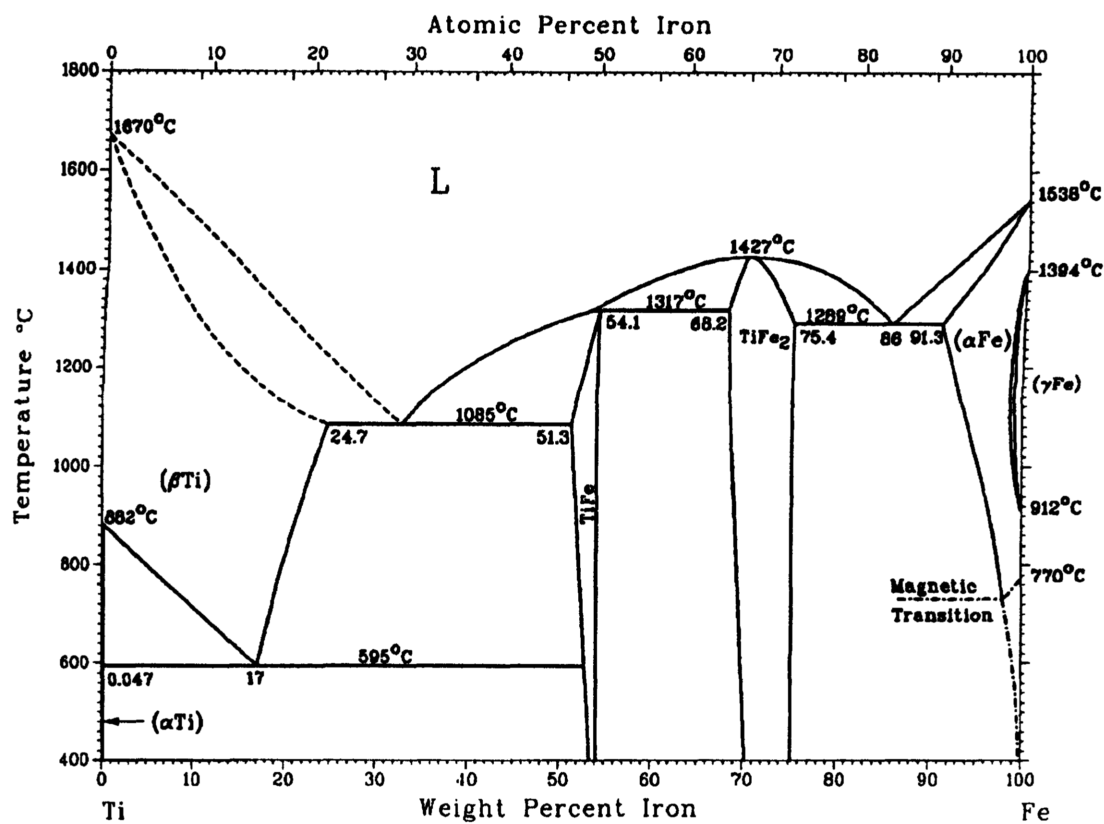

After Massalski, Titanium-Iron Phase Diagram.

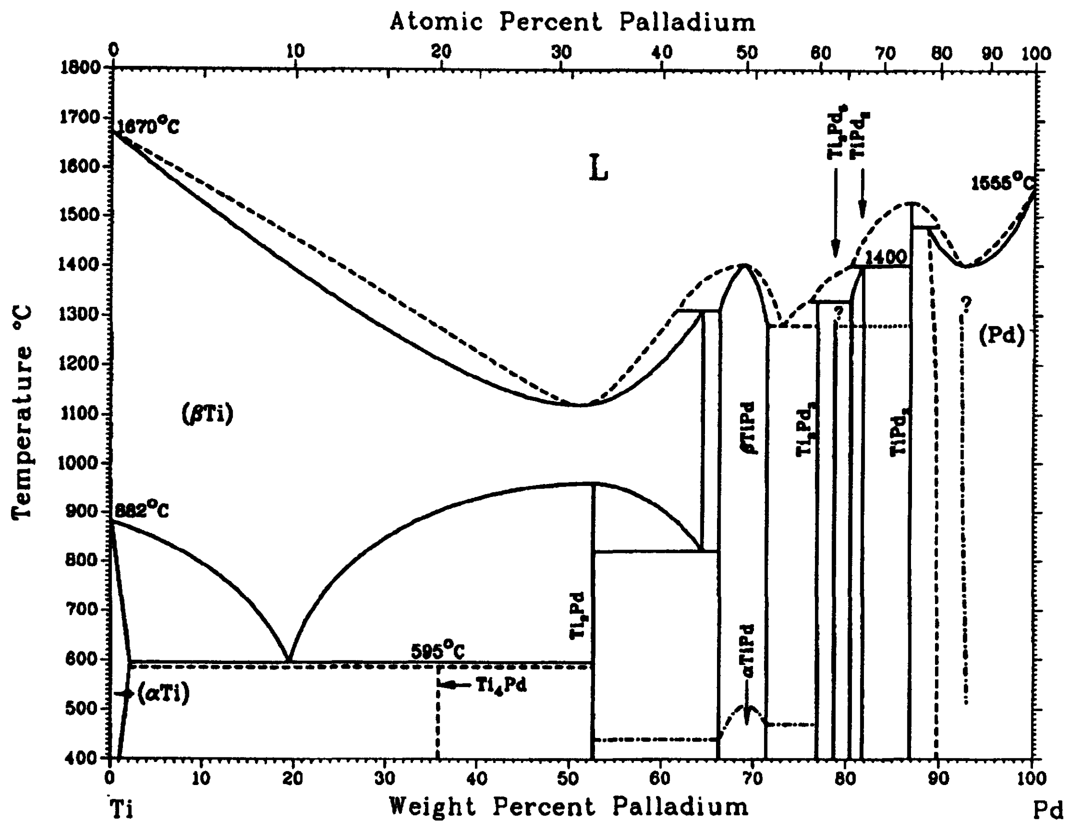

After Massalski, Titanium-Palladium Phase Diagram,

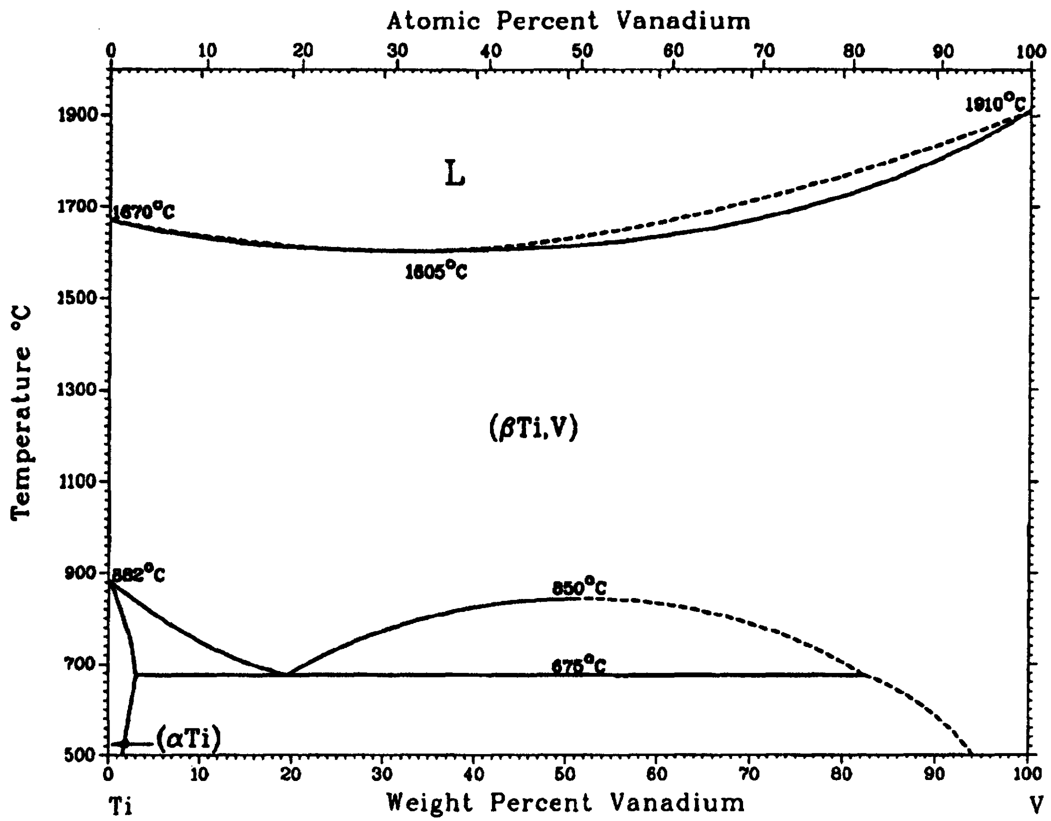

After Massalski, Titanium-Vanadium Phase Diagram.

Presented at 26th International Conference on Brazing and Soldering
Cleveland, OH April, 1995

HIGH TEMPERATURE BRAZING BY LIQUID INFILTRATION

4.1 Abstract

High temperature brazing of nickel-base alloy Inconel 625 by liquid infiltration has been investigated. Nickel-phosphorus, nickel-boron and Ni-41.2Pd-8.8Si were used as melting point depressants (MPDs). They formed wetting liquids at the bonding temperature and infiltrated into the nickel-chromium powder interlayers subsequently. The infiltrated liquid caused shrinkage of the powder interlayer. Calculation showed that residual porosity in the interlayer was related to its initial green density, the amount of liquid and a shrinkage factor. Liquid infiltration greatly reduced the necessary amount of intermetallic forming elements such as phosphorus and boron in the joints, thereby improving mechanical properties of large gap joints. Joints with clearance up to several millimeters (0.2 inch) have been made. Tensile strengths at room temperature, 538°C (1000°F) and 700°C (1300°F) were evaluated.

4.2 Introduction

Nickel-base filler metals have been widely used in brazing processes to produce oxidation and corrosion resistant high strength joints for high temperature service. These filler metals usually contain several melting point depressants (MPDs), such as silicon, boron and phosphorous to ensure proper liquid flow and wetting at the brazing temperature. However, these elements can form eutectic structures that are extremely hard and brittle in the brazed joint. These appear as hard phases in the form of silicides, borides and phosphides. These phases often agglomerate along the centerline of the joint and can greatly decrease the strength and ductility of the joint. Consequently, the maximum joint clearance that is free of intermetallic compounds is generally restricted to be less than

several tens of microns when nickel-base filler metals are used[1-7]. Post-brazing high temperature annealing can help to partially dissolve or eliminate the intermetallics and improve the mechanical properties of the joint. Such beneficial effects can also be accomplished by the transient liquid phase(TLP) bonding process, which has been successfully applied in joining some heat resistant superalloys[8-11]. Instead of cooling down the joint after liquid flow during brazing, the joint is held at the joining temperature for solidification by the TLP process. Isothermal holding makes the MPDs diffuse into the base material and a joint free of brittle intermetallics can be made. However, tens of hours of isothermal holding is generally required to allow solid state diffusion of the MPDs into the base material[12, 13]. Therefore a practical solidification time for the TLP joint also imposes restrictions on the maximum joint gap that can be used.

In this study, a process called liquid infiltrated powder interlayer bonding (LIPB) is used to produce large gap joints using nickel-base filler metals. The filler metals consist of coatings and thin foils on the faying surfaces. A powder interlayer is placed between the two fillers. At brazing temperature, the fillers melt and infiltrate into the powder interlayer. Dissolution and rearrangement of powder particles occur subsequently, followed by homogenization of the joint. By controlling the amount of liquid formed, brittle phases and porosities in the powder interlayer can be reduced to a minimum while a clearance up to several millimeters can be joined. Isothermal solidification time is much shorter as compared to the TLP bonding process since the diffusion path is greatly decreased in the powder interlayer. Thus the LIPB process relaxes the limitation on joint gap set by the TLP bonding process.

4.3 General Considerations of the LIPB Process

One of the ways to decrease the amount of brittle intermetallic compounds in the joint is to reduce the MPDs used for producing the joint. This is achievable through the LIPB process. The process can be divided into four consective stages, which are illustrated in Figure 4.1. This can also be represented in a simple binary eutectic phase diagram, as seen in Figure 4.2. The important parameters of the process can be derived based on such a binary system. Assuming that the powder interlayer has the same composition as the base metal, C_B^i and C_B^o denote the base metal concentration in the infiltrant and overall base metal concentration in the joint, respectively. At the bonding

temperature T_b, liquid starts to form as the MPDs dissolve the base material and change its composition to $C_B^{\alpha L}$. The wetting liquid infiltrates into the powder interlayer while dissolving more base material until the composition of the liquid changes to $C_B^{\beta L}$, which corresponds to the maximum amount of liquid formed. Shrinkage of the interlayer is induced by the infiltrated liquid, and the joint undergoes solidification between $C_B^{\beta L}$ and $C_B^{\beta s}$, followed by homogenization of the joint. An analysis of the residual porosity in the interlayer is derived here under the assumptions of complete wetting and spontaneous infiltration. The initial relative density of the powder interlayer is Δ_0 with a thickness of t_0, and A is the cross sectional area of the interlayer. Assuming uniform dissolution of the powder interlayer, when the infiltrant is unsaturated ($C_B^i < C_B^{\beta L}$) and neglecting the MPD loss by solid state diffusion into the base material, then the weight of powders of the interlayer dissolved in the liquid is:

$$W_{base}^L = W_{MPD}\left(\frac{C_B^{\beta L}}{1-C_B^{\beta L}} - \frac{C_B^i}{1-C_B^i}\right) \tag{1}$$

where W_{MPD} is the total weight of MPDs in the joint. The volume of liquid is given by:

$$V^L = W_{MPD}\left(\frac{C_B^{\beta L}}{\rho_L(1-C_B^{\beta L})} + \frac{1}{\rho_L}\right) \tag{2}$$

where ρ_L is the density of the liquid. Correspondingly, the volume of the remaining solid in the joint is:

$$V^s = \frac{W_{base}}{\rho_s} - \frac{W_{MPD}}{\rho_s}\left(\frac{C_B^{\beta L}}{1-C_B^{\beta L}} - \frac{C_B^i}{1-C_B^i}\right) \tag{3}$$

where ρ_s is the density of the base material. The W_{MPD} can be represented by the overall composition of the base material in the joint, C_B^o:

$$W_{MPD} = A\ \rho_s\ \Delta_o\ t_o \frac{(1 - C_B^i)(1 - C_B^o)}{C_B^o} \tag{4}$$

The weight of the powder interlayer, W_{base}, is given by

$$W_{base} = A\ \rho_s\ \Delta_o\ t_o \tag{5}$$

Assuming no swelling or shrinking of the powder interlayer after infiltration, then the residual volume fraction of porosity after infiltration can be expressed as:

$$P = 1 - \frac{V^s + V^l}{A\ t_o} \tag{6}$$

Substituting equations (1) through (5) into (6), one finally arrives at:

$$P = 1 - \Delta_o \left[1 - \frac{(1 - C_B^o)(C_B^{\beta L} - C_B^i)}{C_B^o (1 - C_B^{\beta L})} + \frac{\rho_s (1 - C_B^o)(1 - C_B^i)}{\rho_L\, C_B^o (1 - C_B^{\beta L})}\right] \tag{7}$$

If assuming the same density of liquid and solid, equation (7) reduces to:

$$P = 1 - \frac{\Delta_o}{C_o} \tag{8}$$

Apart from the calculation above, the powder interlayer can experience additional volume change due to infiltration of the liquid. A constant k is introduced to account for this additional volume change:

$$P = 1 - \frac{\Delta_o}{k\ C_o} \tag{9}$$

$k<1$ indicates shrinkage of the powder interlayer and $k>1$ represents swelling. Obviously, higher initial relative density and lower C_B^o will lead to a denser joint. However, in order to maintain acceptable mechanical properties of the joint, C_B^o is required to be as high as possible. Trade offs exist between the higher MPD concentration or larger volume fraction of residual porosity in the joint. A TLP joint requires C_B^o greater than $C_B^{\beta s}$ as illustrated in Figure 4.1. If we set $C_B^o = C_B^{\beta s}$, then the minimum initial relative density of the powder interlayer needed for a porosity free joint is:

$$\Delta_o = k\, C_B^{\beta s} \qquad (10)$$

It is evident that smaller k, lower $C_B^{\beta s}$ or higher solubility of MPDs in the base metal will allow lower initial packing density of the powder interlayer, which will be easier to infiltrate. Nevertheless, as has been pointed out in [14], diffusional solidification can block the infiltrating liquid if the solubility of MPDs in the base material is high. Therefore the infiltration rate can be retarded significantly because of the solubility effect, as will be shown in our experiments.

4.4 Experimental Work

4.4.1 *Materials*

The infiltrants selected for this investigation were Ni-P eutectic, Ni-B eutectic and Ni-41.2Pd-8.8Si (MBF-1006) alloys. The chemical composition of the infiltrants used are given in Table 4.1 with their solidus and liqudus temperatures. The base metal studied was commercially pure nickel and Inconel 625 nickel-base alloy. The powders investigated were commercially pure nickel and Ni-20wt%Cr powders with sizes less than 44 microns (-325 mesh). The chemical composition of the base metals used are shown in Table 4.2.

4.4.2 *LIPB Procedure*

The Ni-P and Ni-B eutectics were electrolessly plated onto the faying surfaces according to Riedel[15], whereas the silicon containing alloy is in the form of thin

amorphous foils. The powder interlayers were all prepared in a 9.55 mm diameter cylindrical die at 373 MPa compressive pressure. The green density of the interlayers was found to be about 72% by volume. The faying surfaces of the butt joints were polished to 600 grit paper and were ultrasonically cleaned in acetone before joining.

Bonding was performed in a quartz tube resistance furnace. The furnace was first evacuated to 2.7×10^{-3} pa (2×10^{-5} torr), and pre-heated to 900°C (1652°F) before it was placed on the sample. The joining temperature was 980°C (1796°F) for the nickel-phosphorus, 1000°C (1832°F) for the MBF-1006 and 1125°C (2055°F) for the nickel-boron eutectic. The average heating rate for joints using Ni-P and MBF-1006 as infiltrants was 20°C/minute. The rate was dropped to about 14°C/minute for the boron-containing joints. During joining, a minor pressure of about 0.29 MPa (41 psi) was applied on the sample to ensure close contact of the fillers and the powder interlayer. Each joint was cut for metallographic examination. Butt joints were made to evaluate tensile strength of the joints. Room temperature, 538°C (1000°F) and 700°C (1300°F) strength were evaluated.

4.5 Results and Discussion

4.5.1 *Microstructures*

Figure 4.3a shows the microstructure of a joint with 0.6 mm clearance using nickel as the base metal. About 50 microns of Ni-P eutectic was plated on each of the faying surfaces, and nickel powders were used to form the interlayer. Joining was performed at 980°C for 60 minutes. The joint can be seen to have completely homogenized. The overall phosphorus content in the joint after infiltration was 2.4 wt%, which is more than four times lower than in commercial available brazing alloys BNi-6 and BNi-7. In Figure 4.3b, the same joining conditions except a 1.5 mm powder interlayer were applied to make the joint. The powder interlayer was not fully infiltrated, leaving a narrow uninfiltrated zone in the center of the interlayer. Calculation from equation (10) indicates $k<1$ for infiltration using Ni-P eutectic, thus liquid induced shrinkage of the powder interlayer helped to eliminate the pores. It can be estimated from Figure 4.3b that the minimum phosphorus content achievable in the joint through the LIPB process is about 1.8 wt%, and in fact this criteria was applied for all subsequent joints which were infiltrated by Ni-P eutectic.

Figure 4.3c is the microstructure of MBF-1006 infiltrated joint. The 0.65 mm thick interlayer consisted of nickel powders. Infiltration was performed at 1000°C for 30 minutes. The designed silicon content in the joint was 2 wt%, which is below the solubility limit of silicon in nickel (about 7 wt% at 1000°C). Only partial infiltration of the powder interlayer was obtained. As has been pointed out previously (Chapter 2), the lower infiltration rate is due to large solubilities of palladium and silicon in nickel. Diffusional solidification occurs along with the infiltrating liquid, and consumes the liquid before the entire interlayer is infiltrated.

Figures 4.4a and 4.4b are the microstructures of a Ni-P eutectic infiltrated joint with 3.54 mm Ni-20Cr powder interlayer. The joint was soaked at 980°C for 60 minutes. Figure 4.4a shows the interface between the Inconel 625 base metal and the Ni-20Cr powder interlayer. The microstructure of the interlayer after infiltration is shown in Figure 4.4b. Note that oxides from the powder surfaces are trapped in the grain boundaries. Figures 4.4c and 4.4d show the microstructures of Ni-B eutectic infiltrated joint at 1125°C for 60 minutes. The same 3.54 mm Ni-20Cr powder interlayer was used and the designed boron content in the joint was 0.33 wt%. Deeper penetration of boron into the Inconel 625 base metal can be seen as compared to that of phosphorus. This was due to the higher diffusivity of boron and the higher temperature employed to produce the joint. Significant grain growth can be seen in Figure 4.4d, and a large amount of isolated pores remain in the joint. It turned out that the effect of powder interlayer shrinkage was insignificant when using the Ni-B eutectic infiltrant. Higher green density of the interlayer and/or more infiltrant should be used to eliminate residual pores in this sample.

4.5.2 *Tensile Tests*

Figure 4.5 gives the specimen size for tensile tests. Figure 4.6 shows the tensile properties of the LIPB joints using Ni-P eutectic as the infiltrant and 3.54 mm thick Ni-20Cr as the interlayer. Room temperature, 538°C, and 700°C strength were evaluated. Two specimens were used for testing at each temperature. The average room temperature strength was 523 MPa (75 ksi). The 538°C strength decreased to 420 MPa (57 ksi) and the average strength dropped to 300 MPa when tested at 700°C. The data showed about 60% of the Inconel 625 base metal strength within this temperature range. All the specimens tested were found to fracture in the powder interlayer, as shown in Figure 4.7a, indicating strong interfacial bonding between the interlayer and the base metal. Figures 4.7b and 4.7c show the fracture surfaces of the room temperature tested sample. Apart from the effect of the MPDs, the interlayer strength could also be impaired by the oxides

distributed on the surfaces of the alloy powders. A powder cleaning procedure before joining may improve the interlayer strength. The ductility of the joints is still much lower than that of the base metal, although plastic deformation was observed. This is due to a large amount of phosphorus (1.8 wt%) left in each joint, although phosphides are not discernible from the microstructures shown here.

As can be expected from the microstructures revealed in Figure 4.4, the tensile strength of Ni-B eutectic infiltrated joints is degraded by the presence of the residual pores. Figure 4.8 shows the tensile properties and Figure 4.9 depicts the fracture appearance of the sample tested at room temperature. Residual pores can be seen in both of the metallurgraphs.

4.6 Conclusions

In this study the LIPB process was investigated for high temperature brazing of large gap joints. Calculations based on a binary eutectic system show that the volume fraction of residual porosity in the interlayer depends on the initial relative density of the interlayer, the shrinkage factor k, and the solubility of MPDs in the powder material. Ni-P and Ni-B eutectics and MBF-1006 (Ni-41.2Pd-8.8Si) were used as infiltrants, nickel and Ni-20Cr were used as powder interlayers to join nickel and Inconel 625 nickel base alloys. The following results were obtained:

1) Large gap joints could be made by the LIPB process, using Ni-P and Ni-B eutectics as the infiltrants. Intermetallic compounds were greatly decreased because of a much smaller amount of phosphorus or boron contained in these joints, compared to those joined with commercial brazing alloys.

2) Ni-P eutectic was found to cause shrinkage of the nickel base powder interlayer ($k<1$), and contribute to elimination of residual pores in the joint. Whereas Ni-B eutectic showed less benefit in this regard.

3) Infiltration using MBF-1006 as the infiltrant was slow due to high solubility of palladium and silicon in the nickel base powder interlayer. A proper mixture of the infiltrant and the interlayer is important to produce a fully infiltrated joint.

4) Tensile tests showed 60% joint efficiency up to 700°C when Inconel 625 was the base metal and Ni-P eutectic was the infiltrant. Plastic deformation was observed, though the ductility of the joint is still much lower than that of the base metal. Joints infiltrated by Ni-B eutectic revealed poor tensile strength due to isolated pores in the interlayers.

4.7 Acknowledgments

The author would like to thank National Science Foundation (NSF) for supporting this research under contract number DMR-9301444.

4.8 References

1. Manente, D. 1993. Brazing of heat-resistant alloys, low-alloy steels, and tool steels, Welding, Brazing, Soldering, ASM handbook, vol. 6, pp. 924-930.

2. Humpston, G. and Jacobson, D. M. 1993. Principles of Soldering and Brazing, ASM Publication, pp. 47-50.

3. Sakamoto, A., et al. 1989. Optimizing processing variables in high-temperature brazing with nickel-based filler metals. *Welding Journal*, 68(3), pp. 63-71.

4. Schwartz, M. M., 1987. Brazing, ASM Publication, pp. 131-187.

5. Lugscheider, E. and Krappitz, H. 1986. The influence of brazing conditions on the impact strength of high-temperature brazed joints. *Welding Journal*, 65(10), pp. 261-s to 267-s.

6. Lugscheider, E. et al. 1982. Thermal and metallurgical influences on AISI 316 and Inconel 625 by high temperature brazing with nickel base filler metals. *Welding Journal*, 61(10), pp. 299-s to 333-s.

7. Pattee, H. E., 1980. High temperature brazing, Souce Book on Brazing and Brazing Technology, ASM Publication, pp. 17-63.

8. Duvall, D. S., et al. 1974. TLP bonding: a new method for joining heat resistant alloys. *Welding Journal*, 53(4), pp. 203 to 214.

9. Duvall, D.S., et al. 1972. Methods for diffusion welding the superalloy Udimet 700. *Welding Journal*, 51(2), pp. 41-s to 49-s.

10. Hoppin, G. S. et al. 1970. Activated diffusion bonding. *Welding Journal*, 49(11), pp. 505-s to 509-s.

11. Owczarksi, W. A., King, W. H., and Duvall, D. S. 1970. Diffusion welding of the nickel-base superalloys, U.S. Patent #3530568.

12. Liu, S., et al. 1991. Modeling of brazing process that use coatings and interlayers. *Welding Journal*, 70(8), pp. 207-s to 215-s.

13. MacDonald, W. D. 1993. Kinetics of transient liquid phase bonding. Ph.D. Thesis, MIT.

14. Zhuang, W. D., and Eagar, T. W. 1995. A study of liquid metal infiltration of powder compacts with mutual solubility. Submitted to *Metall. Trans.*.

15. Riedel, W. 1991. Electroless nickel plating, Co-published by Finishing publications and ASM, pp. 58.

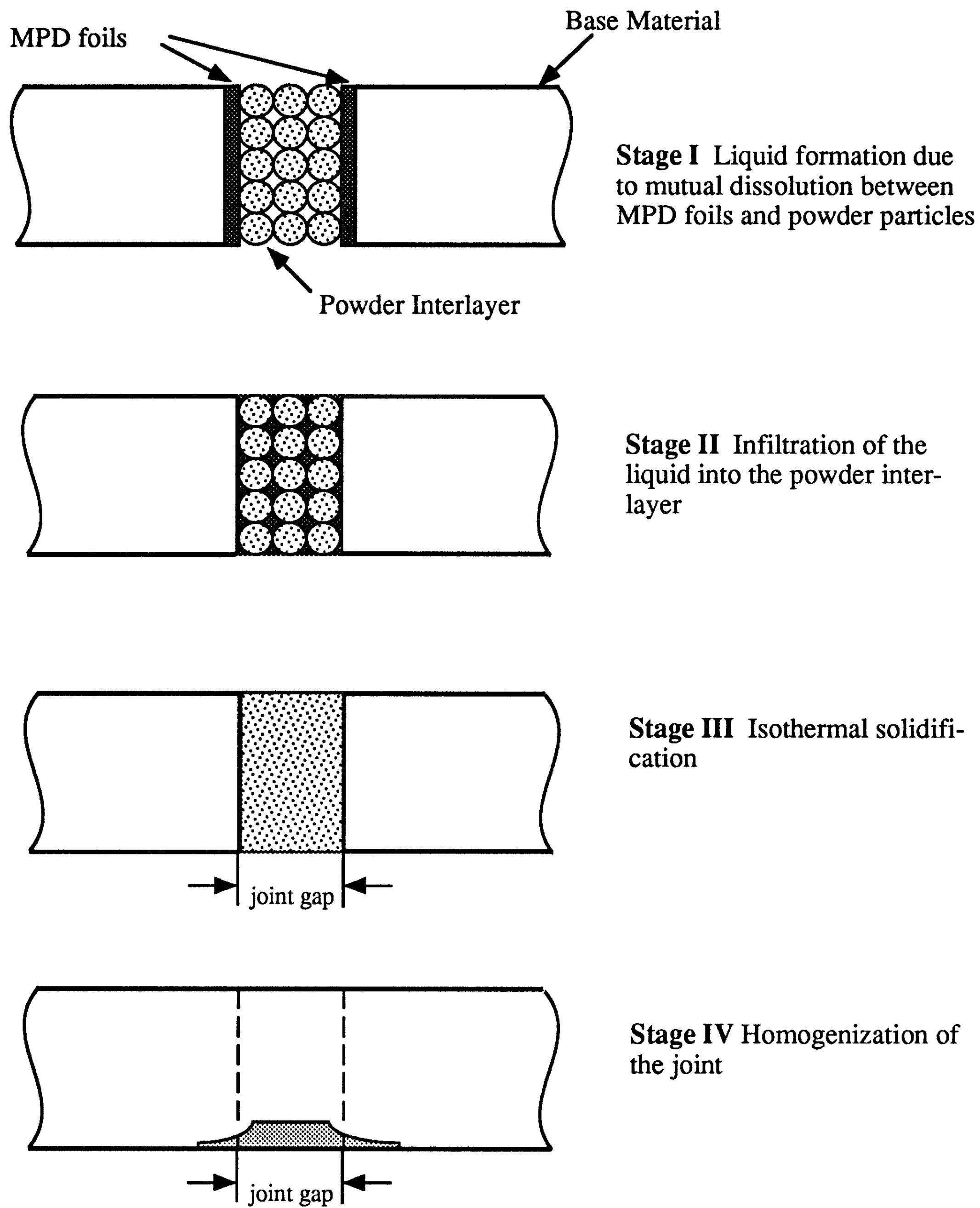

Figure 4.1. Schematic showing the stages of the LIPB process. Widening stage is absent since the dissolution mainly occurs between the powders and the MPD foils. The stages may overlap depending on the rates of infiltration and diffusion.

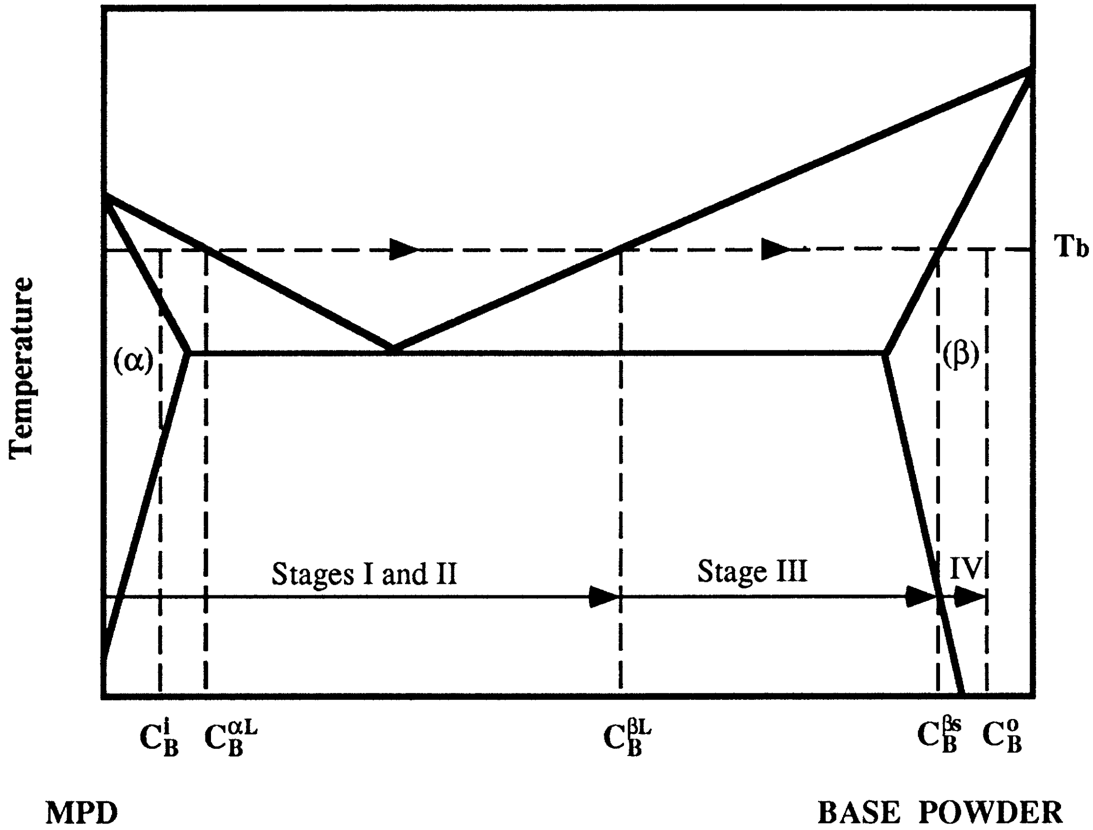

Figure 4.2. Schematic drawing of a phase diagram shows a simple eutectic reaction between the melting point depressant and the powder particles. C denotes the base metal concentration in the diagram. Four stages of the LIPB process is also illustrated.

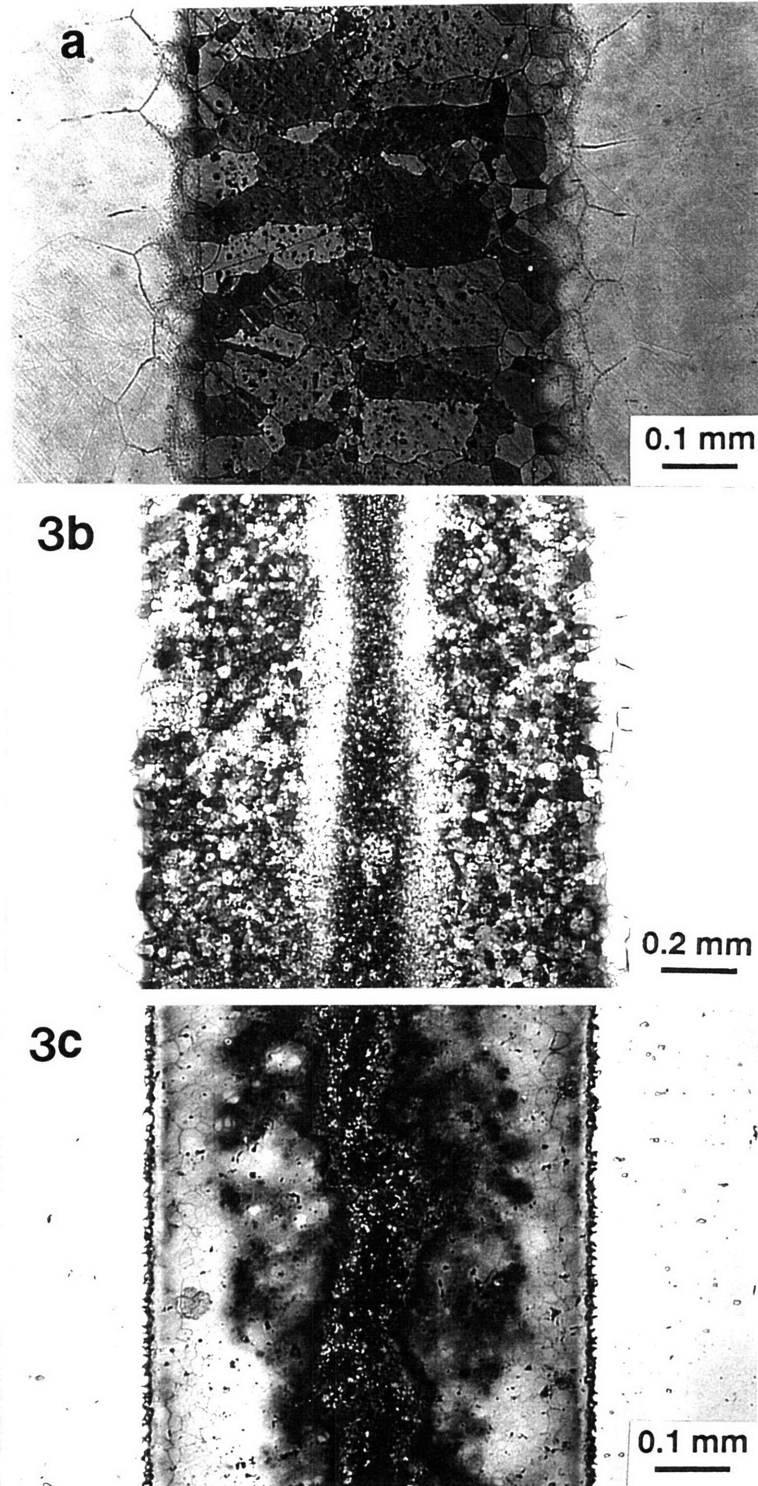

Figure 4.3. Microstructures of infiltrated joints. (3a). 0.6 mm nickel powder interlayer infiltrated by Ni-P eutectic at 950°C for 60 minutes. The base metal is nickel and the phosphorus content in the joint is 2.4 wt%. (3b). Same as (3a), only the interlayer is increased to 1.5 mm. (3c). 0.65 mm nickel powder interlayer infiltrated by MBF-1005 at 1000°C for 30 minutes. The base metal is Inconel 625 and the designed silicon content is 2 wt%.

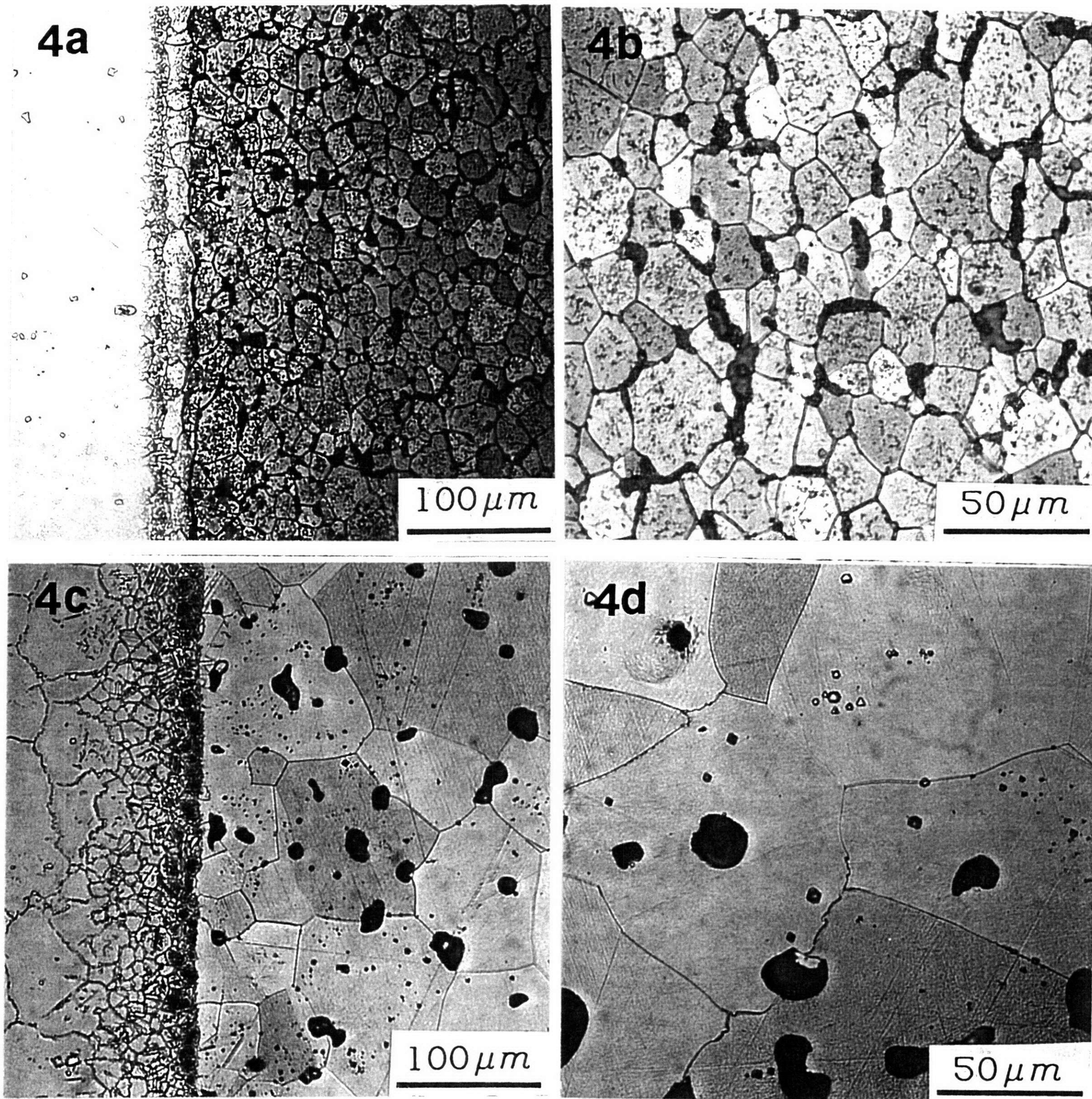

Figure 4.4 Microstructures of infiltrated joints with 3.54 mm thick Ni-20Cr powder interlayers. (4a). Interface between Inconel 625 and the powder interlayer infiltrated by Ni-P eutectic at 980°C for 60 minutes. (4b). Same as (4a), microstructure of the interlayer. (4c). Ni-B eutectic as the infiltrant, 1125°C, 60 minutes infiltrated and (4d). Microstructure of the interlayer.

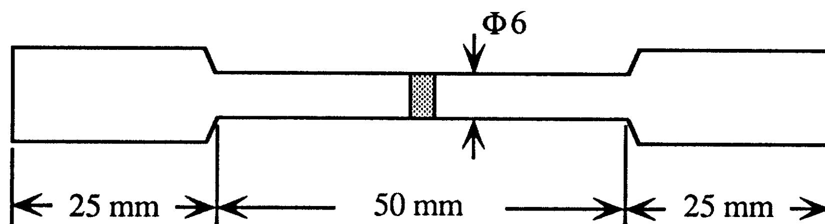

Figure 4.5. Specimen used for tensile tests.

Table 4.1. Chemical compositions of the infiltrants used (wt%).

Materials	Pd	Si	P	B	Ni	Solidus (°C)	Liqudus (°C)
Ni-P	_	_	11	_	Bal.	870	870
Ni-B	_	_	_	3.6	Bal.	1093	1093
MBF-1006	41.2	8.8	_	_	Bal.	714	938

Table 4.2. Chemical compositions of the base metals used (wt%).

Materials	C	Mn	P	Si	Cr	Cu	Mo	Ti	Nb	Fe	Al	Co	Ni
Nickel	0.01	0.2	_	0.04	_	_	_	_	_	0.15	_	_	Bal.
Inconel 625	0.04	0.11	0.01	0.36	22.6	0.18	8.85	0.25	3.68	4.99	0.16	0.2	Bal.

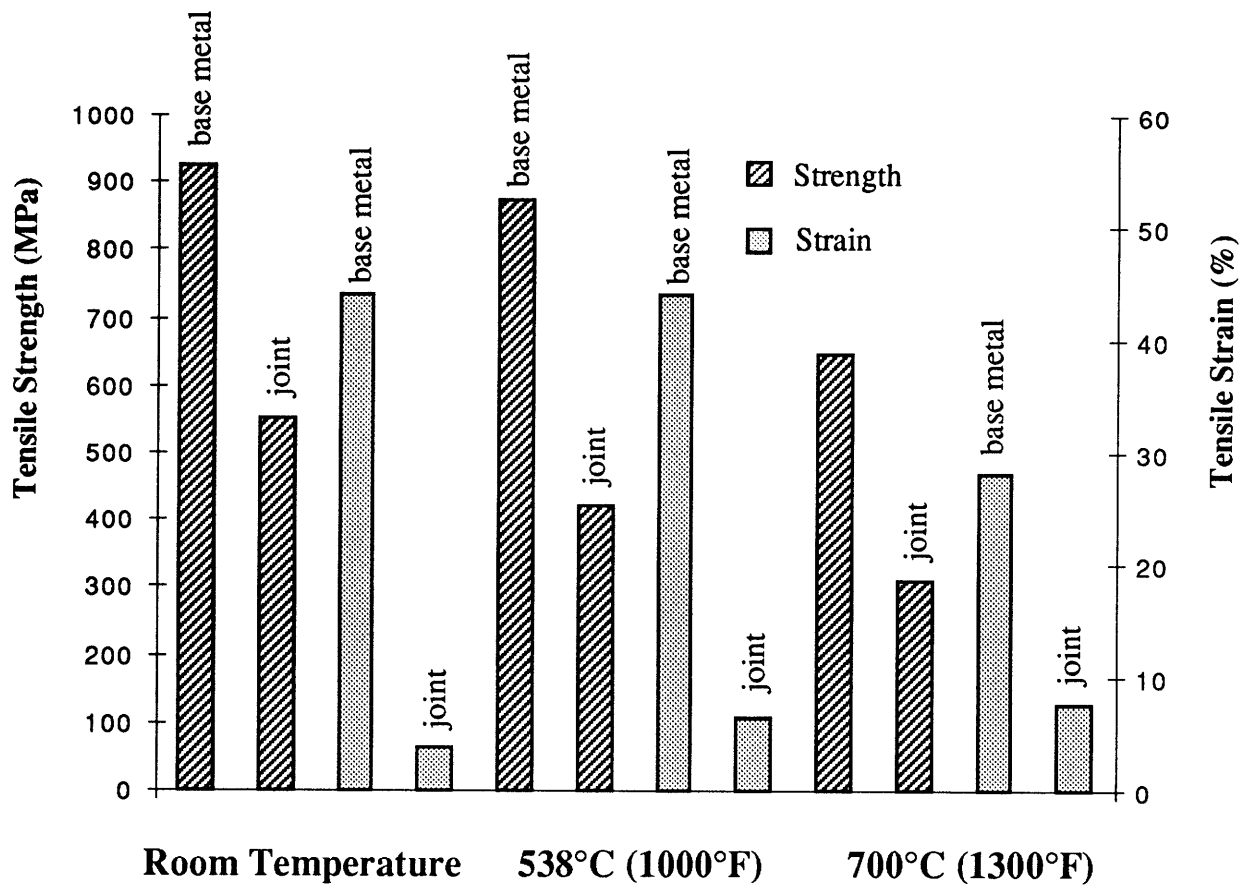

Figure 4.6. Results from tensile tests on the joints infiltrated by Ni-P eutectic at 980°C for 60 minutes. The powder interlayer was Ni-20Cr and the overall phosphorus content in each joint was 1.8 wt%.

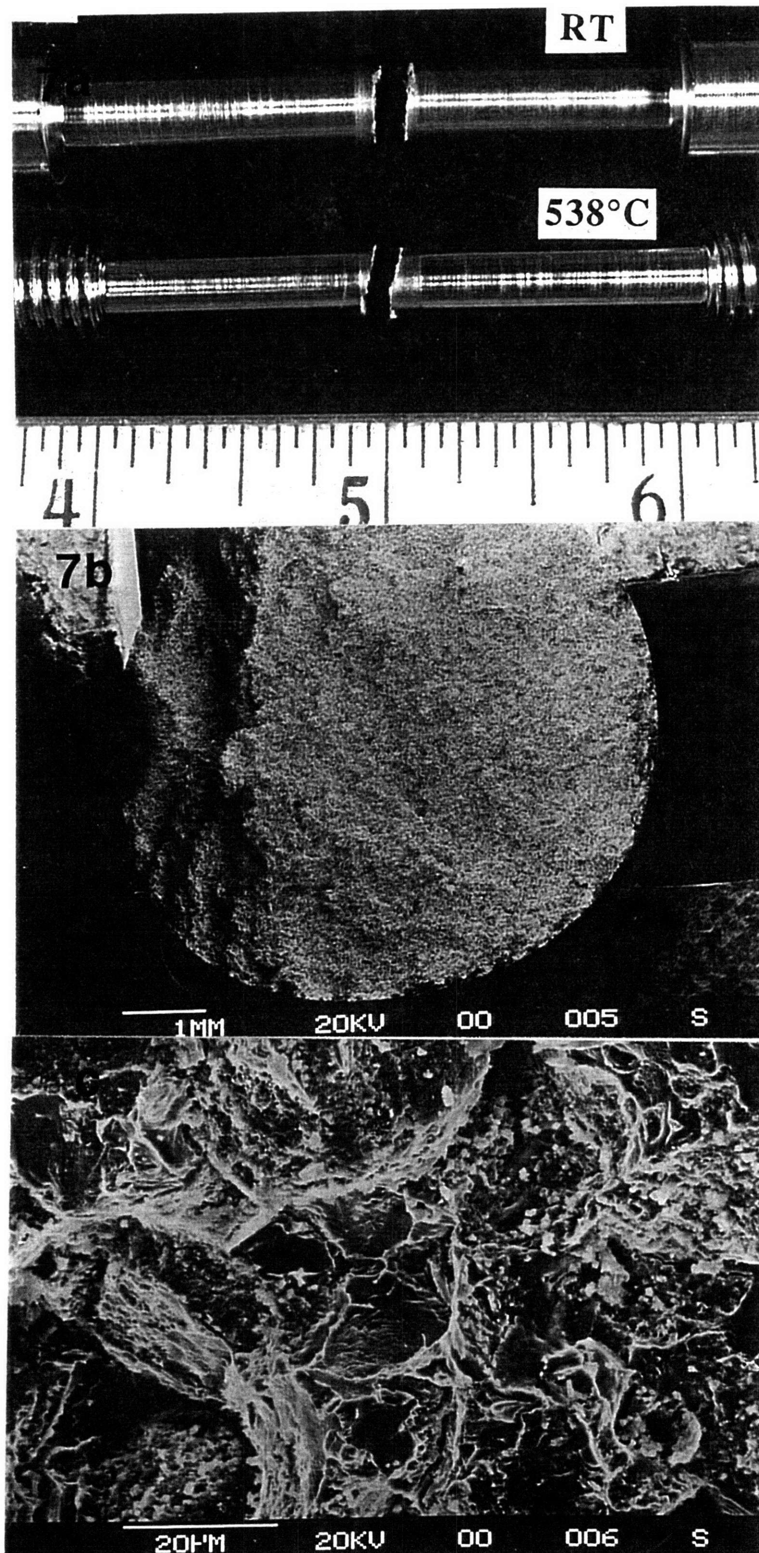

Figure 4.7. Fracture appearence of Ni-P eutectic infiltrated Ni-20Cr powder interlayer joints. (7a). Speicmens showing fracture in the powder interlayers. (7b). Fracture surface of the sample tested at room temperature. (7c). Same as (7b), showing some oxides in the interlayer.

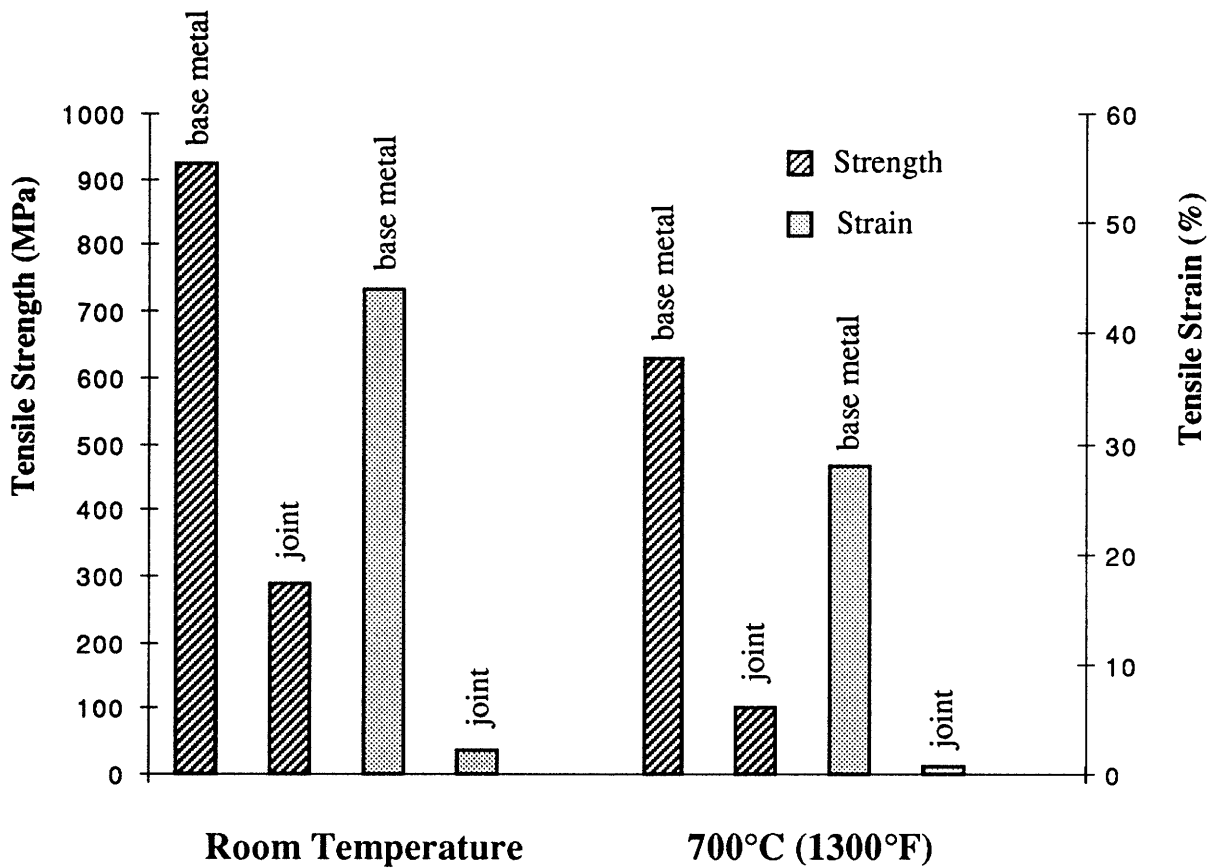

Figure 4.8. Results from tensile tests on the joints infiltrated by Ni-B eutectic at 1125°C for 60 minutes. The powder interlayer was Ni-20Cr and the designed boron content in each joint was 0.33 wt%.

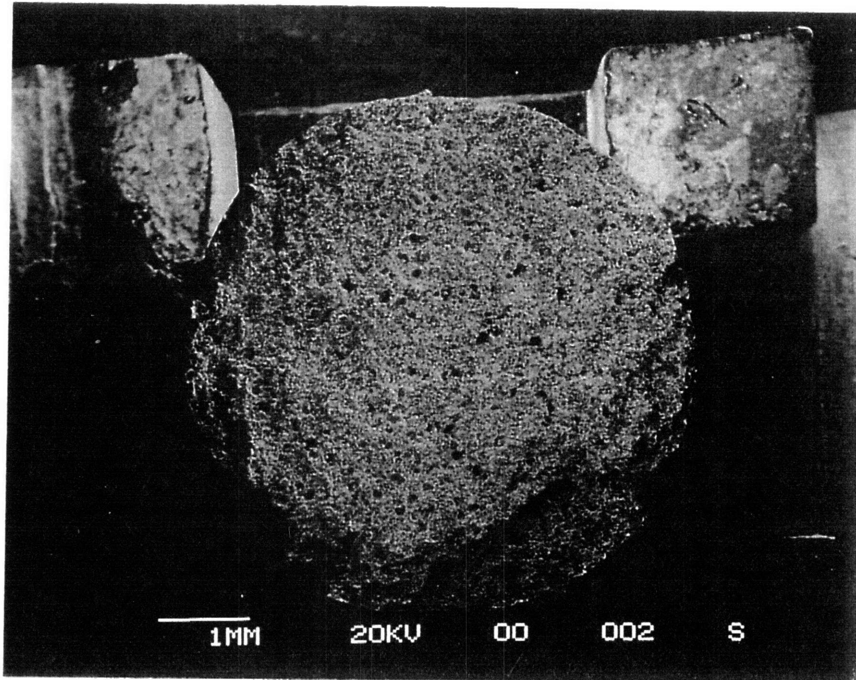

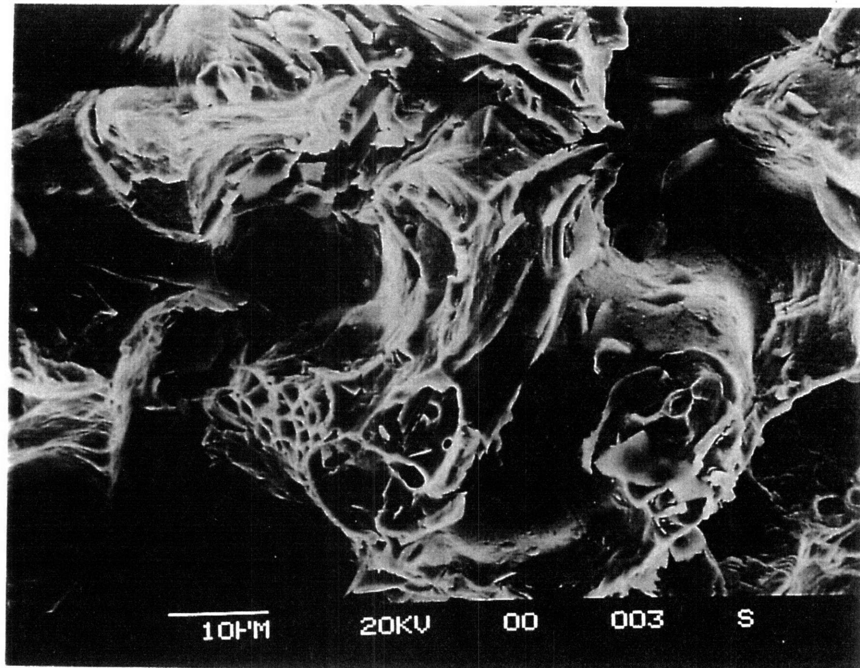

Figure 4.9. Fracture surface of the Ni-B eutectic infiltrated joint. The powder interlayer was Ni-20Cr and the boron content in the joint was about 0.33 wt%. Residual porosities can be seen from the photographs.

DIFFUSIONAL BREAKDOWN OF NICKEL PROTECTIVE COATINGS ON COPPER IN SILVER-COPPER EUTECTIC MELTS

5.1 Abstract

Diffusion couples with electrolessly plated nickel diffusion barriers between copper substrates and silver-copper eutectic alloys were tested at 800°C and 850°C, respectively. Growth of (Cu, Ni, Ag) ternary solid solution into the melt was observed at both temperatures. The growth pattern changed from cellular to dendritic as the temperature was increased from 800°C to 850°C. The non-planar growth morphology can be explained in terms of constitutional supercooling in the melt. Kinetics of (Cu, Ni, Ag) solid solution growth was found to be controlled by interdiffusion at the interface of the nickel barrier and the growing solid state phase. Local breakdown of the nickel diffusion barrier started once the (Cu, Ni, Ag) solid solution reached the copper substrate. Silver diffused from the silver-copper melt, through the ternary solid solution, dissolving copper and forming silver-copper liquid along copper grain boundaries. Ultimately, the nickel barrier was totally converted to the ternary solid solution, broken up and floated into the liquid. Dissolution of the copper substrate occured subsequently. A thin layer of chromium undercoating proves very effective in extending the protection time of the nickel diffusion barrier, due to the extremely low solubility of both copper and silver in the chromium at these test temperatures.

5.2 Introduction

Diffusion barriers are often required to prevent or control interdiffusion between two dissimilar materials, and therefore to retard the degradation of mechanical or electrical properties of the materials in service. The thickness of such diffusion barriers can range from nanometers to micrometers, depending on their applications. For example, in metallization processes for integrated circuit technology, most thin film diffusion barriers such as TiN and

Ti_3Si_5 are only tens of nanometers thick. Such thin films are needed to minimize the size as well as the electrical resistance of the device. In contrast, the thickness of diffusion barriers for high temperature oxidation prevention can reach tens of microns in order that these coatings be able to withstand severe environmental attack.

Three types of diffusion barriers have been categorized by Nicolet [1]: (a) stuffed barrier, (b) passive compound barriers, and (c) sacrificial barriers. Extensive investigations have been undertaken on these diffusion barriers [2-5], however, most of them emphasized the electrical or mechanical properties of the diffusion products. Diffusion-induced structural and morphological changes were studied on only a few systems. Among them, the interdiffusion behavior of the Cu/(Sn-Ni)/Au diffusion couple was studied by Pinnel and Bennet [6]. They found that above 250°C a 12.5 μm Sn-Ni layer disintegrated into fine particles and the gold and copper interdiffuse as if the Sn-Ni layer were never present. Tin rich stringers were found in the gold layer, and also at the gold surface. No mechanism for this behavior was determined. More recently, Lin et al [7] studied diffusional breakdown of a Ag diffusion barrier in a Cu-Ag-Ni diffusion couple at 760°C. The Ag barrier was breached by successive processes of Cu interdiffusion, interface instability of the Ag-Ni interface, and growth of Cu-Ni protrusions from the Ag-Ni interface to ultimately bridge the Ag barrier. Based on their experimental observations, a model of barrier breakdown was proposed by assuming Nabarro-Herring creep of Ag to accommodate protrusion growth of Cu-Ni solid solution.

High temperature diffusion barriers usually consist of passive compounds. One typical system has been investigated by Walters and Covino, Jr. [8]. They studied the effectiveness of diffusion barriers in preventing interdiffusion between a molybdenum alloy (TZM), Mo-0.5Ti-0.07Zr-0.01C, and electrodeposited platinum coatings. The diffusion barriers TiC, TiN, TaC, TiB_2, TiB_2/TiC, and TiB_2/TiN were tested at 1200°C, 1300°C, and 1400°C for 10, 5, and 2.5 hours, respectively. Of the barrier tested, TaC was found most effective as a diffusion barrier between platinum and TZM.

Another class of barrier is the sacrificial type, in which the barrier layer reacts to form a compound with one of the surrounding phases. Shueh et al [9] studied such a system with varied thicknesses of Mo layers sandwiched between Ni and Cu disks. Parabolic growth of the intermetallic phase, NiMo, was observed above 1000°C. Both Mo and NiMo layers acted as barriers for interdiffusion between Ni and Cu. The barrier started to break down once the growing NiMo phase reached the Mo-Cu interface and transformed into a Mo-rich solid solution and a Ni-Cu solid solution. Grain boundary diffusion was thought to be responsible for local breakdown of the barrier.

Of all the diffusion barriers studied, few were exposed to liquid metals. Since diffusion barriers may be attacked by liquid metal more rapidly due to the high reactivity and high diffusivity of the liquid metal, the protection time of barriers will be much shorter as compared to that of diffusion barriers attacked only by solid state solutions. Nonetheless, such a protective effect can be critical to some processes. For instance, in electronic packaging, Ag-Cu eutectic or Ag-15 wt%Cu alloys are used as brazing filler materials for attaching pins to pin-grid arrays (PGAs). During the brazing process, the liquid metal may react with the Ni thin film plated on the ceramic substrate. The extent of the reaction has to be controlled to prevent dewetting of the brazing alloy from the substrate. Chen [10] conducted experiments using 100 μm thick Ni sheet submerged in Ag-Cu eutectic liquid in order to determine the reaction rate. Tests were performed at 790°C. Growth of Cu-Ni solid solution at the solid/liquid interface was observed. Chen concluded that such growth was controlled by Cu diffusion in the liquid metal.

Transient protective coatings may find applications in liquid phase sintering (LPS) and infiltration of P/M parts to full density. In liquid phase sintering, the criteria for selecting the system has been stated in terms of phase diagram features by German and Kipphut [11, 12]. Basically, the liquid must have a high solubility for the base material, while the base should have a very low solubility for the additive (liquid former). If the solubility of the additive in the base is large, swelling may result during sintering. To enhance diffusive transport of the base material, a large melting point difference between the liquid and the base is essential. In the mean time, no high melting intermetallic compounds should form during LPS. Unfortunately, few systems meet such stringent requirements. Choosing and applying a transient coating on the base material may possibly change an unfavorable system into one suitable for LPS.

Similarly, in the process of infiltration of P/M parts, low solubility of the liquid in the part material is desirable. Otherwise, dissolution and diffusion of the material can result in erosion and slumping of the part. Protective coatings on the material may greatly improve its resistance to dissolution by liquid metal and maintain the original shape during infiltration. Little work has been performed in this direction and therefore in this paper, experimental results on a model system, Cu/Ni/Ag-Cu eutectic, where Ni thin films act as protective barriers, is reported.

5.3 Experimental Procedure

Copper sheets of 99.9 percent purity were purchased from Johnson Matthey. The thickness of the sheet was 1.27 mm, and it was cut into 10x10 mm^2 pieces for experimental

use. Ag-Cu eutectic alloy was supplied by Lucas-Milhaupt, Inc., in the form of fine powders. Initially, bright Ni was electroplated on the Cu substrates. Such electroplated Ni films were found to blister in contact with Ag-Cu eutectic liquid at 800°C for unknown reasons. Cracking of the blisters caused premature failure of the Ni films. Alternatively, an electroless Ni-P coating proved to be a better choice. The Cu substrates were activated in a palladium containing solution, rinsed and dried, and then electrolessly plated with 12 μm Ni. About 3 to 5 weight percent of phosphorus was detected in the Ni coatings. However, no effort was made to determine the influence of this small amount of phosphorus in the study. Some Cu substrates were first electroplated with 1 μm Cr, followed by an electrical Ni strike, and finally coated with 12 μm electroless Ni.

Tests were conducted in a quartz tube vacuum furnace at 800°C and 850°C, respectively. The coated Cu substrate was first put into a 5 ml alumina crucible, and a Ag-Cu eutectic powder compact, about 9.5 mm in diameter, was placed on the Cu substrate. To reduce thermal drag during cooling, only 1.5 grams of eutectic powder were used for each run. Firstly, the furnace was heated up to the test temperature, then it was placed over the crucible. A separate thermocouple contacting the crucible was used to monitor the sample temperature, which was maintained within ± 2°C of the test temperature during holding. After holding at the test temperature for various lengths of time, the quartz tube was quenched with cool, flushing air after moving the furnace away. The vacuum was kept at about $1x\ 10^{-5}$ torr for the entire testing circle.

After testing, all the samples were sectioned parallel to the diffusion path with a low speed diamond saw. Sample morphologies were examined in an optical microscope. A JEOL SUPERPROBE 733 electron microprobe (EPMA) was used to measure concentration profiles in the diffusion zone. The size of the electron beam was about one micron.

5.4 Results

5.4.1. *Samples Treated at 800°C*

Microstructural evaluation of the solid/liquid interface is shown in Figure 5.1 (a) through (d). Rippling of the Ni/Ag-Cu eutectic interface is apparent after only one minute at 800°C, as can be seen in Figure 5.1(a). Cellular like growth from the Ni protective coating into the Ag-Cu liquid can be discerned with ncreasing holding time. The cell spacing of the interfacial growth increased markedly, as depicted in Figure 5.1(b), and was maintained roughly constant thereafter (Figure 5.1(c) to (d)). Interdiffusion of Ni and Cu at the Ni/Cu

interface also can be seen from Figure 5.2, especially at the Cu grain boundaries. These grain boundaries provided fast diffusion paths for both Cu and Ni atoms. Consequently, spikes of Cu-Ni solid solution were found to grow and protrude into the grain boundaries.

Figures 5.3(a) and (b) illustrate the EPMA results of diffusion profiles across the Ni coating. After only one minute at 800°C, the Ag concentration in the liquid in front of the growing cells had risen from 72 weight percent, the eutectic composition, to over 80 weight percent; whereas a very small amount of Ni could be detected in the liquid due to the trivial solubility of Ni in Ag at 800°C. The growing cells were Cu-Ni-Ag solid solution, with about 90 weight percent Cu and roughly equal weight percentages of Ni and Ag. A 5 μm interdiffusion zone at the Ni/Cu interface can also be observed in Figure 5.3(b). At this stage, the Ni coating was almost intact although Cu had diffused across the entire coating.

Holding at 800°C for 15 minutes resulted in further growth of the Cu-Ni-Ag solid solution, as shown in Figures 5.4(a) and (b). The Ag concentration at the growth front reached 90 weight pct. Just beneath the ternary solid solution is a binary Ni-Cu solid solution. Growth of the Cu-Ni-Ag cells and diffusion of Ni into the Cu substrate consumed Ni rapidly. During this period, trapping of Ag-rich phases is also noticed from the back scattering image in Figure 5.4(a). Merging of two adjacent growing cells might lead to such trapping. The dark spots in Figure 5.4(a) were found to be Ni_3P phases. Despite the fact that all of the Ni coating had changed into either the ternary solid solution or the binary Ni-Cu solution, the Cu substrate was hardly attacked by the Ag-Cu liquid. Local breakdown was sometimes observed at the junctions where grain boundaries of the Cu substrate met the Ni barrier, as shown in Figure 5.2.

In Figure 5.5(a), concentration profiles across one of the two merged growing cells were determined. After 40 minutes holding, nearly all the Ni coating had turned into Cu-Ni-Ag ternary solid solution. The Ag concentration ahead of the cell was still 90 weight percent, as revealed in Figure 5.5(b). Samples kept at 800°C for one hour showed massive Ag attack of the Cu substrate and the formation of Ag-Cu liquid phase along Cu grain boundaries just underneath the Cu-Ni-Ag solid solution.

5.4.2. *Samples Treated at 850°C*

The growth pattern of the Cu-Ni-Ag solid solution changed from cellular to dendritic when the test temperature was increased from 800°C to 850°C. The microstructures are shown in Figure 5.6(a) through (c) after one, five and fifteen minutes holding, respectively. The growth rate of the Cu-Ni-Ag solid solution was much faster than it was at 800°C. Such high growth rates consumed Ni rapidly and the Cu substrate had been attacked after less than five minutes at the test temperature.

To improve the resistance of the surface protective layer against attack by the Ag-Cu liquid, a 1 μm thick Cr coating was plated on the Cu substrate prior to deposition of 12 μm Ni. Such a combination retarded liquid penetration significantly. Figure 5.7(a) shows the microstructure of the sample held at 850°C for 15 minutes. No penetration of Ag through the coated Cr layer was apparent. Growth of the solid phase into the Ag-Cu liquid still had some dendritic features, but with suppressed growth rate as compared to that without a Cr undercoating. Prolonged holding ultimately resulted in breakdown of the barrier, as depicted in Figure 5.7(b). Diffusion products detached and flowed into the Ag-Cu liquid, and Ag dissolved along grain boundaries of the Cu substrate, forming Ag-Cu liquid.

Figures 5.8(a) and (b) give the EPMA results on the sample shown in Figure 5.7(a). The Cr layer was intact with little interdiffusion at the Cr/Cu interface, because of extremely low mutual solubility between the two components. Ni-rich ternary solid solutions of Ni-Cr-Cu could be found next to the Cr layer. Cu in this solid solution was diffused from the Ag-Cu liquid, as can be seen from the Cu concentration profile. A Ag-rich phase, containing a substantial amount of Ni, and small amounts of Cr and Cu , was formed in front of the Ni-Cr-Cu solid solution. The phase growing into the Ag-Cu liquid was still Cu-Ni-Ag solid solution, which had a higher Ni concentration in comparison with the Cu-Ni-Ag solid solution grown at 800°C.

EPMA across the failed coatings revealed Ag transportation through the diffusion products, which is illustrated in Figures 5.9(a) and (b). Given the solubility limit of about 8 weight percent Ag in Cu and negligible solubility in both Ni and Cr at 850°C, the diffusion products were evidently all saturated with Ag.

5.5 Discussion

5.5.1. *Kinetics of Layer Growth*

A nonplanar interface developing between phases during diffusion at high temperatures is not uncommon in multicomponent diffusion systems. Non-planar growth of diffusional products has been reported in Fe-Cr-Ni [13] and Cu-Ni-Zn [14,15] systems during solid state isothermal annealing. Such phenomena also can be observed in solidification, or even during the isothermal solidification stage of the transient liquid phase (TLP) bonding process [16]. Linear perturbation theory has been applied by Wagner[17], Mullins and Sekerka[18,19], and Langer[20] to explain the morphological instability.

Experimental observations in this study showed an onset of solid/liquid instability shortly after the start of interdiffusion between the Ni barrier and the Ag-Cu liquid. Due to the extremely low solubility of Ag in Ni at the test temperature, most of the Ag was rejected ahead of the growing solid solution. The concentration of Ag or depletion of Cu at the solid/liquid interface shifts the liquid composition from the single liquid phase into a two phase region, as illustrated in Figure 5.10. In other words, the liquid in front of the expanding Cu-rich ternary solid now is undercooled. This constitutional supercooling results in cellular or dendritic growth of the solidifying phase. Several mechanisms like diffusing of Ag away from the tip (Ag rejection), diffusing of Cu from the melt to the tip (Cu diffusion), and interdiffusion at the interface of the Ni barrier and the (Cu, Ni, Ag) ternary solid solution might control this growth rate. Chen [10] suggested that Cu diffusion might be the controlling step based on microstructural analysis. Assuming either Ag rejection or Cu diffusion controlled growth, an analysis following Kutz and Fisher [21] using linear perturbation methods gave several orders of magnitude higher products of V (growth rate) and R (cell radius) than the experimental data of this study (see Appendix); whereas the results based on tracking Ni diffusion into (Cu, Ni, Ag) solid solution was found to fit the experimental data satisfactory. For example, let ξ be the thickness of the (Cu, Ni, Ag) solid solution. After time dt, the solid solution grows by $d\xi$. A mass balance of Ni requirs that:

$$\frac{y\,MW_{Ni}}{x\,MW_{Cu} + y\,MW_{Ni} + z\,MW_{Ag}}\,\rho_s\,d\xi = \frac{D_s\,(\rho_o - \rho_i)}{\xi}\,dt \qquad (1)$$

where MW_{Ni}, MW_{Ag}, and MW_{Cu} are the molecular weights of Ni, Ag and Cu, respectively. x, y and z correspond to the mole fractions of Cu, Ni, and Ag in the solid solution. ρ_s is the density of the (Cu, Ni, Ag) solid solution, ρ_o the density of bulk Ni, and ρ_i is the density of Ni at the solid/liquid interface. D_s is the interdiffusion coefficient. Since there is no diffusivity data available for diffusion in this ternary solid state alloy, the Cu-Ni interdiffusion coefficient was used in the calculation. Integrating equation (1) and neglecting ρ_i, a classic parabolic relation between the thickness of growth and time is obtained:

$$\xi = (\,44.6\,D_s\,t\,)^{1/2} \qquad (2)$$

Differentiating equation (2) gives the growth rate of the (Cu, Ni, Ag) solution:

$$V = (11.1\, D_s / t)^{1/2} \tag{3}$$

Figure 5.11 compares the calculation of equation (2) with experimental data on the thickness of interlayer growth as a function of time. The close agreement indicates that the growth of (Cu, Ni, Ag) solid solution is indeed controlled by solid state diffusion. However, the calculated growth rates at different times showed some discrepancy with the experimental results, which are depicted in Figure 5.12 as a function of cell radius. Both calculations and experiments gave the same trend of retardation of the growth rate, but initially the growth rate was nearly two times higher than the calculated number. This large difference may be explained by the concentration dependence of the diffusivity. According to Silva and Mehl [22], the interdiffusion in the Cu-Ni diffusion couple depends strongly on the copper concentration. With higher Cu concentrations, a larger diffusivity results. In fact, there is a three fold increase in diffusivity as the Cu concentration is increased from 87 weight percent to almost pure Cu. Therefore, the initial fast growth may be attributed to rapid interdiffusion between Cu and the Ni barrier. Once the (Cu, Ni, Ag) phase grows the interdiffusion coefficient decreases and hence there is a decrease of the growth rate. It is difficult to assess the influence of Ag on the interdiffusion coefficient. Nonetheless, such an effect may be neglected, given the fact that the analytical results coincided well with the experimental data.

It is interesting to note from Figure 5.1 that the radius of the growing cells increases with increasing holding time. Based on EPMA it was found that two neighboring cells merged into a single cell, trapping the liquid phase between them behind the growth front. This phenomena causes a slow down of the growth rate, and is well explained by solidification theory [23,24].

Increasing the test temperature from 800°C to 850°C leads to a two fold increase of the interdiffusion coefficient, D_s, which facilitates a higher growth rate of the ternary solid solution and brings about dendritic growth.

5.5.2. *Microstructures of the Diffusion Products*

The as plated Ni barrier was microcrystalline in nature and had a grain size approximately of 0.5 μm [25]. Heating to the test temperature resulted in precipitation of the Ni_3P intermetallic phase, which was found finely dispersed in the Ni barrier. This dispersed

phase later agglomerated behind the growing (Cu, Ni, Ag) solid. Interdiffusion between the Cu substrate and the Ni barrier caused protrusions at the interface. Enhanced diffusivity at the Cu grain boundaries accelerated the consumption of Ni with subsequent barrier breakdown. Samples with 1 μm Cr undercoating on Cu substrates showed layered phases of the diffusion products. The first was rippled (Cu, Ni, Ag) solution from the melt side. Next to it was a non-continuous layer of Ag-rich phase, and then a continuous (Ni, Cr, Cu) phase. This phase might contain some or all of the phosphorus in the Ni barrier. The last was the remains of the Cr layer. Such layered microstructures were developed due to the resistance of the Cr to both Cu and Ag diffusion. Therefore, even if the whole Ni barrier had been converted into the (Ni, Cu, Ag) solid solution, accumulation of Ag in front of the Cr layer was needed to increase its chemical potential sufficiently to penetrate the undercoating.

Once the barrier layer failed, the diffusion products began to fragment and drift into the Ag-Cu liquid. Figure 5.6(c) is a typical section showing these broken diffusion products. Severe dissolution along grain boundaries of the Cu substrate is due to the low surface energy of the Ag-Cu liquid. This dissolution produced many particles of Cu-Ag solid solution, which were saturated with Ag. As has been illustrated in Figure 5.10, the melt is enriched with Ag during the growth of the (Cu, Ni, Ag) ternary solid solution. The breakdown of the diffusion barrier causes dissolution of the Cu substrate. Thus the Ag-Cu liquid regains Cu and its composition moves back toward the eutectic composition. Further dissolution will lead to a melt saturated with Cu.

5.5.3. *Barrier Layer Breakdown*

Summarizing the experimental observations and the discussion above, a four stage model for the Ni barrier layer breakdown is proposed as follows:

Stage 1: Dissolution of Ni into Ag-Cu Eutectic Liquid

The time needed to complete this stage is very short, because solubility of Ni in the Ag-Cu eutectic liquid is quite low below 850°C. Thus, when the Ag-Cu eutectic powder compact forms liquid around the Ni barriers, the melt is immediately saturated with Ni, and diffusional growth of (Cu, Ni, Ag) starts to dominate.

Stage 2: Growth of (Cu, Ni, Ag) Solid Solution

In this stage, the ternary solid solution grows into the melt. The growth rate is several orders of magnitude lower than a prediction based on prevailing solidification theory. Instead of being controlled by solute transportation in the liquid, as required by the solidification theory, the growth of the (Cu, Ni, Ag) solid solution is determined by interdiffusion at the interface of the Ni barrier and the ternary solid solution. During early growth, the (Cu, Ni,

Ag) solid solution maintains its composition of roughly 90 weight percent of Cu, 5 weight percent Ni and 5 weight percent Ag. As the Ni barrier is depleted by the growing phase, the Ni concentration in the ternary solution eventually decreases by diffusion into the Cu substrate.

Stage 3: Local Bridge of the (Cu, Ni, Ag) to the Cu Substrate

Depletion of the Ni diffusion barrier is not uniform. Locations where grain boundaries of the Cu substrate touch the Ni barrier tend to be bridged first by the developing (Cu, Ni, Ag) solid solution. Once the bridge occurs, the diffusion barrier layer initiates breakdown. Ag diffuses from the melt, through the (Cu, Ni, Ag) solid solution and quickly saturates the Cu-Ni solid solution. The diffusing Ag penetrates and forms Ag-Cu liquid along Cu grain boundaries.

Stage 4: Total Penetration of the Barrier Layer

Finally the whole Ni barrier is consumed. Now the surface of the Cu substrate is heavily dissolved and the (Cu, Ni, Ag) ternary solids begin to break up and float into the Ag-Cu melt. A schematic drawing of sequential breakdown of the Ni diffusion barrier is presented in Figure 5.13.

5.6 Conclusions

1. The breakdown of a Ni diffusion barrier between a Cu substrate and the Ag-Cu eutectic liquid is due to growth of a (Cu, Ni, Ag) ternary solid solution, which consumes the Ni barrier and allows Ag diffusion through the (Cu, Ni, Ag) solid phase. Ag diffusion causes dissolution of the Cu substrate.
2. Both cellular and dendritic growth of the (Cu, Ni, Ag) solid solution have been observed. The morphological instability is explained by constitutional supercooling.
3. The growth of the (Cu, Ni, Ag) solid solution into liquid Ag-Cu melts is controlled by interdiffusion at the Ni diffusion barrier and the (Cu, Ni, Ag) interface.
4. Thin layer of Cr undercoating on the Cu substrates has been found to effectively retard both Ag and Cu diffusion, and increases the life time of the Ni diffusion barrier significantly in contacting liquid Ag-Cu melts at 850°C.

5.7 Acknowledgments

Support for this work was provided by the National Science Foundation, under grant No. DMR-9301444.

5.8 References

1. M. A. Nicolet: *Thin Solid Films*, 1978, vol. 52, pp. 415-443.

2. S. G. Young and G. R. Zellars: *Thin Solid Films*, 1978, vol. 53, pp. 241-250.

3. H. Kotake, Y. Oana, and I. Wantanabe: *Thin Solid Films*, 1981, vol. 75, pp. 247-252.

4. S. Kanamori and T. Matzumoto: *Thin Solid Films*, 1983, vol. 110, pp. 205-213.

5. W. D. Nix, *Metall. Trans.*, A, 1989, vol. 20A, pp. 2217-2245.

6. M. R. Pinnel and J. E. Bennett, *Metall. Trans.*, A, 1980, vol. 11A, pp.587-595.

7. C. S. Lin, R. A. Rapp, and J. P. Hirth, *Metall. Trans.*, A, 1986, vol. 17A, pp.933-944.

8. R. P. Walters and B. S. Covino, Jr., *Metall. Trans.*, A, 1988, vol. 19A, pp. 2163-2170.

9. Y. Shueh , J. P. Hirth, and R. A. Rapp, *Metall. Trans.* A, 1991, vol. 22A, pp. 1501-1510.

10. S. W. Chen, *Materials Chemistry and Physics*, 1993, vol. 33, pp. 271-276.

11. R. M. German, "The Use of Phase Diagrams in Predicting Sintering Behavior", Annual Powder Metallurgy Conference Proceedings, Boston, May, 1986, pp.235-247.

12. C. M. Kipphut and R. M. German, *Science of Sintering*, 1988, vol. 20(1), pp. 31-41.

13 J. S. Kirkaldy and D. G. Fedak, *Trans. AIME*, 1962, vol. 224, pp. 490-494.

14. C. W. Taylor, M. A. Dayananda, and R. E. Grace, *Metall. Trans.*, 1970, vol. 1, pp. 127-131.

15. R. D. Sisson, Jr. and M. A. Dayananda, *Metall. Tranns.*, 1972, vol. 3, pp. 647-652.

16. W.D.MacDonald, "Kinetics of Transient liquid Phase Bonding", Ph.D. Thesis, 1993, MIT.

17. C. Wagner, *J. Electrochem. Soc.*, 1956, vol. 103, pp. 571-580.

18. W. W. Mullins and R. F. Sekerka, *J. Appl. Phys.*, 1964, vol. 35, pp. 444-451.

19. R. F. Sekerka, *J. Appl. Phys.*, 1965, vol. 36, pp. 264-268.

20. J. S. Langer and H. Müller-Krumbhaar, *Journal of Crystal Growth*, 1977, vol. 42, pp. 11.

21. W. Kurz and D. J. Fisher, *Acta Metallurgica*, 1981, vol. 29, pp. 11.

22. Luiz C.Correa da Silva and Robert F. Mehl, *AIME. Trans.*, 1951, vol. 191, pp. 155-173.

23. M. C.Flemings, Solidfication Processing, 1974, McGraw-Hill, pp. 58-77.

24. W. Kurz and D. J. Fisher, Fundamentals of Solidification, 1989, third edition, Trans Tech Publications, pp. 245-255.

25. W. Riedel, Electroless Nickel Plating, 1991, Finishing Publications Ltd. and ASM, pp. 38-175.

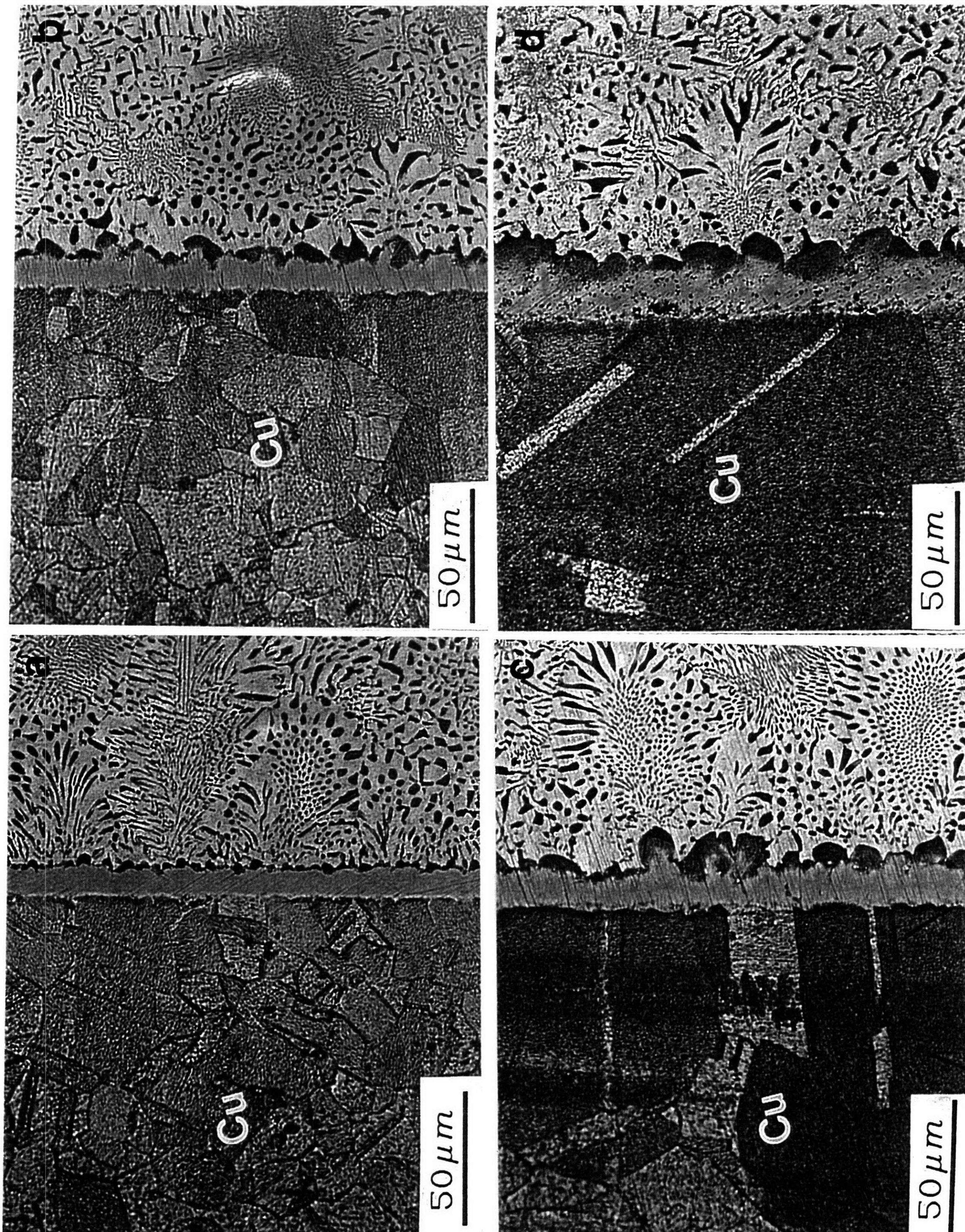

Figure 5. 1. Microstructural evaluation at the solid/liquid interface at 800°C for (a) 1 minute, (b) 8 minutes, (c) 15 minutes, and (d) 40 minutes. The growing phase is (Cu, Ni, Ag) ternary solid solution.

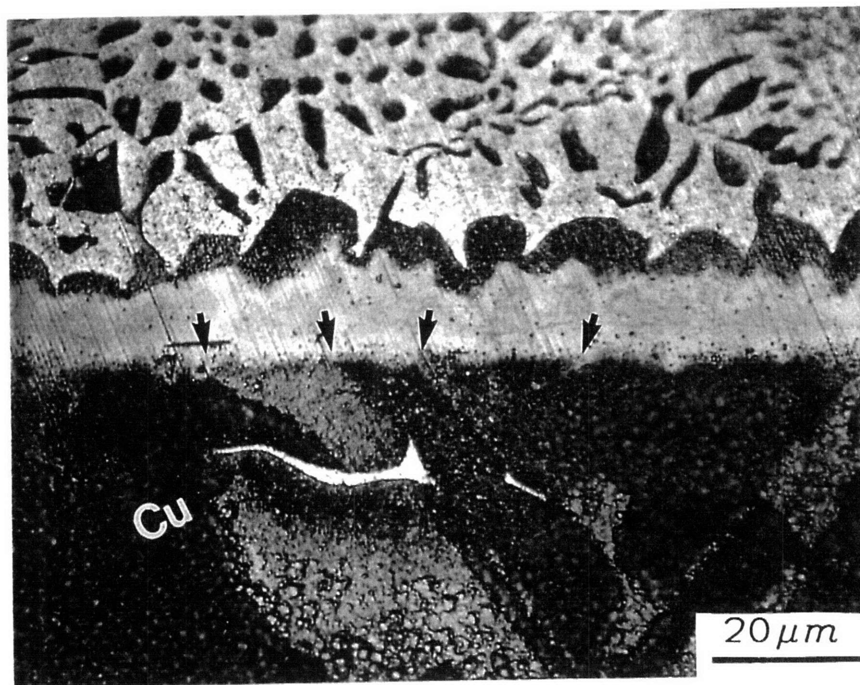

Figure 5.2. Fast interdiffusion between Ni and Cu at grain boundaries of the Cu substrate caused local breakdown of the Ni diffusion barrier. Ag diffused across the (Cu, Ni, Ag) ternary solid solution and penetrated along Cu grain boundaries, forming Ag-Cu liquid. The arrows show the fast diffusion paths. The sample was plated with 12 μm Ni and treated at 800°C for 15 minutes.

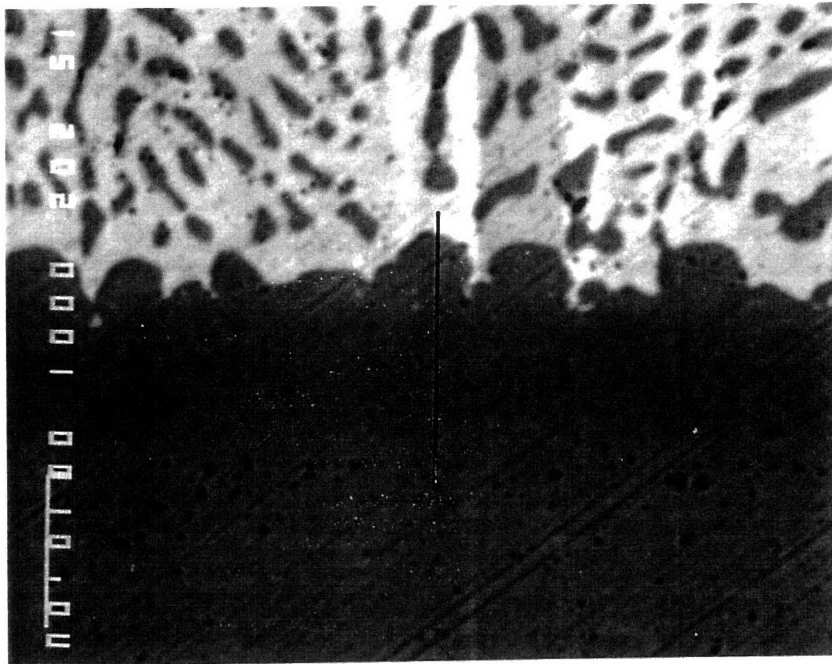

(a)

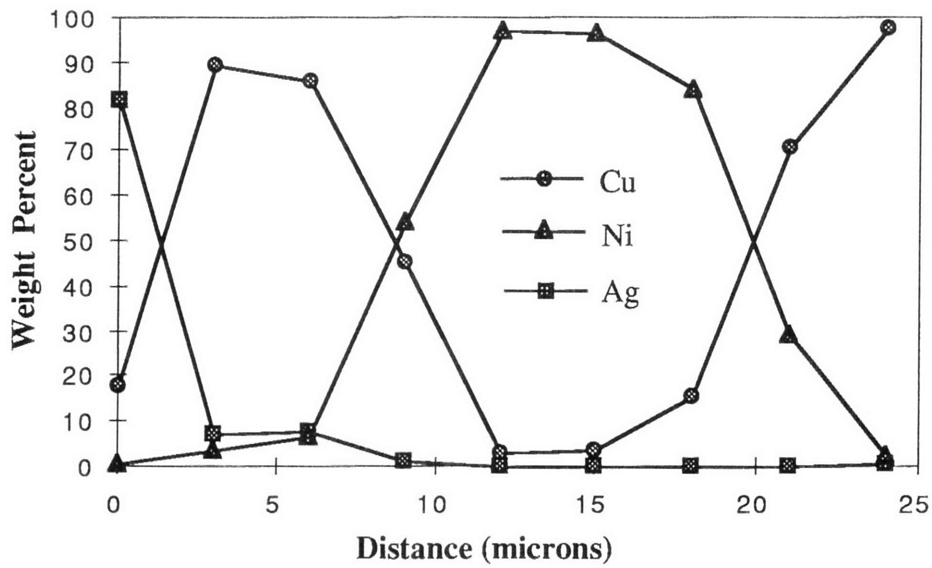

(b)

Figure 5.3. Electron microprobe analysis on the sample tested at 800°C for one minute. (a) back scattering image, the solid line indicates the analysis path., (b) concentration profile.

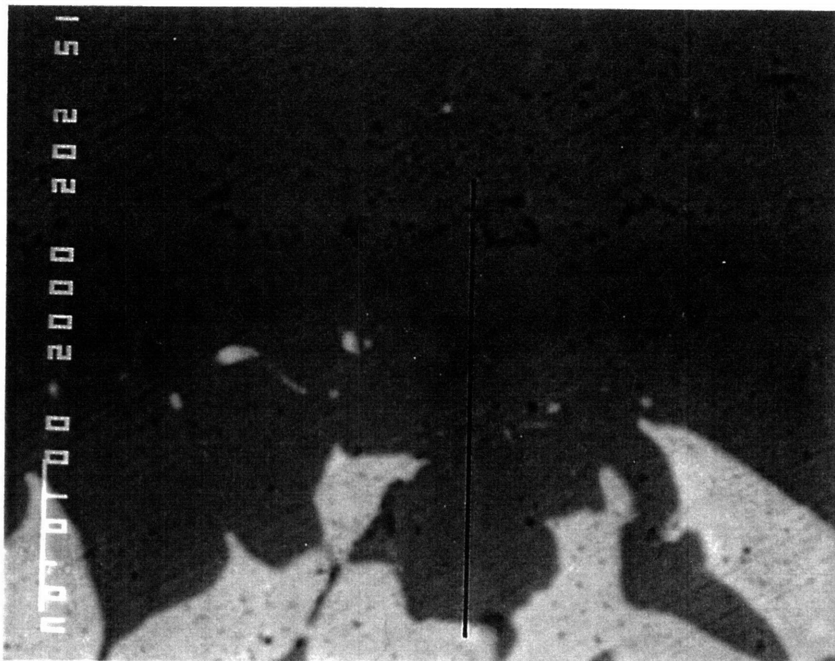

(a)

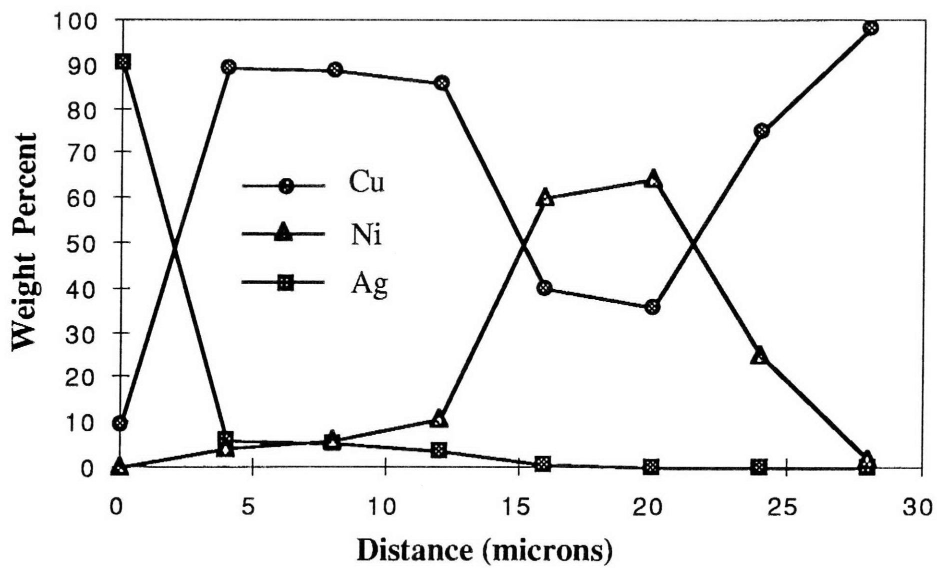

(b)

Figure 5.4. Electron microprobe analysis on the sample tested at 800°C for fifteen minutes. (a) back scattering image, the solid line indicates the analysis path, (b) concentration profile.

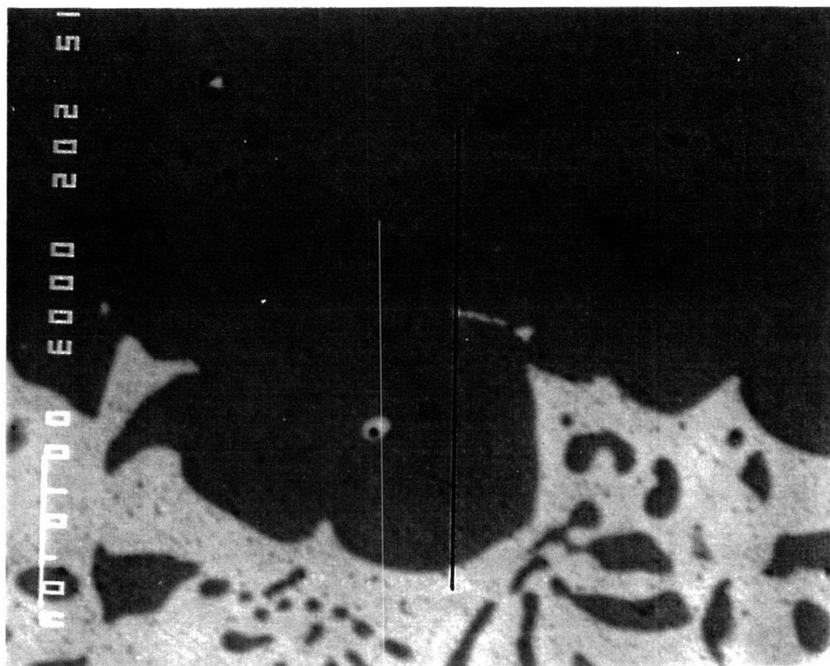

(a)

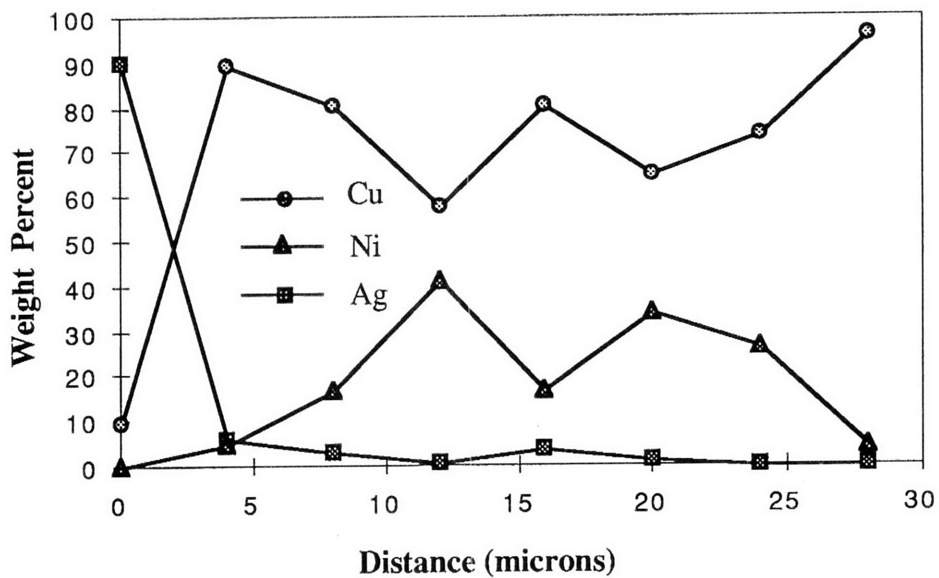

(b)

Figure 5.5. Electron microprobe analysis on the sample tested at 800°C for forty minutes. (a) back scattering image, the solid line indicates the analysis path, (b) concentration profile.

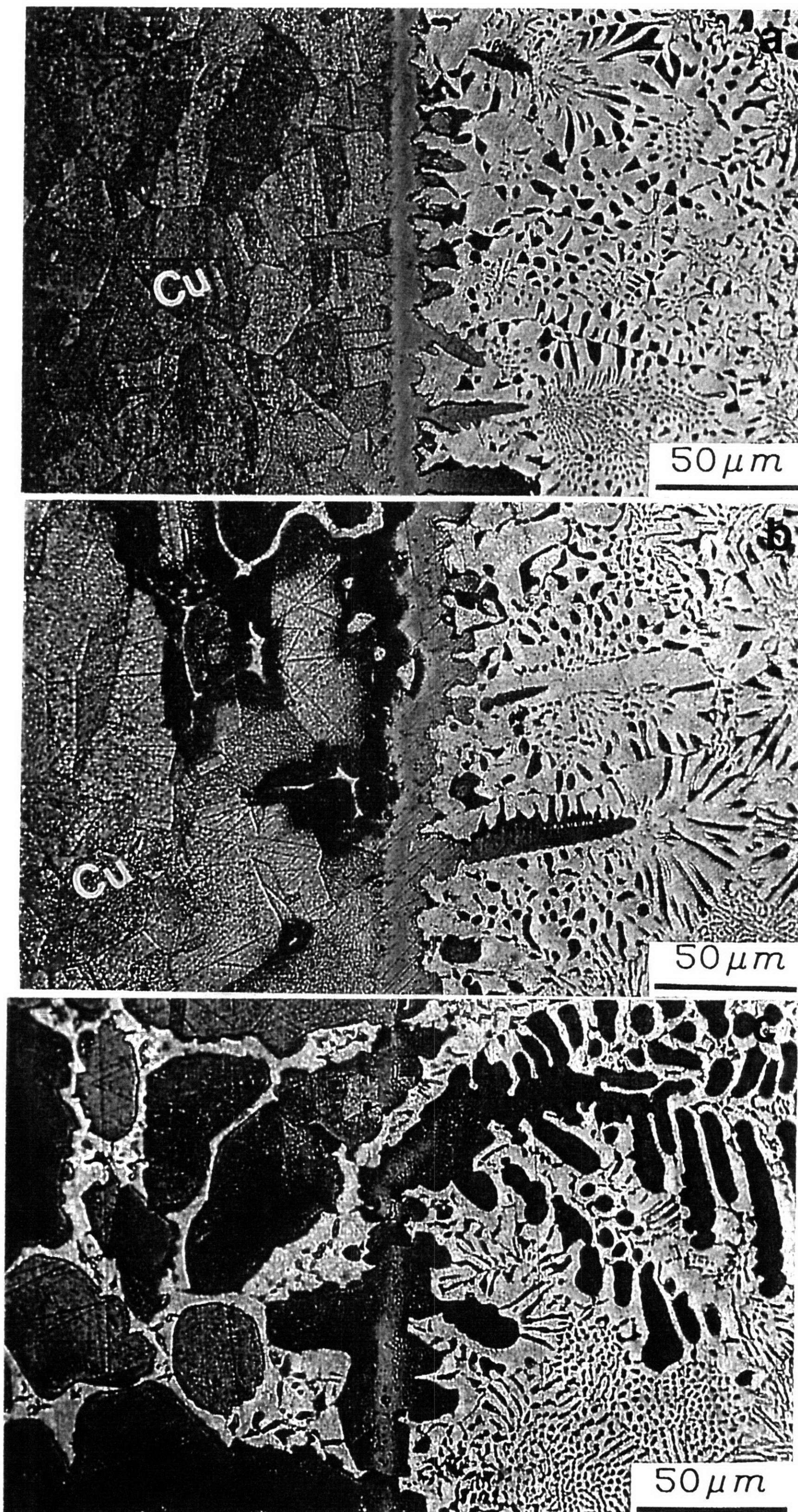

Figure 5.6. Microstructures of the samples with 12 μm Ni plating and soaked in Ag-Cu eutectic liquid at 850°C for (a) 1minute, (b) 5 minutes, and (c) 15 minutes.

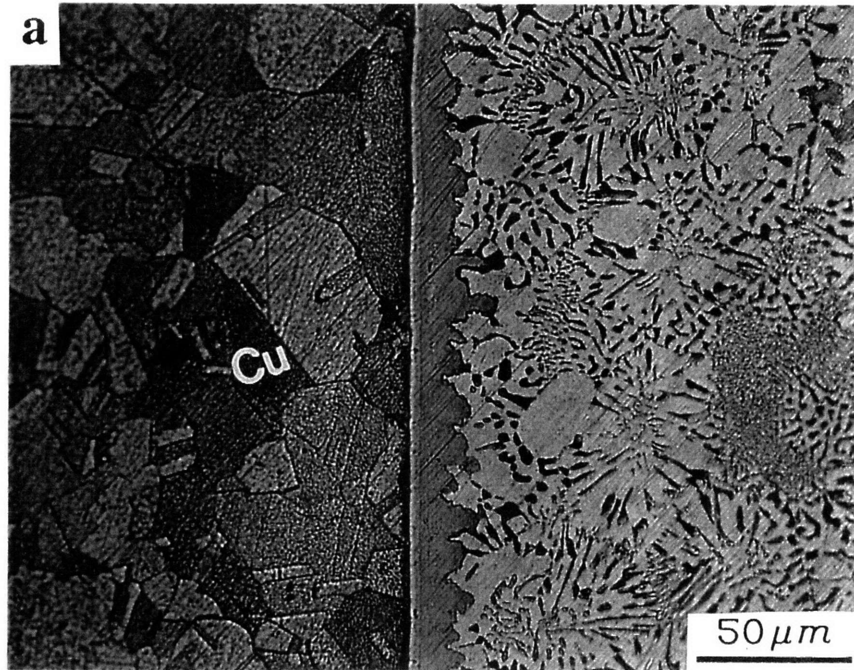

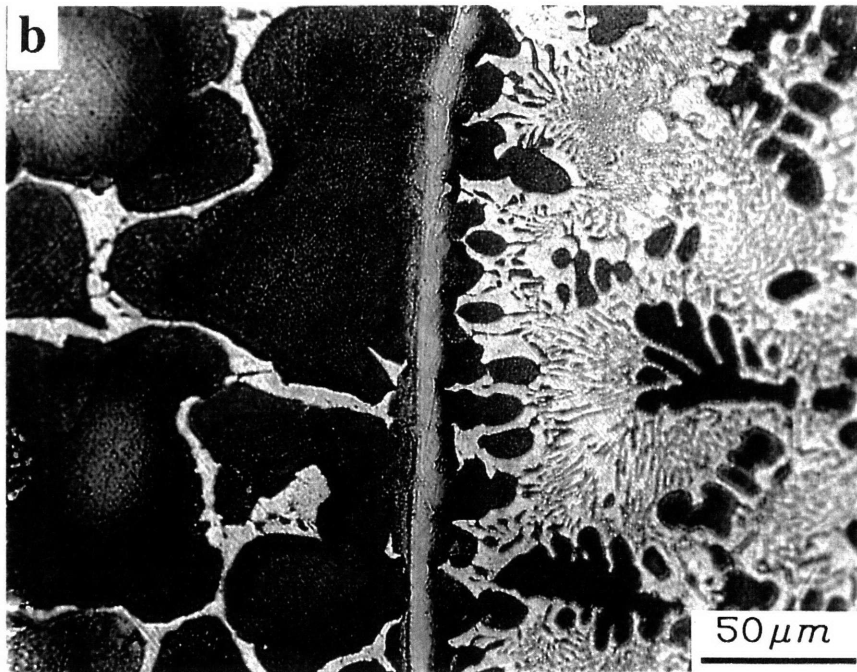

Figure 5.7. Microstructures of the samples with 1μm Cr undercoating prior to 12μm Ni deposition. They were soaked in Ag-Cu eutectic liquid at 850°C for (a) 15 minutes and (b) 40 minutes, respectively.

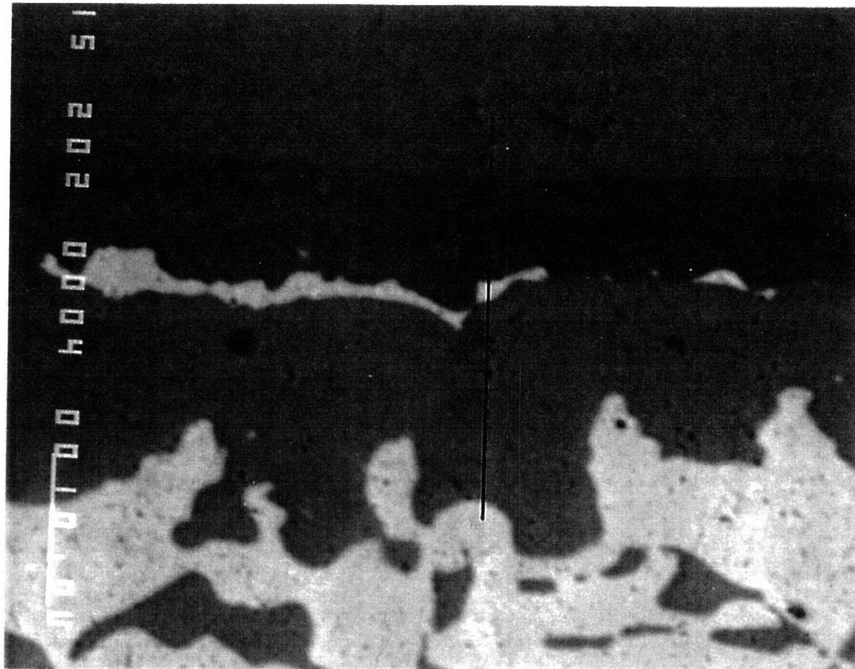

(a)

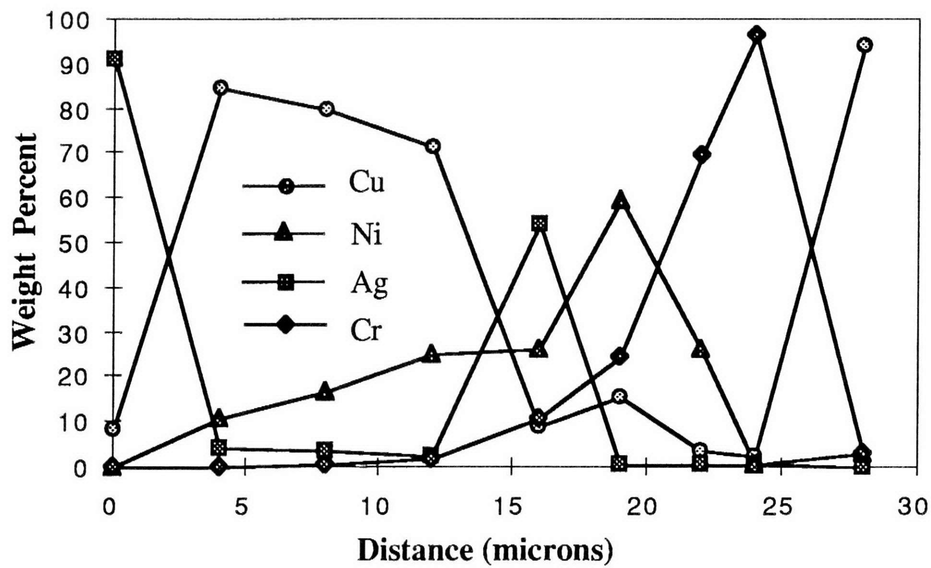

(b)

Figure 5.8. Electron microprobe analysis on the sample with 1 μm Cr undercoating on the Cu substrate. The sample was soaked at 850°C for fifteen minutes. (a) back scattering image, the solid line indicates the analysis path, (b) concentration profile.

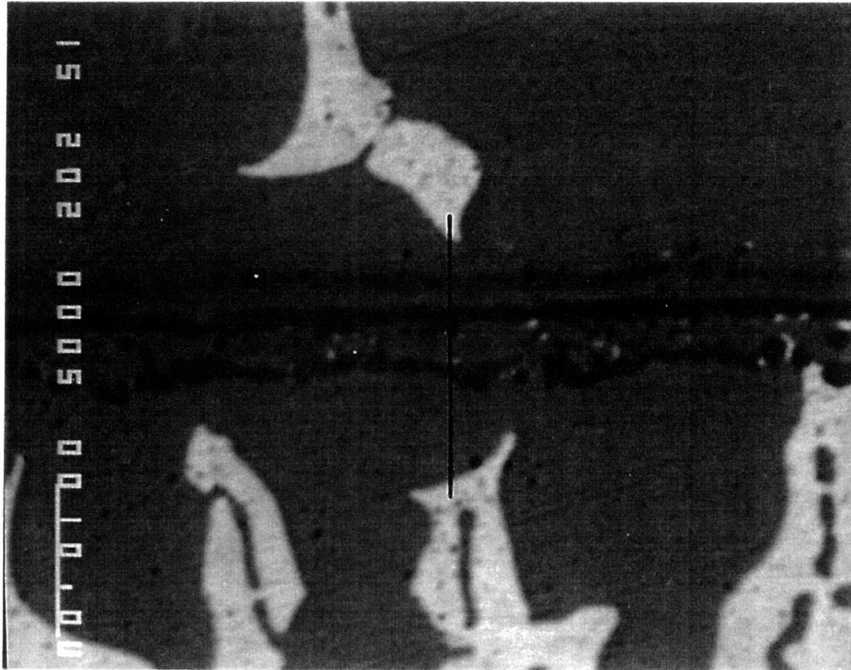

(a)

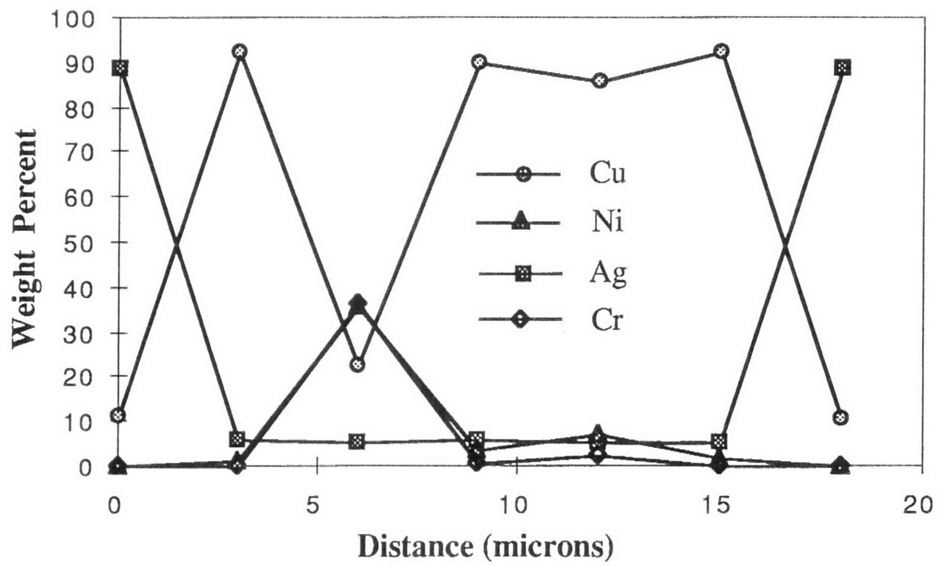

(b)

Figure 5.9. Electron microprobe analysis on the sample with 1 μm Cr undercoating on the Cu substrate. The sample was soaked at 850°C for forty minutes. (a) back scattering image, the solid line indicates the analysis path, (b) concentration profile.

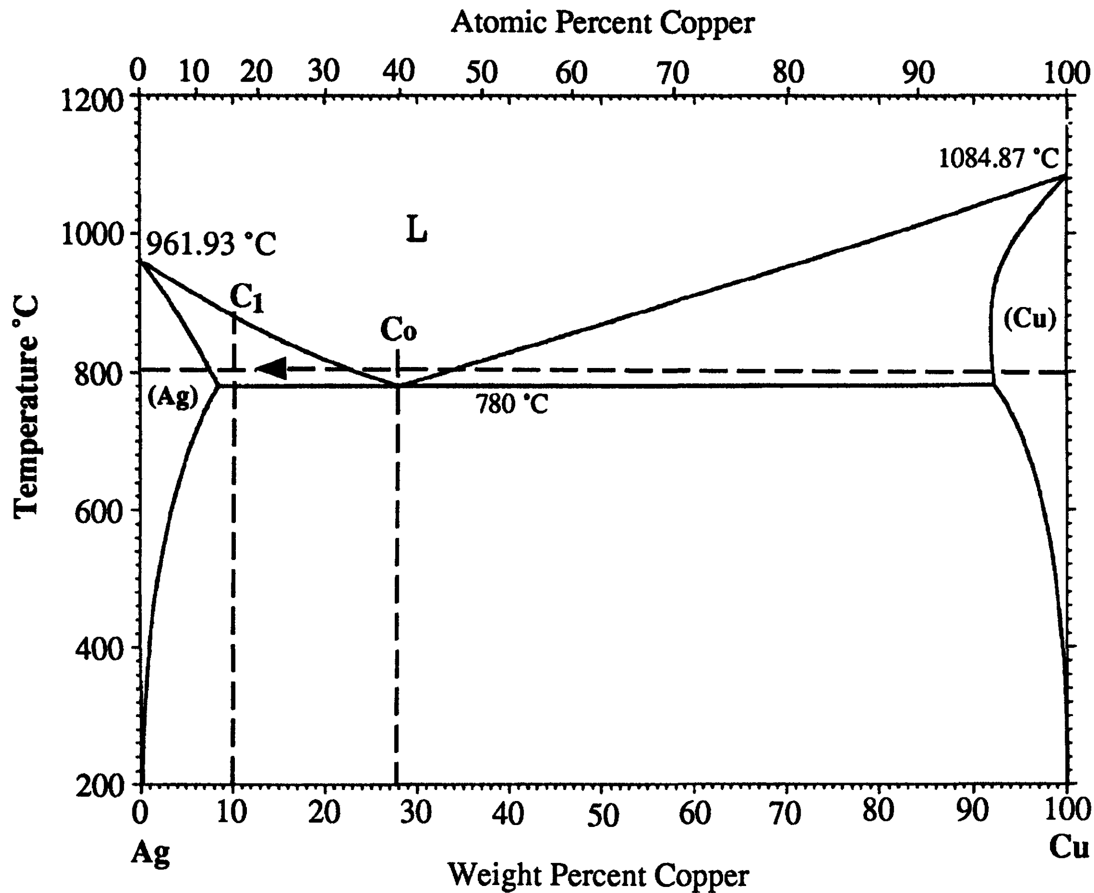

Figure 5.10. Copper-silver binary phase diagram. Co indicates the original eutectic composition of the liquid. At 800 °C, growth of (Cu, Ni, Ag) solid solution depletes Cu in the liquid. Thus the liquid composition ahead of the growing phase moves toward two phase region as illustrated by the arrow in the diagram, which causes interface instablity of the growing front. C1 is the composition detected by EPMA.

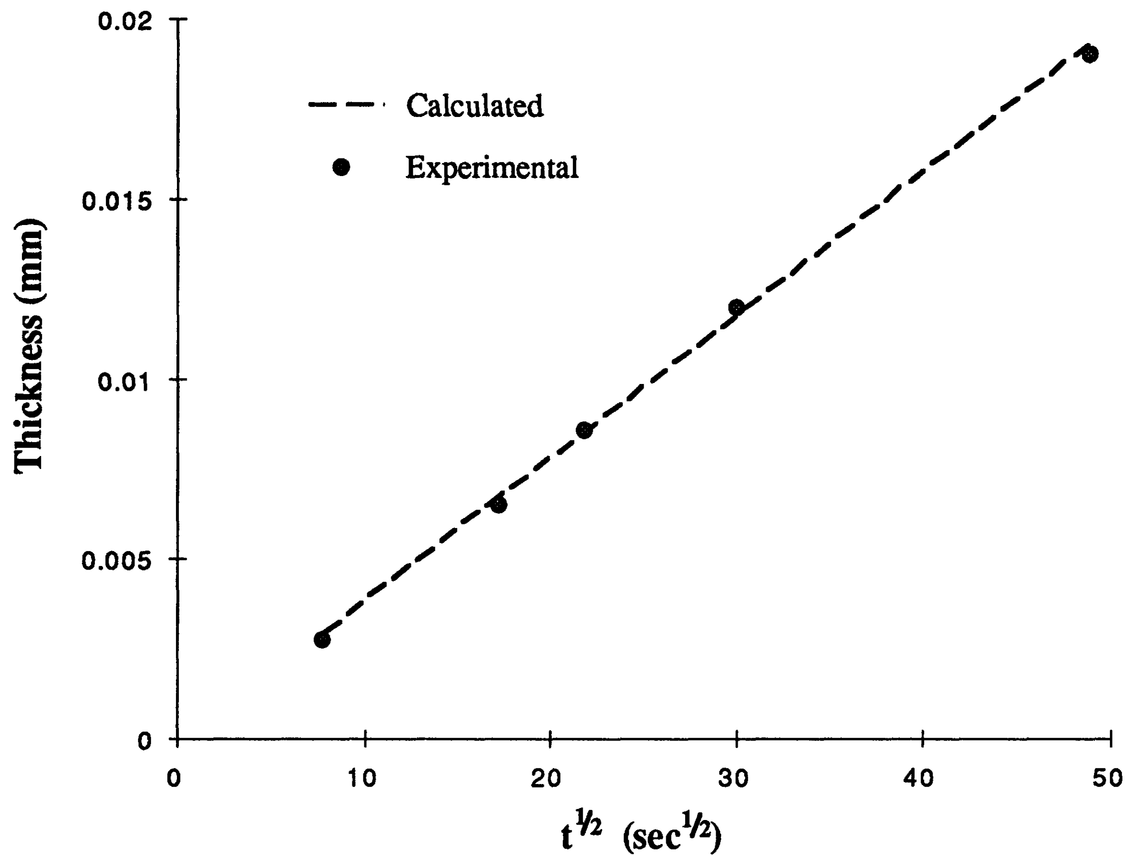

Figure 5.11. The thicknessof the growing (Cu, Ni, Ag) solid solution as a function of square root of time. The tests were performed at 800°C. The dotted line is according to equation (2), with an interdiffusion coefficient of 3.5×10^{-11} cm^2/sec.

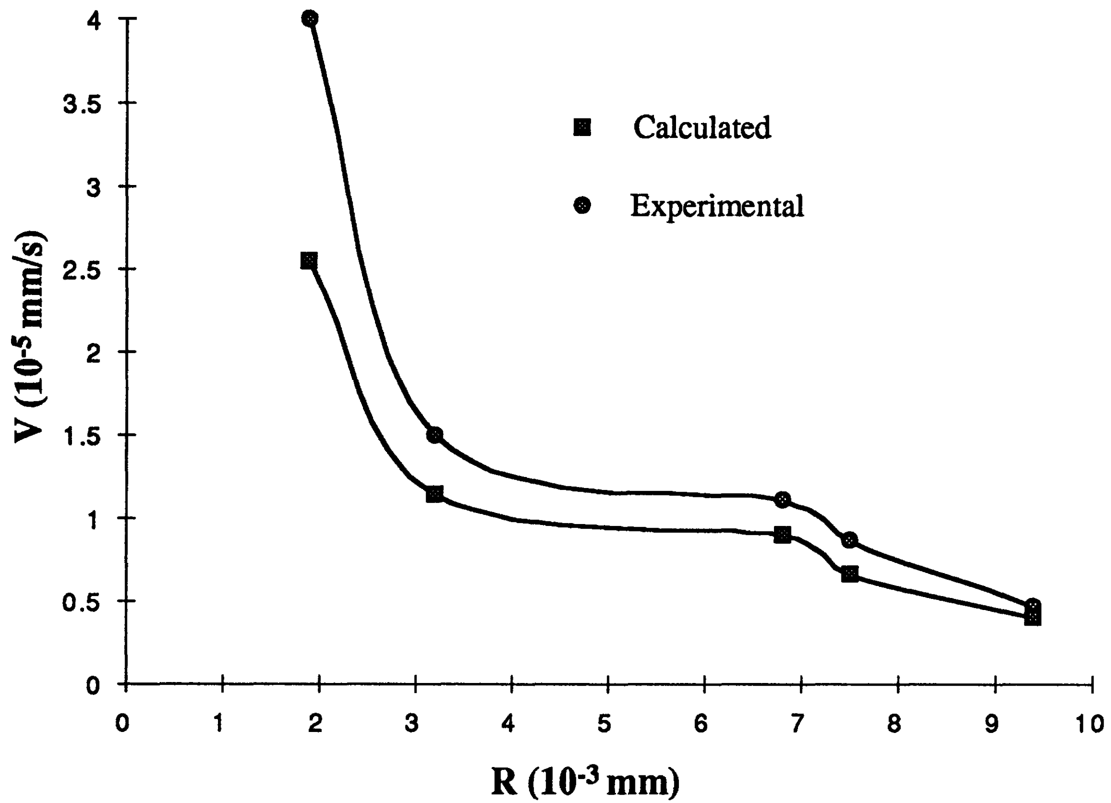

Figure 5.12. The relation between the growth rate V of the ternary (Cu, Ni, Ag) solid solution and R, the average cell radius at 800°C. The calculation is based on equation (3) with an interdiffusion coefficient 3.5×10^{-11} cm^2/sec.

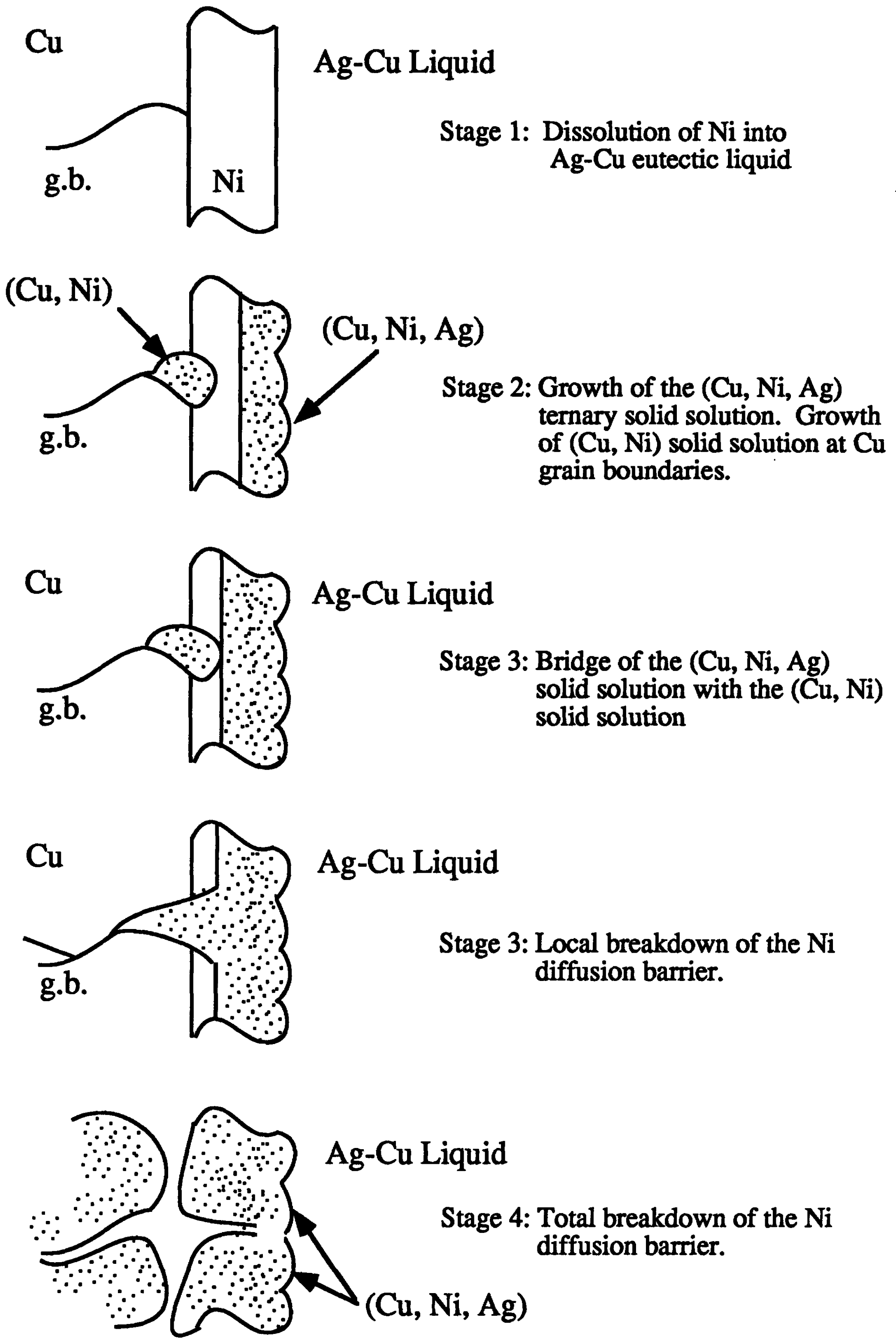

Figure 5.13. Schematic drawing of the four stage sequential breakdown of the Ni diffusion barrier between the Cu substrate and the Ag-Cu eutectic liquid.

TRANSIENT LIQUID PHASE (TLP) BONDING USING COATED METAL POWDERS

6.1 Abstract

Powder particles coated with a small amount of melting point depressant (MPD) reveal different sintering behavior in comparison to a powder mixture with the same composition. Interlayers consisting of the coated powder particles were used in the transient liquid phase (TLP) bonding process. The coating material and the thickness of the deposit are important parameters which influence shrinkage. The amount of MPDs was controlled such that the volume fraction of the liquid was very small, but existed at all contacts, thus improving densification of the interlayer. Ni-20Cr and 304L stainless steel powders coated with Ni-10P were applied to join 304 stainless steels. Fully dense joints with mechanical properties comparable to those of the base metals were obtained with Ni-20Cr powder interlayers, whereas joints with 304L stainless steel powder interlayers showed inferior mechanical properties due to residual porosity in the joints.

6.2 Introduction

The transient liquid phase (TLP) bonding process offers a unique way to join materials with high strength and ductility[1-3]. In this process, a layer of melting point depressant (MPD) is placed between the faying surfaces. The MPD forms a liquid layer at the bonding temperature and eventually diffuses into the base material and causes the joint to solidify. The kinetics of the process is controlled by solid state diffusion of the MPD into the base material to be joined. The TLP bonding process can be divided into four stages, namely, dissolution, liquid widening, isothermal solidification and homogenization, as described by Tuah-Poku et al.[4]. Probably the first report on TLP bonding process is by Lynch et al.[5], who prepared interface free titanium joints using a nickel-copper interlayer. A series of micrographs in their paper showed the progressive dissolution of the

interlayer and the eventual formation of a joint that was "effectively just a grain boundary". Following this work, the TLP process has been applied successfully to a number of material systems. One fruitful such application is in the aerospace industry. Hoppin and Berry[6] working at the Aircraft Engine Group at General Electric developed Activated Diffusion Bonding for joining superalloys such as René 80. The Nor-Ti-Bond process, described by Wu[7], was developed at Northrop by Wells and Mikus[8, 9] to join titanium structures. At Pratt and Whitney, Duvall et al[10] joined superalloy Udimet 700 using a Ni-Co interlayer and a process patented by Owczarski et al.[10]. Ni-B eutectic was also used as the MPD for joining a similar alloy[12]. Niemann and Garrett[13, 14] of MacDonald Douglas, developed Eutectic Bonding for joining boron fiber reinforced aluminum matrix composites with a copper interlayer. Titanium-aluminum joints were made in a similar way. Liquid Interface Diffusion (LID) bonding was developed at Rohr Industries to bond honeycomb sandwich structures using copper-nickel interlayers[15].

Despite the success of the TLP process in producing quality joints for a variety of materials, its use is restricted to small clearance joints (within tens of microns) in order to avoid intermetallic compound formation and/or unacceptably long isothermal solidification times. The time for isothermal solidification of a TLP joint can be expressed as[4]:

$$t_{is} = \left(\frac{C_i}{C_L}\right)^2 \frac{W_o^2}{16\beta^2 D_s} \qquad (1)$$

where W_O is the initial thickness of the filler metal, C_i is the initial MPD concentration in the filler metal, and C_L the saturation concentration of the MPD in the liquid. D_S is the diffusivity of the MPD in the base metal, and β is a dimensionless parameter determined by the solidus and liquidus compositions at the bonding temperature. It is apparent that thinner filler materials require much less time for solidification.

In order to apply the TLP bonding process to large gap joints (100 μm and above), which is frequently required in manufacturing, several efforts have been made. Interlayers with mixtures of base powders and MPDs were studied by Nakao et al.[16] and MacDonald et al[17]. Infiltration of liquid MPDs into the base metal powder interlayers was also investigated previously by the present authors [18, 19]. Nakao used a 250 μm thick IN-100 powder sheet and a 44 μm thick filler metal MBF-80 (Ni-15Cr-4B) to join superalloy MM007. It was found that the time for isothermal solidification can be reduced more than two orders of magnitude as compared with the joint without the powder sheet.

MacDonald applied interlayers consisting of mixtures of titanium and Ti-15Cu-15Ni powders to join Ti-6Al-4V. In order to eliminate the residual pores in the interlayer, a relatively large amount of MPD (Ti-15Cu-15Ni) has to be used (> 30 vol.%). Unfortunately, the resulting joints showed impaired mechanical properties due to excessive brittle intermetallic phases such as Ti_2Cu and TiNi. The present authors found that infiltrating the powder interlayer of the base metal with MPD was capable of producing fully dense joints while allowing much less usage of the MPD (see Chapter 2 and Chapter 4). Large gap copper joints were successfully made by infiltrating a copper powder interlayer with Ag-Cu eutectic alloy. However, the infiltration process is difficult to apply to material systems where there is a strong interaction between the powder particles and the liquid. The fast kinetics of chemical reaction can easily block the paths for infiltration as in the case of joining titanium. Also, the process parameters have to be controlled carefully to produce mechanically sound joints.

In this paper, metal particles coated with MPDs are used as interlayers for large gap TLP bonding. The amount of MPD is controlled by the coating thickness. In contrast to localized shrinkage induced by the liquid in the case of mixed powder interlayers, which usually needs more than thirty volume percent of liquid to fully densify the joint, full densification is obtainable with much less MPD for the coated powder interlayers, since the liquid is present at all powder-powder contact points which leads to uniform shrinkage of the interlayer. Decreasing the amount of MPDs in the joint allows much shorter isothermal solidification time, and makes it possible to produce strong and tough large gap joints. Meanwhile, the coated powders can be used just like homogeneous particles, greatly simplifying the joining procedure. In this study, Ni-20Cr and 304L stainless steel powders with Ni-10P coatings were studied to join 304 stainless steels. Mechanical properties of the resulting joints were also evaluated.

6.3 Experimental Procedure

Commercial Ni-20Cr and 304L stainless steel powders with particle sizes less than 44 microns (-325 mesh) were used. Figure 6.1 shows the general features of the powders. They were activated in a palladium containing solution and electrolessly coated with Ni-10P in an aqueous solution. The phosphorus content was maintained by adjusting the pH value of the solution[20]. The coated powders were rinsed and dried. The amount of the deposit was determined by the weight gain of the powders.

Powder compacts of 10 mm diameter were made in a cylindrical die. The compression pressure was 350 MPa. The finished compacts were ready to be used as interlayers to join 304 stainless steels.

Joining was performed in a resistance-heated vacuum furnace with vacuum level better than $3x10^{-5}$ torr. Three joining temperatures 1000°C, 1055°C and 1100°C were chosen to make the joints. The average heating rate was determined to be about 20°C/minute. At the bonding temperature, a compressive pressure of 0.29 MPa (41 psi) was applied to the joint. Butt joints for tensile tests were prepared in the same furnace. All the samples were air cooled to room temperature after joining with no further heat treatment.

After bonding, the joints were cut and polished for metallurgical examination in an optical microscope. Tensile tests of the joints were performed on an Instron test machine at room temperature, and the fracture surfaces were observed under SEM.

6.4 Results and Discussion

6.4.1 *Microstructures*

Figure 6.2 shows the features of coated Ni-20Cr and 304L stainless steel powders. 16 wt% and 16.3 wt% Ni-10P were deposited for the powders illustrated in Figure 6.1, respectively. The corresponding overall phosphorus content in the interlayers made of these coated powders was about 1.6 wt%. Phosphorus content from 0.7 wt% to 2.3 wt% was used to produce the joints. The microstructure of a joint with 3.8 mm thick Ni-20Cr powder interlayer is shown in Figure 6.3. The powder interlayer had fully densified after soaking at 1000°C for one hour. Almost no liquid remanants can be detected in the microstructure, indicating complete solidification of the joint. Some phosphides can be seen at the grain boundaries as well as in the grains due to the phosphorus in the joint. Heat treating to achieve diffusion of phosphorus into the base metal (SS304) is difficult, because of the large joint clearance, and hence the long diffusion distance.

A quite different microstructure was observed for the joints using 304L stainless steel powder interlayers, as illustrated in Figure 6.4. After one hour holding at 1000°C, the powder interlayer exhibits uniformly distributed, fine phosphides. However, many residual pores can be found in the joint. The distribution of the pores in Figure 6.4

suggests localized shrinkage of the particles in the interlayer. Firstly, it was suspected that poor wetting between the liquid and the base powder particles might be the cause, since surface oxides of the particles may retard wetting. To verify this, sessile drop tests were performed using compacted Ni-20Cr and 304L stainless steel powder substrates. Good wetting and flow of Ni-10P on both substrates were observed in vacuum at 1000°C, therefore excluding the possible wetting problem. The partial liquidus projection of the ternary Ni-Fe-P system is given in Figure 6.5[21], which indicates an increase of the liquidus temperature as Fe is introduced into the Ni-10P coating. Figure 6.6 shows a vertical section of the ternary system with varying phosphorus contents[21]. Interdiffusion between the Ni-10P coating and the 304L stainless steel powders during heating may increase the liquid incipient temperature. Thus at the joining temperature, the liquid amount can be effectively reduced due to the diluted phosphorus concentration, as can be seen in Figure 6.6. Furthermore, since both nickel and phosphorus are soluble in the 304L stainless steel powders at the joining temperature, the liquid may disappear well before the powder particles can rearrange themselves and reach maximum shrinkage. As a result, a large number of residual pores remain in the interlayer. Elimination of such pores depends on further solid state sintering. In contrast, since phosphorus is almost insoluble in Ni-20Cr powders, the liquid lasts much longer and fully dense joints can be produced. Increasing the joining temperature may help to increase the liquid amount and reduce pores in these stainless steel powder interlayers. However, such a beneficial effect may be offset by accelerated diffusion kinetics, which consumes the liquid more rapidly at the higher joining temperature. Indeed, this was observed in tensile testing where the tensile strength of the joints with 304L stainless steel powder interlayers showed no significant increase as the joining temperature was increased from 1000°C to 1100°C.

6.4.2 *Mechanical Properties*

Figure 6.7 shows a typical as bonded tensile test sample. The interlayer contained 1.6 wt%P and was bonded at 1000°C for one hour. Bulging of the powder interlayer can be seen in Figure 6.7 because of the compressive load at the joining temperature. All the test samples were found to break in the interlayers. Considerable plastic deformation of the base metal is apparent during tensile testing when Ni-20Cr powder interlayers were used, as shown in Figure 6.8. Figures 6.9 and 6.10 reveal the fracture surface of the sample shown in Figure 6.8. The tensile strength as well as strain were found to vary with the interlayer thickness, which is illustrated in Figure 6.11. When the interlayer thickness exceeds 1 mm, the tensile strength of the joint approaches that of the base metal. The

strength of the joints with thinner interlayer thickness was not consistent in current experiments. One sample with 0.3 mm clearance was found to fail at the interlayer/base metal interface with about one third of the area unbonded. This could be caused by improper alignment of the sample during joining.

Interlayers of stainless steel powders exhibited lower strength and the strength decreased with increasing interlayer thickness, as depicted in Figure 6.12. Obviously residual pores impair the strength of these joints. More Ni-10P deposits on the 304L stainless steel powders will produce more liquid at the bonding temperature. Nonetheless, this showed no improvement on the tensile strength, as can be seen from Figure 6.13. This may be caused by the trade-off between the amount of liquid and the amount of intermetallic compounds. Increasing the joining temperature improved tensile strength and strain, as shown in Figure 6.14. However, the effect is more likely due to solid state sintering of the interlayers rather than the increased amount of liquid, since the tensile strain showed better improvement than the tensile strength as the bonding temperature was raised.

6.5 Conclusions

Transient liquid phase bonding using coated metal powder interlayers was investigated. Ni-20Cr and 304L stainless steel powders coated with Ni-10P melting point depressants were used as the interlayers to produce large gap joints. Based on the microstructures and tensile properties of the joints made, the following results were obtained:

1). A thick TLP joint can be produced by applying a powder interlayer with its individual particles coated with a layer of MPD. Such configuration provides a way of using less MPD for a thick TLP joint. Uniform shrinkage of the interlayer due to liquid existing at all powder-powder contacts at the bonding temperature can lead to a fully dense, mechanically sound joint.

2). Tensile strength close to the base metal (SS304) strength is obtained by using powder interlayers of Ni-20Cr coated with 16 wt% Ni-10P. Joints fail in the powder interlayers due to phosphides formed in the joints. A considerable amount of plastic deformation is observed before joint failure. Microstructural examination reveals full density of the interlayer.

3). Residual pores exist in the 304L stainless steel powder interlayers after joining, which degrades the mechanical properties of the joints. The tensile strength decreased with

increasing joint clearance and phosphorus content. Increasing the joining temperature improved mechanical properties due to enhanced solid state sintering.
4). Interlayers with MPD coated powder particles can produce TLP joints of virtually any thickness. However, successful joints depend upon careful considerations of the combination of the MPD with the powder particles, such as interdiffusion, reaction and solubility effects.

6.6 Acknowledgments

The author wish to thank National Science Foundation (NSF) for supporting this research under contract number DMR 9301444.

6.7 References

1. W. D. MacDonald and T. W. Eagar, 1991. Transient liquid phase bonding process, Proc. TMS Symposium on The Metal Science of Joining; pp. 93-100.

2. W. D. MacDonald and T. W. Eagar, 1992. Transient liquid phase bonding, Annual Reviews of Materials Science 22; pp. 23-46.

3. Y. Nakao, K. Nishimoto, K. Shinozaki, C. Kang, and H. Shigeta, 1991. *Quarterly Journal of the Japan Welding Society,* 9, (4), pp. 550-555.

4. I. Tuah-Poku, M. Dollar, and T. B. Massalski, 1988. A study of the transient liquid phase bonding process applied to a Ag/Cu/Ag sandwich joint", *Metall. Trans.*, 19A (3), pp. 675-686.

5. J. F. Lynch, et al., 1959. Brazing by the diffusion-controlled formation of a liquid intermediate phase, *Journal of the American Welding Society*, February, pp. 85-s to 89-s.

6. G.S. Hoppin III and T.F. Berry, 1970. Activated diffusion bonding, *Welding Journal,* 49 (1), pp. 505-s to 509-s.

7. K. C. Wu, 1971. Resistance NOR-Ti-BOND joining of titanium shapes. *Welding Journal* , 50 (9), pp. 386-s to 393-s.

8. R. R. Wells and E. B. Mikus, 1968. Thin film diffusion brazing titanium members utilizing copper intermediaries, U.S. Patent #3417461.

9. R. R. Wells, 1976. Microstructural control of thin-film diffusion-brazed titanium. *Welding Journal* , 55 (1), pp. 20-s to 27-s.

10 D. S. Duvall, W. A. Owczarski, D. F. Paulonis and W. H. King, 1972. Methods for diffusion welding the superalloy Udimet 700, *Welding Journal,* 51(2), pp. 41-s to 49-s.

11. W. A. Owczarksi, W. H. King and D. S. Duvall, 1970. Diffusion welding of the nickel-base superalloys, U.S. Patent #3530568.

12. D. S. Duvall, et al., 1974. TLP bonding: a new method for joining heat resistant alloys. *Welding Journal* , 53 (4), pp. 203 to 214.

13. J. T. Niemann and R. A. Garrett, 1974. Eutectic bonding of boron-aluminum structural components, *Welding Journal,* 53(4), pp. 175-s to 183-s.

14. J. T. Niemann and R. A. Garrett, 1974. Eutectic bonding of boron-aluminum structural components, part 2, *Welding Journal,* 53(8), pp. 351-s to 360-s.

15. B. Norris, 1986. Liquid interface diffusion (LID) bonding of titanium structures, Designing with Titanium, Proceedings of the Institute of Metals Conference, Bristol, pp. 205-213.

16. Y. Nakao, et al., 1990. Transient liquid insert metal Diffusion bonding of nickel-base superalloys", Advanced Joining Technologies, Proceedings of the International Institute of Welding Congress on Joining Research, July, pp. 129-144.

17. W.D.MacDonald, W.D.Zhuang, X.Y.Liu and T.W.Eagar, 1993. Kinetics of TLP bonding using powder interlayers", presented at 74th AWS Annual Convention, Houston, submitted to *Welding Journal.*

18. W.D.Zhuang and T.W.Eagar, 1995. A study of liquid metal infiltration of powder compacts with mutual solubility. 26th International Brazing and Soldering Conference, April 2-6, Cleveland, OH, submitted to *Metall. Trans..*

19. W.D.Zhuang and T.W.Eagar, 1995. High temperature brazing by liquid infiltration. 26th International Brazing and Soldering Conference, April 2-6, Cleveland, OH, submitted to *Welding Journal.*

20. W. Riedel, Electroless Nickel Plating, 1991. Co-published by Finishing publications and ASM, pp. 25-78.

21. Handbook of Ternary Phase Diagrams, 1995. Edited by P. Villars, A. Prince, and H. Okamoto, ASM Publication, vol. 8, pp. 10,568-10,577.

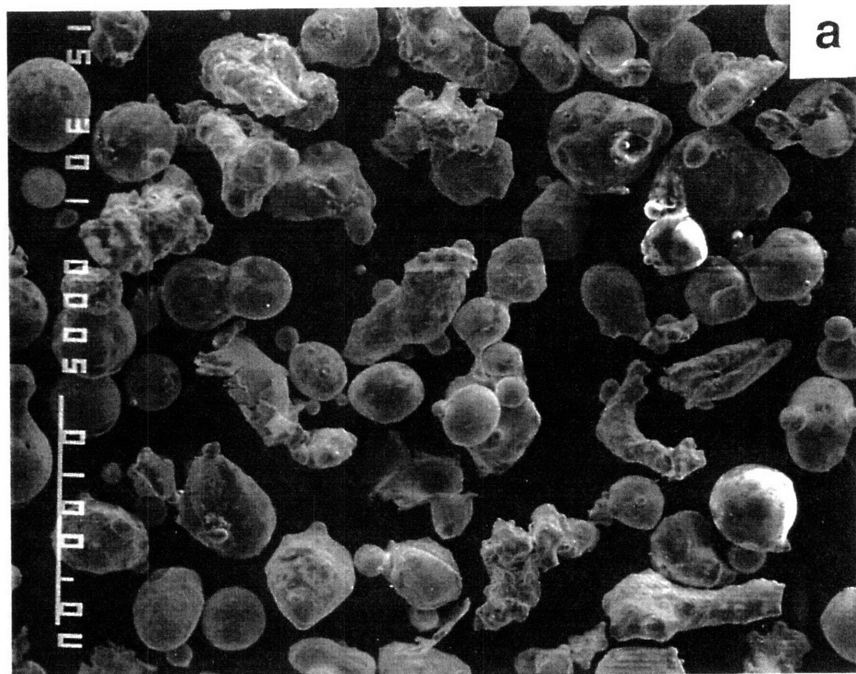

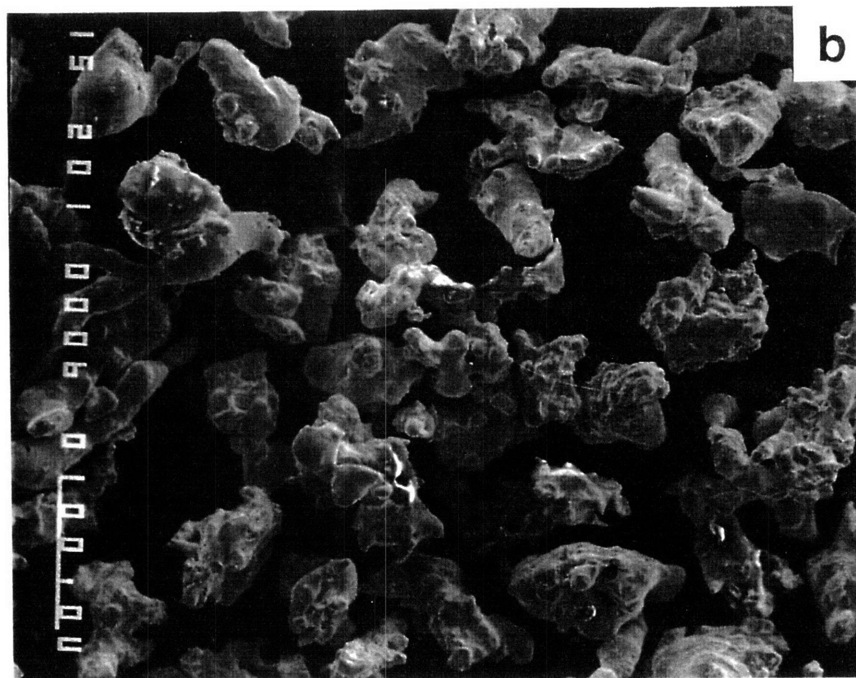

Figure 6.1. Features of the as-received metal powders. (a) Ni-20Cr alloy powders, and (b) 304L stainless steel powders.

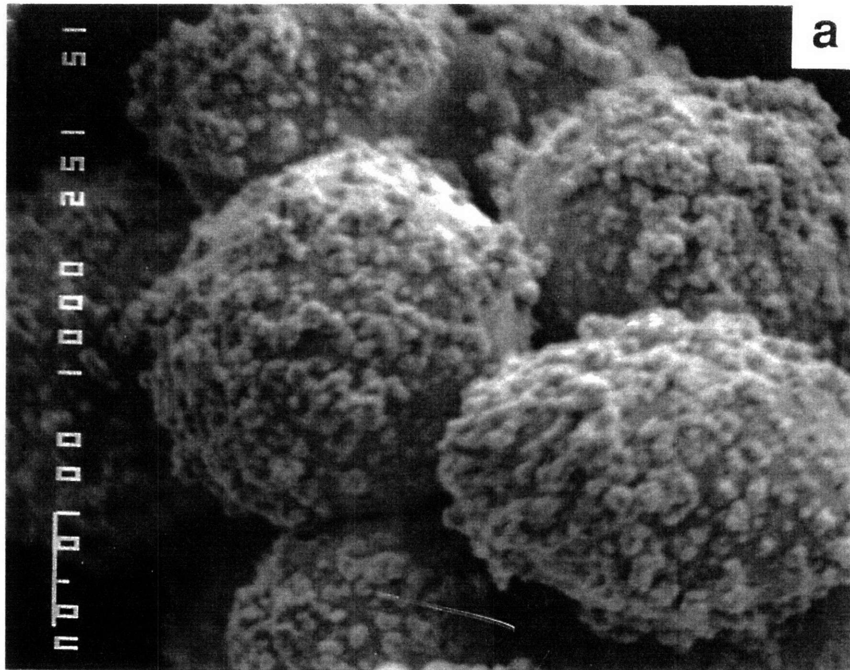

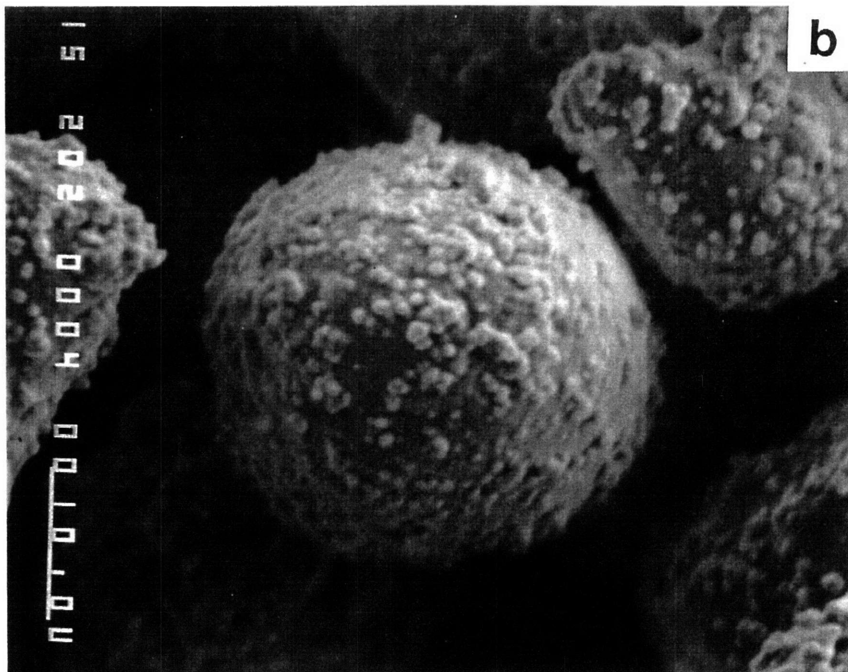

Figure 6.2. Ni-10 wt%P electrolessly coated base metal powders. (a) Ni-20Cr alloy powders with 16 wt% coating. (b) 304L stainless steel powders with 16.3 wt% coating.

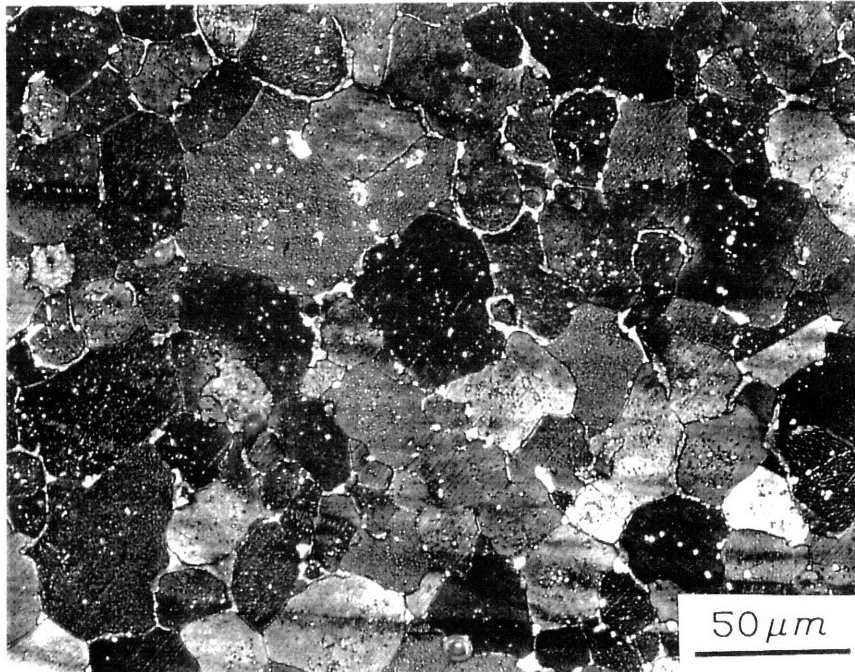

Figure 6.3. Microstructure of the Ni-20Cr powder interlayer after bonding at 1000°C for 1 hour in vacuum. The overall phosphorus content in the joint is about 1.6 wt%. Phosphides are uniformly distributed in the interlayer.

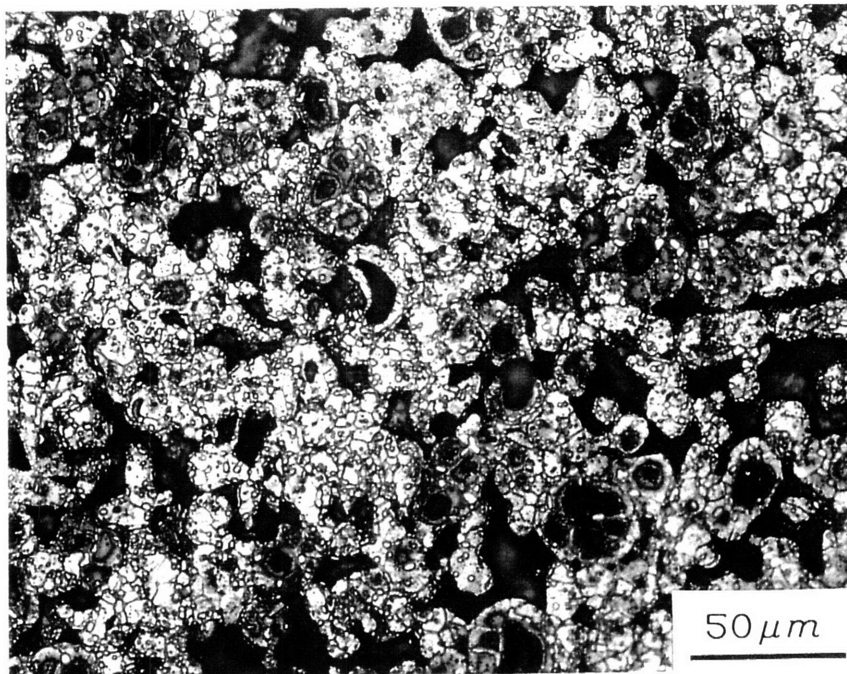

Figure 6.4. Microstructure of the 304L stainless steel powder interlayer after bonding at 1000°C for 1 hour in vacuum. The overall phosphorus content in the joint is about 1.63 wt%. Many residual pores indicates little shrinkage of the interlayer.

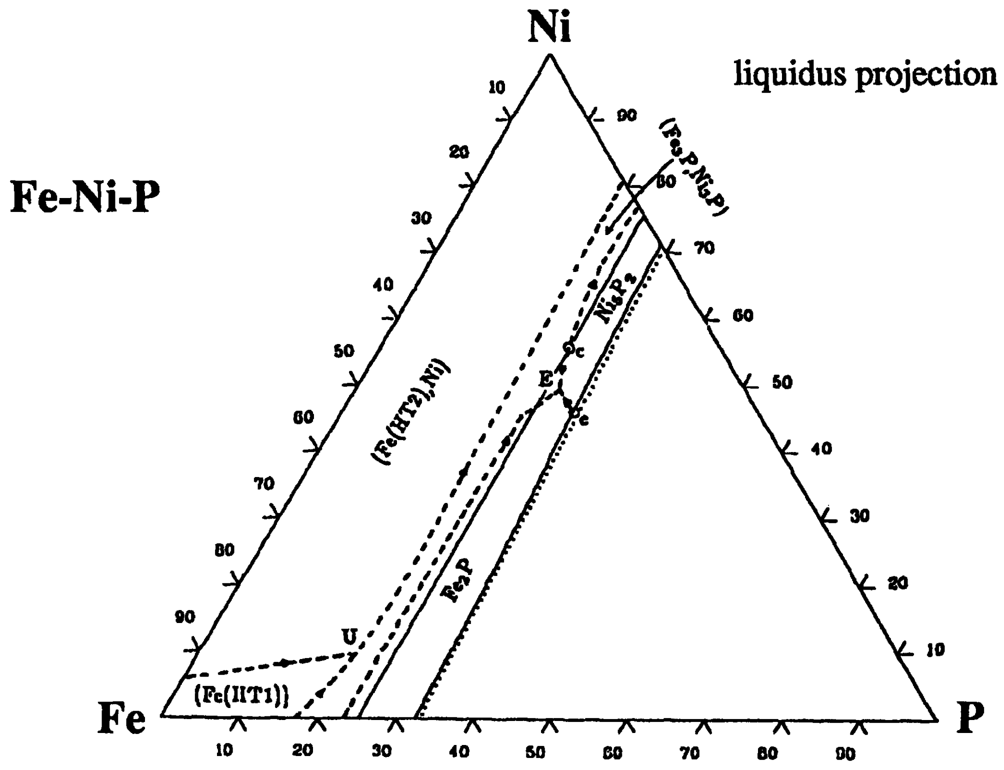

Figure 6.5. Liquidus projection of the Fe-Ni-P ternary phase diagram.

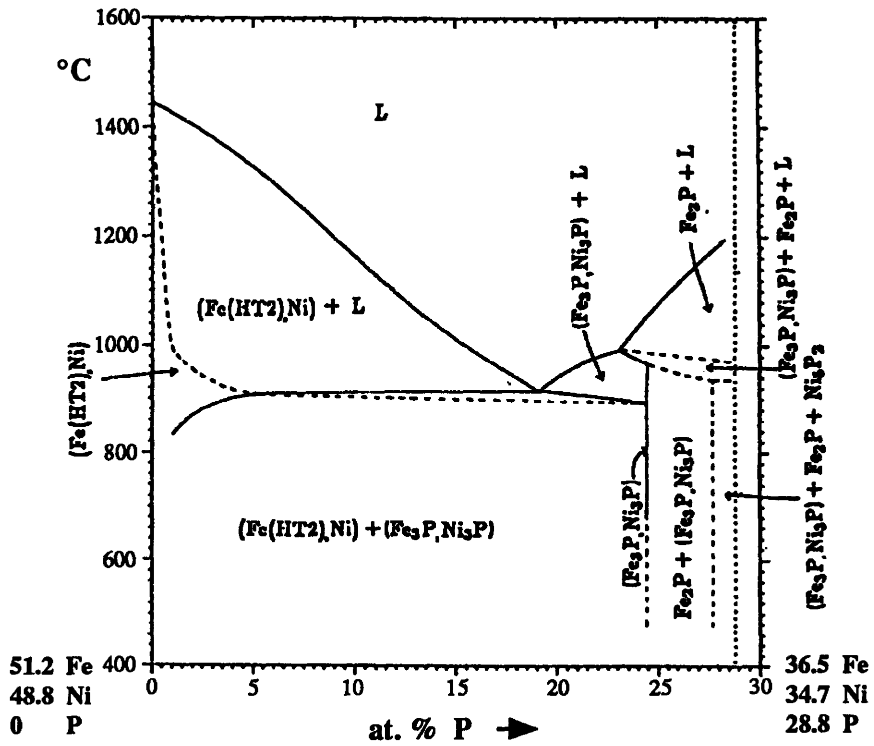

Figure 6.6. Vertical section of the Fe-Ni-P ternary phase diagram with varying phosphorus concentration.

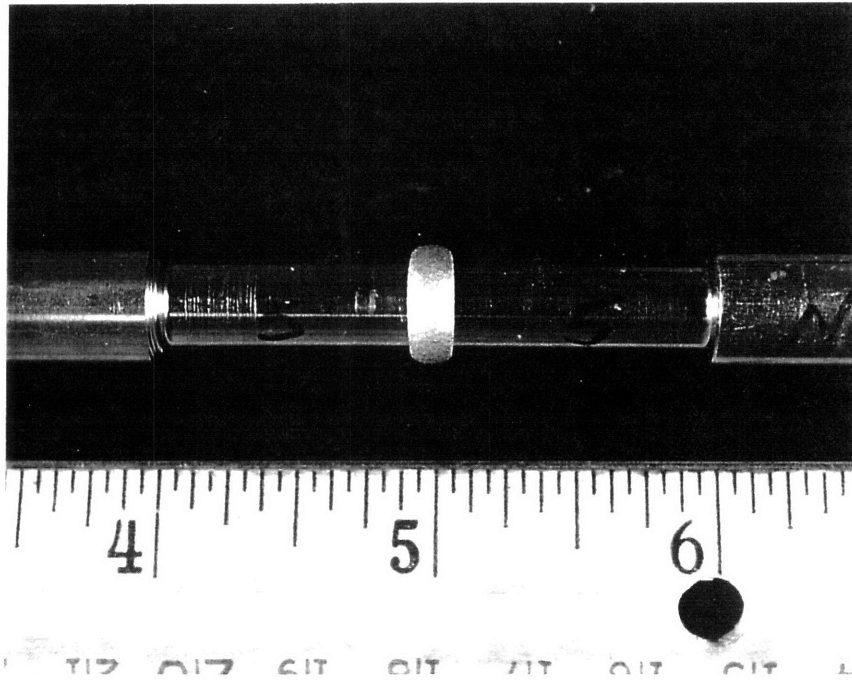

Figure 6.7. Fracture surface of the Ni-20Cr powder interlayer.

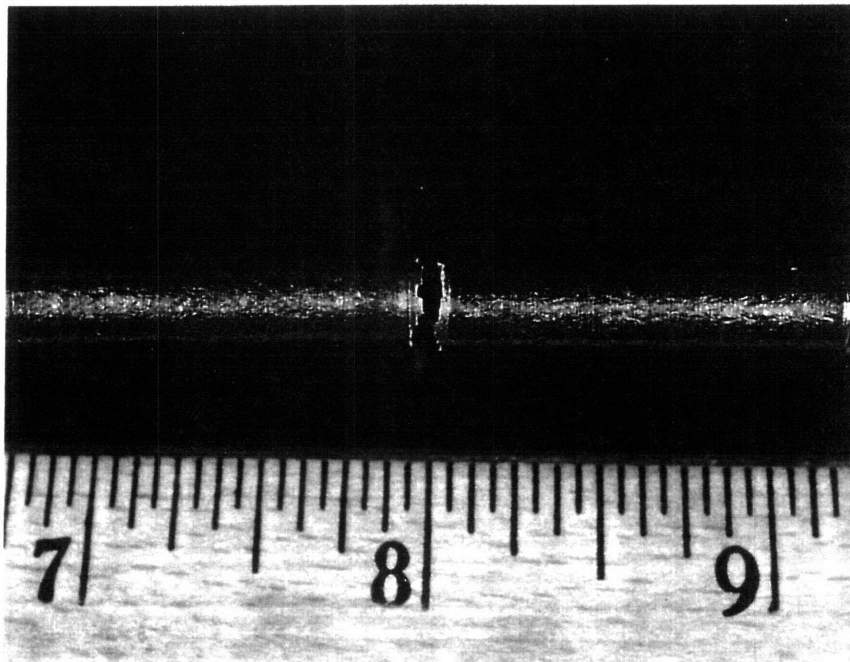

Figure 6.8. Fracture surface as shown in Fig.7. Under higher magnification, considerable ductility of the joint is evident.

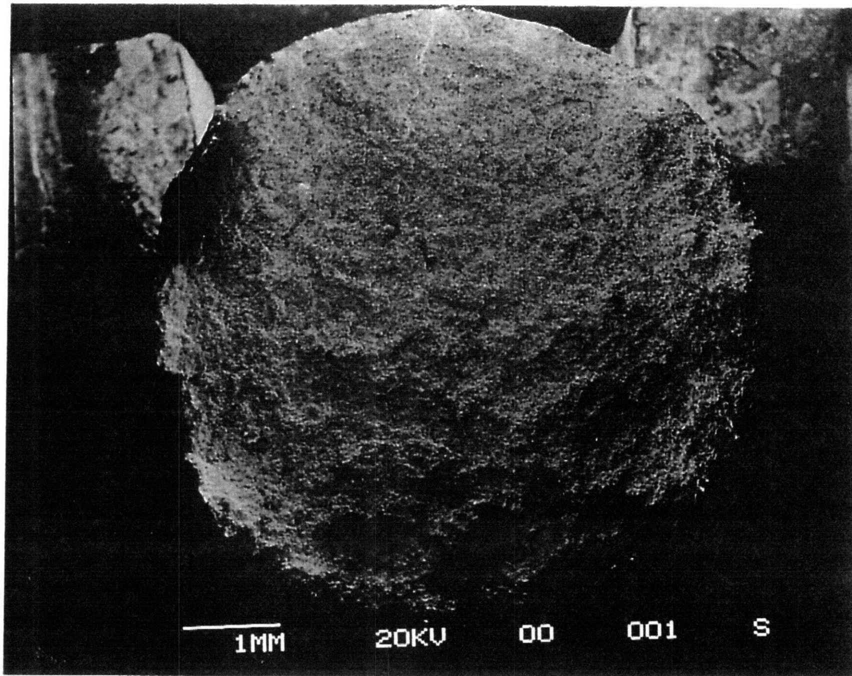

Figure 6.9. Fracture surface of the Ni-20Cr powder interlayer.

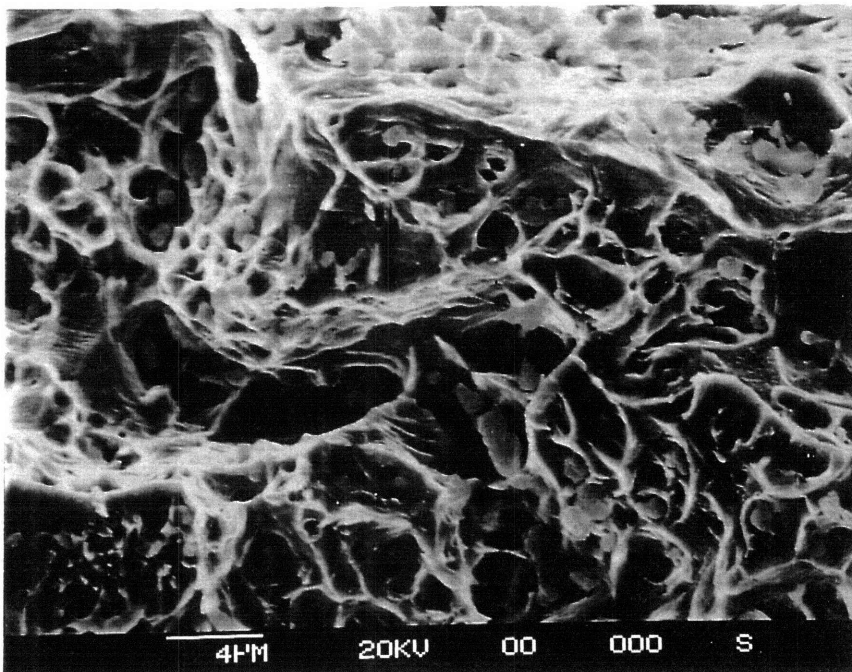

Figure 6.10. Fracture surface as shown in Figure 9. Under higher magnification, considerable ductility of the joint is evident.

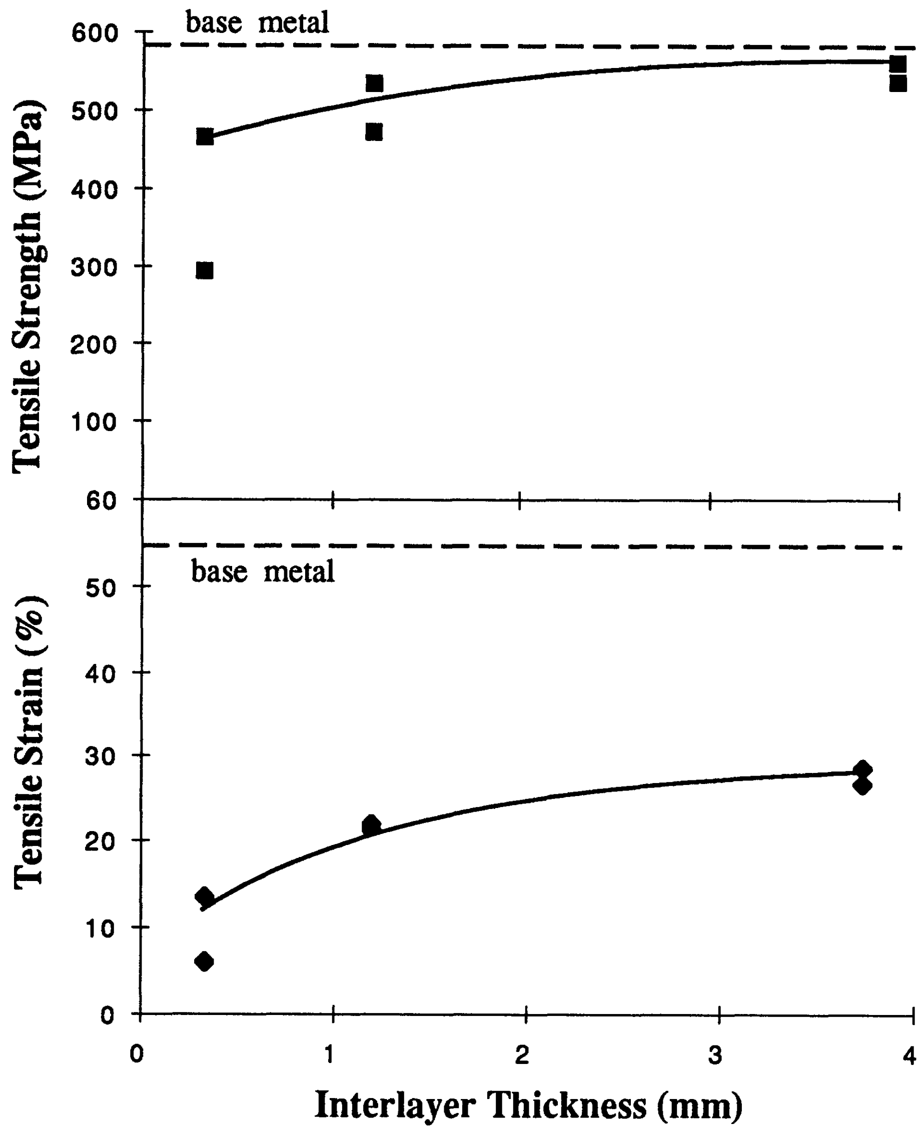

Figure 6.11. Mechanical properties of the joints with Ni-20Cr powder interlayers bonded at 1000°C for 1 hour, showing tensile strength and strain as relating to interlayer thickness.

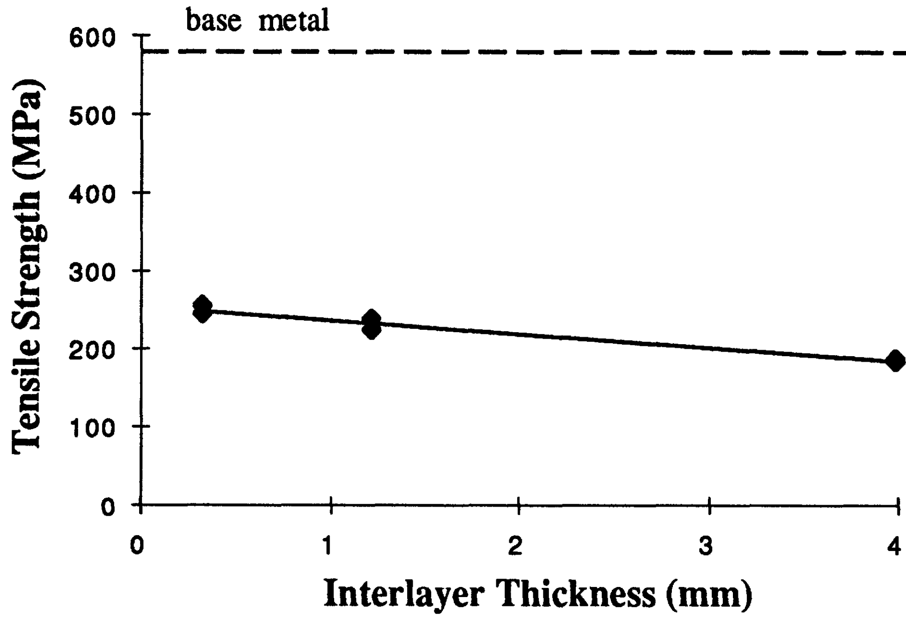

Figure 6.12. Tensile strength of joints with 304L stainless steel powder interlayers bonded at 1000°C for 1 hour.

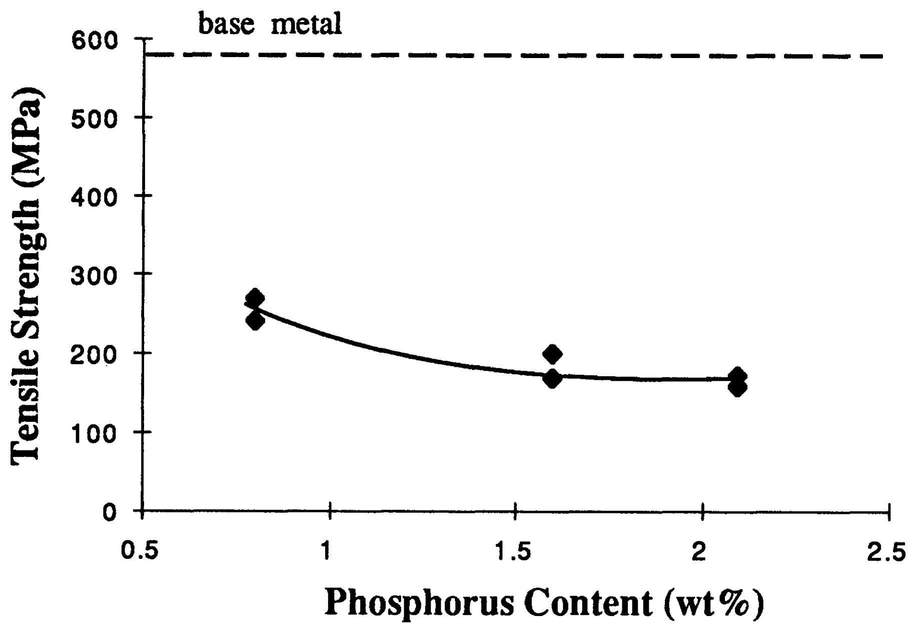

Figure 6.13. Tensile strength of joints with 304L stainless steel powder interlayers bonded at 1000°C for 1 hour.

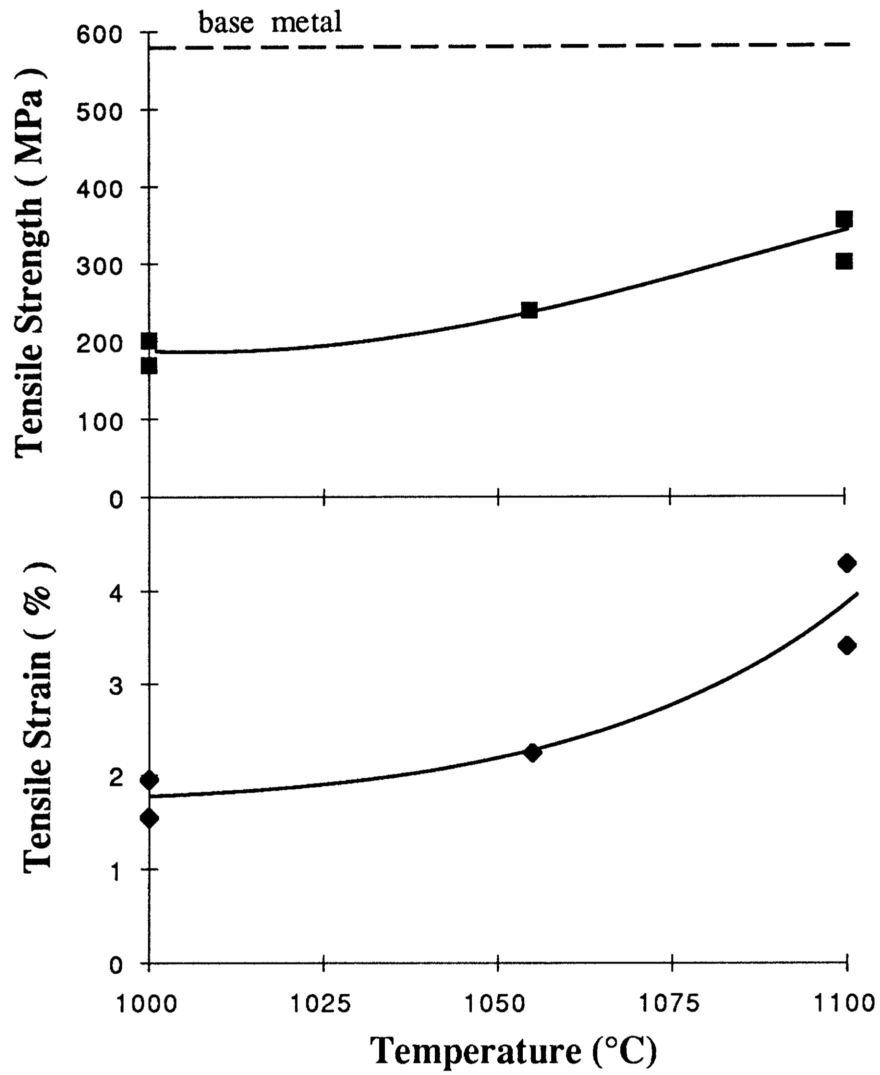

Figure 6.14. Mechanical properties of joints with 1.2 mm 304L stainless steel powder interlayers. Higher bonding temperature increases the joint strength and ductility.

THESIS SUMMARY AND FUTURE WORK

7.1 Thesis Summary

This work focuses on using powder interlayers to produce large clearance TLP joints. Different approaches have been studied to address the need of such thick joints. One of the methods is using a mixture of powders of the MPD and the base material. To reduce the amount of MPD in the joint, the liquid infiltration (LIPB) process is developed. For the material system that has a large mutual solubility between the liquid and the solid at the bonding temperature, a protective coating on the particles of the base material is usually needed to avoid excessive dissolution and early diffusional solidification, which can block the infiltration path. Direct coating of the MPD on the particles of the base material proves highly effective on producing tough and strong joints for certain material systems.

The classic LPS theory is adopted to explain the physical process in the powder interlayer during joining. Despite the general applicability of the theory, there are several other important factors which must be considered as well. For example, the chemical reaction between the MPD and the base material can markedly affect densification of a mixed powder interlayer, since fast growth of the intermetallic compounds as a result of reaction can significantly retard flow of the liquid. For a material system with large mutual solubility or high reaction rate between the base powder and the MPD, large amount of liquid is often needed for the interlayer densification. Experimental results on joining Ti-6Al-4V showed that at least 50 volume percent of liquid is needed in a mixed powder interlayer to eliminate residual porosity in the joint. Since the MPDs usually form brittle intermetallic compounds and impair the mechanical properties of the joint, their concentration must be controlled in a powder interlayer. Apparently, such a requirement is extremely difficult to meet when employing the mixed powder method.

The LIPB process is developed to address such requirement. In this process, the MPD is removed from the powder interlayer, and a powder compact of base material is used. Kinetics of base metal dissolution and diffusional solidification of a straight capillary were investigated. They were found to largely depend on the mutual solubility between the liquid (infiltrant) and the solid (powder interlayer). In a mutual soluble system, dissolution is much faster than infiltration or diffusional solidification, and saturate the infiltrant

quickly. As the capillary radius decreases, the infiltrant will solidifiy before full infiltration. When infiltrating powder compacts, dissolution is needed to open up closed pores in these compacts. However, excessive dissolution is undesirable due to rapid liquid saturation and subsequent diffusional solidification, which may prevent complete infiltration of the interlayer. Experiments on infiltrating copper powder compacts using Cu-Ag eutectic melt showed that the liquid amount can be reduced to less than 20 volume percent. However, an open pore structure of the compact is essential for complete infiltration of a thick joint.

Clearly, successful infiltration of a thick powder interlayer needs to slow down the dissolution kinetics. A protective coating on the particles of the base material provides a way of reducing the dissolution rate, which facilitates full infiltration of the interlayer. Studies on the diffusion couple, Cu substrate/Ni barrier/Cu-Ag eutectic melt, indicated that a thin nickel protective coating may prevent dissolution of copper and provide time for full infiltration.

The third process for large gap TLP bonding involves direct coating of the MPD on the particles of the base material. In this process, the solubility factor is also of great importance. Larger solubility of the base material in the MPD is preferred to keep enough liquid for complete densification. In contrast to the mixed powder method, which is characterized by localized densification, uniform densification can be achieved in the latter process since the liquid is present at all particle contacts. Thus much less liquid is needed to produce a fully dense joint.

For practical material systems where large gap joints are required, careful considerations must be taken on selecting the joining methods. The mixed powder interlayer method is simple, and can be applied successfully to the material systems with low mutual solubility and no formation of intermetallic compound between the liquid and solid components. In the case there is significant solubility and/or chemical reaction between the solid and the liquid, a relatively large amount of MPD has to be used to eliminate the residual porosity in the joint, usually at the sacrifice of the mechanical properties of the resultant joints. The LIPB process is more flexible, and can be applied to a number of material systems provided effective protective coatings are available. Since less MPD is needed, the mechanical properties can be improved. However, the process is complex since it is affected by the pore structure of the powder interlayer. The joint clearance may be limited by the infiltration distance. Hence it may be more difficult to obtain joints with consistent quality. Direct coating of the MPD provides a possible solution to use less MPD while maintaining a relatively simple process. These coated powders can be used as conventional brazing powders and virtually there is no limitation

on the joint clearance. But techniques of coating the MPD on the base powders are limited and the process may be costly to apply. Therefore the applicability of this process may be limited to only a few material systems.

7.2 Future Work

7.2.1 *Ceramic/Metal Heterogeneous Joint*

Ceramic materials should be joined to other components or parts of a structure, which are most frequently metals, to fully exploit the inherent characteristics of ceramics. The need to join these materials may arise because of the difficulty of machining ceramics once they are sintered. Joining is the only way to produce complex-shaped components. Alternatively, joining may allow the use of ceramics in highly stressed, high temperature applications, where it is not possible for the whole component to be made of ceramic. Localized protection against wear, erosion, heat or corrosion can also be provided for metal parts by cladding them to ceramics.

Methods for joining ceramics to metals can include mechanical fastening, adhesive bonding, diffusion bonding and vacuum brazing. Among them, mechanical fastening can easily be dismantled, but can cause premature failure of the ceramic because of localized stress concentrations. The relative simplicity and low cost of adhesive bonding is offset by the limited temperature capability of adhesives and doubts on their environment resistance. While diffusion bonding can lead to a temperature resistant joint, the lengthy bonding time and the need for extremely careful surface preparation raise questions on the commercial viability of the process. In contrast, vacuum brazing is a well established joining process, having been widely used in industry for the fabrication of metal structures. So far, most research and progress on ceramic/metal joining are made through the process of vacuum brazing[1-10].

In the vacuum brazing process, an important feature is the ability of the braze to both wet and react with the faying surfaces being joined. While brazing alloys readily wet and react with metals, it is not the same in the case of ceramics. This is because of the different atomic structures found in the two materials. Ceramics commonly have very stable structures, involving covalent or ionic bonding, which contrast markedly with the free electron state in most metals.

The chemical inertness of ceramics has been addressed by a variety methods. One of the earliest methods was the Molybdenum-Manganese process, developed in late 1930's

in Germany[11]. An alternative method of ceramic surface modification is the "Hydride" process, in which the hydride of an active metal such as titanium or zirconium, is placed on the ceramic surface to be joined. The active metal brazing is another way of promoting wetting of, and reaction with, the ceramic surface. Active metal brazing route proved to be much simpler than metallization methods such as the "Mo-Mn" process, as illustrated in Figure 7.1.

A number of commercial active metal brazing alloys, with titanium additions, are available today. Titanium is used in relatively small amounts, e.g., 1-5 weight percent, because it readily reacts with oxygen, carbon, nitrogen and silicon, the elements which form the basis of many ceramics. The interfacial reaction results in low wetting angles with many ceramics.[12-18].

In addition to their low wettability and reactivity, ceramics also tend to have very low coefficients of thermal expansion (CTE) relative to common engineering metals. The CTEs of some common engineering ceramics and metals are given in Figure 7.2.

Any ceramic-metal joint made at elevated temperature will be affected by differential thermal expansion between the two materials. The manifestation of such processing is residual stress, which starts to develop in a joint as soon as it can transmit stress, at the so-called critical temperature.

The level of residual stress that builds up in a joint depends on factors such as the difference between the critical and ambient temperatures; the difference in the CTEs of the two materials; and the ability of the materials in the joint to absorb the differential strain which develops, by undergoing plastic deformation. Essentially the latter ability is confined to metallic components, including the brazing alloy. The ceramic will normally not plastically deform.

At best, residual stress will weaken a ceramic-metal joint and, at worst, actually cause the joint to fail during cooling down after brazing. The magnitude of the residual stress is related to the joint geometry as well as the size of the joint. As depicted in Figure 7.3, the residual stress in a cylindrical joint increases with increase of the faying surface area. Meanwhile, a rectangular joint with the same bonding area produces higher residual stress as compared with the cylindrical one.

The mismatch in the thermal expansion between ceramics and metals can be addressed in a number of ways, including materials selection, minimizing the brazing temperature, and using accommodating interlayers. By carefully choosing materials used in the joint, the difference in the CTEs of the ceramic and metal can be minimized. Also, minimizing the brazing temperature reduces the difference between the critical and ambient temperature, which helps to reduce the level of residual stress.

The freedom of these first two options is often limited by the operational requirements of the joint. For example, by examining Figure 7.2, it can be seen that choosing Mo/AlN, or steel/zirconia combinations can minimize the difference in CTEs. However, neither of these combinations is acceptable to the gas turbine designer due to other specified material properties. Nickel-base superalloy/silicon nitride turns out to be the favored combination, but has a large CTE mismatch. To minimize the residual stress that can be generated by such large CTE mismatch, a low melting point brazing alloy like Ag-Cu-In-Ti (mp. 620°C) is likely to be used. However, operation of a gas turbine typically needs a ceramic-metal joint to withstand temperature up to 800°C. Therefore, higher melting point brazing alloys must be used. This leads to another approach, i.e., the use of strain accommodating interlayers. A number of ideas have been proposed concerning the ideal characteristics of such interlayers. These include the use of metals, such as copper, aluminum or nickel, whose CTEs are not well matched to those of ceramics, but have significant ductility; the use of metals such as molybdenum and tungsten, which are much more closely matched to the CTEs of ceramics, but have poor ductility; and the use of combinations of metals having a gradation of expansion and/or ductility, such as Cu/Mo. These methods are illustrated in Figure 7.4.

Currently, the maximum bonding area that can be achieved by direct brazing is limited to about 400 mm^2, but commercial applications of ceramics require a bonding area more than 2000 mm^2. It is apparent that new approaches are needed to close this gap. Joining with multiple powder interlayers offers a possible solution to accommodate residual stresses in large ceramic/metal joints. In this process, the CTE of each individual powder interlayer can be tailored, which offers more freedom in designing the joint than using different bulk metal interlayers. By incorporating high modulus ceramic particles, the powder interlayer can possess much higher Young's modulus than Mo or W, and thus be able to control the deformation of the metal part more effectively. Direct brazing is achieved by using active brazing alloy powders as the bonding agent for the powder interlayers as well as for the metal and the ceramic parts. Since the interlayers can be applied by screen printing techniques, it is also very flexible for different joint geometries.

Primary work on the joining of Si_3N_4 to plain carbon steel using three powder interlayers with a bonding area of 625 mm^2 showed promising results, which are presented in Figure 7.5. The first layer adjacent to the steel for both samples in Figure 7.5 consists of 15 vol.% Nb powders, with a thickness about 0.2 mm. The middle layer in samples A and B contains 70 vol.% WC particles with a thickness around 1 mm. The third layer which joins Si_3N_4 contains 15 vol.% short P-55 graphite fibers and 35 vol.% Nb powders

for samples A and B, respectively. The layer thickness is about 0.6 mm. The bonding agent is Ag-Cu eutectic plus 4.5 wt% Ti. No crack of the Si_3N_4 was observed as these samples were furnace cooled from the bonding temperature (880°C). Figure 7.6 shows fully densified middle layer, and Figure 7.7 is the back scattering image under the SEM showing the interface between the ceramic and the third layer. The gray particles are Nb.

To further reduce the residual stress for large area joints, patterning of the powder interlayers can be introduced. This is illustrated in Figure 7.8. The small unbonded areas can effectively change the stress distribution in the joint, but not significantly affect the strength. By patterning the middle layer, a Si_3N_4/Steel joint with 1250 mm^2 bonding area has been successfully made. Further work is needed on the following aspects:

(i) Numerical modeling of the joint with multiple composite interlayers, including the patterned interlayers.

(ii) Different combinations of powder interlayers as well as the number and relative thickness of the interlayers.

(iii) Developing a bonding agent other than Ag-Cu-Ti which is able to withstand higher temperature exposure, and

(iv) Producing a ceramic-metal joint with bonding area exceeding 2000 mm^2, with excellent room temperature and high temperature mechanical properties.

7.2.2 *Near-Net-Shape Manufacturing*

In recent years, a number of rapid prototyping (RP) technologies have been developed for more efficient manufacturing. Among them, selective laser sintering (SLS) [19-23] and three dimensional printing (3DP) [24-29] processes are capable of producing near net shape metal components with low cost and high speed. The SLS process begins by first depositing a thin layer of powder into a container. The powder surface is raster-scanned with a high power laser to sinter the particles occupying the cross section of the part to be built. In the areas not sintered, the powder remains loose and may be removed once the part is completed. Successive layers of powder are then deposited and sintered until the entire part is produced. The 3DP process creates parts in layers similar to the SLS by spreading powder materials on a build platform. But 3DP selectively joins the powder

in the layer by inkjet printing a binder material. The platform lowers and the process is repeated, as illustrated in Figure 7.9.

The metal parts formed by the SLS or 3DP processes are porous in nature, and direct use of these parts usually needs further treatment to densify the parts and hence increase their mechanical properties. Post-form sintering offers a simple solution. However, the complex-shaped components may undergo extensive dimensional change (shrinkage) due to high temperature sintering, and this may impose severe difficulties for near-net-shape manufacturing. An alternative method is to infiltrate the porous parts with another liquid metal to eliminate porosity. Due to high volume fraction of porosity (typically from 40% to 50%) in those parts formed by the SLS or the 3DP, infiltration without causing significant dimensional change is more difficult as compared to infiltrating conventional PM parts with much lower volume fraction of porosity (usually less than 30%). In addition, for the systems having extensive interactions between the infiltrant and the part material, dimensional changes associated with swelling, shrinking or even slumping can be expected. Protective coatings on the particles for the RP processes may prevent such adverse effects during infiltration. Pioneering work has been performed by some researchers[30, 31] on the infiltration of rapidly formed metal parts. However, much work is still required before the end-use parts can be satisfactory produced by these novel RP processes.

7.2.3 New Materials for Dental Amalgam

Mercury-containing dental amalgam has been around since 659 A.D., and it is still widely used in dental clinics today with much improved properties. The basic procedure for making amalgam involves a simple diffusion reaction at room or mouth temperature between silver alloy fillings and liquid mercury mixed as a metallic paste in various proportions, but typically[32]:

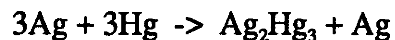

$$3Ag + 3Hg \rightarrow Ag_2Hg_3 + Ag$$

Due to the existence of excessive mercury, evaporating or leaching of mercury during the service life of the amalgam (up to 30 years) is possible. Recently, the toxicity of mercury in the traditional dental amalgam has aroused much concern and a non-toxic substitute is demanded.

Gallium-based dental amalgam GF and Galloy have been developed as a consequence of such demand in Japan and Australia, respectively[33, 34]. Instead of

using mercury, a ternary alloy consisting of gallium, indium, and tin, which is a liquid at room temperature is used. The solid filler usually contains silver, copper, and tin. Small amount of platinum or palladium is added to enhance the corrosion resistance of the amalgam. As compared with commercial mercury-based products, the gallium amalgam is claimed to have superior wear resistance, lower dimensional change during setting, and good mechanical properties. Nonetheless, clinical evaluation of these alloys revealed that they are not suitable for dental restorations[35] because of their poor corrosion resistance accompanied by considerable amount of gallium release. Thus successful replacement of mercury amalgam by the gallium alloys depends largely on improvement of the corrosion resistance. One of the approaches is by removing free gallium in the amalgam. Figure 7.10 shows the microstructure of an experimental gallium-based amalgam 72 hours after trituration. The solid particles are Ag-Cu eutectic alloy. It is apparent that large particles exhibit less reaction than the smaller ones. Therefore a uniform distribution of smaller size filler particles will consume more gallium which may increase the corrosion resistance. Secondarily, new filler materials which are more corrosion resistant than the current available alloys have to be investigated. Silver or copper-based alloys with additions of titanium, nickel, or chromium are possible candidates for such a purpose.

7.3 References

1. A. J. Moorhead and H. Keating, *Direct Brazing of Ceramics for Advanced Heavy-Duty Diesels*, Welding Journal, vol. 65, no. 10, pp. 17-31, 1986.

2. H. Mizuhara and E. Huebel, *Joining Ceramic to Metal with Ductile Active Filler Metal*, Welding Journal, vol. 65, no. 10, pp. 43-51, 1986.

3. H. Mizuhara, *Vacuum Brazing Ceramics to Metals*, Advanced Materials & Processes, pp. 53-55, February, 1987.

4. M. M. Schwartz, Ceramic Joining, ASM Publication, 1990.

5. A. K. Chattopadhyay, H. E. Hintermann, *On Brazing of Cubic Boron Nitride Abrasive Crystals to Steel Substrate with Alloys Containing Cr or Ti*, J. Mat. Sci., vol. 28, pp. 5887-5893, 1993.

6. J. H. Selverian and S. Kang, *Ceramic-to-Metal Joints Brazed with Palladium Alloys*, Welding Journal, vol. 71, no. 1, 1992.

7. R. L. Peaslee, *Brazing: Yesterday's Art has Become Today's Science*, Welding Journal, vol. 71, no. 10, pp. 25-31, 1992.

8. F. Moret and N. Eustathopoulos, *Ceramic to Metal direct Brazing*, Journal de Physique IV, vol. 3, pp. 1043-1052, November, 1993.

9. A. J. Moorhead and W. H. Elliott, *Brazing of Ceramic and Ceramic-to-Metal Joints*, ASM Handbook, vol. 6, Welding, Brazing and Soldering, 1994.

10. A. G. Foley and D. J. Andrews, *Active Brazing for Joining Ceramics to Metals*, GEC Alsthom Technical Review, no. 13, pp. 49-64, 1994.

11. H. E. Pattee, *Joining Ceramics to Metals by Brazing*, Welding Research Council Bulletin, no. 178, November, 1972.

12. M. Naka and O. Okamoto, *Wetting of Silicon nitride Cearmics by Copper-Titanium or Copper-Zirconium Alloys*, Transactions of JWRI, vol. 14, no. 1, pp. 29-34, 1985.

13. R. R. Kapoor and T. W. Eagar, *Tin-Based Reactive Solders for Ceramic/Metal Joints*, Metall. Trans., vol. 20B, pp. 919-924, 1989.

14. E. Lugscheider and W. Tillmann, Development of New Active Filler Metals in a Ag-Cu-Hf System, Welding Journal, vol.69, no. 11, pp. 416-s to 421-s, 1990.

15. L. Pejryd, *Metal Ceramic Joining for High Temperature Applications*, 4th International Symposium on Ceramic Materials and Components for Engines, 1991, Gotebörg, Sweden.

16. J. M. Howe, *Bonding, Structure, and Properties of Metal/Ceramic Interfaces: Part 1 Chemical Bonding, Chemical Reaction and Interfacical Structure*, International Materials Reviews, vol. 38, no. 5, pp. 233-256, 1993.

17. M. G. Nicholas and S. D. Peteves, *Joining of Silicon Nitride Ceramics*, 4th International Symposium on Ceramic Materials and Components for Engines, 1991, Gotebörg, Sweden.

18. Y. Adda et al., *Reactive Wetting by Liquid Metals in Materials Science*, Materials Science Forum, vols. 155-156, pp. 511-526, 1994.

19. H. M. Marcus et al., *From Computer to Component in 15 Minutes: The Integrated Manufacture of Three Dimensional Objects*, Journal of Metal, pp. 8-10, April, 1990.

20. D. L. Bourell et al., Selective Laser sintering of Metals and Ceramics, International Journal of Powder Metallurgy, vol. 28, no. 4, pp. 369-381, 1992.

21. B. Badrinarayan and J. W. Barlow, *Metal Parts from Selective Laser Sintering of Metal-Polymer Powders*, Solid Free Form Fabrication Symposium, pp. 141-146, 1992, Austin, TX.

22. M. Sindel, et al., *Direct Selective Laser Sintering of Metals and Metal Melt Infiltration for Near Net Shape Fabrication of Components*, Solid Freeform Fabrication Proceedings, pp. 94-101, 1994, Austin, TX.

23. C. Nelson, K. McAlea, and D. Gray, *Improvements in SLS Part Accuracy*, Solid Freeform Fabrication Proceedings, pp. 159-169, 1995, Austin, TX.

24. S. Michaels, *Production of Metal Parts Using the Three Dimensional printing Process*, MIT Master Thesis, November, 1993.

25. S. Michaels, E. Sachs, and M. Cima, *Three Dimensional Printing of Metal and Ceramic Parts*, Proceedings on the Advances in Powder Matallurgy and Particulate Materials, May 8-11, 1994, Toronto, Canada.

26. E. Sachs et al., *CAD-Casting: the Direct Fabrication of Ceramic Shells and Cores by Three Dimensional Printing*, Manufacturing Review, vol. 5, no. 2, pp. 118-126, 1992.

27. E. Sachs et al., *Three Dimensional Printing: Rapid Tooling and Prototypes Directly from a CAD Model*, Journal of Engineering for Industry, vol. 114, no. 4, pp. 481-488, 1992.

28. E. Sachs, et al., *Surface Texture by 3D Printing*, Solid Freeform Fabrication Proceedings, pp. 56-64, 1994, Austin, TX.

29. M. J. Cima, et al., Structural Ceramic Components by 3D Printing, Solid Freeform Fabrication Proceedings, pp. 479-488, 1995, Austin, TX.

30. E. Sachs et al., *Production of Injection Modeling Tooling with Conformal Cooling Channels Using the Three Dimensional Printing Process*, Solid Freeform Fabrication Proceedings, pp. 448-467. September, 1995, Austin, TX.

31. T. Pintat, M. Greul, and M. Greulich, *Accuracy and Mechanical Behavior of Metal Parts Produced by Lasersintering*, Solid Freeform Fabrication Proceedings, pp. 72-79. September, 1995, Austin, TX.

32. R. M. Waterstrat, *Brushing up on the History of Intermetallics in Dentistry*, J. Metals, pp. 8-14, March, 1990.

33. T. Yamashita, Japanese Journal of Conservative Dentistry, vol. 32, no. 1, 1989.

34. *Galloy*. Product Brochure by Southern Dental Industries (SDI), Bayswater, Victoria, Australia.

35. M. Navarro, E. Franco, P. Bastos, R. Carvalho, and L. Teixeira, *Clinical Evaluation of Gallium Alloy*, J. Dent. Res. (IADR Abstracts), no. 925, 1993.

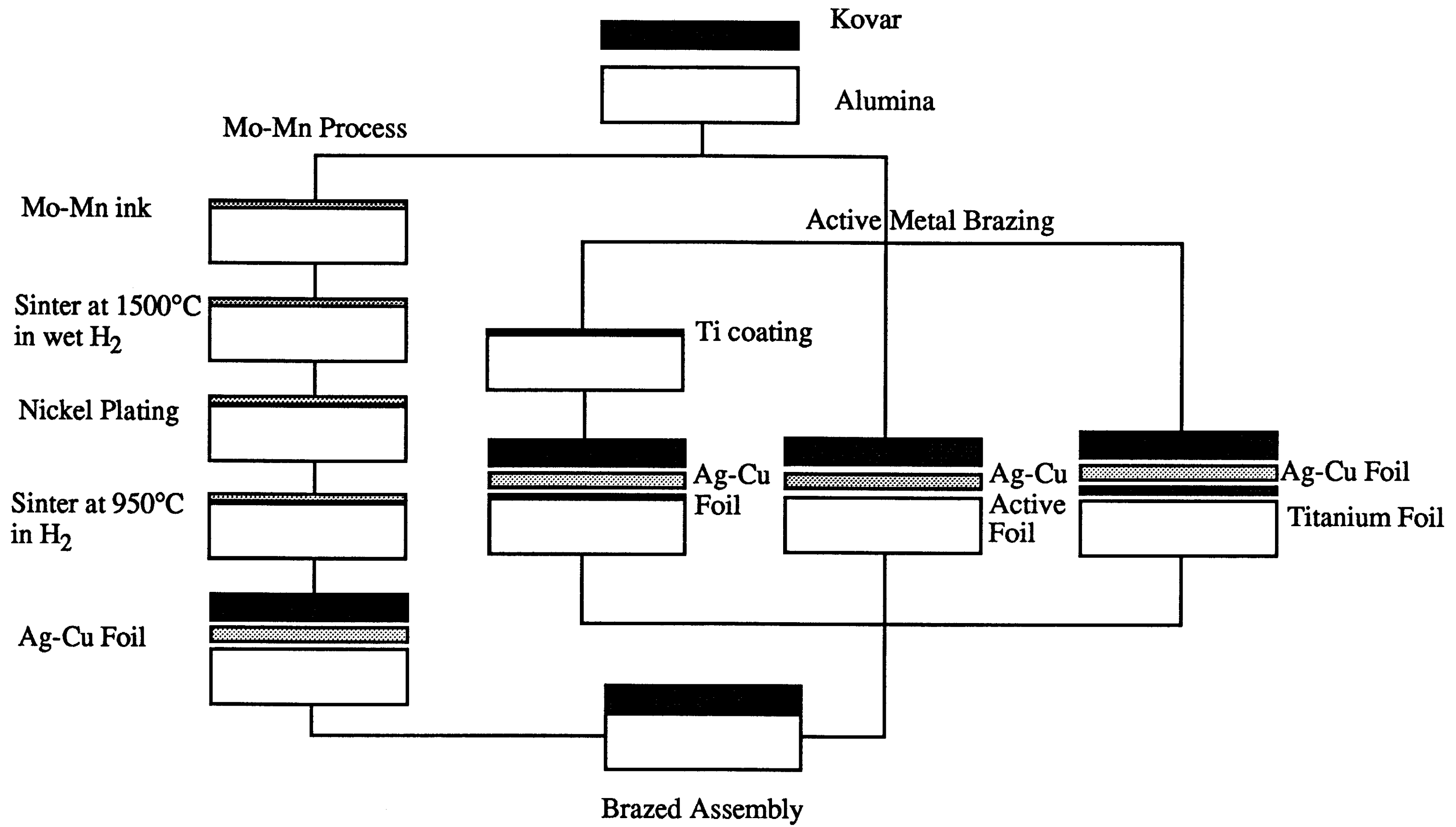

Figure 7.1. Comparison of methods for brazing alumina to Kovar.

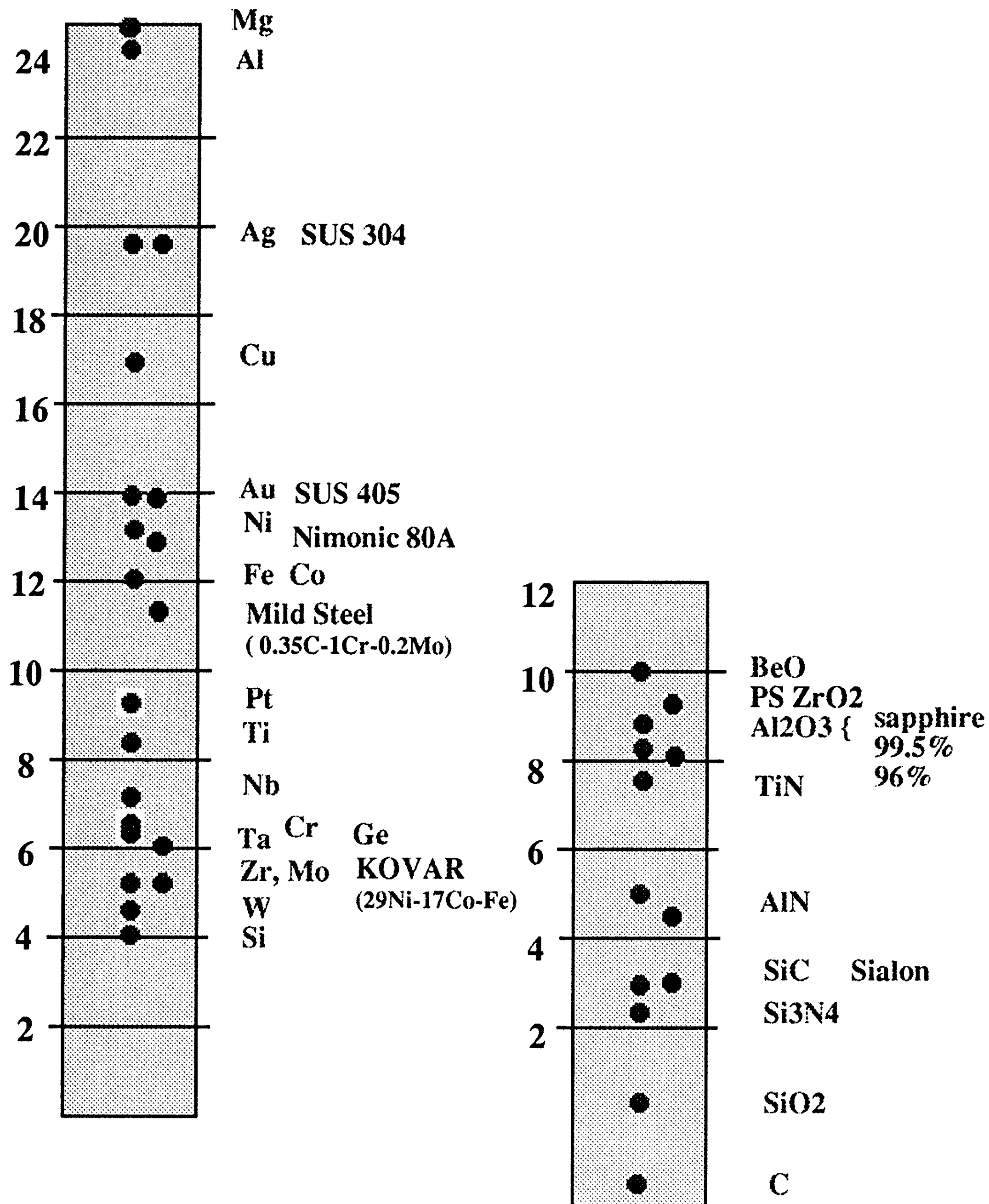

Figure 7.2. Coefficient of thermal expansion (CTE) of some metals and ceramics.

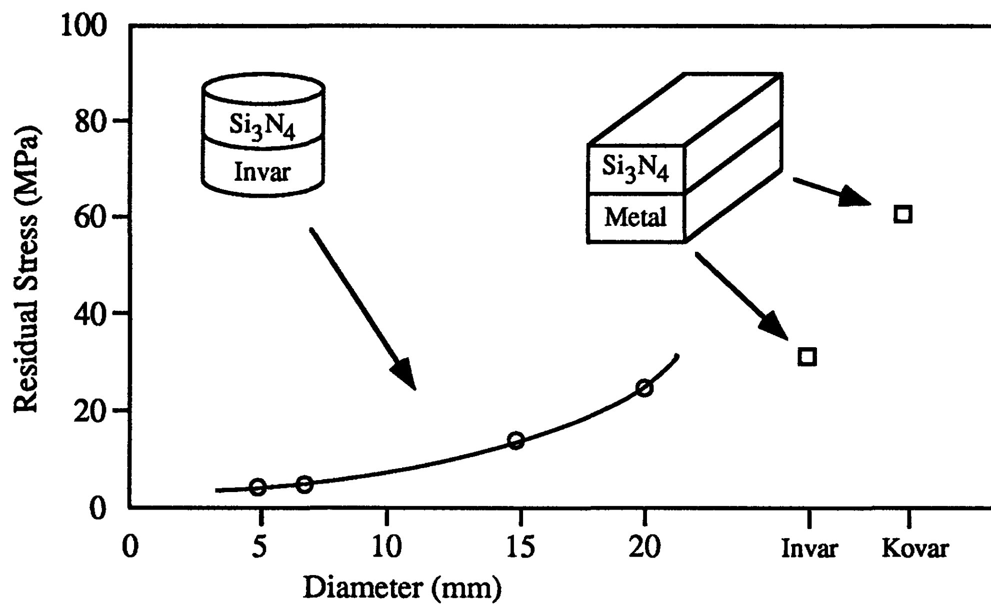

Figure 7.3. Residual stress as a function of bonded area and geometry (Suganuma et al., 1987).

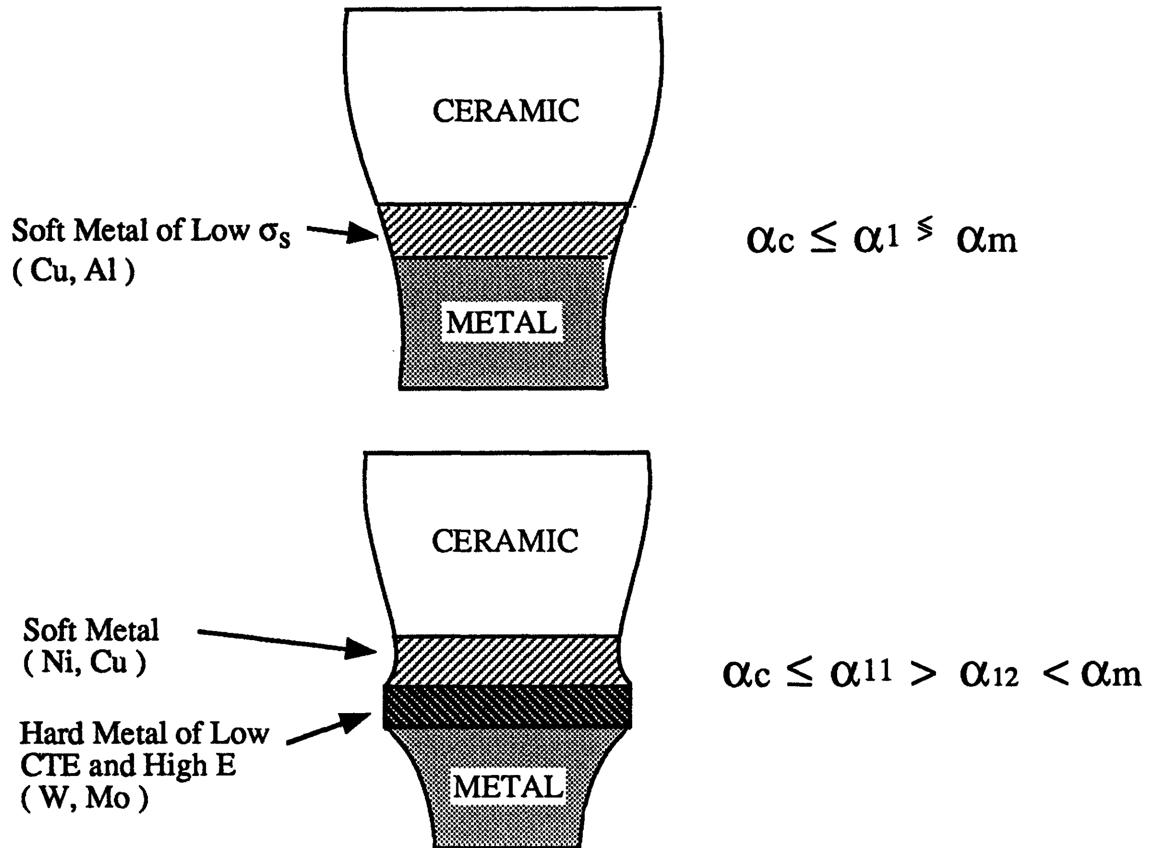

Figure 7.4. Methods of reducing thermal stresses (T.Suga, 1988).

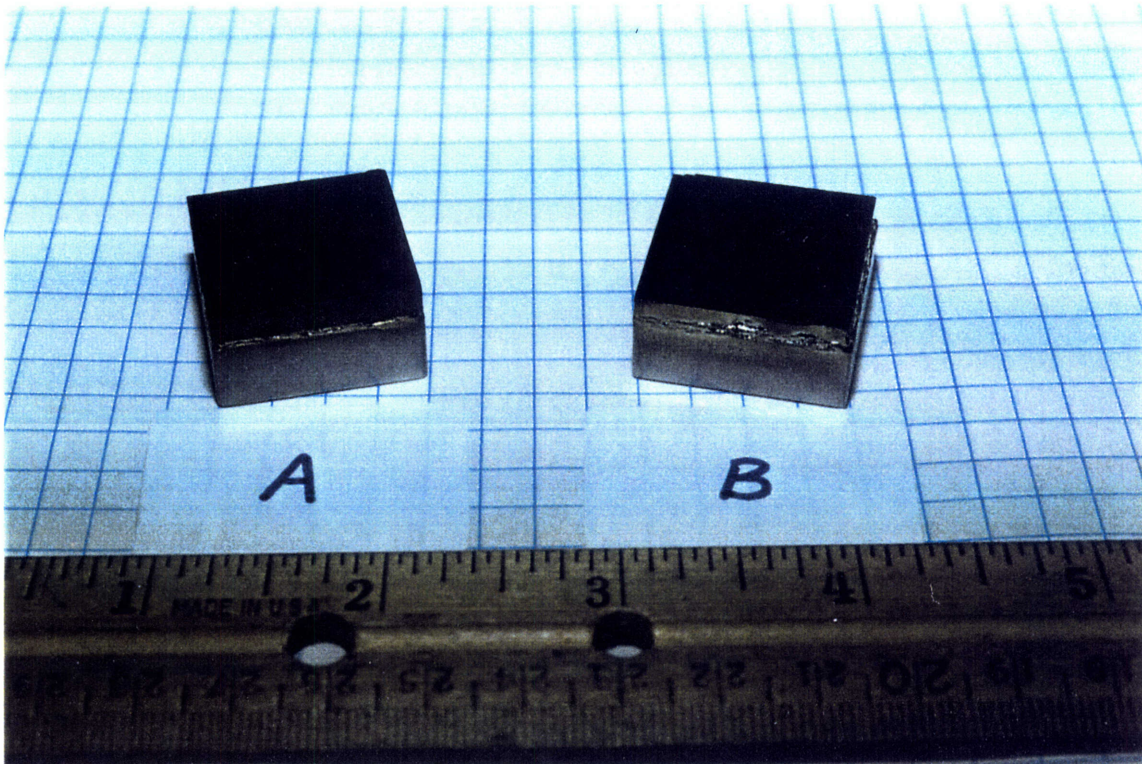

Figure 7.5. Si_3N_4/Steel joints directly brazed by three powder interlayers. The first layer adjacent to the steel for both samples contains 15 vol.% Nb powders, and the thickness is about 0.2 mm. The middle layer in samples A and B contains 70 vol.% WC particles with a thickness of 1 mm. The third layer which joins Si_3N_4 contains 15 vol.% short P-55 graphite fibers and 35 vol.% Nb powders for samples A and B, respectively. The layer thickness is about 0.6 mm. The bonding agent is Ag-Cu eutectic plus 4.5 wt% Ti for all the layers. Joining was performed at 880°C in a vacuum furnace.

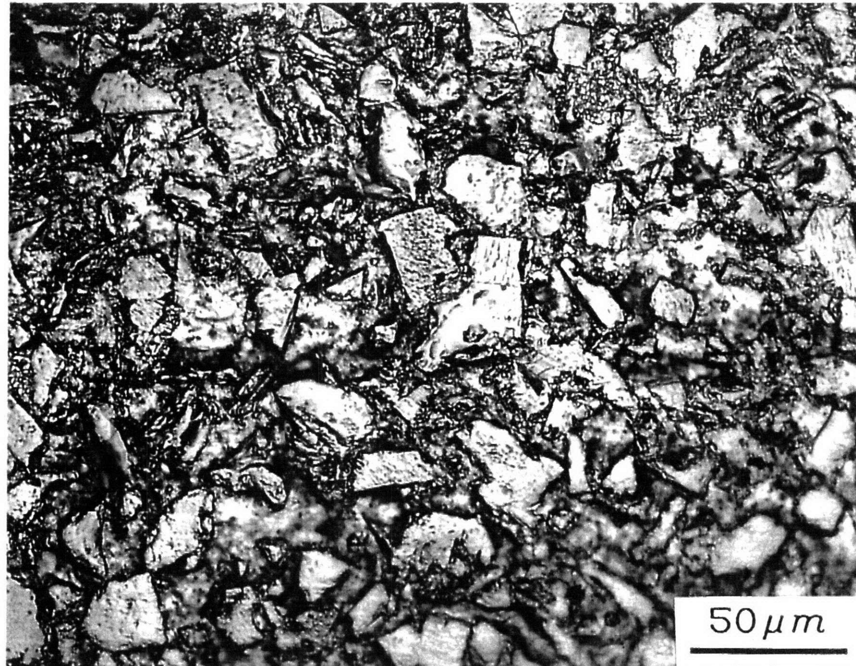

*Figure*7.6. Microstructure of the middle powder interlayer (70 vol.%WC) after bonding, showing full densification of the interlayer. The particles are WC.

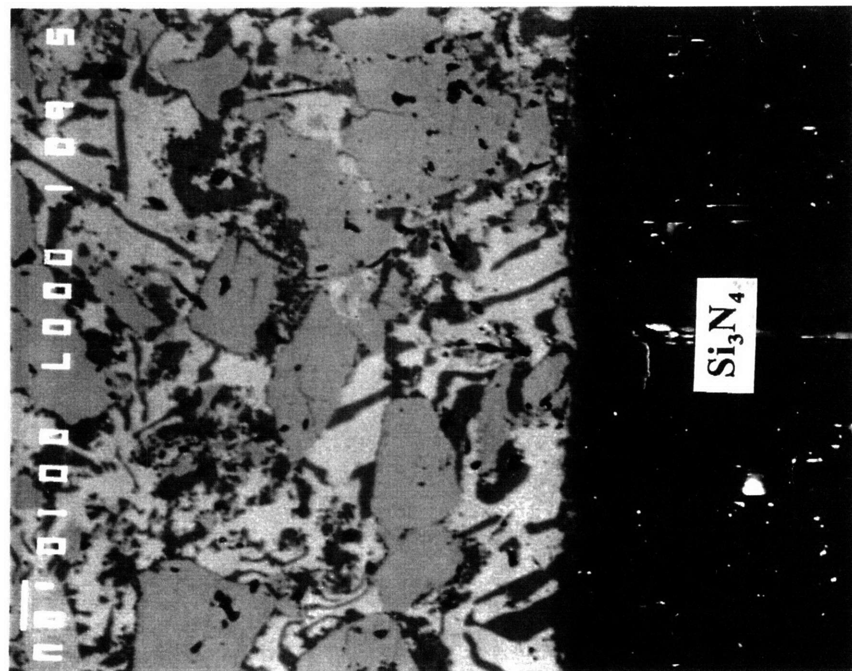

Figure 7.7. Back scattering image under SEM showing the interface between the third interlayer and Si_3N_4. The gray particles are Nb powders.

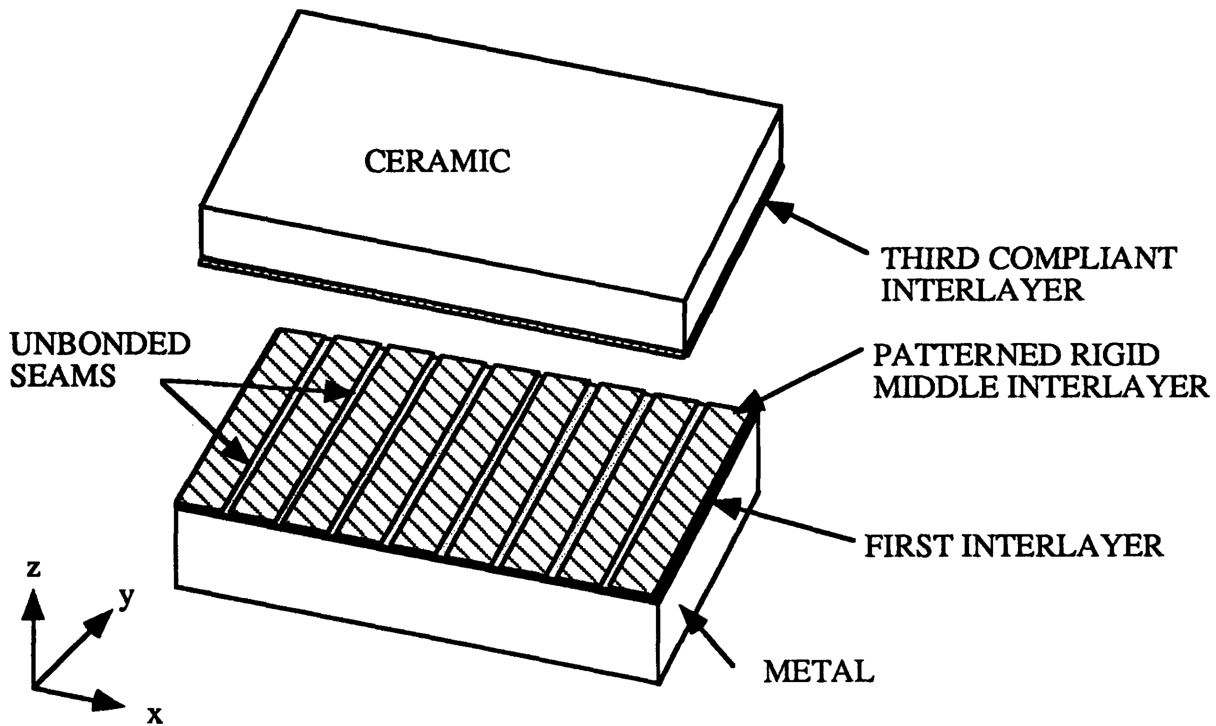

Figure 7.8. Concept of reducing residual stresses for large area ceramic to metal bonding by applying a patterned powder interlayer. The unbonded seams along x-direction are believed to be able to accommodate thermal strains in the joint. One such sample with dimensions of 1" x 2" has been successfully made.

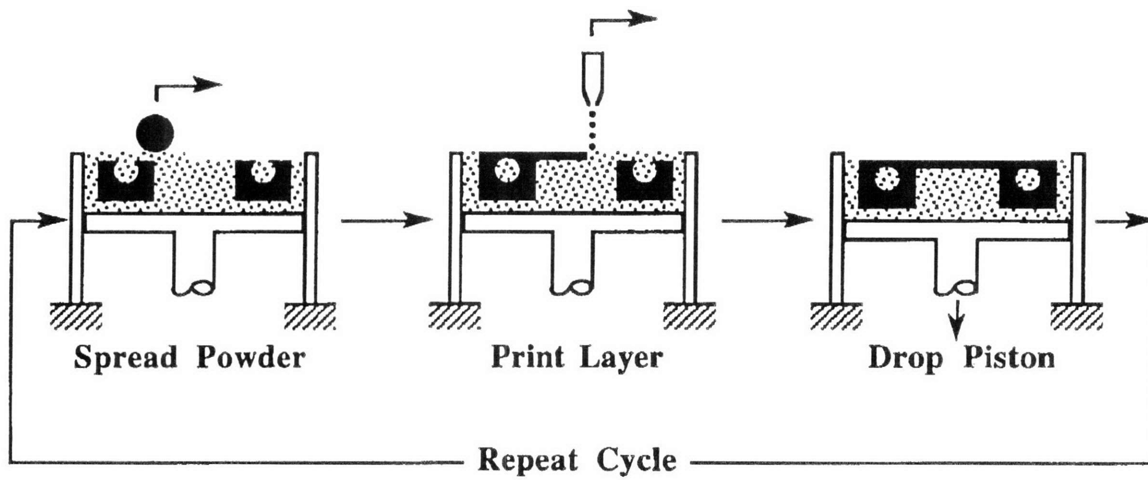

Figure 7.9. The sequence of three dimensional printing (3DP) process.

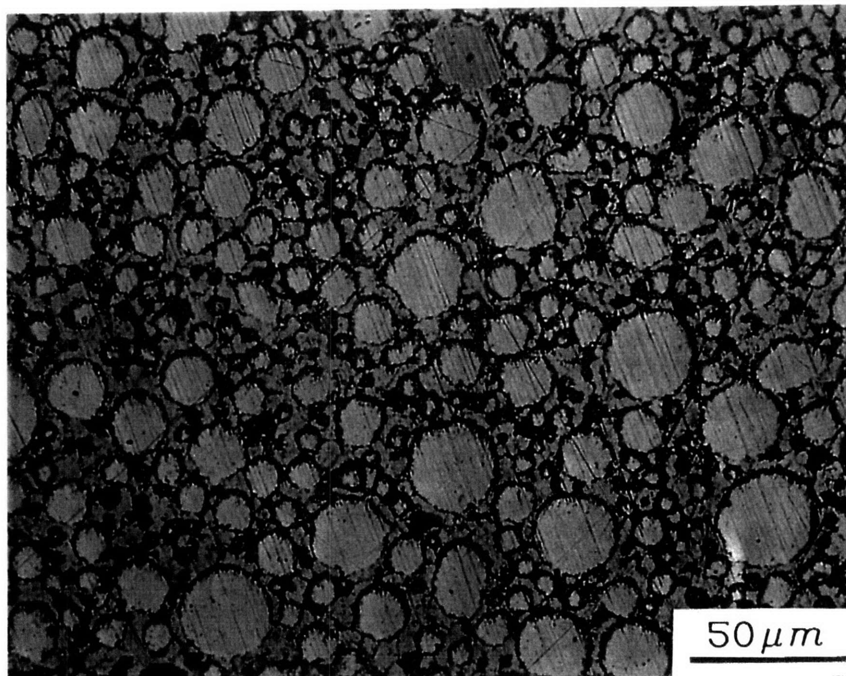

Figure 7.10. Microstructure of an experimental gallium-based dental amalgam after 72 hours of trituration. The particles are Ag-Cu eutectic alloy.